Effect of Doping and Defect Structures on Thermo Physical Properties of Thermoelectric Materials

Khaliq, Jibran

Effect of Doping and Defect Structures on Thermo Physical Properties of Thermoelectric Materials

Jibran Khaliq

Submitted in partial fulfillment of the requirements of the Degree of Doctor of Philosophy

School of Engineering and Materials Science,
Queen Mary, University of London
London, United Kingdom
October 2014

Declaration

I hereby declare that the present work is prepared solely by myself during the course of my doctoral studies at the Queen Mary, University of London. It has not been submitted anywhere for any award. Work of other people is fully acknowledged according to standard referencing.

This thesis fully complies with the regulations set by the University of London and the Queen Mary, University of London.

Jibran Khaliq

October 2014

Abstract

Development of thermoelectric materials to date has focused on materials that can operate at lower temperatures. However; there is now an increased need to develop materials for higher temperature applications. In this research, medium to high temperature oxide and non-oxide thermoelectric materials were fabricated and characterized. For oxide thermoelectric materials, $La_4Ti_4O_{14}$ and $Sr_4Nb_4O_{14}$ were chosen. These compounds are members of the homologous $A_4B_4O_{14}$ series and possess perovskite-like layered structure (PLS). PLS compounds have low thermal conductivity due to a layered structure compared to the perovskite materials (e.g. $SrTiO_3$). These atomic scale layers help to reduce the thermal conductivity of PLS compounds. Doping in PLS materials also creates atomic scale disorders. The effect of acceptor-donor doping and oxidation-reduction on the thermal conductivity of PLS ceramics were investigated in relation to mass contrast and compositional non-stoichiometry. High resolution TEM and XPS revealed that acceptor doping of $La_4Ti_4O_{14}$ produced nanoscale intergrowth regions of n=5 layered phase inside n=4 layered phase, while donor doping produced nanoscale intergrowth regions of n=3 layered structure. As a result of these nanoscale intergrowths, the thermal conductivity value reduced by ~ 20% compared to the theoretical value. Pure $La_4Ti_4O_{14}$ has a thermal conductivity value of ~ 1.1 W/m.K which dropped to a value of ~ 0.98 W/m.K in Sr doped $La_4Ti_4O_{14}$ and ~ 0.93 W/m.K in Ta doped $La_4Ti_4O_{14}$. Pure $Sr_4Nb_4O_{14}$ has a thermal conductivity value of ~ 1.05 W/m.K which dropped to ~ 0.6 W/m.K after La doping. The factors influencing the thermal conductivity of PLS compounds were also discussed.

For non-oxide ceramics, $CoSb_3$ was chosen due to its cage-like structure and ideal for the application of Phonon Glass Electron Crystal Concept. The cage like structure gives room to engineer its electrical and thermal properties without affecting the other. For the first time, $CoSb_3$ stuffed with Yb and substituted with Te ($Yb_yCoSb_{3-x}Te_x$) was synthesized by mechanical alloying and spark plasma sintering. The electrical and thermal properties were characterized for pure and doped material. A Seebeck coefficient value of ~ 160 μV/K was obtained at ~ 600-800 K for $Yb_{0.075}CoSb_{2.85}Te_{0.15}$. The electric resistivity dropped from ~ 1000 μΩm for pure $CoSb_3$ to ~ 9 μΩm for $Yb_{0.075}CoSb_{2.85}Te_{0.15}$. Lattice thermal conductivity was significantly reduced to a very low value of 1.17 W/m.K by the addition of Yb atoms into $CoSb_{2.85}Te_{0.15}$ without significantly affecting its Seebeck coefficient and electrical resistivity. This value is comparable to those produced by the costly processing of nanostructured materials. A zT value of ~ 0.70 was obtained at 600 K.

This research has shown that by engineering the defect chemistry of thermoelectric materials, it is possible to significantly reduce their thermal conductivity without compromising their electrical properties.

Acknowledgement

I would like to express my deepest gratitude to my Supervisor, Prof. Michael John Reece for his excellent guidance, caring, patience, and providing me with an excellent atmosphere for doing research which kept me motivated throughout my PhD. He persuasively conveyed an interest in my work, and I am grateful for my inclusion in his research group. I would also like to thank my secondary supervisor Dr. Haixue Yan, whose critical analysis, illuminating discussions and friendly jokes helped me to produce this piece of research.

I would like to thank Dr. Zofia Luklinska and Dr. Rory Wilson, for their generous help. I would also like to thank Dr. Na Ni and Samuel Jackson for their help with sample characterization.

I acknowledge various stimulating discussions, ideas and support provided by member of our research group Dr. Giuseppe Viola, Dr. Salvatore Grasso, Dr. Huanpo Ning, Dr. Zhipeng Gao, Chunchun Li, Harshit Porwal, Chen Chen, Kan Chen and Qinghui Jiang without their synergistic excellence and ideas, I could possibly not have reached this far.

A special thanks to my family. Words cannot express how grateful I am to my mother and father for all of the sacrifices that they've made on my behalf. Their prayers for me were what sustained me thus far. I would also like to thank my brothers and sister for their endless love and support all through my career. I would also like to thank my parents in law for their love, support and encouragement. I would also like to extend my acknowledgement to all my friends who supported me in writing, and encouraged me to strive towards my goal.

At the end I would like to express appreciation to my beloved wife Amina who spent sleepless nights with me and was always my support in the moments when there was no one to answer my queries. Without any doubt, I dedicate this thesis to my family.

Thanks for the financial support from QMUL and Nanoforce Technology Limited, U.K.

Table of Contents

Abstract i

Acknowledgement iii

Table of Contents v

Chapter I. Introduction 1

References 4

Chapter II. Literature Review 6

2.1 Introduction to thermoelectrics 6

2.2 Efficiency of thermoelectric materials 7

2.3 Thermoelectric Materials 9

2.4 Oxide Thermoelectrics 15

2.5 Perovskite Related Structures 23

2.6 Thermal Conductivity 35

2.7 Oxide Thermoelectric Modules 38

References 40

Chapter III. Experimental Details 50

3.1 Powder Preparation 50

3.2 Sintering by spark plasma sintering 52

3.3 Post Sintering treatment 53

3.4 Characterization 54

References 60

Chapter IV. Characterization of $La_4Ti_4O_{14\pm\delta}$ 61

4.1 Introduction 61

4.2 Experimental Details 62

4.3 $La_{4-x}Sr_xTi_4O_{14-\frac{x}{2}\pm\delta}$ 65

4.4 $La_4Ti_{4-x}Ta_xO_{14+\frac{x}{2}\pm\delta}$ 79

4.5 $La_4Ti_{4-x}Nb_xO_{14+\frac{x}{2}\pm\delta}$ 88

4.6 Conclusion 93

References 94

Chapter V. Characterization of $Sr_4Nb_4O_{14\pm\delta}$ 96

5.1 Introduction 96

5.2 Experimental Details 97

5.3 Results and Discussions 98

5.4 Conclusion 110

References 111

Chapter VI. Thermal Conductivity of PLS Compounds 112

6.1 Introduction 112

6.2 Experimental Details 113

6.3 $La_4Ti_4O_{14}$ 114

6.4 $Sr_{4-x}La_xNb_xO_{14+\frac{x}{2}\pm\delta}$ 135

6.5 Discussions 141

6.6 Conclusion 148

References 149

Chapter VII. Thermoelectric Properties of Co-doped $CoSb_3$ 150

7.1 Introduction 150

7.2 Experimental Details 151

7.3 Results and Discussions 152

7.4 Conclusion 161

References 162

Chapter VIII. Conclusions and Future Work 165

8.1 Conclusion 165

8.2 Future Work 168

List of my publications 170

List of Figures

Figure 2.1: Typical thermoelectric modules: (a) for cooling; (b) for power generation

Figure 2.2: (a) zT values of different thermoelectric materials; (b) development in thermoelectrics over the past 20 years

Figure 2.3: (a) crystal structure of typical skutterudite Rh_4Sb_{12} filled with In (red balls), while blue balls represent Rh atoms and yellow balls Sb atoms; (b) shows a cage formed by 12 Sb atoms with In filler inside

Figure 2.4: Effect of hall carrier concentration on electrical resistivity and Seebeck coefficient

Figure 2.5: Variation of: (a) electrical conductivity; (b) Seebeck coefficient; (c) thermal conductivity; (d) zT for $Yb_{0.2}Co_4Sb_{12}$with temperature

Figure 2.6: Crystal structures of some of the layered cobalt oxides

Figure 2.7: Crystal Structure of ZnO (wurtzite)

Figure 2.8: Typical structure of In_2O_3 crystal

Figure 2.9: Influence of Sn and Ti in In_2O_3 on thermal conductivity and zT

Figure 2.10: Cubic perovskite unit cell. Red spheres represent the A cation, Blue spheres represent the B cation and Grey spheres represent X anions

Figure 2.11: Perovskite crystal structure showing the oxygen

Figure 2.12: Typical structure of distorted $CaMnO_3$

Figure 2.13: Schematic drawing of structure of Aurivillius compounds Bi_2WO_6 (n=1), $SrBi_2Ta_2O_9$ (n=2) and $Bi_4Ti_3O_{12}$ (n=3)

Figure 2.14: Crystal Structure of Dian Jacobson phase $CsBiNb_2O_7$

Figure 2.15: Crystal structure of $Sr_3Ti_2O_7$

Figure 2.16: Structural diagram of non-distorted $A_nB_nO_{3n+2}$ projected along a axis

Figure 2.17: Thermal conductivity as a function of temperature for $Bi_4Ti_3O_{12}$

Figure 2.18: Temperature dependence of power factor, thermal conductivity and figure of merit for rare earth doped $Sr_3Ti_2O_7$

Figure 2.19: Temperature dependence of thermal conductivity of various oxides

Figure 2.20: Crystal Structure of $Sr_4Nb_4O_{14}$

Figure 2.21: Variation in: (a) thermal conductivity; (b) Seebeck coefficient; (c) electrical resistivity with temperature for $Sr_{3.6}La_{0.4}Nb_4O_{14}$

Figure 2.22: Variation of room temperature thermal conductivity with increasing amount of La

Figure 2.23: Thermal conductivity as a function of temperature for the textured and randomly oriented polycrystalline $Sr_{3.9}La_{0.1}Nb_4O_{14}$

Figure 2.24: Crystal structure of pyrochlore $La_2Ti_2O_7$

Figure 2.25: Temperature dependence of thermal conductivity in $CoSb_{3-x}Te_x$

Figure 3.1: (a) QM-3SP4 Planetary ball mill machine (b) carbolite HTF 1800 Chamber furnace

Figure 3.2: Saffron scientific glove box used for powder handling under inert environment

Figure 3.3: Spark Plasma Sintering furnace (FCT, Germany) with a schematic of its chamber

Figure 3.4: Schematic representation of: (a) SPS Die set; (b) photo of the graphite die during SPS process

Figure 3.5: Lab build (in china) electrical resistivity and Seebeck coefficient measurement system

Figure 3.6: Netzsch laser flash LFA 457

Figure 4.1: Typical processing parameters during sintering of: (a) $La_4Ti_4O_{14\pm\delta}$; (b) $La_{3.2}Sr_{0.8}Ti_4O_{13.6\pm\delta}$

Figure 4.2: Photos of ceramic disc: (a) after sintering; (b) after air annealing; (c) after reduction

Figure 4.3: XRD patterns of the $La_{4-x}Sr_xTi_4O_{14-\frac{x}{2}\pm\delta}$: (a) powders; (b) sintered; (c) air annealed; (d) reduced samples

Figure 4.4: Typical SEM images of $La_{3.2}Sr_{0.8}Ti_4O_{13.6\pm\delta}$ powder after calcination: (a) before ball milling; (b) after ball milling

Figure 4.5: SEM images of LST ceramics after polishing and etching: (a) $La_{3.8}Sr_{0.2}Ti_4O_{13.6\pm\delta}$; (b) $La_{3.6}Sr_{0.4}Ti_4O_{13.6\pm\delta}$; (c) $La_{3.6}Sr_{0.6}Ti_4O_{13.6\pm\delta}$; (d) $La_{3.2}Sr_{0.8}Ti_4O_{13.6\pm\delta}$

Figure 4.6: TEM images of air annealed: (a) $La_4Ti_4O_{14\pm\delta}$; (b) high magnification image of $La_4Ti_4O_{14\pm\delta}$;(c) diffraction pattern of the air annealed $La_4Ti_4O_{14\pm\delta}$; (d) $La_{3.2}Sr_{0.8}Ti_4O_{13.6\pm\delta}$ showing the large defect (intergrowth) number; (e) $La_{3.2}Sr_{0.8}Ti_4O_{13.6\pm\delta}$; (f) $La_{3.2}Sr_{0.8}Ti_4O_{13.6\pm\delta}$ showing termination of intergrowths; (g-h) $La_{3.2}Sr_{0.8}Ti_4O_{13.6\pm\delta}$ showing two regions of intergrowths

Figure 4.7: TEM images of reduced: (a) $La_4Ti_4O_{14\pm\delta}$; (b) high magnification image of $La_4Ti_4O_{14\pm\delta}$; (c-d) $La_{3.2}Sr_{0.8}Ti_4O_{13.6\pm\delta}$ showing the large defect (intergrowth) density;(e) a high magnification image of a typical region in $La_{3.2}Sr_{0.8}Ti_4O_{13.6\pm\delta}$ showing intergrowths; (f) corresponding diffraction pattern of $La_{3.2}Sr_{0.8}Ti_4O_{13.6\pm\delta}$

Figure 4.8: XPS spectrum of $La_{4-x}Sr_xTi_4O_{14-\frac{x}{2}\pm\delta}$: (a) La 3d; (b) Ti 2p; (c) O1s; (d) Sr 3d

Figure 4.9: XRD patterns of the $La_4Ti_{4-x}Ta_xO_{14\pm x}$: (a) powders; (b) sintered; (c) air annealed; (d) reduced samples

Figure 4.10: TEM images of: (a) air annealed $La_4Ti_{3.6}Ta_{0.4}O_{14.2\pm\delta}$; (b) high magnification image of air annealed $La_4Ti_{3.6}Ta_{0.4}O_{14.2\pm\delta}$; (c) reduced $La_4Ti_{3.6}Ta_{0.4}O_{14.2\pm\delta}$; (d) high magnification image of reduced d $La_4Ti_{3.6}Ta_{0.4}O_{14\pm\delta}$ (e) high magnification image of reduced d $La_4Ti_{3.6}Ta_{0.4}O_{14.2\pm\delta}$ with d spacing; (f) diffraction pattern of high magnification image of reduced d $La_4Ti_{3.6}Ta_{0.4}O_{14\pm\delta}$

Figure 4.11: XPS spectrum of $La_4Ti_{4-x}Ta_xO_{14+\frac{x}{2}\pm\delta}$: (a) La 3d; (b) Ti 2p; (c) O1s; (d) Ta 4f

Figure 4.12: XRD patterns of the $La_4Ti_{4-x}Nb_xO_{14+\frac{x}{2}\pm\delta}$: (a) powders; (b) sintered; (c) air annealed; (d) reduced samples

Figure 4.13: TEM images of: (a) air annealed $La_4Ti_{3.4}Nb_{0.6}O_{14.3\pm\delta;}$ (b) air annealed $La_4Ti_{3.4}Nb_{0.6}O_{14.3\pm\delta}$ showing region of $LaNbO_4$; (c) typical grain of reduced $La_4Ti_{3.4}Nb_{0.6}O_{14.3\pm\delta}$ ceramic showing $LaNbO_4$ grain; (d) corresponding diffraction pattern of $LaNbO_4$ grain; (e) a typical region showing cluster of $La_4Ti_4O_{14}$ grains in reduced ceramic; (f) a typical $LaNbO_4$ grain showing planar defects in reduced ceramic

Figure 5.1: XRD patterns of $Sr_{4-x}La_xNb_4O_{14+\frac{x}{2}\pm\delta:}$ (a) powder; (b) sintered; (c) air annealed; (d) reduced samples

Figure 5.2: SEM images of $Sr_{4-x}La_xNb_4O_{14\pm\delta}$ ceramics after polishing and etching (a) $Sr_4Nb_4O_{14}$; (b) $Sr_{3.8}La_{0.2}Nb_4O_{14.1\pm\delta}$ and; (c) $Sr_{3.2}La_{0.8}Nb_4O_{14.4\pm\delta}$

Figure 5.3: TEM images of: (a) air annealed $Sr_4Nb_4O_{14}$; (b) high magnification image of air annealed $Sr_4Nb_4O_{14\pm\delta}$; (c) corresponding diffraction pattern for $Sr_4Nb_4O_{14\pm\delta;}$ (d) air annealed $Sr_{3.2}La_{0.8}Nb_4O_{14.4\pm\delta;}$ (e) air annealed $Sr_{3.2}La_{0.8}Nb_4O_{14.4\pm\delta}$ showing regions of $Sr_4Nb_4O_{14}$ and $LaNbO_4$; (f) high magnification image of a single $LaNbO_4$ grain

Figure 5.4: TEM images of: (a) reduced $Sr_4Nb_4O_{14\pm\delta}$; (b) high magnification image of reduced $Sr_4Nb_4O_{14\pm\delta}$; (c-d) typical regions of reduced $Sr_{3.2}La_{0.8}Nb_4O_{14.4\pm\delta}$; (e) high magnification image of a typical Sr/Nb rich region

Figure 5.5: XPS spectrum of $Sr_{3.6}La_{0.4}Nb_4O_{14.2\pm\delta}$: (a) Sr 3d; (b) Nb 3d; (c) O1s and; (d) La3d

Figure 6.1: Variation in thermal diffusivity of $La_{4-x}Sr_xTi_4O_{14\pm\delta}$ ceramics: (a) air annealed; (b) reduced

Figure 6.2: Variation in specific heat capacity of sapphire with temperature

Figure 6.3: Variation in specific heat capacity of: (a) $La_4Ti_4O_{14\pm\delta}$; (b) $La_{3.2}Sr_{0.8}Ti_4O_{13.6\pm\delta}$ ceramics with temperature

Figure 6.4: Variation in specific heat capacity of reduced $La_4Ti_4O_{14\pm\delta}$ with temperature

Figure 6.5: Variation in thermal conductivity of: (a) air annealed $La_{4-x}Sr_xTi_4O_{13.6\pm\delta}$; (b) reduced $La_{4-x}Sr_xTi_4O_{14-\frac{x}{2}\pm\delta}$; (c) $La_{3.2}Sr_{0.8}Ti_4O_{13.6\pm\delta}$; (d) $La_4Ti_4O_{14\pm\delta}$ with temperature

Figure 6.6: Variation of thermal conductivityof reduced $La_{4-x}Sr_xTi_4O_{14-\frac{x}{2}\pm\delta}$ with Sr content at 573 K

Figure 6.7: Variation in thermal diffusivity of $La_4Ti_{4-x}Ta_xO_{14+\frac{x}{2}\pm\delta}$ ceramics: (a) air annealed; (b) reduced

Figure 6.8: Variation in specific heat capacity of: (a) $La_4Ti_4O_{14\pm\delta}$; (b) $La_4Ti_{3.4}Ta_{0.6}O_{14.3\pm\delta}$ ceramics with temperature

Figure 6.9: Variation in thermal conductivity of: (a) air annealed $La_4Ti_{4-x}Ta_xO_{14+\frac{x}{2}\pm\delta}$; (b) reduced $La_4Ti_{4-x}Ta_xO_{14+\frac{x}{2}\pm\delta}$; (c) $La_4Ti_4O_{14\pm\delta}$; (d) $La_4Ti_{3.4}Ta_{0.6}O_{14.3\pm\delta}$ with temperature

Figure 6.10: Variation of thermal conductivity with Ta content for reduced $La_4Ti_{4-x}Ta_xO_{14+\frac{x}{2}\pm\delta}$ at 573 K

Figure 6.11: Variation in thermal diffusivity of $La_4Ti_{4-x}Nb_xO_{14+\frac{x}{2}\pm\delta}$ ceramics: (a) air annealed; (b) reduced

Figure 6.12: Variation in specific heat capacity of: (a) $La_4Ti_4O_{14\pm\delta}$; (b) $La_4Ti_{3.4}Nb_{0.6}O_{14.3\pm\delta}$ ceramics with temperature

Figure 6.13: Variation in thermal conductivity of: (a) air annealed $La_4Ti_{4-x}Nb_xO_{14+\frac{x}{2}\pm\delta}$; (b) reduced $La_4Ti_{4-x}Nb_xO_{14+\frac{x}{2}\pm\delta}$; (c) $La_4Ti_4O_{14\pm\delta}$; (d) $La_4Ti_{3.4}Nb_{0.6}O_{14.3\pm\delta}$ with temperature

Figure 6.14: Variation of thermal conductivity with Nb content for reduced $La_4Ti_{4-x}Nb_xO_{14+\frac{x}{2}\pm\delta}$ at 573 K

Figure 6.15: Variation in thermal diffusivity of $Sr_{4-x}La_xNb_4O_{14+\frac{x}{2}\pm\delta}$ ceramics: (a) air annealed; (b) reduced

Figure 6.16: Variation in specific heat capacity of: (a) $Sr_4Nb_4O_{14\pm\delta}$; (b) $Sr_{3.2}La_{0.8}Nb_4O_{14.4\pm\delta}$ ceramics with temperature

Figure 6.17: Variation in thermal conductivity of: (a) air annealed $Sr_{4-x}La_xNb_4O_{14\pm\delta}$; (b) reduced $Sr_{4-x}La_xNb_4O_{14+\frac{x}{2}\pm\delta}$; (c) $Sr_4Nb_4O_{14\pm\delta}$; (d) $Sr_{3.2}La_{0.8}Nb_4O_{14.4\pm\delta}$ with temperature

Figure 6.18: Variation of thermal conductivity with La content at 573 K: (a) air annealed and; (b) reduced

Figure 6.19: Schematic representation of a typical non distorted $La_4Ti_4O_{14}$ projected along a axis

Figure 7.1: (a) X ray diffraction patterns for $CoSb_3$ based materials, (b) SEM micrograph of $CoSb_3$

Figure 7.2: Variation of: (a) electrical resistivity; (b) Seebeck coefficient with temperature for $CoSb_3$ compositions

Figure 7.3: Variation of: (a) total thermal conductivity; (b) lattice thermal conductivity with temperature for $CoSb_3$ based compositions

Figure 7.4: Components of total thermal conductivity with T^{-1} for YCST

Figure 7.5: Temperature dependence of zT for $CoSb_3$ based compositions

List of Tables

Table 4.1: Theoretical and relative densities of $La_{4-x}Sr_xTi_4O_{14-\frac{x}{2}\pm\delta}$ ceramics

Table 4.2: amount of 5 layer PLS compound in $La_{4-x}Sr_xTi_4O_{14-\frac{x}{2}\pm\delta}$ ceramics

Table 4.3: XPS data of $La_{4-x}Sr_xTi_4O_{14-\frac{x}{2}\pm\delta}$ ceramics

Table 4.4: Theoretical and relative densities of $La_4Ti_{4-x}Ta_xO_{14+\frac{x}{2}\pm\delta}$ ceramics

Table 4.5: FWHM of the $La_4Ti_{3.6}Ta_{0.4}O_{14.2\pm\delta}$ ceramics

Table 4.6: XPS data of $La_4Ti_{3.6}Ta_{0.4}O_{14.2\pm\delta}$ ceramics

Table 4.7: Theoretical and relative densities of $La_4Ti_{4-x}Nb_xO_{14+\frac{x}{2}\pm\delta}$ ceramics

Table 5.1: Theoretical and relative densities of $Sr_{4-x}La_xNb_4O_{14+\frac{x}{2}\pm\delta}$ ceramics

Table 5.2: Amount of 2 layer PLS compound in $Sr_{4-x}La_xNb_4O_{14+\frac{x}{2}\pm\delta}$ ceramics

Table 5.3: Percentage mass amount of different elements in $Sr_{4-x}La_xNb_4O_{14+\frac{x}{2}\pm\delta}$ ceramics

Table 5.4: XPS data of $Sr_{3.2}La_{0.4}Nb_4O_{14.2\pm\delta}$ ceramics

Table 6.1: Change in measured densities after Sr substitution and hydrogen reduction

Table 6.2: Change in measured densities after Ta substitution and hydrogen reduction

Table 6.3: Change in measured densities after Nb substitution and hydrogen reduction

Table 6.4: Change in measured densities after La substitution and hydrogen reduction

Table 6.5: Relative Formula weights, mean atomic volume and minimum thermal conductivity of $La_4Ti_4O_{14}$ and $Sr_4Nb_4O_{14}$ based compositions

Table 6.6: Phonon mean free path and Debye temperature for air annealed $La_4Ti_4O_{14}$ and $Sr_4Nb_4O_{14}$ based compositions

Chapter I. Introduction

With increasing demand for energy, there is a need to develop new and efficient ways to generate energy. Current efficiencies of internal combustion engines and power generation plants are in the range of 30-38% with the remaining energy being wasted into the environment as heat [1]. This heat can be utilized usefully, for example, to generate electricity. Thermoelectric materials are one class of environment friendly materials that can convert heat into electricity [2]. Unlike traditional generators and engines, thermoelectric modules have no moving parts, and are light weight with little to no service needed. These modules are not as efficient (efficiency is <6%) as traditional generators and engines, but for smaller applications, they are competitive with other technologies [3].

In order to establish the potential difference in a thermoelectric material, the temperature gradient must be maintained which allows the electrons to flow from the hot side to the cold side. For an ideal thermoelectric material, the thermal conductivity must be on the lower side (typical values < 1W/m.K). Also, a high electrical conductivity material (~ $8x10^5$ S/m) is necessary to produced significant flow of electrons [4]. The efficiency of a thermoelectric material depends upon electrical conductivity (σ) and thermal conductivity (κ) and simultaneously on Seebeck coefficient (S). These three quantities are linked together by a dimensionless quantity zT.

$$zT=\frac{\sigma S^2}{\kappa} \qquad (1.1)$$

One can increase either Seebeck coefficient or electrical conductivity or lower thermal conductivity to make an efficient thermoelectric material. A zT value of ~ 2 has been reported [5] which gives an efficiency of ~ 8.6% across a temperature difference of 200 ^{o}C [6], which could be doubled if a zT value of 3 was achievable across the same temperature range. As all of these properties are interconnected, it is therefore difficult to improve the efficiency. This research focuses on the effect of structural defects and compositional non stoichiometry on the thermal conductivity of oxide and non-oxide materials.

Typical examples of thermoelectric materials are Bi_2Te_3, PbTe, skutterudites ($CoSb_3$, $FeSb_3$ and $ZnSb_3$), silicides (Mg_2Si and $MnSi_{1.72-1.74}$) and layered oxides ($Ca_3Co_4O_9$, $Sr_4Nb_4O_{14}$, $SrTiO_3$). Commercially used bismuth telluride (Bi_2Te_3) operates near room temperature due to its low melting point and maximum efficiency at this temperature [7]. Power generation industries involve applications of thermoelectric materials at high temperatures (> 800 ^{o}C) [8] and thermoelectric materials with high operating temperatures are desirable. The focus of this research will therefore be on skutterudites and oxides thermoelectric materials.

Skutterudites are efficient for intermediate temperature applications (25 ^{o}C to ~ 600 ^{o}C) [9, 10], such as cobalt antimonide ($CoSb_3$) [11]. $CoSb_3$ has a cubic structure (space group Im3) with two naturally formed atomic cages per unit cell. It has a melting point of 873 ^{o}C [12] but its high thermal conductivity (~ 10 W/m.K) limits its zT value [13]. Skutterudites are good compounds for utilizing the idea of a phonon glass electron crystal (PGEC), in which electrical properties are separated from thermal properties and optimized at the same time [14]. Their cage like structure favours the PGEC approach and can be partially filled with a variety of atoms like rare earths or alkali metals [15]. These atoms are loosely bonded and

rattle inside the cage which causes phonons to scatter, which effectively decreases thermal conductivity without degrading the electrical properties [16, 17].

Oxide thermoelectric materials on the other hand possess higher melting temperatures and they are chemically stable in air. The perovskite-like layer structure (PLS) materials belongs to the homologous series of $A_nB_nO_{3n+2}$ where n denotes the number of BO_6 octahedral layers. These materials inherently have lower thermal conductivity values due to their layered structure. These layers scatter phonon more efficiently giving low thermal conductivity compared to the perovskite materials which are the end member of the homologous series $A_nB_nO_{3n+2}$ (with $n=\infty$). For example, single crystal $Sr_4Nb_4O_{14}$ has a thermal conductivity of ~ 2 W/m.K [18] while $SrTiO_3$ has a much higher thermal conductivity of ~ 12 W/m.K [19]. The reason for anomalously low thermal conductivity for PLS compounds lies in the fact that both PLS and perovskite compounds have the same thickness of the octahedral layers, but PLS compounds have a layered crystal structure [20]. These atomic scale layers help to reduce thermal conductivity by creating extra phonon scattering centres.

Due to the unique crystal structure of skutterudite and PLS materials, it is desirable to research these materials for their low thermal conductivity. This work focuses on the investigation of skutterudites and PLS materials fabricated by Spark plasma sintering. Thermal conductivity and microstructure of the materials were studied in relation to the compositional non stoichiometry and oxidation-reduction.

REFERENCES

[1] K.M. Saqr, M.N. Musa, Therm Sci, 13 (2009) 165-174.

[2] G.F. Rinalde, L.E. Juanico, E. Taglialavore, S. Gortari, M.G. Molina, International Journal of Hydrogen Energy, 35 (2010) 5818-5822.

[3] F.J. Weinberg, D.M. Rowe, G. Min, J Phys D Appl Phys, 35 (2002) L61-L63.

[4] G. Min, Journal of Electronic Materials, 39 (2010) 2459-2461.

[5] R. Venkatasubramanian, E. Siivola, T. Colpitts, B. O'Quinn, Nature, 413 (2001) 597-602.

[6] G. Chen, D. Kraemer, A. Muto, K. McEnaney, H.P. Feng, W.S. Liu, Q. Zhang, B. Yu, Z.F. Ren, Micro- and Nanotechnology Sensors, Systems, and Applications Iii, 8031 (2011).

[7] O.C. Yelgel, G.P. Srivastava, Journal of Applied Physics, 113 (2013).

[8] R. Funahashi, S. Urata, Int J Appl Ceram Tec, 4 (2007) 297-307.

[9] G. Li, J.Y. Yang, Y. Xiao, L.W. Fu, J.Y. Peng, Y. Deng, P.W. Zhu, H.X. Yan, Journal of Electronic Materials, 42 (2013) 675-678.

[10] J.J. Zhang, B. Xu, L.M. Wang, D.L. Yu, Z.Y. Liu, J.L. He, Y.J. Tianb, Applied Physics Letters, 98 (2011).

[11] A. Harnwunggmoung, K. Kurosaki, H. Muta, S. Yamanaka, Applied Physics Letters, 96 (2010) 202107.

[12] H.Y. Geng, S. Ochi, J.Q. Guo, Applied Physics Letters, 91 (2007).

[13] G.S. Nolas, M. Kaeser, R.T. Littleton, T.M. Tritt, Applied Physics Letters, 77 (2000) 1855.

[14] G.A. Slack, New Materials and Performance Limits for Thermoelectric Cooling, in: D.M. Rowe (Ed.) CRC Handbook of Thermoelectrics, CRC, Boca Raton, 1995, pp. 407.

[15] B.C. Sales, D. Mandrus, R.K. Williams, Science, 272 (1996) 1325-1328.

[16] X. Shi, H. Kong, C.P. Li, C. Uher, J. Yang, J.R. Salvador, H. Wang, L. Chen, W. Zhang, Applied Physics Letters, 92 (2008) 182101.

[17] H. Li, X.F. Tang, Q.J. Zhang, C. Uher, Applied Physics Letters, 93 (2008).

[18] A. Sakai, T. Kanno, K. Takahashi, A. Omote, H. Adachi, Y. Yamada, X.D. Zhou, Journal of the American Ceramic Society, 95 (2012) 1750-1755.

[19] H. Muta, K. Kurosaki, S. Yamanaka, Journal of Alloys and Compounds, 392 (2005) 306-309.

[20] T.D. Sparks, P.A. Fuierer, D.R. Clarke, Journal of the American Ceramic Society, 93 (2010) 1136-1141.

Chapter II. Literature Review

2.1 INTRODUCTION TO THERMOELECTRICS

Thermoelectrics are materials which have the ability to convert a temperature gradient to an electromotive force by utilizing the Seebeck effect. Although this effect was discovered in the earlier part of the 19th century [1], thermoelectric generation was only practical in the second half of the 20th century [2]. The voltage generated by metals is low (~ 50 µV/K) while semiconductors can generate much higher voltages (several hundreds of µV/K). A thermoelectric module is a device fabricated by using n type (in which electrons are the charge carriers) and p type (in which holes are the charge carriers) elements to enhance the overall voltage. These two elements are connected electrically in series and thermally in parallel as shown in Figure 2.1.

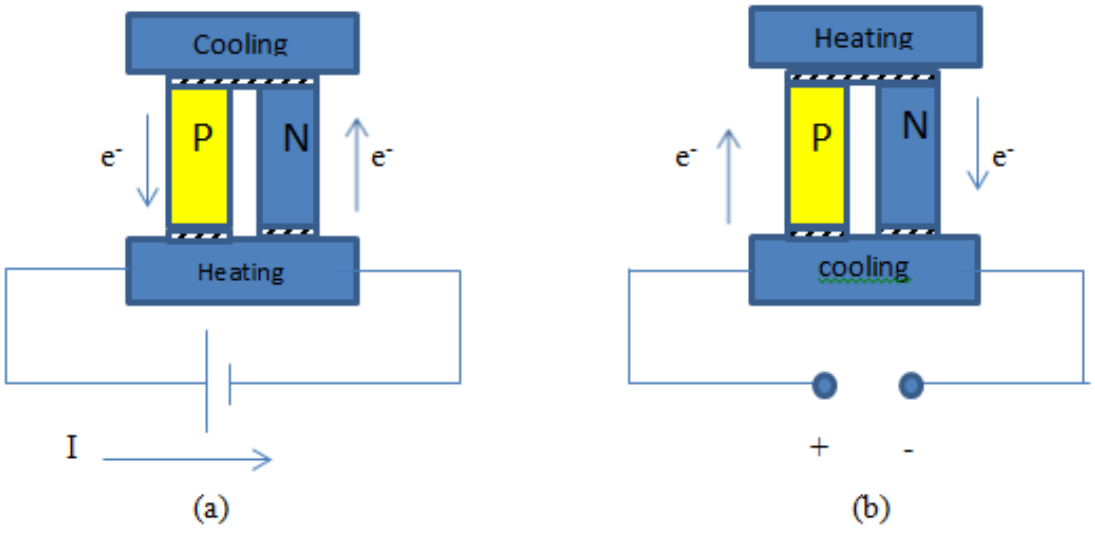

Figure 2.1: *Typical thermoelectric modules: (a) for cooling; (b) for power generation*

2.2 EFFICIENCY OF THERMOELECTRIC MATERIALS

Generally the performance of a thermoelectric material is expressed in the form a dimensionless figure of merit zT. 'zT' denotes the figure of merit of a thermoelectric material, while 'ZT' denotes the figure of merit of a thermoelectric module.

$$ZT = \frac{\sigma S^2}{\kappa} T \qquad (2.1)$$

Where σ is electrical conductivity, S is the seebeck coefficient, κ is thermal conductivity and T is absolute temperature. A high Seebeck coefficient, high electrical conductivity and low thermal conductivity make for an efficient thermoelectric material. zT values of more than 2 have been reported to date [3-5]. The efficiency of a thermoelectric material is given by [6]

$$\Phi = \frac{\Delta T}{T_h} . \frac{(\sqrt{1+zT}-1)}{(\sqrt{1+zT}+\frac{T_c}{T_h})} \qquad (2.2)$$

ΔT is the temperature difference between the hot and the cold side. T_h is the temperature of the hot side (in Kelvin) and T_c is the temperature of the cold side. Efficiencies of 5-10% have been reported so far [7].

Apart from the figure of merit, a more convenient term to use is power factor, which is defined as $S^2\sigma$. This term is useful because S and σ depend more strongly on charge carrier concentrations while κ depends more strongly on the lattice contribution to thermal conductivity [8]. However all of these properties are

interconnected and it is therefore difficult to improve zT. Since electrical conductivity and Seebeck coefficient are inversely proportional to each other, a compromise has to be made between these two to obtain optimum values. Semiconductors are the better choice for thermoelectric materials since they have reasonable Seebeck coefficient and electrical conductivity values and can be further tuned by doping to improve power factor values. Slack suggested the idea of the phonon glass electron concept (PGEC) in which the electrical properties are separated from thermal properties [9]. By utilizing the PGEC, thermal conductivity can be reduced significantly without affecting electrical conductivity and the Seebeck coefficient [10]. The material is ideally designed in such a way that it behaves as a glass in terms of scattering phonons to give a low thermal conductivity. At the same time the material has the electrical properties of a narrow band gap semiconductor. Skutterudites are the best example to illustrate this concept which will be discussed later.

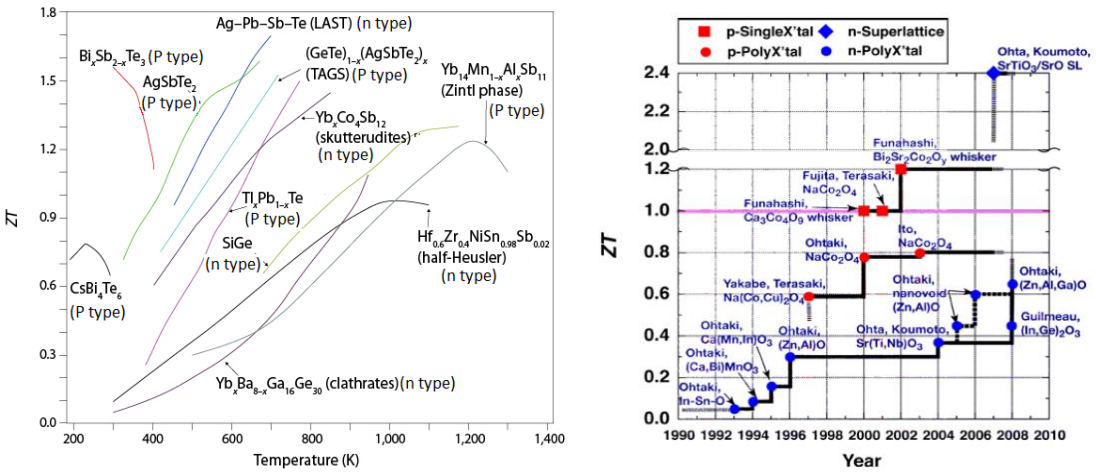

Figure 2.2: *(a) zT values of different thermoelectric materials [11]; (b) development in thermoelectrics over the past 20 years [12]*

Until the 1990s, conventional thermoelectric materials were developed based on the above mentioned characteristics. These materials tend to have heavy elements for lower thermal conductivity and covalent bonding character for higher charge mobility. Examples of these kinds of materials are Bi_2Te_3 [13] and PbTe [14]. Figure 2.2 shows typical thermoelectric materials and the improvement in zT with time for thermoelectric materials. Bi_2Te_3 is the most widely used thermoelectric material due to its high inherent Seebeck coefficient value of (200 μV/K) and electrical conductivity ($2x10^5$ S/m) [15]. Great care must be taken during fabrication of these materials as they readily oxidise when left in open air. The toxicity of these materials is also a big issue and the powders of these materials must be kept under a controlled environment.

2.3 THERMOELECTRIC MATERIALS

2.3.1 Skutterudites

Skutterudites have the general formula AX_3 where A is a transition metal such as Co or Rh and X is a pnicogen (a member of group 15 of periodic table) atom such as As or Sb. Each transition metal forms a MX_6 octahedra by coordinating with 6 pnicogen atoms. It has a cubic structure with 32 atoms per unit cubic cell as shown in Figure 2.3.

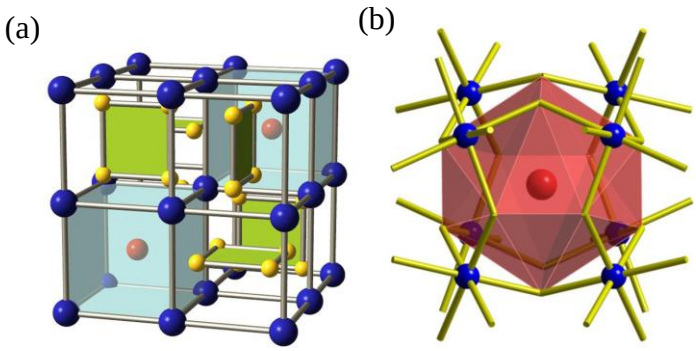

Figure 2.3: *(a) crystal structure of typical skutterudite Rh_4Sb_{12} filled with In (red balls), while blue balls represent Rh atoms and yellow balls Sb atoms; (b) shows a cage formed by 12 Sb atoms with In filler inside [16]*

Skutterudites such as cobalt antimonide ($CoSb_3$) [19] have been the focus of research for intermediate temperature thermoelectric applications (298 K to 850 K) [17, 18]. Caillat et al. first compared thermoelectric properties of single crystalline n and p type $CoSb_3$ grown by the gradient freeze technique [20]. They estimated the effective mass of holes and electrons using hall mobility and Seebeck coefficient measurements. The hall mobility of p type was much higher than the n type at room temperature and their effect on Seebeck coefficient and electrical resistivity is shown in the Figure 2.4.

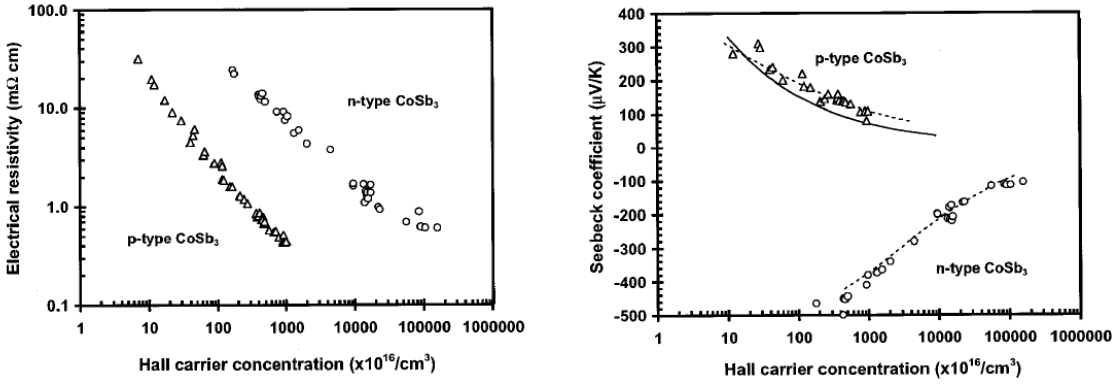

Figure 2.4: *Effect of hall carrier concentration on electrical resistivity and Seebeck coefficient [20]*

Despite their good power factor values, the thermal conductivity of Skutterudites is on the higher side (~ 10 W/m.K) [10]. As mentioned earlier, the crystal structure of skutterudites is excellent for applying the PGEC concept. It has interstitial space for dopant elements that can be filled without changing the structure. The doping elements drastically change the thermoelectric properties especially thermal conductivity and increase zT values. The phonon mean free path is kept as small as possible while the electron mean free path as long as possible [21,22]. Sales et. al first reported Ce and La filled $Fe_{4-x}Co_xSb_{12}$ by melt quenching and hot pressing [23]. They reported a zT value of ~ 1 at 800 K with further enhancement to 1.4 after optimizing the composition. This high zT value was the result of low thermal conductivity caused by the ‘‘rattling’’ of La or Ce atoms inside the cage like structure of $FeSb_3$.

Chen et al. found that the 44 % of the cages in $CoSb_3$ can be filled if Ba is used as filler [24]. They used a two-step method for synthesising this composition. In the first step, $BaSb_3$ was synthesised by reacting Ba and Sb at 903 K and then in the second step, additional Sb and Co were added and melted at 1323 K. Increasing Ba concentration decreased the Seebeck coefficient, but increased electrical and thermal conductivity which achieved a zT value of 1.1 at 850 K.

Indium and Ce doping into the cage like structure of $CoSb_3$ gave a zT value of 1.43 at 800 K [25]. The materials were prepared by melt spinning and park plasma sintering. The Seebeck coefficient increased with increasing indium doping due to an increased carrier concentration. Indium formed nanoscale $InSb_2$ phase precipitates in the matrix which was believed to enhance the Seebeck coefficient. For double filled $CoSb_3$ with Yb and Ba, synthesised by melt spinning and spark plasma sintering, a zT value of ~ 1 at 773 K was reported [26]. They used different speeds of the

quenching wheel which affected the individual thermoelectric properties, but the overall zT remained almost the same. The minimum thermal conductivity obtained was ~ 3.2 W/m.K, which is still higher for the doped $CoSb_3$ materials. Double filled Yb and Ba and Fe substituted $CoSb_3$ synthesised by melting, annealing and hot pressing had a thermal conductivity value of 1.8 W/m.K. This is amongst the lowest values reported for skutterudite materials. The power factor on the other hand had a lower value than Yb and Ba filled $CoSb_3$ [26].

Li et al. reported a high zT value of 1.22 at 800 K in Yb filled $CoSb_3$ [27]. The ingots of $Yb_{0.2}Co_4Sb_{12}$ were prepared by melt quenching. These ingots were inserted into a cylindrical quartz tube and melt spun at different speeds to obtain thin ribbons which were then sintered by SPS. They concluded that higher speeds of melt spinning increased the purity of the phase and decreased grain size. This affected the thermal conductivity and also contributed in increasing the Seebeck coefficient, while electrical conductivity seemed independent of the speed as shown in Figure 2.5.

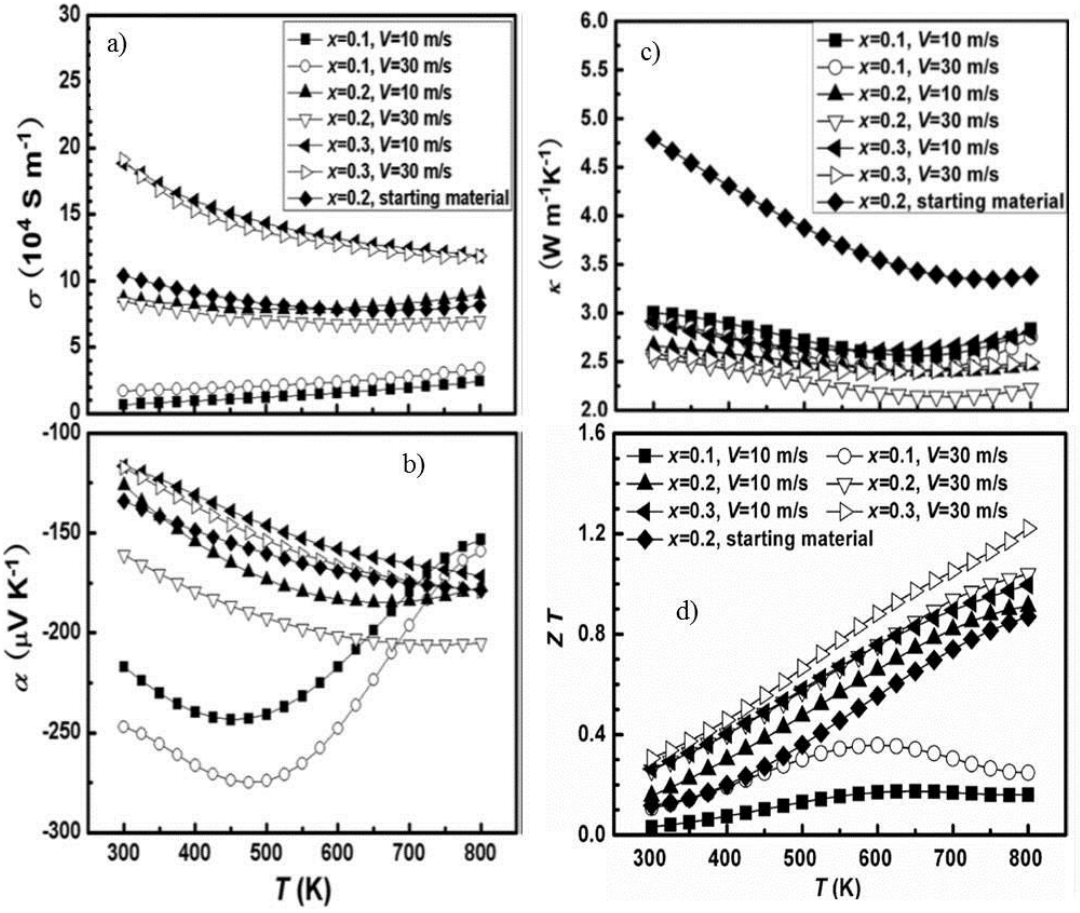

Figure 2.5: *Variation of: (a) electrical conductivity; (b) Seebeck coefficient; (c) thermal conductivity; (d) zT for $Yb_{0.2}Co_4Sb_{12}$ with temperature [27]*

Changing the amount of Sb in $Yb_{0.2}CoSb_{3+y}$ increased the zT slightly reaching a value of 1.26 at 800 K for $Yb_{0.2}CoSb_{12.3}$ [28]. Air annealing had no effect on overall zT [29], which suggests that materials melt spun in air are stable.

P type skutterudite, $FeSb_3$ had a zT value of ~ 0.9 at 800 K when filled with Ce and synthesised by melt spinning and SPS [30]. $Ce_yFe_{8-x}Ni_xSb_{24}$ was prepared by melt spinning, but its thermoelectric properties were not reported [31].

$CoSb_3$ has a melting point of 873^oC [32] with high carrier concentration and Seebeck coefficient (~ 60 μV/K) [33]. However, due to strong covalent bonding, the intrinsic thermal conductivity is ~ 10 W/m.K, which is a high value for thermoelectric applications [34]. This high thermal conductivity limits the zT of

$CoSb_3$ based materials. Nano structuring is another way to reduce thermal conductivity of $CoSb_3$, but it also decreases its electrical conductivity by creating more scattering centres for electrons [35]. In addition, making nanostructured materials is not a cost effective processing route. In order to improve the electrical properties of $CoSb_3$, tellurium (Te) substitution for antimony (Sb) is effective [36]. A significant reduction in electrical resistivity for $Co_4Sb_{12-x}Te_x$ was observed as compared to pure $CoSb_3$ because Te serves as an electron donor in the $CoSb_3$ structure [37, 38].

$CoSb_3$ has a cubic structure (Space group Im3) with two naturally formed atomic cages per unit cell. These cages favour the PGEC approach and can be partially filled with a variety of atoms like rare earths or alkali metals [23]. These atoms are loosely bonded and rattle inside the cage, which causes phonons to scatter and effectively decreases thermal conductivity without degrading the electrical properties [39, 40]. Ytterbium (Yb) is an effective additive to the $CoSb_3$ structure due to its high atomic mass and small size. By partially filling the cages in $CoSb_3$ structure with Yb, the thermal conductivity is significantly decreased [41] while only slightly affecting Seebeck coefficient and electrical resistivity [34]. Tellurium (Te) substitution for antimony (Sb) is effective in improving the electrical properties of $CoSb_3$, [36]. A significant reduction in electrical resistivity for $Co_4Sb_{12-x}Te_x$ was observed as compared to pure $CoSb_3$ because Te serves as an electron donor in the $CoSb_3$ structure [37, 38].

In terms of industrial applications, it is desirable for both the n and p type legs of a thermoelectric module to have similar thermal and mechanical properties to avoid any mechanical or thermal stress during thermal cycling. $CoSb_3$ is an excellent

choice for medium temperatures as both n and p type materials can be made from the same material.

2.4 OXIDE THERMOELECTRICS

High processing cost, toxicity, low working temperatures (doped Bi_2Te_3 working temperature less than 200^oC) and environmental hazards of traditional thermoelectric materials are always a concern. This has stimulated the idea of using oxides as thermoelectrics. Oxide materials on the other hand use nontoxic, inexpensive and environmentally friendly elements. They are stable in air even at higher temperatures (> 500^oC). Oxide thermoelectrics generally have low Figure of merit as compared to the bismuth telluride and skutterudites, but these materials have no or less effect on environment and are chemically stable.

In the 1980s researchers started looking into oxide thermoelectrics. They first investigated oxide superconductors, but their thermoelectric power values were only in the order of a few μV/K [42, 43]. The superconductors did not appear to be promising materials for thermoelectric application; however the layered cobalt oxides showed some promising high thermoelectric performance [44, 45].

2.4.1 Layered Cobalt oxides and cobaltate

Layered cobalt oxides and cobaltate structures offer promising thermoelectric properties due to phonon scattering at the interface between the layers giving low thermal conductivity [44]. All of these oxides have a CdI_2 type structure with CoO_2 layers alternatively stacked with various NaCl type block layers (Figure 2.5), except

for $NaCo_2O_4$ which has Na atoms inserted in between the CoO_2 sheets. The most commonly investigated compounds of the layered oxide thermoelectric materials are Na_xCoO_2, $Ca_3Co_4O_9$ and $Ca_2Co_2O_5$ as shown in Figure 2.6.

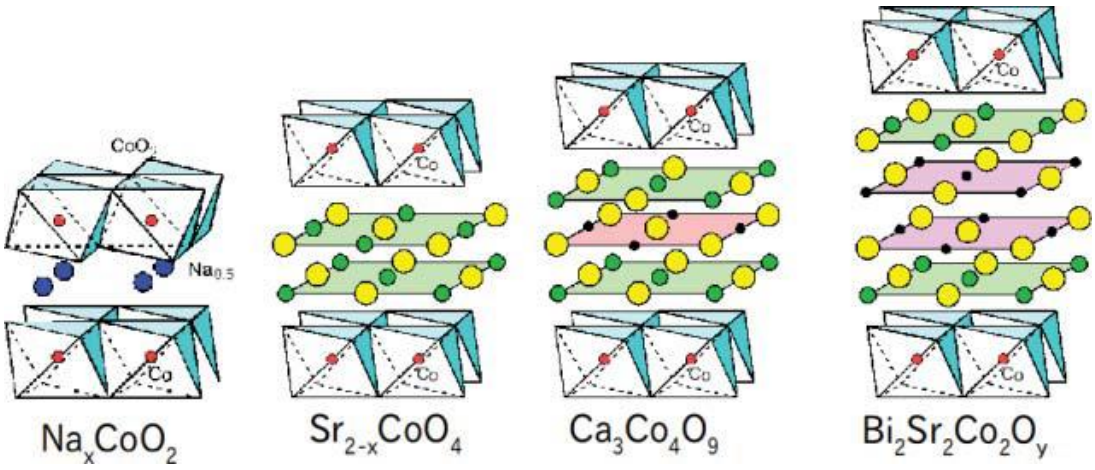

Figure 2.6: *Crystal structures of some of the layered cobalt oxides [45]*

Terasaki et al. reported the power factor of $NaCo_2O_4$ to be higher than Bi_2Te_3 at room temperature, which set the ground for oxide thermoelectric research [46]. In general, the zT values for $NaCo_2O_4$ remained the same for doped and undoped materials [47, 48]. On the other hand $Na_xCo_2O_4$ has low humidity resistance and the volatility of Na is a big issue in controlling its composition. In addition Na forms electrically insulating compounds which decreases thermoelectric properties [12]. $Ca_3Co_4O_9$ and $Ca_2Co_2O_5$ are more commonly used due to their chemical and compositional stability. Due to a strong anisotropy in the structure, single crystal $Ca_3Co_4O_9$ shows enhanced thermoelectric properties compared to the bulk polycrystalline ceramic. Single crystal $Ca_3Co_4O_9$ reported to have a zT value of 0.87 at 973 K [49], but for polycrystalline $Ca_3Co_4O_9$ the zT value was ~ 0.3 at 1000 K [50]. Sintered $Ca_3Co_4O_9$ nanofibres densified by SPS were reported to have a zT value of 0.16 at 800 K [51]. Partially doped $Ca_3Co_4O_9$ with Bi was estimated to

produce a zT value of 1.2 -2.7 for single crystal $Ca_2Co_2O_5$ whiskers at temperatures greater than 873 K [52].

2.4.2 ZnO based thermoelectrics

ZnO is a well-known wide band gap semiconductor which exists in two crystallographic forms, hexagonal (wurtzite), cubic (zinc blende). Wurtzite is the most stable under ambient conditions and shown in Figure 2.7. ZnO is n type semiconductor with a band gap of ~ 3.3 eV at room temperature and a carrier mobility of 200 cm^2/Vs for the single crystal [53]. One disadvantage of ZnO is a high thermal conductivity which is around 54 W/m.K for the single crystal [54] and 30 W/m.K. for the bulk ceramic at 300 K [55].

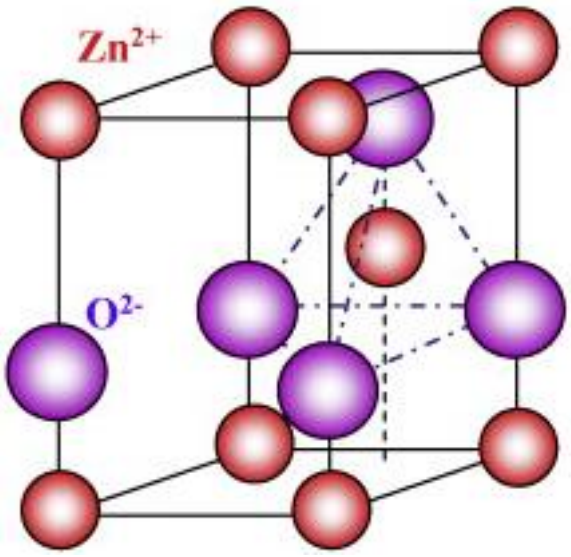

Figure 2.7: *Crystal Structure of ZnO (wurtzite) [56]*

Al is the most commonly used dopant in ZnO. A small amount of Al significantly increases the electrical conductivity [57]. Ohtaki et al. reported that double doping of ZnO with Al and Ga achieved a zT value of 0.65 at 1247 K with a

room temperature thermal conductivity of 5W/mK [58]. Attempts have been made to decrease thermal conductivity, but it degrades the electrical conductivity and Seebeck coefficient which in turn decreases zT. Al doped ZnO nanocomposite showed a thermal conductivity of 2 W/m.K but produced a lower zT of 0.44 [59]. Similarly MgO doped $Zn_{1-x}Al_xO$ suppressed the thermal conductivity to half the value of undoped ZnO, but it decreased electrical conductivity which in turn was unsuccessful in improving zT [60].

2.4.3 Indium based oxides

Indium oxide (In_2O_3) is highly electrically conductive and is used in many industrial applications as a conductive coating. It has bixibyite type cubic crystal structure (Figure 2.8). It has an electrical conductivity value of 0.34×10^5 S/m [61] while its thermal conductivity value is ~ 10 W/m.K.

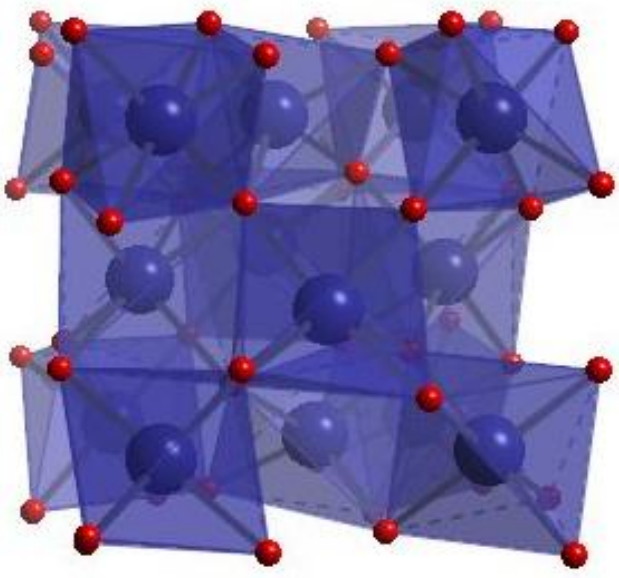

Figure 2.8: *Typical structure of In_2O_3 crystal*

Ge doping in In_2O_3 reduced its thermal conductivity from 10 W/m.K to 3 W/m.K, which in turn gave a zT value of 0.46 at 1273 K [62]. The thermal conductivity was reduced by scattering of phonons from the fine precipitates of $In_2Ge_2O_7$. Ce doped nanostructured In_2O_3 was reported to have a zT value of 0.4 at 1050 K by reducing the thermal conductivity to 2.2 W/m.K, but sacrificing on electrical conductivity [63]. SPS processing and Co doping produced ceramic with a grain size of 0.3-0.4 µm. This resulted in a thermal conductivity value of 1.8 W/mK for 80 % dense material, which is the lowest ever thermal conductivity reported for an indium based oxide [64]. Despite very low thermal conductivity, the zT value was 0.26 at 1073 K due to a decrease in the Seebeck coefficient value.

Guilmeau et. al found that low doping levels of Ti, Zr, Sn, Ta and Nb (0.002-0.006 mole percent) in In_2O_3 gives the highest zT [61] since higher doping levels tend to increase thermal conductivity due to an increase in the electronic part of thermal conductivity as shown in Figure 2.9.

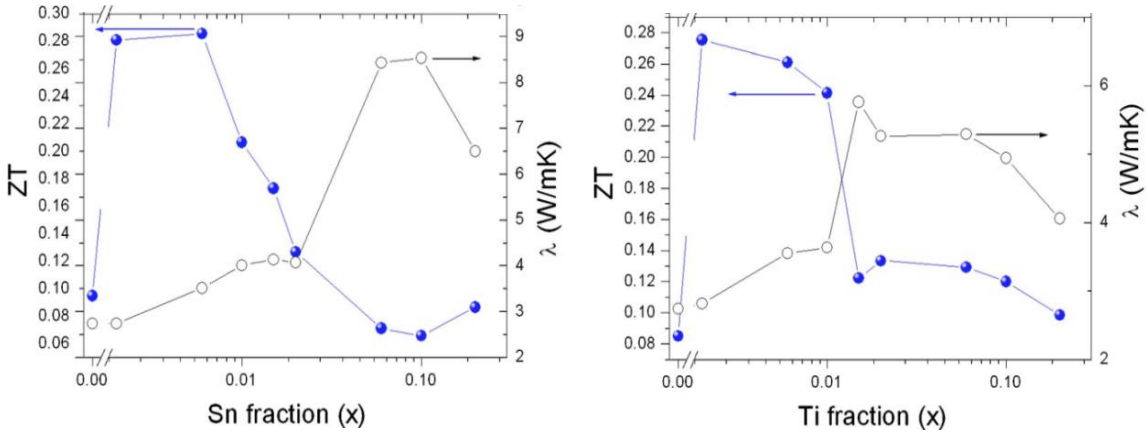

Figure 2.9: *Influence of Sn and Ti in In_2O_3 on thermal conductivity and zT*

2.4.4 Perovskite

In 1839 Gustav Rose discovered the mineral Perovskite ($CaTiO_3$) which was named in the honour of Russian Mineralogist Lev Alexeievich Perovsky [65]. After its discovery, many compounds with similar stoichiometric ratio and structure were identified. Figure 2.10 represents a typical perovskite unit cell.

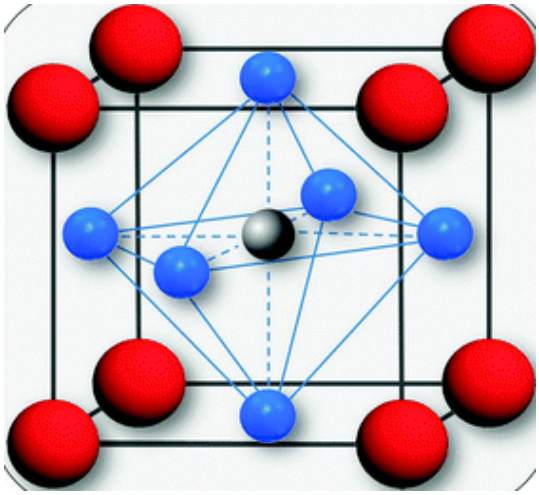

Figure 2.10: *Cubic perovskite unit cell. Red spheres represent the A cation, Blue spheres represent the B cation and Grey spheres represent X anions [66]*

The structure of perovskite is described by a general formula ABX_3, where A and B are cations and X is an anion. Generally, the A cations are large and are positioned at the corners of the cube while the B cations are small and positioned at the centre of the unit cell in an octahedrally coordinated site. Both of the cations can have a variety of charges. Oxygen is the anion and it occupies the face centred position in the cube. The perovskite structure is more commonly represented in the form of oxygen octahedra with B cations in the centre of octahedra and A cation in between the oxygen octahedra. The octahedra are generally connected to each other by the corner giving a typical perovskite structure as shown in Figure 2.11. For these

reasons, the perovskite structure has great flexibility to accommodate different elements and these octahedral layers can give rise to different layered compounds with highly anisotropic properties. Examples of compounds with perovskite structure are $CaTiO_3$, $CaMnO_3$ and $BaTiO_3$.

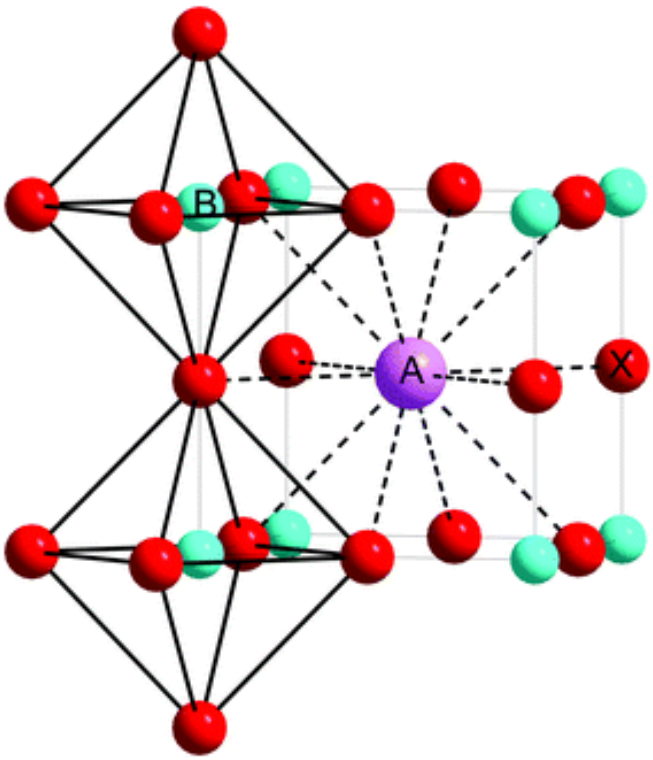

Figure 2.11: *Perovskite crystal structure showing the oxygen octahedra [67]*

2.4.4.1 Strontium Titanate

$SrTiO_3$ has a cubic perovskite structure at room temperature (space group $Pm\bar{3}m$) with a wide band gap of ~ 3.2 eV. It has applications in the field of superconductivity, ferroelectricity and dielectric capacitors. In the pure form, $SrTiO_3$ does not behave as a good thermoelectric material but doping, alloying and introduction of oxygen vacancies can significantly enhance its thermoelectric properties [68]. Kinaci et al. discussed the effect of dopants on the electronic transport properties of $SrTiO_3$ ceramic [69]. At higher concentration of dopants (12

mol. %), lattice thermal conductivity is reduced due to an increase in scattering centres, but the electronic part of the thermal conductivity also increased.

La doping increased the zT value of $SrTiO_3$ by increasing its carrier concentration and reached a value of ~ 0.37 at 1073 K for single crystal $SrTiO_3$ [70] and 0.21 for polycrystalline $SrTiO_3$ [71]. The oxygen vacancies and La doping acted as electron donors which increased the electrical conductivity. La doped $SrTiO_3$ sintered using SPS produced a zT value of 0.37 at 1045 K, which is the highest value for La doped $SrTiO_3$ poly crystals [72].

Nb doping in $SrTiO_3$ created larger carrier effective mass by expanding the unit cell resulted in a higher Seebeck coefficient. A zT value of 0.27 at 1073K was obtained when Nb was doped into single crystal $SrTiO_3$ [70], while Nb doping of epitaxial thin films gave a zT value of 0.37 [73]. A Seebeck coefficient value of 480 μV/K was reported for a single layer of Nb doped $SrTiO_3$ due to strong confinement of electrons. From this idea a two dimensional electron gas was fabricated at the interface of a $TiO_2/SrTiO_3$ interface and a huge increase in Seebeck coefficient value was observed. The value reached up to 1050 μV/K at room temperature. By taking the minimum thermal conductivity of $SrTiO_3$ based materials, a theoretical zT value of ~ 2.4 was calculated [74].

2.4.4.2 Manganates

$CaMnO_3$ has a typical perovskite structure as shown in Figure 2.12. It has a room temperature electrical resistivity value of 0.3 Ωcm [75]. Substitution of Ca^{2+} ions by trivalent ions greatly enhances the transport properties [75] and the octahedral layers help to reduce thermal conductivity by scattering more phonons.

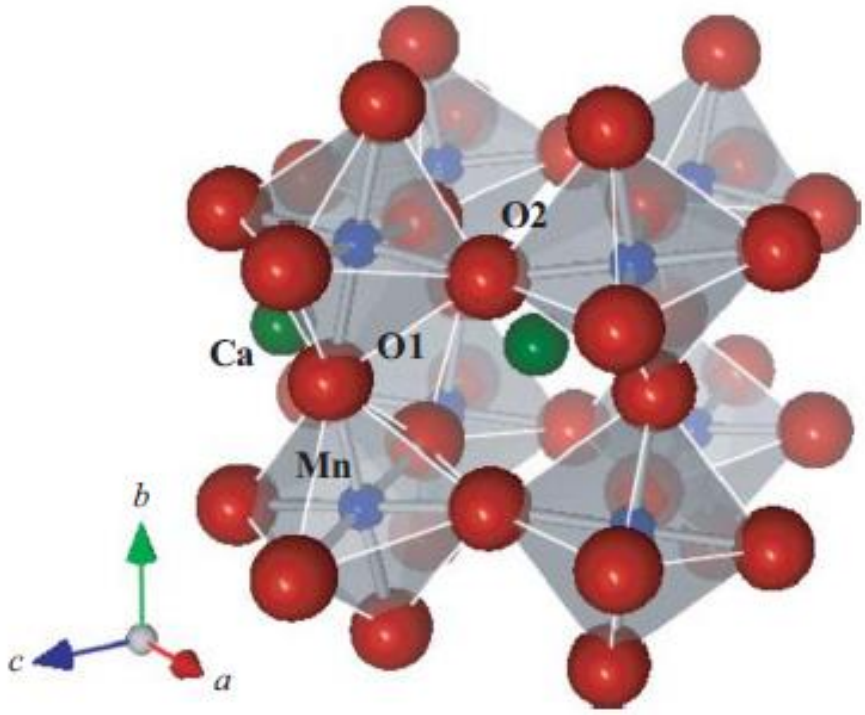

Figure 2.12: *Typical structure of distorted $CaMnO_3$ [76]*

Formation of oxygen vacancies during fabrication process should be avoided in n type material, because they degrade the electrical conductivity [77]. Ultrasonic combustion synthesis of Nb doped $CaMnO_3$ yielded very fine spheroidal particles (10-50 nm) of manganate phase [78]. A zT value of 0.32 was reported at 1060 K. A low thermal conductivity value of ~ 0.5 W/m.K was reported in 67-80% dense samples, which can be related to the phonon scattering from the pores.

2.5 PEROVSKITE RELATED STRUCTURES

Layered perovskite structures have attracted attention due to their highly anisotropic properties. By orienting the planes in one preferred direction, their properties can be tuned to optimise their thermoelectric properties. There are many

structures related to the perovskite structure. Examples of these types of structures are Aurivillius [79], Dion Jacobson structure [80], Ruddlesden-Popper (RP) [81] and Perovskite Like Layered Structure (PLS) [82].

Aurivillius phases are composed of perovskite blocks with general formula $A_{n-1}B_nO_{3n+1}$ separated and shared by alternating Bi_2O_2 layers. A can be mono, di or trivalent element (or combination), B is a transition element and n is the number of octahedral layers in the perovskite structure [83]. The representative compounds include Bi_2WO_6 (n=1), $SrBi_2Ta_2O_9$ (n=2) and $Bi_4Ti_3O_{12}$ (n=3) as shown in Figure 2.13.

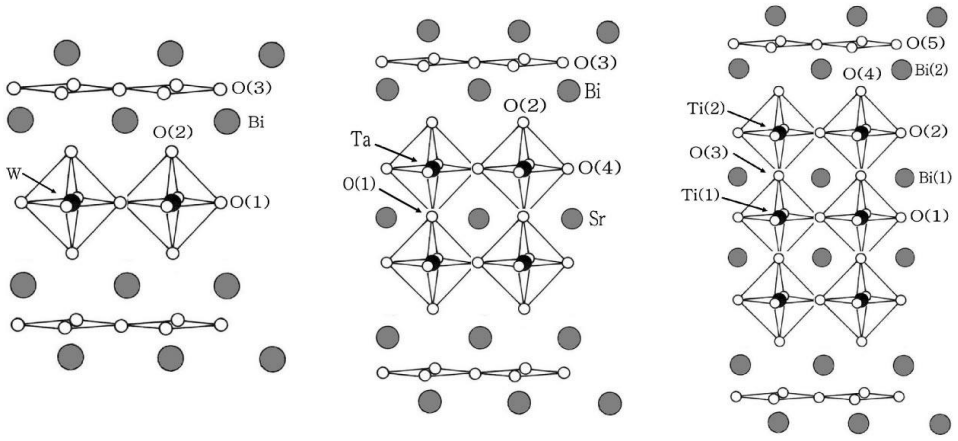

Figure 2.13: *Schematic drawing of structure of Aurivillius compounds Bi_2WO_6 (n=1), $SrBi_2Ta_2O_9$ (n=2) and $Bi_4Ti_3O_{12}$ (n=3) [83]*

Dion-Jacobson type phases ($A'A_{n-1}B_nO_{3n+1}$), perovskite-like layered structure (PLS) ($A_nB_nO_{3n+2}$) and hexagonal type phases $A_nB_{n-1}O_{3n}$ are related structures and they can be considered by cutting the cubic perovskite ABO_3 structure along [100], [110] and [111] direction, respectively and inserting an additional row of oxygen. The respective structure is given in the Figure 2.14.

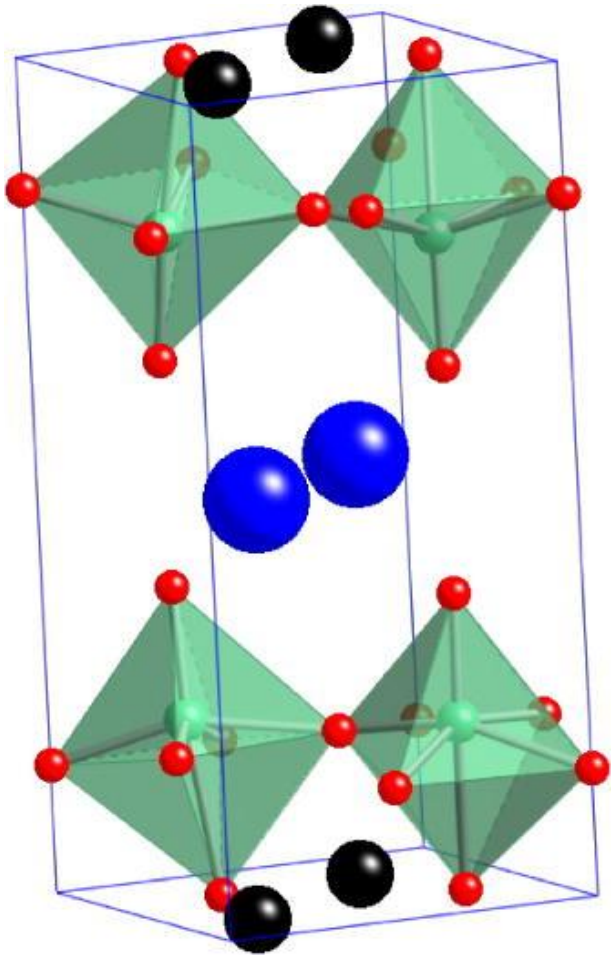

Figure 2.14: *Crystal Structure of Dian Jacobson phase $CsBiNb_2O_7$ [84]*

Ruddlesden-Popper (RP) phases are another type of layered perovskites, They have the general formula $A_{n+1}B_nO_{3n+1}$ (or $AO(ABO_3)_n$) where B is Ti, Mn, Al or Nb. There crystal structure generally consists of alternating perovskite type layer of ABO_3 located within the rock salt type layers of AO. Corner sharing BO_6 octahedra form layers, with A cations occupying the interstitial sites with 9 and 12 coordination. The first characterised RP phases were the $SrO(SrTiO_3)n$ series by Ruddlesden and Popper [85] and shown in Figure 2.15.

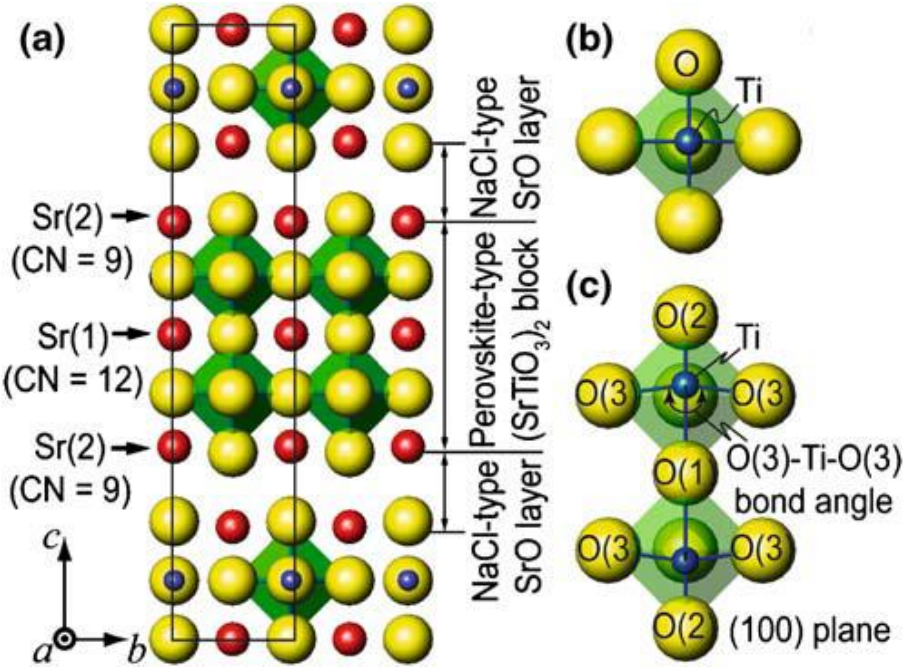

Figure 2.15: *Crystal structure of $Sr_3Ti_2O_7$ [86]*

$A_nB_nO_{3n+2}$ (PLS) compounds are formed by the perovskite layers when they are cut through the (110) plane of the cubic perovskite structure. n in the general formula represents the number of BO_6 octahedra (or layers) in one block. In the case of a mixed number of layers, n specifies the average number of octahedral layers per block. The A cations are often alkaline earth or lanthanide metals and the B cations are usually titanium, tantalum or niobium. The general formula for all the PLS compound is same but they have different structure and properties due to different numbers of layers, different tilting of BO_6 octahedra and displacement of A and B cations [87].

Figure 2.16 shows some of the common PLS compounds with different numbers of layers (n =2 to ∞).

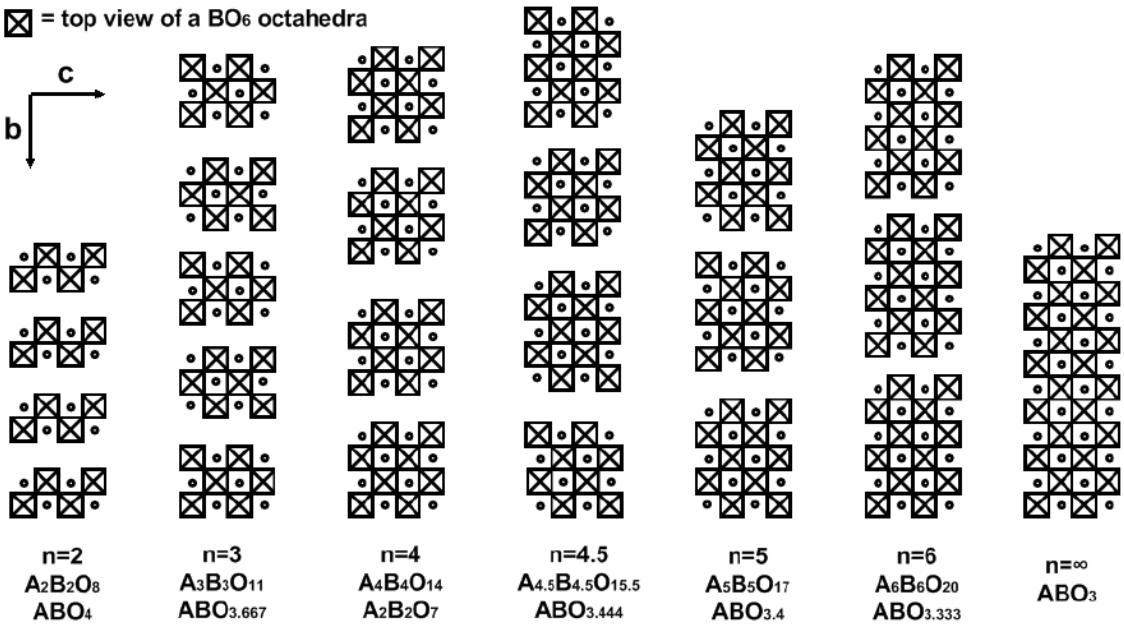

Figure 2.16: *Structural diagram of non-distorted $A_nB_nO_{3n+2}$ projected along a axis*

2.5.1 Properties of Layered Perovskite Thermoelectrics

Layered perovskites have been studied extensively for their ferroelectric and piezoelectric properties. These materials are known for their high curie points. The Curie temperature is defined as the temperature at which a material experiences a phase transition from (low-temperature) ferroelectric to (high-temperature) paraelectric phase. $La_4Ti_4O_{14}$ has a curie point of 1485 ^oC [88] while $Sr_4Nb_4O_{14}$ has 1325 ^oC [82]. As mentioned before, $SrTiO_3$ doped ceramics tend to have high thermo power values in the range of -550 to -700 µV/K [89, 90]. However, due to their relatively high thermal conductivity (~ 10 W/m.K), their zT value are very low. In layered perovskite structure ceramics, for instance the RP structure, they tend to have a rock salt type layer in between the perovskite structure. This rock salt layer serves as a phonon scattering centre, which decreases the phonon mean free path and as a result lowers its thermal conductivity. These kinds of structural features are common

in layered perovskite structures which make them available to use in variety of applications for example in thermal barrier coatings [91, 92]. By tuning the stoichiometry, thermoelectric properties of layered perovskites can be enhanced [93].

2.5.1.1 Aurivillius Structure Thermoelectrics

$Bi_4Ti_3O_{12}$ is a member of the aurivillius family with n= 3. Its structure can be defined by alternate stacking of $[Bi_2O_2]^{2+}$ and $[Bi_2Ti_3O_{10}]^{2-}$ layers. Randomly oriented ceramics of $Bi_4Ti_3O_{12}$ have a thermal conductivity value of ~ 1.5 W/m.K which decreased to ~ 1W/m.K when textured and shown in Figure 2.17 [94]. This tells that the thermal conductivity is anisotropic in these materials and depends on the orientation. The reason for such a low thermal conductivity is the phonon mean free path being equal to the interatomic spacing along the pressing direction and it cannot be reduced further which also explains the nearly temperature independent nature of thermal conductivity [94].

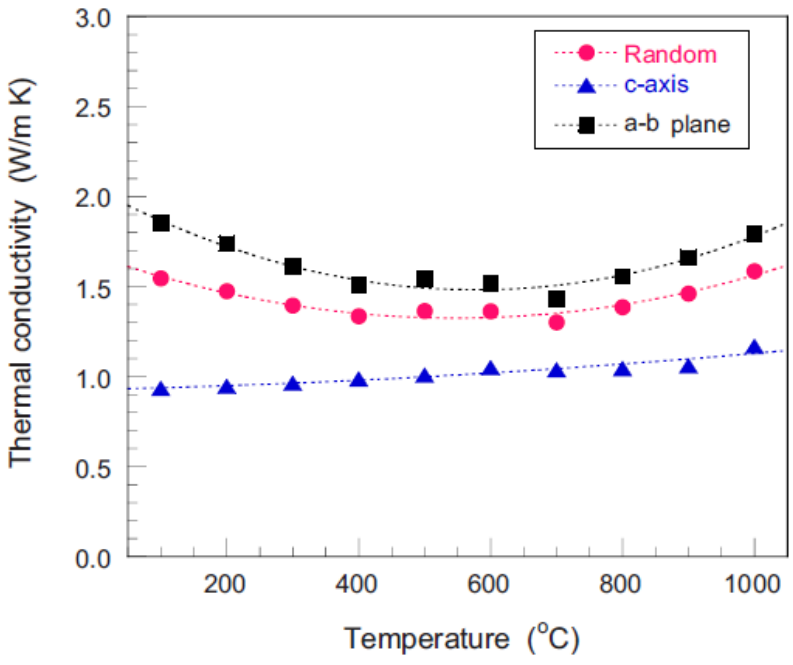

Figure 2.17: *Thermal conductivity as a function of temperature for $Bi_4Ti_3O_{12}$ [94]*

2.5.1.2 Ruddlesden Popper (R-P) Structure Thermoelectrics

$Sr_{n+1}Ti_nO_{3n+1}$ with n = 2 is the most studied thermoelectric material in the RP family. This structure has alternate stacking of NaCl type SrO and a perovskite type $SrTiO_3$ layer. This structure combines the excellent carrier transport features of $SrTiO_3$ with phonon scattering at the interface. $Sr_3Ti_2O_7$ structures exhibit anisotropic properties and showed a 50% drop in thermal conductivity at room temperature when doped with Nb as compared to Nb doped $SrTiO_3$ along the longest axis [86]. It is observed that the electrical conduction behaviour of Nb and rare earth doped $Sr_3Ti_2O_7$ is almost the same. The electrical conductivity decreased with increasing temperature for all compositions. A zT value of 0.25 was obtained for Gd doped $Sr_3Ti_2O_7$ as shown in Figure 2.18.

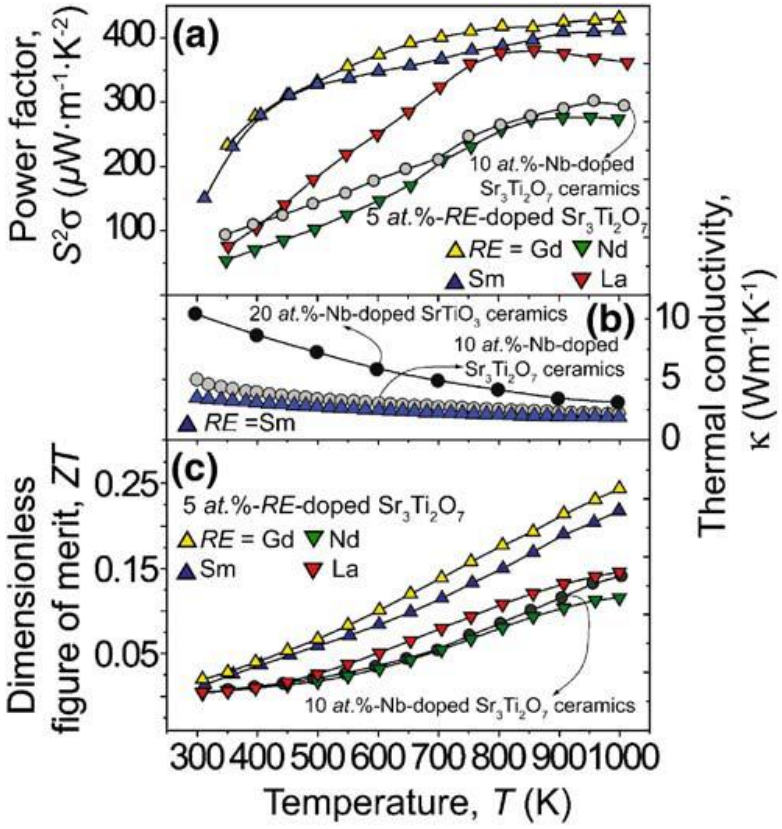

Figure 2.18: *Temperature dependence of power factor, thermal conductivity and figure of merit for rare earth doped $Sr_3Ti_2O_7$ [86]*

Double substitution of Gd and Ta in $Sr_3Ti_2O_7$ resulted in a lower thermal conductivity value (~ 3.4 W/m.K), but the Seebeck coefficient dropped [95]. This was due to the decrease in the effective mass of the charge carriers. Double substitution of Ca and Nb in $Sr_3Ti_2O_7$ gave a thermal conductivity value of ~ 4 W/m.K which decreased with increasing temperature [96]. The Seebeck coefficient also dropped as the amount of dopant increased showing similar trends to Gd and Ta substitution in $Sr_3Ti_2O_7$ giving a zT value of ~ 1.5 at 1000 K. Single substitution of Nb or La resulted in a zT value of 0.15 at 1000 K [97, 98]. This increase in zT was due to the increased electrical conductivity and Seebeck coefficient values. These results suggest single doping to be more effective than double doping.

2.5.1.3 Dion Jacobson Structure Thermoelectrics

Epitaxial layers of $CsBiNb_2O_7$ showed an extremely low thermal conductivity of 0.4 W/m.K, when they were synthesised by pulsed laser deposition technique. The reason for this ultra-low thermal conductivity is unknown, but the author relates it to the large amount of defects in the crystal structure [99]. These results may not be accurate due to the difficulty in physical property measurement of thin films which incorporates large errors. Figure 2.19 compares thermal conductivity of $CsBiNb_2O_7$ with other materials.

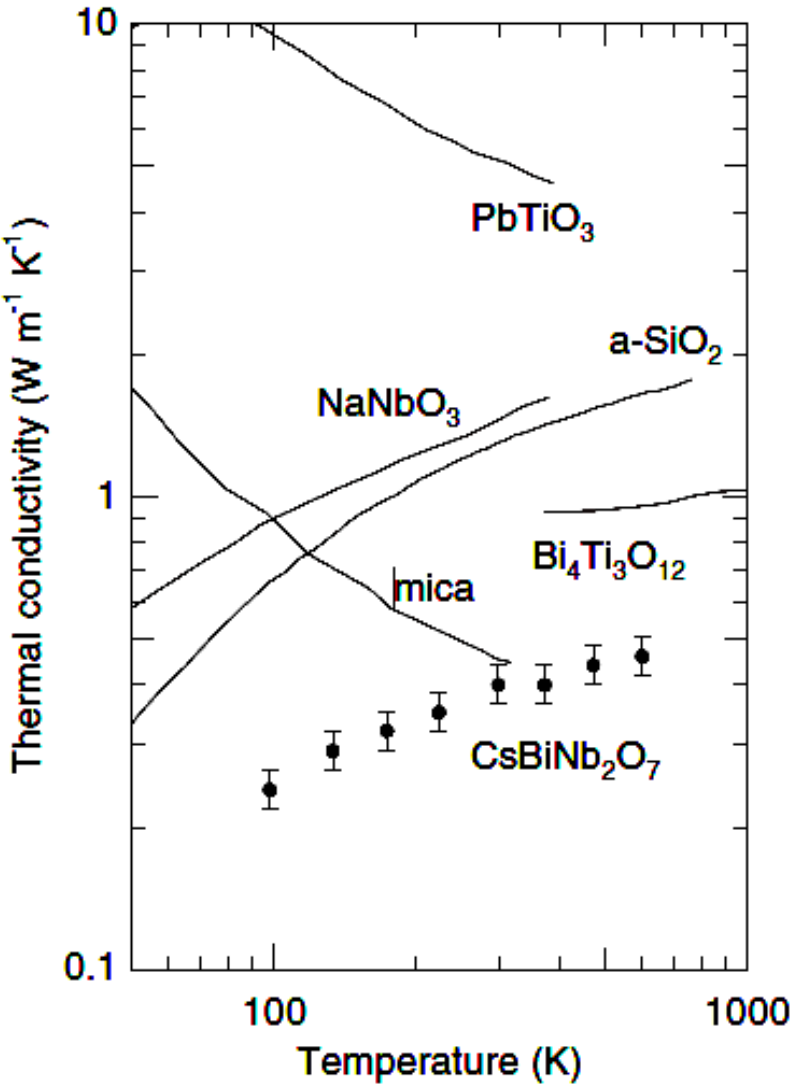

Figure 2.19: *Temperature dependence of thermal conductivity of various oxides [47]*

2.5.1.4 $A_4B_4O_{14}$ Thermoelectrics

$A_4B_4O_{14}$ compounds belong to the PLS compounds ($A_nB_nO_{3n+2}$) with n=4 i.e. the unit cell contains 4 octahedral layers. Their molecular formula is $A_4B_4O_{14}$, but they are best known by their empirical formula $A_2B_2O_7$. Examples of these structures are $Sr_4Nb_4O_{14}$, $La_4Ti_4O_{14}$ and $Ca_4Nb_4O_{14}$ [82, 100, 101].

$Sr_4Nb_4O_{14}$ is also one of the derivatives of the layered perovskite structures with general formula of $Sr_nNb_nO_{3n+2}$ (n=4) n denotes the number of corner shared

NbO_6 octahedra layers as shown in Figure 2.20. It has orthorhombic crystal system and space group of Cmc21. The lattice parameters for $Sr_4Nb_4O_{14}$ are a=3.933 Å, b=26.726 Å, c=5.683 Å [102].

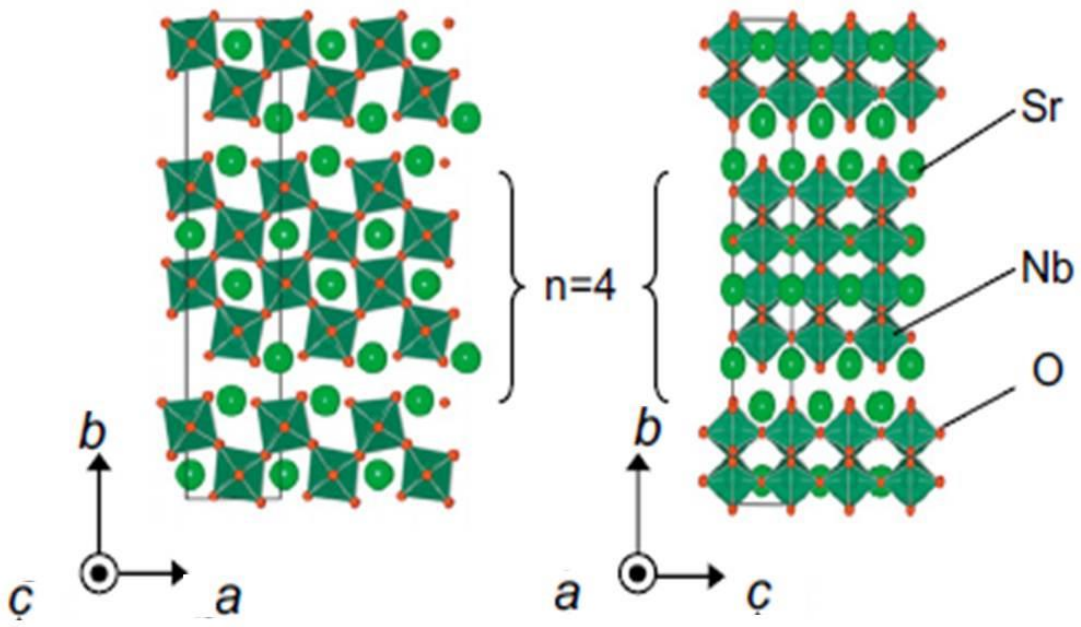

Figure 2.20: *Crystal Structure of $Sr_4Nb_4O_{14}$ [93]*

$Sr_4Nb_4O_{14}$ is a wide band gap semiconductor which makes it inherently insulator but 1 mol % doping of La in a single crystal makes it electrically conductive [93]. The single crystal was prepared by the floating zone method under a mixture of Ar+0.75%H_2. The room temperature resistivity across the b axis is high as compared to the other two axes due to the scattering of electrons from NbO_6 octahedral layers. Thermal conductivity also behaved in the same way and a very low thermal conductivity value of 0.4 W/m.K was observed along the b axis as shown in Figure 2.21. Similar results were obtained by Kobayashi et al. [103].

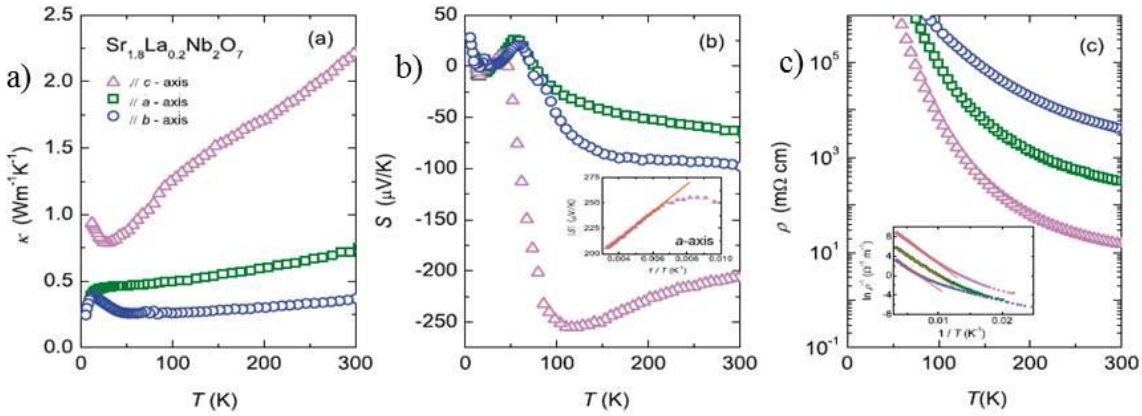

Figure 2.21: *Variation in: (a) thermal conductivity; (b) Seebeck coefficient; (c) electrical resistivity with temperature for* $Sr_{3.6}La_{0.4}Nb_4O_{14.2\pm\delta}$ *[94]*

When more La was added to the $Sr_4Nb_4O_{14}$ the thermal conductivity dropped further [104]. The measurement was done for all the axes but La doped $Sr_4Nb_4O_{14}$ showed better properties along the c axis. The trend in thermal conductivity with increasing La content along c axis is shown in the Figure 2.22.

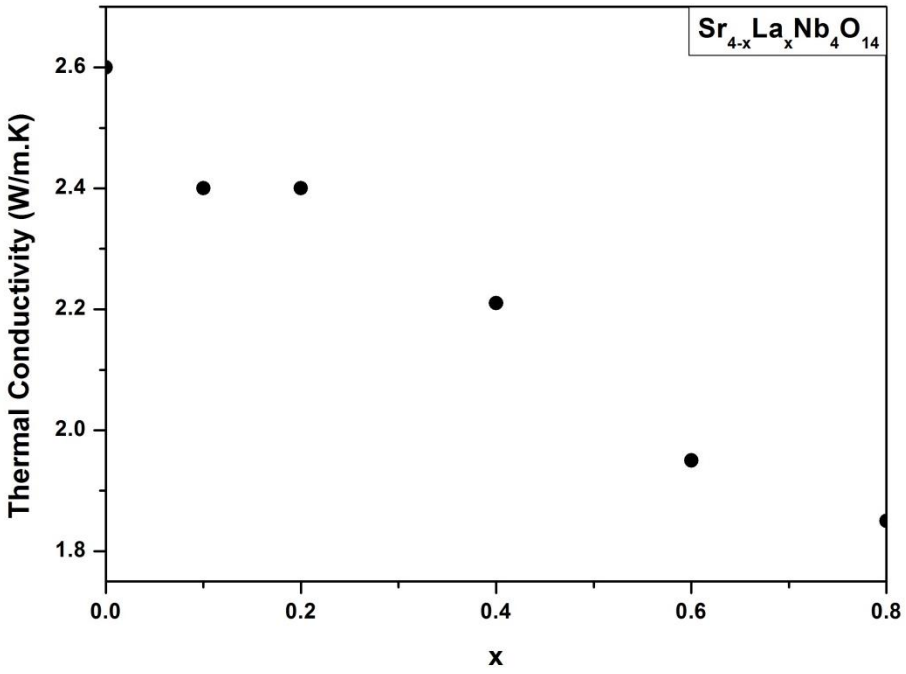

Figure 2.22: *Variation of room temperature thermal conductivity with increasing amount of La [104]*

In the case of polycrystalline ceramics, prepared by the co precipitation method, the thermal conductivity remained almost temperature independent [105]. Textured ceramics had lower values of thermal conductivity along the pressing direction as compared to the randomly oriented ceramics as shown in Figure 2.23. This was due to the phonon mean free path approaching the distance between perovskite blocks and the length of individual perovskite blocks.

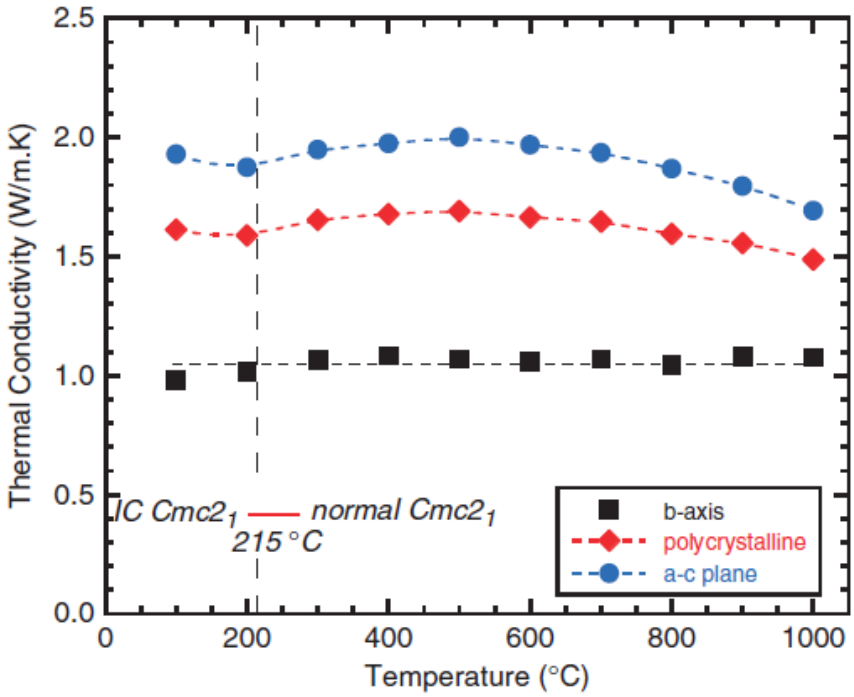

Figure 2.23: *Thermal conductivity as a function of temperature for the textured and randomly oriented polycrystalline* $Sr_{3.9}La_{0.1}Nb_4O_{14}$ *[105]*

The room temperature crystal structure of $La_4Ti_4O_{14}$ has been observed to be monoclinic. The lattice parameters are a = 7.80 Å, b = 13.011 Å and c = 5.546 Å and $\beta = 98.6^{o}$ with space group $P2_1$ [105]. At 780 ^{o}C the monoclinic structure transforms into an orthorhombic structure and the lattice parameters change to a = 3.954 Å, b = 25.952 Å and c = 5.607 Å with space group $Cmc2_1$. PLS $La_4Ti_4O_{14}$ doped with Sr

showed an electrical conductivity value of $3.4x10^{-6}$ S/cm at 700 ^{o}C [107]. Calculated minimum thermal conductivity value was found to be 1.46 W/m.K [106] but the measured value was 2.28 W/m.K at room temperature [108].

Apart from PLS, $La_4Ti_4O_{14}$ also exists in pyrochlore form which has cubic crystal structure as shown in Figure 2.24.

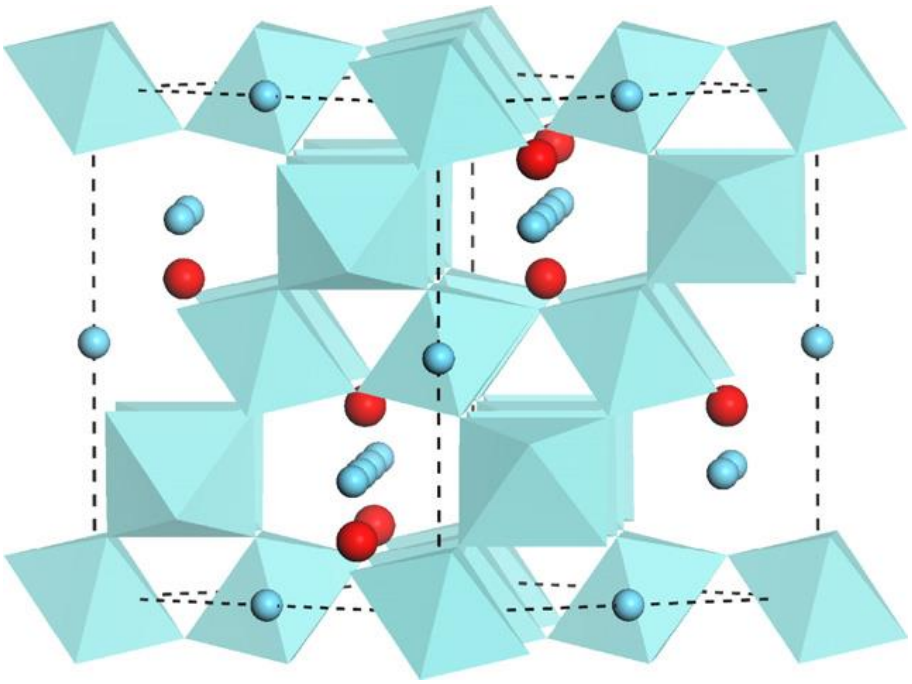

Figure 2.24: *Crystal structure of pyrochlore $La_2Ti_2O_7$ [106]*

2.6 THERMAL CONDUCTIVITY

Thermal conductivity is the ability of a material to conduct heat. In terms of thermoelectrics, thermal conductivity plays a very important role. For efficient thermoelectric materials, the temperature gradient must be maintained for an infinite period of time. Unfortunately, every material has a minimum thermal conductivity, due to the electrons and the lattice vibrations (phonons contributions). Researchers

are trying different ways to reduce thermal conductivity by various methods to improve zT.

Thermal conductivity is defined as when a temperature gradient is applied, the heat flow rate through a unit length of a material in a direction perpendicular to a unit area

$$\kappa = -\frac{L\vec{Q}}{A\Delta\vec{T}} \tag{2.3}$$

Where L is a unit length (or thickness) Q is the heat flow rate, A is the cross sectional area and T is the absolute temperature.

Thermal conductivity mainly comes from two contributions lattice and electronic thermal conductivity. In materials with low electrical conductivity (insulators) the contribution of total thermal conductivity mainly comes from lattice vibrations. In the case of electrical conductors, the contribution to the total thermal conductivity comes from electronic thermal conductivity and lattice thermal conductivity. The lattice thermal conductivity can be calculated by subtracting the electronic contribution to thermal conductivity (κ_{elec}) from total thermal conductivity. κ_{elec} can be calculated by using Weidman- Franz Law which is written as

$$\kappa_{elec} = LT\sigma \tag{2.4}$$

Where L is the Lorenz number, T is the absolute temperature and σ is the electrical conductivity. Assuming the case of a homogeneous material with a

parabolic band dominated by acoustic phonon scattering at low temperatures ($\kappa_{Lattice} \alpha T^{-1}$), the Lorenz number is given as [109]

$$L = \left(\frac{k_B}{e}\right)^2 \left(\frac{3F_0(\xi)F_2(\xi) - 4F_1^{\,2}(\xi)}{F_0^{\,2}(\xi)}\right) \tag{2.5}$$

Where k_B is the Boltzmann constant, e is the unit charge and Fn(ξ) is the nth order Fermi integral and ξ is the reduced Fermi energy which can be calculated by considering the Fermi Dirac statistics, the Seebeck coefficient values can be expressed as [109]

$$S = \frac{k_B}{e}\left(2\frac{F_1(\xi)}{F_0(\xi)} - \xi\right) \tag{2.6}$$

This holds true for the materials which have only one type of charge carrier. For materials which have both types of charge carriers, i.e. electrons and holes, the total electronic thermal conductivity can be represented by [8]

$$\kappa e = \kappa e1 + \kappa e2 + \frac{\sigma 1 \sigma 2}{\sigma 1 + \sigma 2} (S2 - S1)^2 T \tag{2.7}$$

Where κe1 and κe2 are the partial thermal conductivity contributions by holes and electrons respectively. Similarly σ1 and σ2 are the partial electrical conductivity contributions by holes and electrons while S1-S2 is the partial difference in Seebeck coefficient of both charge carriers. The third term [$\frac{\sigma 1 \sigma 2}{\sigma 1 + \sigma 2} (S2 - S1)^2 T$] in the above equation is related to bipolar diffusion. This happens most commonly in small

energy gap semiconductors. Electrons-holes pairs are generated by the absorption of energy at the hot end. These pairs recombine by releasing energy when they move to the cold end and thus increasing thermal conductivity. This co-existence of both charge carriers explains the increase in thermal conductivity with increasing temperature. In compounds like $CoSb_3$, the intrinsic contribution starts to operate at higher temperature (> 400 ^oC) which causes the increase in thermal conductivity as shown in the Figure 2.25 [37].

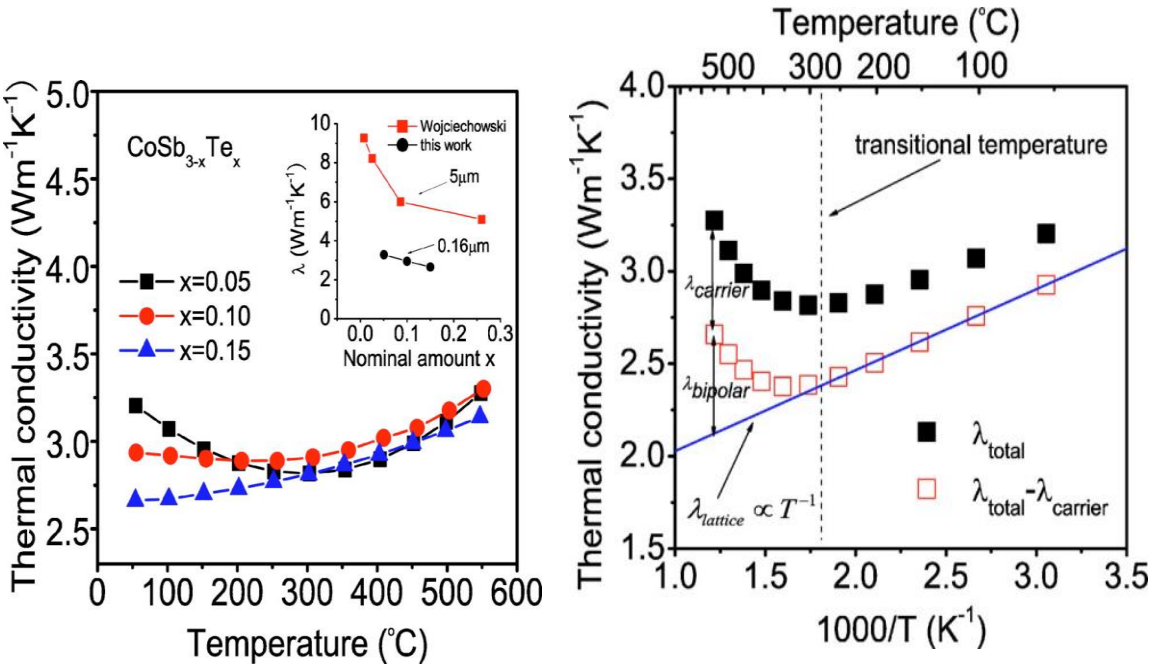

Figure 2.25: *Temperature dependence of thermal conductivity in $CoSb_{3-x}Te_x$ [37]*

2.7 OXIDE THERMOELECTRIC MODULES

A thermoelectric module fabricated by using p type $Ca_3Co_4O_9$ and n type $(ZnO)_7In_2O_3$ legs generated a maximum power output of 423 mW with 44 p-n junctions at a temperature difference of ~ 850 K (cold side at 427 K and hot side at 1100 K) [110]. The P type leg has a Z value of $0.55x10^{-4}$/K while the n type has a value of $1.35\ x10^{-4}$/K at 1100K. [110] .The main degrading factors for the low power

generation are dry joints and pores originating from the difference between the electrodes and legs of the module. Funahashi et al. also fabricated an oxide thermoelectric module by using 140 pairs of these layered oxides (p-type $Ca_{2.7}Bi_{0.3}Co_4O_9$ and n-type $La_{0.9}Bi_{0.1}NiO_3$) and showed that a battery of a cell phone can be charged with this [111]. A maximum power output of ~0.15 W was achieved at a temperature difference of ~ 550 K. The contact resistance in the module can effectively be reduced by mixing n or p type powder in the Ag paste used as the adhesive material between thermoelectric legs and the substrate. A maximum power of 0.17 W was achieved by using this technique in a module prepared using eight pairs of p-type $Ca_{2.7}Bi_{0.3}Co_4O$ and n-type $CaMn_{0.98}Mo_{0.02}O_3$ as shown in Figure 2.26 [112].

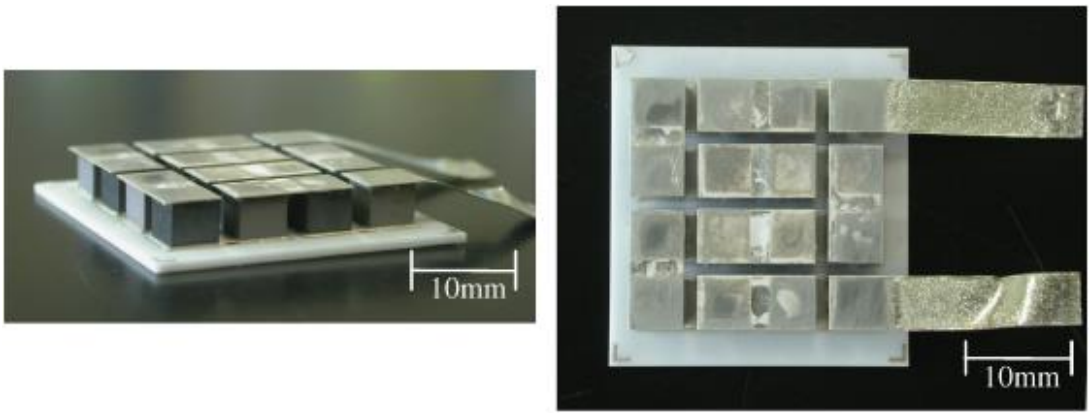

Figure 2.26: *A typical oxide thermoelectric module made from $Ca_{2.7}Bi_{0.3}Co_4O_9$ and $CaMn_{0.98}Mo_{0.02}O_3$ [112]*

REFERENCES

[1] H.J. Goldsmid, The thermoelectric and related effects, in: J.P. Robert Hull, R.M. Osgood, Jr., Hans Warlimont (Ed.) Introduction to thermoelectricity, Springer Heidelberg Dordrecht London, New York, 2010, pp. 1.

[2] H.J. Goldsmid, R.W. Douglas, British Journal of Applied Physics, 5 (1954) 386.

[3] K. Biswas, J.Q. He, I.D. Blum, C.I. Wu, T.P. Hogan, D.N. Seidman, V.P. Dravid, M.G. Kanatzidis, Nature, 489 (2012) 414-418.

[4] R. Venkatasubramanian, E. Siivola, T. Colpitts, B. O'Quinn, Nature, 413 (2001) 597-602.

[5] K.F. Hsu, S. Loo, F. Guo, W. Chen, J.S. Dyck, C. Uher, T. Hogan, E.K. Polychroniadis, M.G. Kanatzidis, Science, 303 (2004) 818-821.

[6] G.J. Snyder, E.S. Toberer, Nature materials, 7 (2008) 105-114.

[7] A. Patyk, Appl Energ, 102 (2013) 1448-1457.

[8] G.S.N.a.H.J. Goldsmid, Thermal Conductivity of Semiconductors, in: T.M. Tritt (Ed.) Thermal conductivity Theory, Properties and applications, Kluwer Academic / Plenum Publishers, 2004, pp. 112.

[9] G.A. Slack, New Materials and Performance Limits for Thermoelectric Cooling, in: D.M. Rowe (Ed.) CRC Handbook of Thermoelectrics, CRC, Boca Raton, 1995, pp. 407.

[10] J. Khaliq, Q. Jiang, J. Yang, K. Simpson, H. Yan, M.J. Reece, Scripta Materialia, 72–73 (2014) 63-66.

[11] J.-F. Li, W.-S. Liu, L.-D. Zhao, M. Zhou, NPG Asia Materials, 2 (2010) 152-158.

[12] M. Ohtaki, Journal of Ceramic Society Japan, 119 (2011).

[13] S. Grasso, N. Tsujii, Q.H. Jiang, J. Khaliq, S. Maruyama, M. Miranda, K. Simpson, T. Mori, M.J. Reece, Journal of Materials Chemistry C, 1 (2013) 2362-2367.

[14] Z. Dashevsky, S. Shusterman, M.P. Dariel, I. Drabkin, Journal of Applied Physics, 92 (2002) 1425.

[15] M. Saleemi, M.S. Toprak, S. Li, M. Johnsson, M. Muhammed, Journal of Materials Chemistry, 22 (2012) 725.

[16] J. Eilertsen, J. Li, S. Rouvimov, M.A. Subramanian, Journal of Alloys and Compounds, 509 (2011) 6289-6295.

[17] G. Li, J.Y. Yang, Y. Xiao, L.W. Fu, J.Y. Peng, Y. Deng, P.W. Zhu, H.X. Yan, Journal of Electronic Materials, 42 (2013) 675-678.

[18] J.J. Zhang, B. Xu, L.M. Wang, D.L. Yu, Z.Y. Liu, J.L. He, Y.J. Tianb, Applied Physics Letters, 98 (2011) 072109.

[19] A. Harnwunggmoung, K. Kurosaki, H. Muta, S. Yamanaka, Applied Physics Letters, 96 (2010) 202107.

[20] T. Caillat, A. Borshchevsky, J.P. Fleurial, Journal of Applied Physics, 80 (1996) 4442-4449.

[21] S.W. Kim, Y. Kimura, Y. Mishima, Advanced Materials for Energy Conversion Ii, (2004) 377-384.

[22] G.S. Nolas, C.A. Kendziora, Physical Review B, 59 (1999) 6189-6192.

[23] B.C. Sales, D. Mandrus, R.K. Williams, Science, 272 (1996) 1325-1328.

[24] L.D. Chen, T. Kawahara, X.F. Tang, T. Goto, T. Hirai, J.S. Dyck, W. Chen, C. Uher, Journal of Applied Physics, 90 (2001) 1864-1868.

[25] H. Li, X.F. Tang, Q. J. Zhang, C. Uher, Applied Physics Letters, 94 (2009) 102114.

[26] J.R. Salvador, R.A. Waldo, C.A. Wong, M. Tessema, D.N. Brown, D.J. Miller, H. Wang, A.A. Wereszczak, W. Cai, Materials Science and Engineering: B, 178 (2013) 1087-1096.

[27] H. Li, X.F. Tang, X.L. Su, Q.J. Zhang, C. Uher, J Phys D Appl Phys, 42 (2009) 145409.

[28] H. Li, X. Tang, X. Su, Q. Zhang, Applied Physics Letters, 92 (2008) 202114.

[29] H. Li, X. Tang, Q. Zhang, Journal of Electronic Materials, 38 (2009) 1224-1228.

[30] G. Tan, W. Liu, S. Wang, Y. Yan, H. Li, X. Tang, C. Uher, J Mater Chem A, 1 (2013) 12657-12668.

[31] T. Morimura, M. Hasaka, Scripta Materialia, 48 (2003) 495-500.

[33] W.-S. Liu, B.-P. Zhang, J.-F. Li, L.-D. Zhao, Journal of Physics D: Applied Physics, 40 (2007) 566-572.

[34] G.S. Nolas, M. Kaeser, R.T. Littleton, T.M. Tritt, Applied Physics Letters, 77 (2000) 1855.

[35] P.-X. Lu, F. Wu, H.-L. Han, Q. Wang, Z.-G. Shen, X. Hu, Journal of Alloys and Compounds, 505 (2010) 255-258.

[36] X.Y. Li, L.D. Chen, J.F. Fan, W.B. Zhang, T. Kawahara, T. Hirai, Journal of Applied Physics, 98 (2005).

[37] W.-S. Liu, B.-P. Zhang, J.-F. Li, H.-L. Zhang, L.-D. Zhao, Journal of Applied Physics, 102 (2007) 103717.

[38] M.J. Kim, I.H. Kim, Met Mater Int, 16 (2010) 459-463.

[39] X. Shi, H. Kong, C.P. Li, C. Uher, J. Yang, J.R. Salvador, H. Wang, L. Chen, W. Zhang, Applied Physics Letters, 92 (2008) 182101.

[40] H. Li, X.F. Tang, Q.J. Zhang, C. Uher, Applied Physics Letters, 93 (2008).

[41] G. S. Nolas M. Kaeser, R. T. Littleton IV, T. M. Tritt, Applied Physics Letters, 77 (2000) 1855.

[42] M. Ausloos, K. Durczewski, S.K. Patapis, C. Laurent, H.W. Vanderschueren, Solid State Communications, 65 (1988) 365-368.

[43] A.T. Burkov, A. Heinrich, M.V. Vedernikov, AIP Conference Proceedings, 316 (1994) 76-80.

[44] A. Chernatynskiy, R.W. Grimes, M.A. Zurbuchen, D.R. Clarke, S.R. Phillpot, Applied Physics Letters, 95 (2009) 161906.

[45] I. Terasaki, M. Iwakawa, T. Nakano, A. Tsukuda, W. Kobayashi, Dalton Trans, 39 (2010) 1005-1011.

[46] I. Terasaki, Y. Sasago, K. Uchinokura, Physical Review B, 56 (1997) 12685-12687.

[47] M. Ito, D. Furumoto, Journal of Alloys and Compounds, 450 (2008) 517-520.

[48] P.H. Tsai, T. Norby, T.T. Tan, R. Donelson, Z.D. Chen, S. Li, Applied Physics Letters, 96 (2010) 141905.

[49] M. Shikano, R. Funahashi, Applied Physics Letters, 82 (2003) 1851-1853.

[50] D. Wang, L. Chen, Q. Yao, J. Li, Solid State Communications, 129 (2004) 615-618.

[51] T. Yin, D. Liu, Y. Ou, F. Ma, S. Xie, J.-F. Li, J. Li, The Journal of Physical Chemistry C, 114 (2010) 10061-10065.

[52] R. Funahashi, I. Matsubara, H. Ikuta, T. Takeuchi, U. Mizutani, S. Sodeoka, Japanese Journal of Applied Physics 2, 39 (2000) L1127-L1129.

[53] P. Wagner, R. Helbig, Journal of Physics and Chemistry of Solids, 35 (1974) 327-335.

[54] G.A. Slack, Physical Review B, 6 (1972) 3791-3800.

[55] K.F. Cai, E. Müller, C. Drašar, A. Mrotzek, Materials Science and Engineering: B, 104 (2003) 45-48.

[56] Z.L. Wang, Materials Science and Engineering: R: Reports, 64 (2009) 33-71.

[57] M. Ohtaki, T. Tsubota, K. Eguchi, H. Arai, Journal of Applied Physics, 79 (1996) 1816-1818.

[58] M. Ohtaki, K. Araki, K. Yamamoto, Journal of Electronic Materials, 38 (2009) 1234-1238.

[59] P. Jood, R.J. Mehta, Y.L. Zhang, G. Peleckis, X.L. Wang, R.W. Siegel, T. Borca-Tasciuc, S.X. Dou, G. Ramanath, Nano Letters, 11 (2011) 4337-4342.

[60] T. Tsubota, M. Ohtaki, K. Eguchi, H. Arai, Journal of Materials Chemistry, 8 (1998) 409-412.

[61] E. Guilmeau, D. Berardan, C. Simon, A. Maignan, B. Raveau, D.O. Ovono, F. Delorme, Journal of Applied Physics, 106 (2009) 053715-053717.

[62] D. Berardan, E. Guilmeau, A. Maignan, B. Raveau, Solid State Communications, 146 (2008) 97-101.

[63] J.L. Lan, Y.H. Lin, Y. Liu, S.L. Xu, C.W. Nan, Journal of the American Ceramic Society, 95 (2012) 2465-2469.

[64] Y. Liu, Y.H. Lin, J.L. Lan, W. Xu, B.P. Zhang, C.W. Nan, H.M. Zhu, Journal of the American Ceramic Society, 93 (2010) 2938-2941.

[65] M.C. Knapp, in Investigations into the structure and properties of ordered perovskites, layered perovskites, and defect pyrochlores, The Ohio State University, 2006.

[66] E. Fabbri, D. Pergolesi, E. Traversa, Chemical Society Reviews, 39 (2010) 4355-4369.

[67] S. Stolen, E. Bakken, C.E. Mohn, Physical Chemistry Chemical Physics, 8 (2006) 429-447.

[68] T. Okuda, K. Nakanishi, S. Miyasaka, Y. Tokura, Physical Review B, 63 (2001) 113104.

[69] A. Kinaci, C. Sevik, T. Çağın, Physical Review B, 82 (2010) 155114.

[70] S. Ohta, T. Nomura, H. Ohta, K. Koumoto, Journal of Applied Physics, 97 (2005) 092108.

[71] J. Liu, C.L. Wang, W.B. Su, H.C. Wang, P. Zheng, J.C. Li, J.L. Zhang, L.M. Mei, Applied Physics Letters, 95 (2009) 162110.

[72] A. Kikuchi, N. Okinaka, T. Akiyama, Scripta Materialia, 63 (2010) 407-410.

[73] S. Ohta, T. Nomura, H. Ohta, M. Hirano, H. Hosono, K. Koumoto, Applied Physics Letters, 87 (2005) 092108.

[74] H. Ohta, S. Kim, Y. Mune, T. Mizoguchi, K. Nomura, S. Ohta, T. Nomura, Y. Nakanishi, Y. Ikuhara, M. Hirano, H. Hosono, K. Koumoto, Nature Materials, 6 (2007) 129-134.

[75] A. Srivastava, N.K. Gaur, Journal of Magnetism and Magnetic Materials, 321 (2009) 3854-3865.

[76] T. Okuda, Y. Fujii, Journal of Applied Physics, 108 (2010) 103702.

[77] F.P. Zhang, Q.M. Lu, X. Zhang, J.X. Zhang, Journal of Alloys and Compounds, 509 (2011) 542-545.

[78] L. Bocher, M.H.Aguire, D. Logvinovich, A. Shkabko, R. Robert, M. Trottmann, and A. Weidenkaff, Inorganic Chemistry, 47 (2008) 8077.

[79] H.X. Yan, H.T. Zhang, Z. Zhang, R. Ubic, M.J. Reece, Journal of the European Ceramic Society, 26 (2006) 2785-2792.

[80] L. Viciu, V.O. Golub, J.B. Wiley, Journal of Solid State Chemistry, 175 (2003) 88-93.

[81] K.H. Lee, S.W. Kim, H. Ohta, K. Koumoto, Journal of Applied Physics, 100 (2006) 063717.

[82] H. Ning, H. Yan, M.J. Reece, Journal of the American Ceramic Society, 93 [5] (2010) 1409.

[83] R. Machado, M.G. Stachiotti, R.L. Migoni, A.H. Tera, Physical Review B, 70 (2004) 214112.

[84] C.J. Fennie, K.M. Rabe, Applied Physics Letters, 88 (2006) 262902.

[85] F. Lichtenberg, A. Herrnberger, K. Wiedenmann, Progress in Solid State Chemistry, 36 (2008) 253-387.

[86] Y. Wang, K.H. Lee, H. Hyuga, H. Kita, H. Ohta, K. Koumoto, Journal of Electroceramics, 24 (2010) 76-82.

[87] I. Levin, L.A. Bendersky, Acta Crystallographica Section B-Structural Science, 55 (1999) 853-866.

[88] H. Yan, H. Ning, Y. Kan, P. Wang, M.J. Reece, Journal of the American Ceramic Society, 92 (2009) 2270-2275.

[89] H. Frederikse, W. Thurber, W. Hosler, Physical Review, 134 (1964) A442-A445.

[90] B. Jalan, S. Stemmer, Applied Physics Letters, 97 (2010) 042106.

[91] W. Ma, D.E. Mack, R. Vassen, D. Stover, Journal of the American Ceramic Society, 91 (2008) 2630-2635.

[92] W. Ma, M.O. Jarligo, D.E. Mack, D. Pitzer, J. Malzbender, R. Vassyen, D. Stover, Journal of Thermal Spray Technology, 17 (2008) 831-837.

[93] A. Sakai, T. Kanno, K. Takahashi, Y. Yamada, H. Adachi, Journal of Applied Physics, 108 (2010) 103706.

[94] Y. Shen, D.R. Clarke, P.A. Fuierer, Applied Physics Letters, 93 (2008) 102907.

[95] R.R. Sun, X.Y. Qin, L.L. Li, D. Li, J. Zhang, Q.Q. Wang, Journal of Physics D Applied Physics, 45 (2012) 124904.

[96] K.H. Lee, S.W. Kim, H. Ohta, K. Koumoto, Journal of Applied Physics, 101 (2007) 326.

[97] R.R. Sun, X.Y. Qin, L.L. Li, D. Li, N.N. Wang, J. Zhang, Q.Q. Wang, Journal of Applied Physics, 112 (2012) 124904.

[98] K.H. Lee, Y.F. Wang, S.W. Kim, H. Ohta, K. Koumoto, International Journal of Applied Ceramic Technology, 4 (2007) 326-331.

[99] D.G. Cahill, A. Melville, D.G. Schlom, M.A. Zurbuchen, Applied Physics Letters, 96 (2010) 121903.

[100] Z. Gao, H. Ning, C. Chen, R. Wilson, B. Shi, H. Ye, H. Yan, M.J. Reece, J.L. Jones, Journal of the American Ceramic Society, 96 (2013) 1163-1170.

[101] Z.P. Gao, H.X. Yan, H.P. Ning, R. Wilson, X.Y. Wei, B. Shi, H. Ye, M.J. Reece, Journal of the European Ceramic Society, 33 (2013) 1001-1008.

[102] N. Ishizawa, F. Marumo, T. Kawamura, M. Kimura, Acta Crystallographica Section B, 31 (1975) 1912-1915.

[103] W. Kobayashi, Y. Hayashi, M. Matsushita, Y. Yamamoto, I. Terasaki, A. Nakao, H. Nakao, Y. Murakami, Y. Moritomo, H. Yamauchi, M. Karppinen, Physical Review B, 84 (2011) 085118.

[104] A. Sakai, T. Kanno, K. Takahashi, A. Omote, H. Adachi, Y. Yamada, X.D. Zhou, Journal of the American Ceramic Society, 95 (2012) 1750-1755.

[105] T.D. Sparks, P.A. Fuierer, D.R. Clarke, Journal of the American Ceramic Society, 93 (2010) 1136-1141.

[106] B. Liu, J.Y. Wang, F.Z. Li, Y.C. Zhou, Acta Materialia, 58 (2010) 4369-4377.

[107] K.E. H. Takamura, A. Kamegawa, M. Okada, Solid State Ionics, 154–155 (2002) 581-588

[108] I.N. Katsunori Akiyama, Masato Shida, Satoshi Ota, in, Mitsubishi Heavy Industries, Ltd., (2009) US2007/0151481 A1.

[109] H. Anno, K. Matsubara, Y. Notohara, T. Sakakibara, H. Tashiro, Journal of Applied Physics, 86 (1999) 3780-3786.

[110] S.-M. Choi, K.-H. Lee, C.-H. Lim, W.-S. Seo, Energy Conversion and Management, 52 (2011) 335-339.

[111] R. Funahashi, M. Mikami, T. Mihara, S. Urata, N. Ando, Journal of Applied Physics, 99 (2006) 066117.

[112] S. Urata, R. Funahashi, T. Mihara, A. Kosuga, S. Sodeoka, T. Tanaka, Int J Appl Ceram Tec, 4 (2007) 535-540.

Chapter III. Experimental Details

3.1 POWDER PREPARATION

The starting materials for the preparation of oxide powders were La_2O_3 (99.99% purity, Sigma Aldrich), $SrCO_3$ (99.9% purity, Sigma Aldrich), TiO_2 (anatase) (99.6% purity, Alfa aesar) and Nb_2O_5 (99.9% purity, Alfa aesar). Different powders according to their stoichiometric ratios were added to Nylon pots with ZrO_2 balls as the grinding agent and ethanol as the milling medium. A mixture of 5 mm and 10 mm diameter ZrO_2 balls was used. The loaded pots were put in a planetary ball mill (QM-3SP4, Nanjing University Instrument Plant, China) as shown in Figure 3.1(a) and rotated at a speed of 350 rpm for 2 hours to mix the powders. The ratio of balls to powder was 10:1. After mixing, the powders were dried overnight at 80 ^oC in a drying oven (Elite). After drying, the powders were sieved through a stainless steel sieve with an aperture size of 250 µm.

In order to synthesise the required composition, the solid state reaction method was employed. Mixed dried powders were put in to alumina crucible and calcined at 1250-1300 ^oC for 4 hours using a chamber furnace (Carbolite HTF 1800) as shown in Figure 3.1(b). After calcination, the synthesised powders were remilled for 4 hours at 350 rpm to break the agglomerates and reduce the particle size. After remilling, the powders were dried overnight at 80 ^oC and passed through a 250 µm mesh sieve to control the particle size.

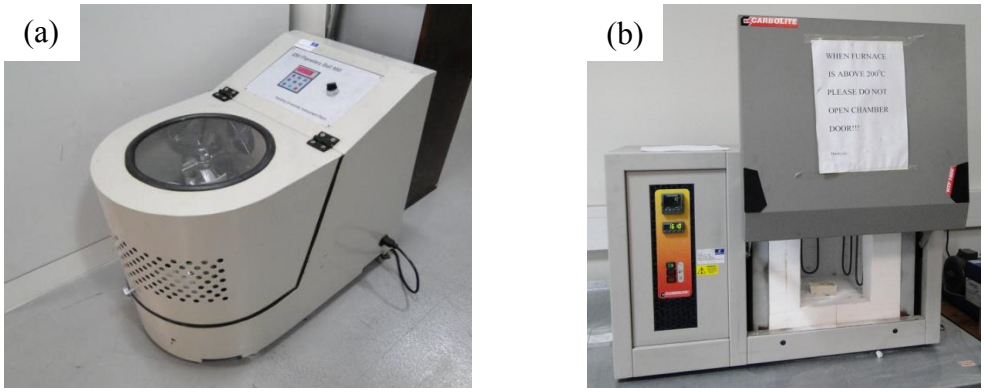

Figure 3.1: (a) *QM-3SP4 Planetary ball mill machine (b) carbolite HTF 1800 Chamber furnace*

For the synthesis of skutterudite powder, mechanical alloying technique was used. Commercially available powders of Co (99.8% pure), Sb (99.5% pure), Te (99.999% pure) and Yb (99.8% pure) were added to steel jars according to the required stoichiometric ratios. This process was carried out in an Ar filled glove box (as shown in Figure 3.2) to avoid oxidation of the powders. The jars were sealed under a vacuum and loaded into the ball mill for 40 hours at 350 rpm. After mixing, the steel jars were put inside the glove box to avoid oxidation of the powder.

Figure 3.2: *Saffron scientific glove box used for powder handling under inert environment*

3.2 Sintering by spark plasma sintering

Spark plasma sintering (SPS) is an efficient technique to sinter non equilibrium, nanosized material by using high current pulsed DC and uniaxial pressure. The main advantage of SPS is that it is a rapid sintering technique which helps to retain the nanosize grains of the powders and lowering thermal conductivity by orienting the grains in a preferred direction.

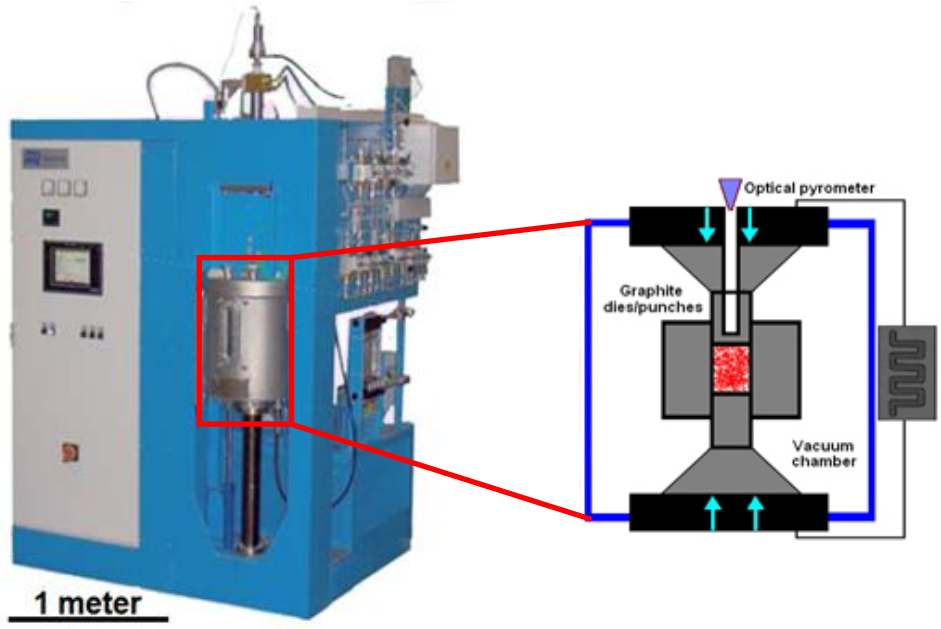

Figure 3.3: *Spark Plasma Sintering furnace (FCT, Germany) with a schematic of its chamber*

In this study, an SPS furnace (25/1 GCT, Germany) was used and shown in Figure 3.3. It can achieve a heating rate of 600 ^{o}C/minute with a maximum temperature of 2200 ^{o}C. The high pressure combined with rapid heating rate, helps to make material with properties that cannot be achieved with conventional sintering. In SPS, the grain growth is suppressed due to rapid sintering which helps to reduce thermal conductivity. Apart from maintaining the grain size, SPS can also impart defects in the structure which further helps to reduce thermal conductivity [1].

Calcined oxide powders were sintered using a SPS furnace. A set of graphite dies and punches were used as a mould. Graphite dies and punches were manufactured by Erodex (ISO 63). A graphite foil of 0.35 mm (supplied by SGL Sigmaflex TH Foil) was used as a conducting barrier between graphite dies (and punches) and the powder to avoid contamination and reaction. The powders were cold pressed with a 0.5 tonne force. The cold pressed powders were sintered at 1350 ^{o}C under 50 MPa of pressure for 5 minutes. The vacuum level inside the furnace was ~ 5 Pa.

For skutterudite, the powder was loaded into the graphite dies inside a glove box and then sintered at 600 ^{o}C under Argon environment at 50 MPa pressure.

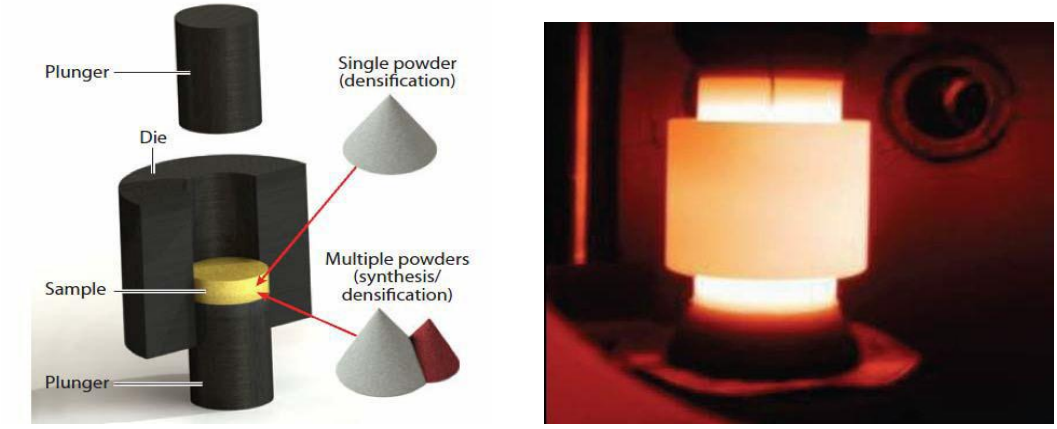

(a) (b)

Figure 3.4: *Schematic representation of: (a) SPS Die set; (b) photo of the graphite die during SPS process*

3.3 Post Sintering treatment

The sintered discs of oxide ceramics were annealed at 1000 ^{o}C in air for 6 hours in a chamber furnace (Carbolite HTF 1800) to remove any diffused carbon during SPS processing. After air annealing, the ceramic samples were colourless and

electrically insulating. In order to enhance electrical conductivity, the ceramic samples were annealed in an atmosphere of 10 % H_2 + 90 % Ar. The samples were annealed at 1250 ^oC for 4 hours in a thermal technology LLC furnace (Model number 1100 2560 1/2). No post sintering treatment was done on skutterudites. The samples were then ground to even out the surfaces using a Struers TegraPol-21 grinder/polisher. For electrical resistivity and Seebeck coefficient measurement, ceramic samples were cut in to rectangular bars with dimensions of 3x3x15 mm using an Accutom-5, Struers Cutting machine.

3.4 Characterization

3.4.1 Density measurement

The bulk densities of the sintered and air annealed and reduced ceramic discs were measured by using the Archimedes principle and using the following relation [2]

$$\rho = \frac{m_1 \rho_0}{m_2 - m_3} \tag{3.1}$$

Where m_1 is the mass of the sample in air, m_2 is the mass of water soaked sample, m_3 is the mass of sample inside water, ρ_0 is the density of water and ρ is the density of the sample. For nearly fully dense samples or the samples containing closed porosity, $m_1 = m_2$ and the relation then become:

$$\rho = \frac{m_1 \rho_0}{m_1 - m_3} \quad (3.2)$$

3.4.2 X-ray Diffraction and X-ray Photoelectron Spectroscopy

X-ray diffraction (XRD) is an analytical technique providing detailed structural and compositional information of a material. It is a non-destructive technique based on Bragg's law. XRD patterns for the powders, sintered, air annealed and hydrogen annealed ceramics were recorded using Siemens D5000 X-ray diffractometer with Ni filtered Cu Kα radiation (λ = 1.54Å). Data were recorded in the 2θ range of 10^0-70^0 with a step width of 0.0334^0 and a count time of 200 seconds per step.

All the diffraction patterns were collected by experimental officer Dr. Rory M. Wilson. Powder samples were sprinkled on top of a zero background single crystal silicon substrate for the analysis. The bulk ceramics were ground to a flat surface and then mounted for recording their XRD pattern. Phase identification was carried out by using PANalytical's X'Pert HighScore version 2.1software.

In order to analyse the surface bond and chemical state of the elements, an ESCALAB 250 X-ray Photoelectron Spectrometer (Thermo Corp.) was employed. The equipment is set up at Aston University Birmingham. The equipment had a pass energy of 20 eV and is equipped with monochromatized Al Kα (1486.5 eV) X-ray source. Carbon was used as a reference material and XPSPEAK41 was used for fitting XPS spectra.

3.4.3 Scanning and Transmission Electron Microscopy

The microstructure of the bulk ceramics were determined by Scanning Electron Microscopy (SEM) (FEI, Inspect F). Samples for SEM were prepared by grinding and polishing using silicon carbide papers up to grade 4000. After polishing, all of the samples were thermally etched inside the chamber furnace to reveal the grain boundaries. After thermal etching, the samples were cleaned with acetone and gold coated to make them conductive.

Transmission Electron Microscope (TEM Jeol JEM 2010) was used to study the detailed microstructure of the bulk samples. Samples for TEM were prepared by grinding and polishing the bulk samples down to a thickness of ~ 30-50 μm. The samples for polishing were mounted on to a transparent piece of glass with adhesive 'crystal bond 590'. After polishing, the samples were immersed in acetone and ultrasonicated for 10 minutes to dissolve crystal bond 590 and detach the sample from glass substrate. The samples were then mounted onto nickel grid having an aperture size of 1 mm with Araldite® adhesive. Before analysis, the samples were left to dry overnight. After drying, the samples were put inside a Precision Ion polishing System (PIPS^{TM}) to reduce the thickness of the sample to electron transparency. Image J analysis software was used to analyse the images and the diffraction patterns obtained through TEM.

3.4.4 Electrical Characterisation

The samples were cut into 3x3x15 mm bars from the ceramic disc for electrical resistivity and Seebeck coefficient measurements via four-point probe and temperature differential methods. All the measurements were done in laboratory-

made apparatus under vacuum. The equipment is shown in Figure 3.5. The equipment was tested for calibration by comparing the test results with PbTe sample supplied by the Laboratory of Thermoelectrics, Ben-Gurion University of the Negev, Israel [3]. Measurements were carried out from room temperature to 500^{o}C at an interval of 100 ^{o}C. A heating rate of 10 ^{o}C/minute was employed to raise the temperature to the test temperature. All the samples were rerun to check the reproducibility of the measurements.

Figure 3.5: *Lab built (in China) electrical resistivity and Seebeck coefficient measurement system*

3.4.5 Thermal Characterisation

For the measurement of thermal conductivity the following relationship was used,

$$\kappa = \rho C_p D \quad (3.3)$$

Where κ is thermal conductivity, ρ is the density, C_p is the specific heat and D is the thermal diffusivity. Specific heat was measured by using a Netzsch STA (449 F3 Jupiter®). A sapphire disc (trade name white Sapphire No 12 $^1/_2$ boules) supplied by Stetcher Thun GmbH with thickness of ~ 1 mm and diameter of 3 mm was used to calibrate the instrument and the resulting data was within the error range of 7- 9 %. The samples for the measurement was prepared by cutting a 3x3 mm square from the bulk and polishing the bulk samples to a thickness of ~ 1 mm. All the measurements were carried out in a N_2 environment.

D is the thermal diffusivity which is 'how fast a heat wave travels across a certain area'; it has units of mm^2/s. Thermal diffusivity was measured using a netszch LFA 457 microflash as shown in Figure 3.6. The equipment was tested for calibration with the standard samples provided by the manufacturer and the acquired data was within the acceptable limit of the error (±3%). All the samples used had a diameter of 20 millimetres with thickness of ~ 2.5-3 mm. The surfaces were ground flat but left unpolished to minimise laser reflectance. A Kontakt-chemie Graphite 33 spray was used to coat both surfaces of the sample to maximise the absorption of the laser. A laser beam diameter of 25.4 mm was used as there was no provision for 20 mm diameter laser beam. All the measurements were carried out under Ar environment with a flow rate of 100 ml/min. Measurements were carried out from room temperature to 800^{o}C at 100^{o}C intervals. A heating rate of 10^{o}C/min was used to raise the temperature within 10^{o}C of the testing temperature, after which, a heating rate of 1^{o}C/minute was used to achieve the testing temperature. The maximum

temperature fluctuations were set to ±1^{o}C/minute In order to enhance accuracy and reduce the scatter, three measurements per temperature point were recorded.

Figure 3.6: *Netzsch laser flash LFA 457*

REFERENCES

[1] S. Ballikaya, H. Chi, J.R. Salvador, C. Uher, Journal of Materials Chemistry A, 1 (2013) 12478-12484.

[2] R.M. German, in: Sintering Theory and Practice, John Wiley & Sons, Inc., New York, 1996.

[3] Y. Gelbstein1, J. Davidow1, S. N. Girard, D. Young Chung and M. Kanatzidis, Journal of Advanced Energy Materials, 3 (2013) 815-820.

Chapter IV. Characterization of $La_4Ti_4O_{14\pm\delta}$

4.1 INTRODUCTION

The aim of this research was to investigate the effect of acceptor-donor substitution and oxygen stoichiometry on the thermoelectric properties (especially thermal conductivity) of the PLS $La_4Ti_4O_{14}$. PLS ceramics tend to have very low thermal conductivity (typically ~ 1-2 W/m.K) [1, 2]. Since polycrystalline $La_4Ti_4O_{14}$ is an electrical insulator with high electrical resistivity (~ 10^{15} Ωcm) [3], reduction by hydrogen may cause a partial valence change of Ti from +4 to +3, which produces more conduction electrons. As the temperature increases, more and more electrons reach the conduction band thus decreasing electrical resistivity. Also, by substituting La or Ti in the crystal structure with suitable cations, it creates compositional non-stoichiometry and mass contrast which affects the thermal conductivity [4, 5]. There is no reported literature on the thermal conductivity of $La_4Ti_4O_{14}$ ceramics. In the current research Sr, Ta and Nb substituted $La_4Ti_4O_{14}$ were synthesized and their microstructures were characterized in relation to compositional non-stoichiometry.

4.2 EXPERIMENTAL DETAILS

$La_{4-x}Sr_xTi_4O_{14-\frac{x}{2}\pm\delta}$, $La_4Ti_{4-x}Ta_xO_{14+\frac{x}{2}\pm\delta}$ and $La_4Ti_{4-x}Nb_xO_{14+\frac{x}{2}\pm\delta}$ (where x=0, 0.2, 0.4, 0.6 and 0.8), were prepared by Solid State Reaction. The starting materials were La_2O_3 (99.99% purity, Sigma Aldrich), $SrCO_3$ (99.9% purity, Sigma Aldrich) Nb_2O_5 (99.9% Alfa Aesar) and TiO_2 (anatase) (99.6% purity, Alfa Aesar). These powders were mixed in stoichiometric ratios and ball milled using ethanol as the milling medium in a planetary ball mill. Mixed powders were calcined at 1300^{o}C for 4 hours. After calcination, the powders were remilled for 4 hours to break the agglomerates and reduce the particle size.

Calcined powders were sintered using a SPS furnace at a heating rate of 100^{o}C/min. The powders were cold pressed into a 20 millimetre graphite die and sintered at 1350^{o}C under 50 MPa of pressure for 5 minutes. Figure 4.1 shows typical SPS processing parameters for the pure and doped $La_4Ti_4O_{14}$.

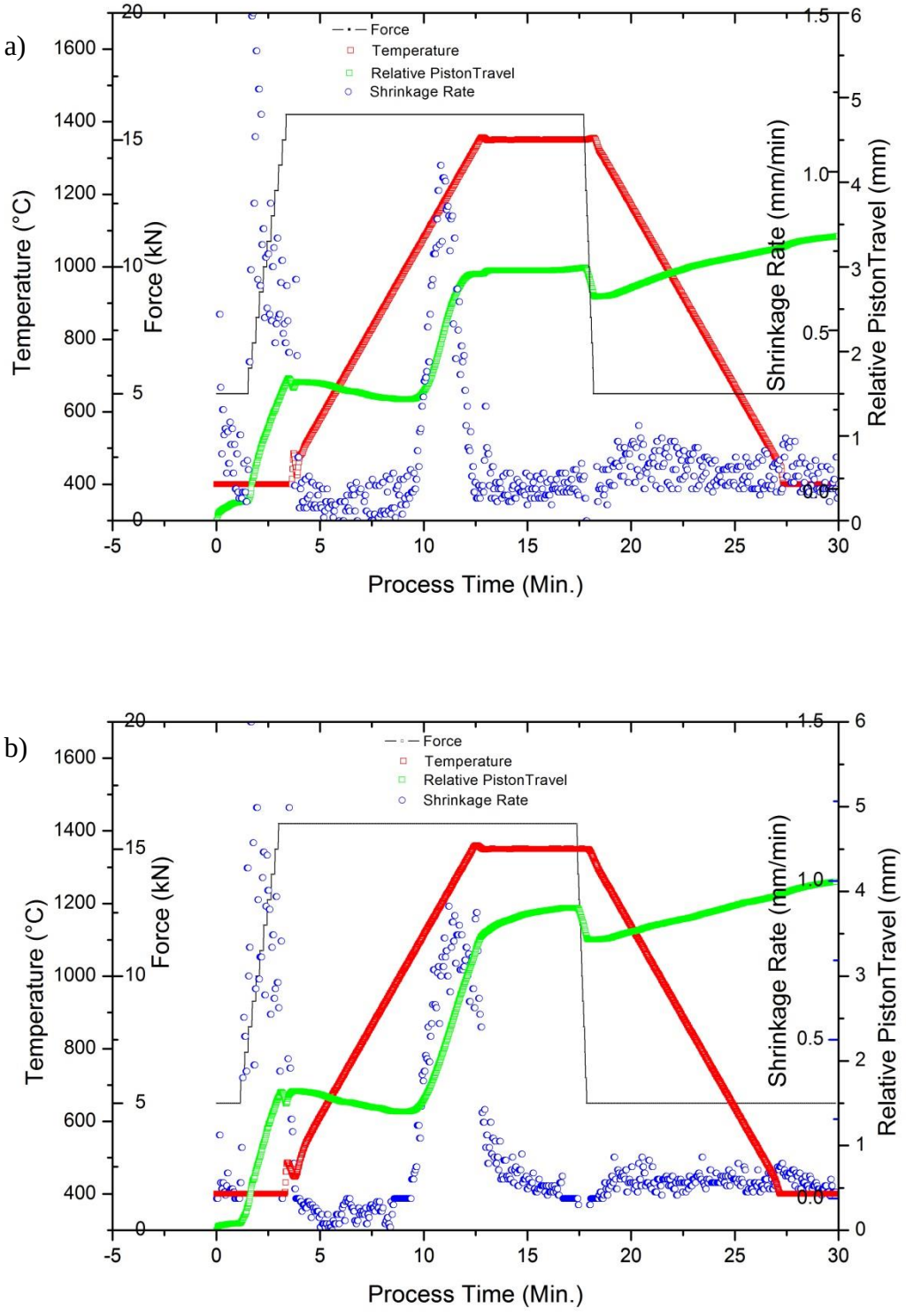

Figure 4.1: *Typical processing parameters during sintering of: (a) $La_4Ti_4O_{14\pm\delta}$; (b) $La_{3.2}Sr_{0.8}Ti_4O_{13.6\pm\delta}$*

Figure 4.2 shows photos of ceramic disc of sintered $La_4Ti_4O_{14}$. The disc just after SPS was black (Figure 4.2(a)) because of carbon contamination from the graphite dies/ punches and the low level of vacuum (~ 5 Pa). The sintered discs were air annealed at 1000^{o}C for 6 hours to remove any diffused carbon during SPS processing. After air annealing the ceramic disc were colourless (Figure 4.2(b)). The air annealed discs were reduced at 1200^{o}C for 4 hours in a mixture of 10 % H_2 90% Ar to increase the electrical conductivity and the disc again turned black (Figure 4.2(c)).

Figure 4.2: *Photos of ceramic disc: (a) after sintering; (b) after air annealing; (c) after reduction*

RESULTS AND DISCUSSIONS

4.3 $La_{4-x}Sr_xTi_4O_{14-\frac{x}{2}\pm\delta}$

Table 4.1 shows the theoretical and measured densities of the $La_{4-x}Sr_xTi_4O_{14-\frac{x}{2}\pm\delta}$ compositions. The bulk density was measured by the Archimedes method and theoretical density was calculated by

$$\rho = \frac{MZ}{\omega N_A} \tag{4.1}$$

Where M is the average molar mass, Z is the number of atoms per unit cell, ω is the unit cell volume and N_A is the Avogadro's number. All the sintered samples were more than 98% dense and the theoretical density decreased with increasing Sr substitution.

Table 4.1: Theoretical and relative densities of $La_{4-x}Sr_xTi_4O_{14-\frac{x}{2}\pm\delta}$ ceramics

	Theoretical Density (gcm^{-3})	Relative Density (%)
$La_4Ti_4O_{14\pm\delta}$	5.78	99.3
$La_{3.8}Sr_{0.2}Ti_4O_{13.9\pm\delta}$	5.71	99.4
$La_{3.6}Sr_{0.4}Ti_4O_{13.8\pm\delta}$	5.64	99.6
$La_{3.4}Sr_{0.6}Ti_4O_{13.7\pm\delta}$	5.57	99.8
$La_{3.2}Sr_{0.8}Ti_4O_{13.6\pm\delta}$	5.50	99.8

Figure 4.3(a) shows the X-ray diffraction patterns for $La_{4-x}Sr_xTi_4O_{14-\frac{x}{2}\pm\delta}$ (x=0, 0.2, 0.4, 0.6 and 0.8) powder. The peaks matched with $La_4Ti_4O_{14}$ ($LaTiO_{3.5}$), n=4 (PDF card # 28-0517). The peaks were shifted towards lower angles indicating that the lattice parameter increased as a result of substitution of La^{3+} (ionic radius 1.17Å) by Sr^{2+} (ionic radius 1.32Å). All the peaks were sharp giving an indication of a large particle size of the powder according to the Scherrer formula [6]. A secondary phase was also generated which cannot be indexed and marked as *.

After sintering the unidentified secondary phase disappeared and a new phase was produced, the 5 layer perovskite compound $La_5Ti_5O_{17}$, (PDF # 00-048-0480) which is indicated with the symbol ♦ in Figure 4.3(b). The amount of $La_5Ti_5O_{17}$ increased with increasing Sr content. $La_5Ti_5O_{17}$ ($LaTiO_{3.4}$) has a monoclinic structure with the Space group Pc. After air annealing, the amount of $La_5Ti_5O_{17}$ decreased slightly as shown in Figure 4.3(c). This is due to the fact that the $La_5Ti_5O_{17}$ is stable in low partial pressure of oxygen as it has a smaller oxygen ratio with the A and B site elements compared to $La_4Ti_4O_{14}$ (A:B:O is 1:1:3.5 for $La_4Ti_4O_{14}$ and 1:1:3.4 for $La_5Ti_5O_{17}$) [7]. This effect is reversed slightly during reduction as seen in Figure 4.3(d).

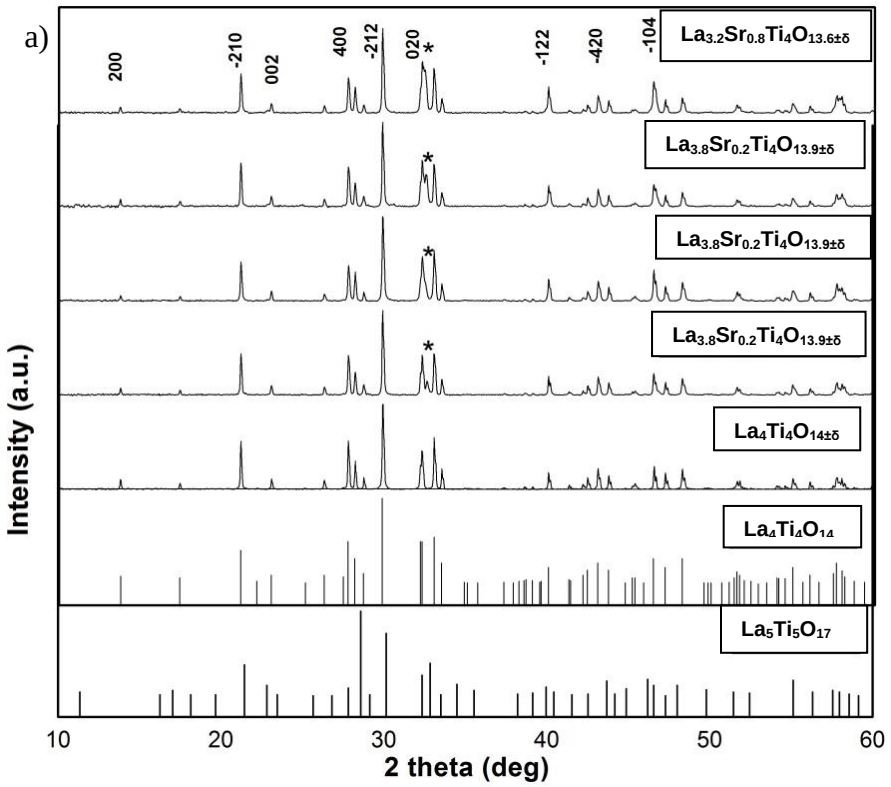
a)
200
-210
002
400
-212
020
*
-122
-420
-104
La3.2Sr0.8Ti4O13.6±δ
La3.8Sr0.2Ti4O13.9±δ
La3.8Sr0.2Ti4O13.9±δ
La3.8Sr0.2Ti4O13.9±δ
La4Ti4O14±δ
La4Ti4O14
La5Ti5O17
Intensity (a.u.)
10
20
30
40
50
60
2 theta (deg)

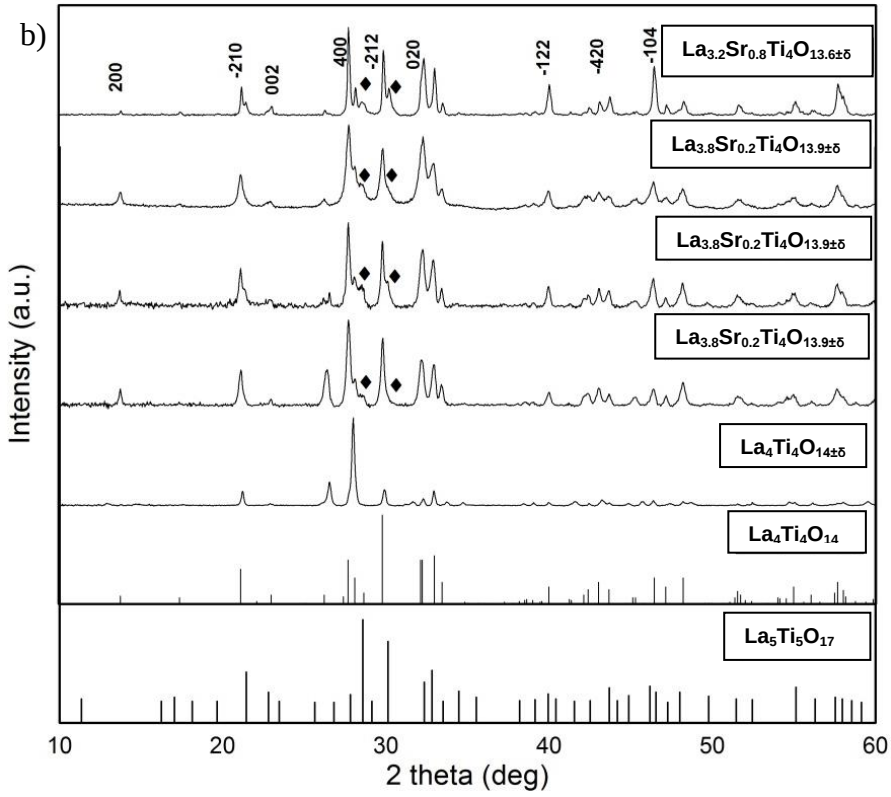
b)
200
-210
002
400
-212
020
-122
-420
-104
La3.2Sr0.8Ti4O13.6±δ
La3.8Sr0.2Ti4O13.9±δ
La3.8Sr0.2Ti4O13.9±δ
La3.8Sr0.2Ti4O13.9±δ
La4Ti4O14±δ
La4Ti4O14
La5Ti5O17
Intensity (a.u.)
10
20
30
40
50
60
2 theta (deg)

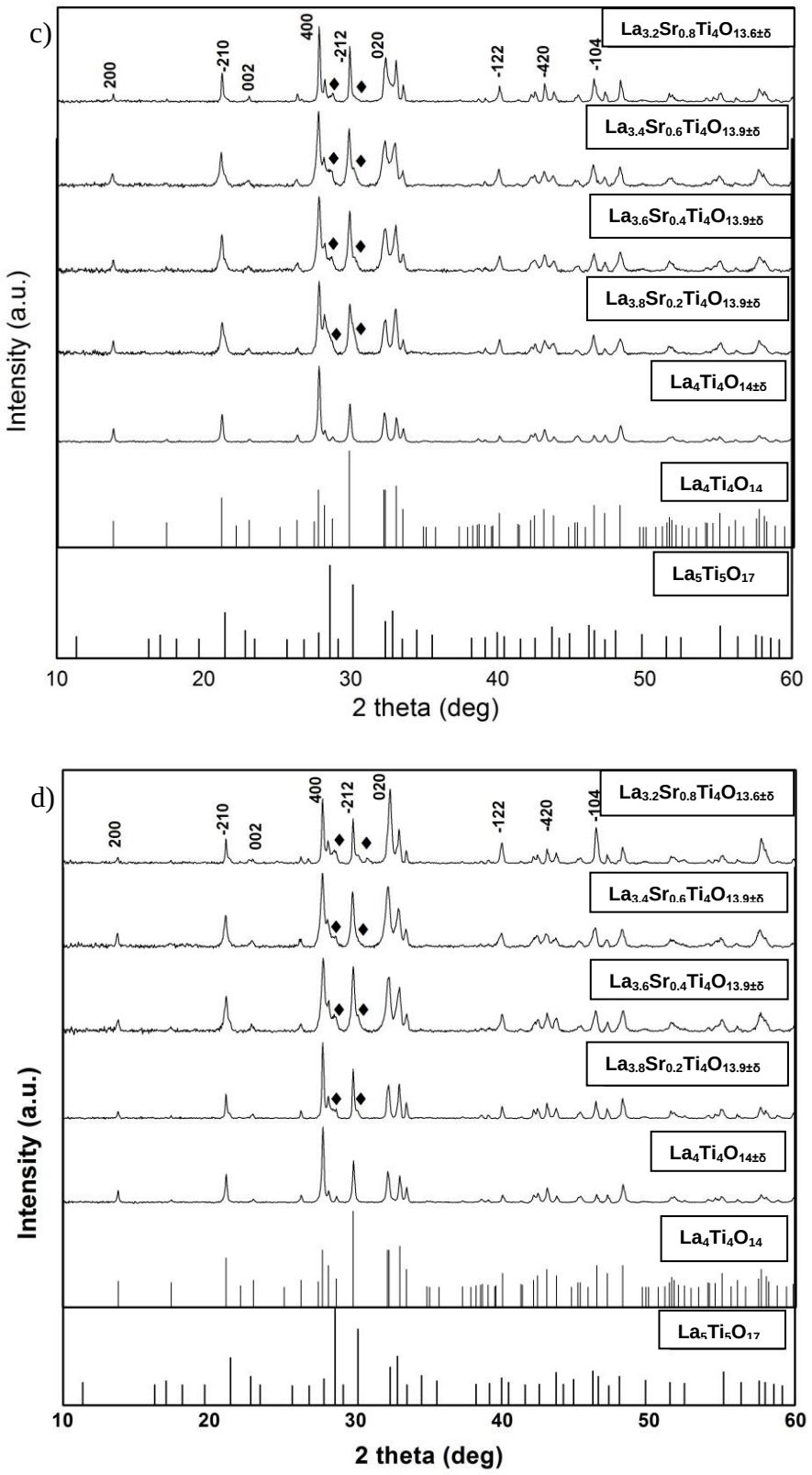

Figure 4.3: *XRD patterns of the $La_{4-x}Sr_xTi_4O_{14-\frac{x}{2}\pm\delta}$: (a) powders; (b) sintered; (c) air annealed; (d) reduced samples*

The amount of $La_5Ti_5O_{17}$ was calculated using the Normalized Relative Intensity Ratio (RIR) method proposed by Chung [8] and is presented in Table 4.2.

Table 4.2: amount of 5 layer PLS compound in $La_{4-x}Sr_xTi_4O_{14-\frac{x}{2}\pm\delta}$ ceramics

	Sinter (mass %)	Air Annealed (mass %)	Reduced (mass %)
$La_{3.8}Sr_{0.2}Ti_4O_{13.9\pm\delta}$	-	-	-
$La_{3.6}Sr_{0.4}Ti_4O_{13.8\pm\delta}$	5.4	2.1	2.6
$La_{3.4}Sr_{0.6}Ti_4O_{13.7\pm\delta}$	6.8	2.2	3.4
$La_{3.2}Sr_{0.8}Ti_4O_{13.6\pm\delta}$	8.4	3.0	7.8

Figure 4.4 shows typical scanning electron microscope (SEM) images of calcined $La_{4-x}Sr_xTi_4O_{14-\frac{x}{2}\pm\delta}$ powder before and after ball milling. After calcination, some of the powder was agglomerated with a particle size of ~ 2 µm. The ball milling process broke the agglomerates and reduced the average particle size to ~ 0.7 µm and the particles became more homogeneous.

a) b)

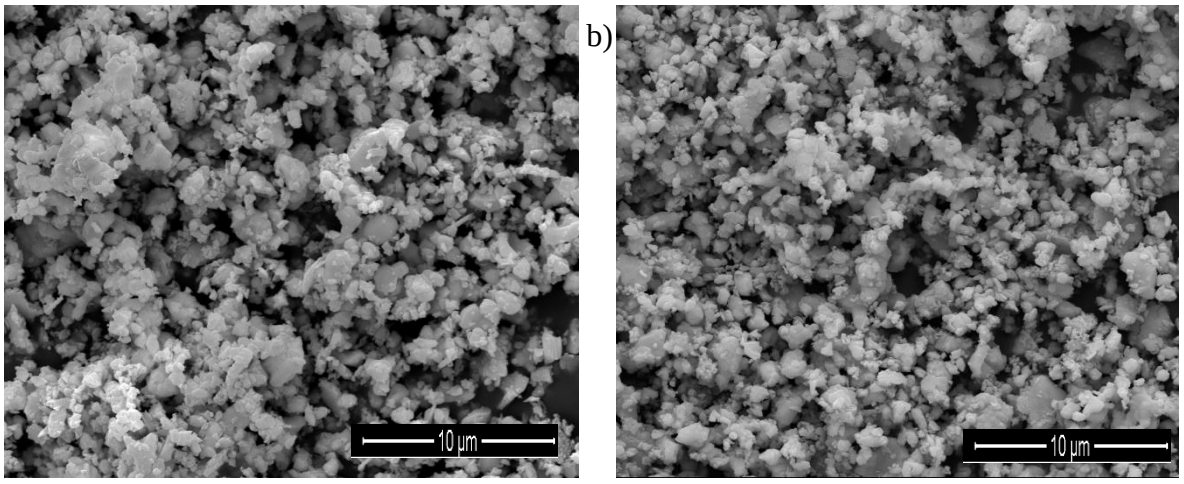

Figure 4.4: *Typical SEM images of $La_{3.2}Sr_{0.8}Ti_4O_{13.9\pm\delta}$ powder after calcination: (a) before ball milling; (b) after ball milling*

SEM images of polished and etched $La_{4-x}Sr_xTi_4O_{14-\frac{x}{2}\pm\delta}$ ceramics (x=0.2-0.8 sintered at 1350°C are shown in Figure.4.5. The plate like nature of the $La_4Ti_4O_{14}$ grains decreased with the addition of Sr which is in consistent with a previous report in which the plate-like nature of $La_4Ti_4O_{14}$ was suppressed by the addition of Ce [3]. There were still some grains that showed plate-like behaviour. The grain size was typically in the range of 0.3-0.7 µm with a few larger grains.

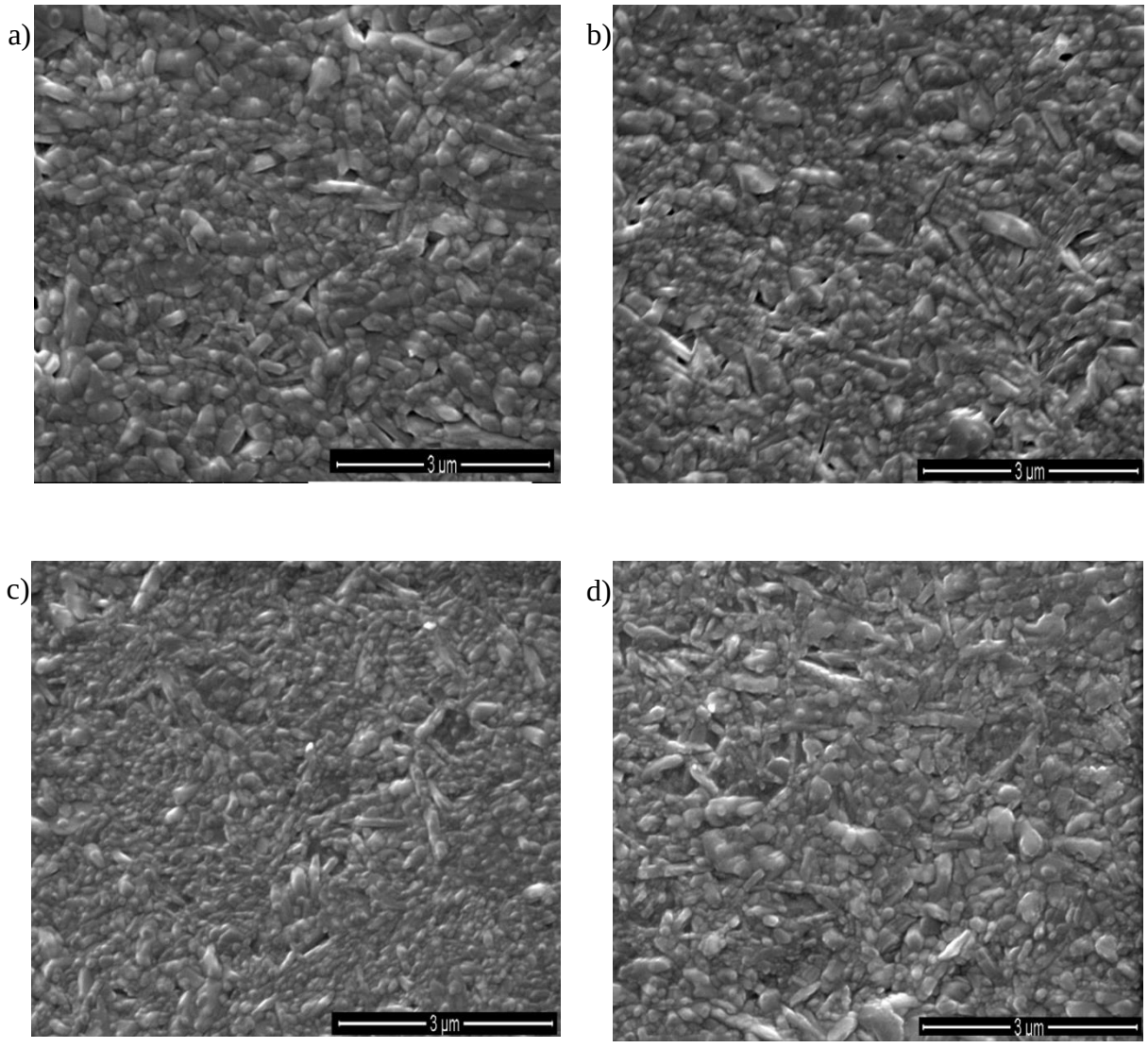

Figure 4.5: *SEM images of LST ceramics after polishing and etching: (a) $La_{3.8}Sr_{0.2}Ti_4O_{13.9\pm\delta}$; (b) $La_{3.6}Sr_{0.4}Ti_4O_{13.8\pm\delta}$; (c) $La_{3.6}Sr_{0.6}Ti_4O_{13.7\pm\delta}$; (d) $La_{3.2}Sr_{0.8}Ti_4O_{13.6\pm\delta}$*

Figure 4.6(a) shows a typical bright field TEM image of the $La_4Ti_4O_{14}$ ceramics after air annealing. The typical grain size of the ceramic was ~ 0.7 μm and most of the grains were defect free except for a few planar defects. Figure 4.6(b) shows a high resolution image of (100) lattice planes. The inter-planar spacing corresponds to the 4 layer $La_4Ti_4O_{14}$ (~ 12.63Å). The corresponding diffraction pattern is shown in Figure 4.6(c). Figures 4.6(d-e) show bright field TEM images of $La_{3.2}Sr_{0.8}Ti_4O_{13.6\pm\delta}$ air annealed ceramic, which has a large number of nanoscale intergrowths. These intergrowths were distributed homogeneously throughout the ceramic. Some of the intergrowths terminated or moved to a different plane of the $La_4Ti_4O_{14}$ as shown in the Figure 4.6(f). When two intergrowths terminated, they disturbed the neighbouring planes and created a 'bulging' of the planes in between as clearly seen in the Figure 4.6(f). The inter-planar spacing also changed when there was an intergrowth. The spacing difference before and after the intergrowth corresponds to one octahedral layer in the PLS compounds, which means the structure is changing from a $La_4Ti_4O_{14}$ (4 layer, d spacing = 12.63 Å) to a $La_5Ti_5O_{17}$ (5 layer, d spacing of 15.7 Å) perovskite compound as a result of intergrowth of the 5 layer PLS compound as shown in Figure 4.6(g-h).

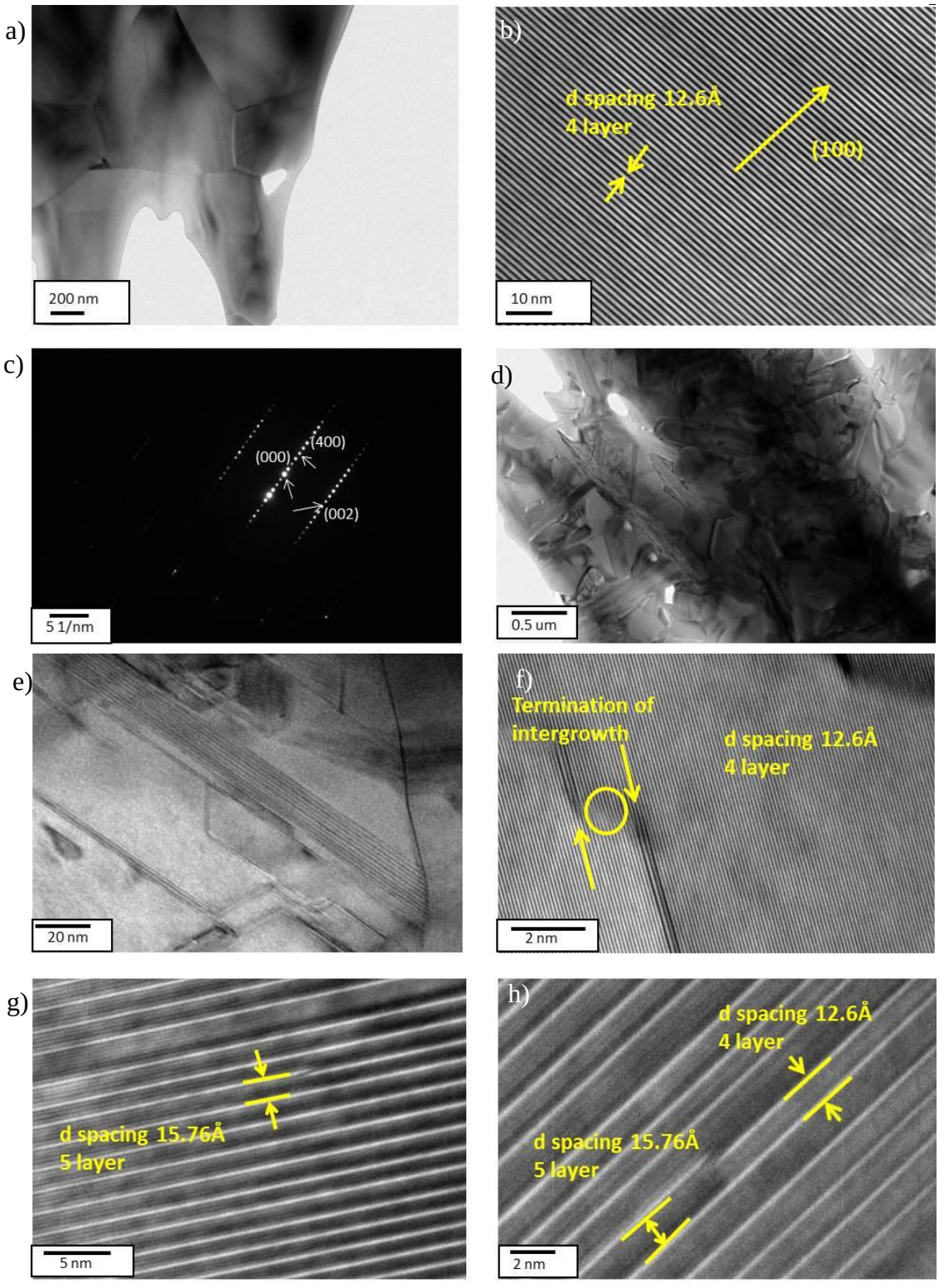

Figure 4.6: *TEM images of air annealed: (a) $La_4Ti_4O_{14\pm\delta}$; (b) high magnification image of $La_4Ti_4O_{14\pm\delta}$;(c) diffraction pattern of the air annealed $La_4Ti_4O_{14}$; (d) $La_{3.2}Sr_{0.8}Ti_4O_{13.6\pm\delta}$ showing the large defect (intergrowth) number; (e) $La_{3.2}Sr_{0.8}Ti_4O_{13.6\pm\delta}$; (f) $La_{3.2}Sr_{0.8}Ti_4O_{13.6\pm\delta}$ showing termination of intergrowths; (g-h) $La_{3.2}Sr_{0.8}Ti_4O_{13.6\pm\delta}$ showing two regions of intergrowths*

Figure 4.7(a) shows a bright field image of reduced $La_4Ti_4O_{14}$ based ceramic. After reduction the density of $La_4Ti_4O_{14}$ decreased slightly (from 5.74 g cm^{-3}to5.62 g cm^{-3}) and few planar defects appeared. Figure 4.7(b) represents high resolution image of a typical planar defect in reduced $La_4Ti_4O_{14\pm\delta}$ ceramic. After reduction the density of $La_{3.2}Sr_{0.8}Ti_4O_{13.6\pm\delta}$ decreased slightly (from 5.53 g $cm^{-3}$to 5.47 g cm^{-3}). The structure still has a high density of intergrowths as shown in Figure 4.7(c-d). It is inconclusive to comment on difference in intergrowth number between air annealed and reduced ceramics from the TEM images, but the XRD clearly indicated an increased amount of $La_5Ti_5O_{17}$ intergrowths in reduced $La_{3.2}Sr_{0.8}Ti_4O_{13.6\pm\delta}$. Figure 4.7(e) shows a magnified region of intergrowths and their termination. The corresponding diffraction pattern is also shown in Figure 4.7 (f). The structure still shows bulging of planes as observed in Figure 4.6 (e and f).

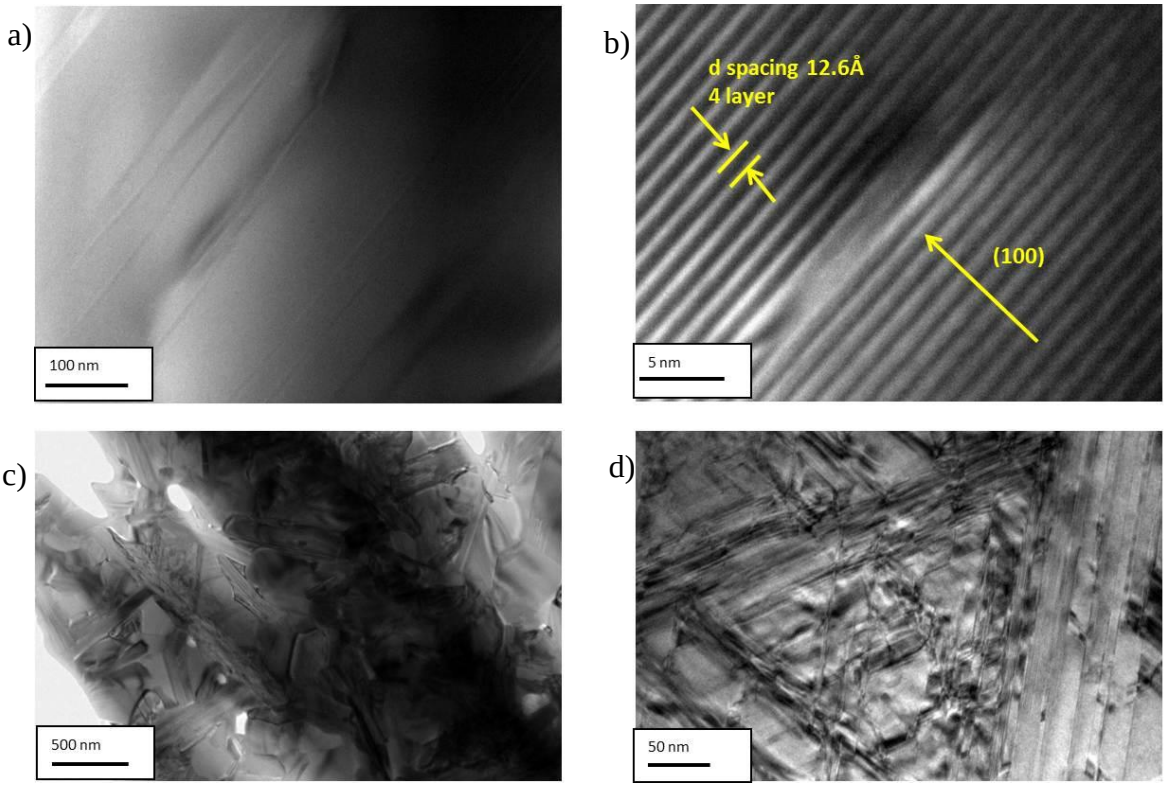

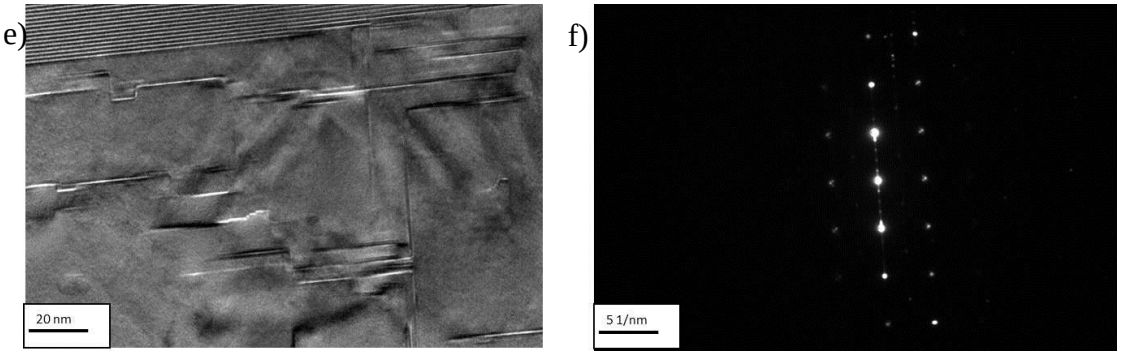

Figure 4.7: *TEM images of reduced: (a) $La_4Ti_4O_{14\pm\delta}$; (b) high magnification image of $La_4Ti_4O_{14\pm\delta}$; (c-d) $La_{3.2}Sr_{0.8}Ti_4O_{13.6\pm\delta}$ showing the large defect (intergrowth) number;(e) a high magnification image of a typical region in $La_{3.2}Sr_{0.8}Ti_4O_{13.6\pm\delta}$ showing intergrowths; (f) corresponding diffraction pattern of $La_{3.2}Sr_{0.8}Ti_4O_{13.6\pm\delta}$*

Figure 4.8(a–d) shows the XPS spectra of surface electrons for different elements in $La_4Ti_4O_{14}$ based ceramics after ion beam etching. The ion beam etching was done for 5 min. Since the C reference used by different labs varies, the absolute value of each element varies in a range. Figure 4.8(a) shows the XPS spectra of La 3d electrons. The binding energy (BE) values for La 3d showed a clear doublet for both components ($La3d_{5/2}$ and $La3d_{3/2}$) which is a characteristic of La containing oxide compounds [9]. The binding energy difference between the splitting of La $3d_{5/2}$ and La $3d_{3/2}$ was ~ 4.6eV and ~ 4.4 eV, respectively, for all of the ceramics. Figure 4.8(b) shows the XPS spectra of a typical Ti 2p doublet. For air annealed $La_4Ti_4O_{14}$, the peak position marked as A (459.17 eV) and the FWHM match the Ti^{4+} state [3]. The Ti 2p peak is slightly asymmetric and it gives rise to another peak at 457.67 eV which is marked as B. It is inconclusive to say whether this peak was caused by the ion beam etching damage and (or) because of the presence of Ti^{3+} state [10]. After reduction, one additional peak can be seen at 453.9 eV which is marked as C. This peak can be attributed to the Ti^{2+} state as reported in literature [11, 12]. The intensity of the peak marked as B' also increased in the reduced ceramic. Since

both the samples were subjected to the same amount of etching; it is conclusive to determine the presence of Ti^{3+} state also.

The corresponding O 1s core level spectra are shown in the Figure 4.8(c). All the spectra show same symmetry towards the lower binding energy side which can be attributed to the bonded oxygen in the structure as reported in literature [13]. The higher binding energy component indicates chemisorbed oxygen or absorbed hydroxyl ions [9]. In the case of the air annealed $La_4Ti_4O_{14\pm\delta}$, the peak position for the oxygen was 530.7 eV which changed to 529.6 eV after hydrogen reduction. This decrease in binding energy can be related to the loss of oxygen or the oxygen being compromised during the formation of nanoscale intergrowths.

Figure 4.8(d) gives the Sr 3d core level spectrum. The peak shape and position matched well with the reported value [13]. After Sr addition, there was no noticeable difference in the peak size and shape for La3d electrons, the binding energy difference between La $3d_{5/2}$ and La $3d_{3/2}$ doublets in air annealed $La_{3.2}Sr_{0.8}Ti_4O_{14\pm\delta}$ was 4.44 eV. For Ti 2p electrons, the peak marked as B'' increased which indicates the presence of Ti^{3+} ions. Since the TEM and XRD results showed the presence of localized 5 layer structure, the decrease in binding energy can be related to an increase in separation of the oxygen interlayer. For O1s, the peak position was at 530.4 eV which is on the lower side as compared to air annealed $La_4Ti_4O_{14\pm\delta}$ (529.6 eV). Since 5 layer PLS compound has less oxygen content than 4 layer PLS compound and the amount of 5 layer intergrowths increase in the air annealed $La_{3.2}Sr_{0.8}Ti_4O_{13.6\pm\delta}$ ceramic as compared to $La_4Ti_4O_{14\pm\delta}$. This indicates that the oxygen has been compromised during the formation of an intergrowth.

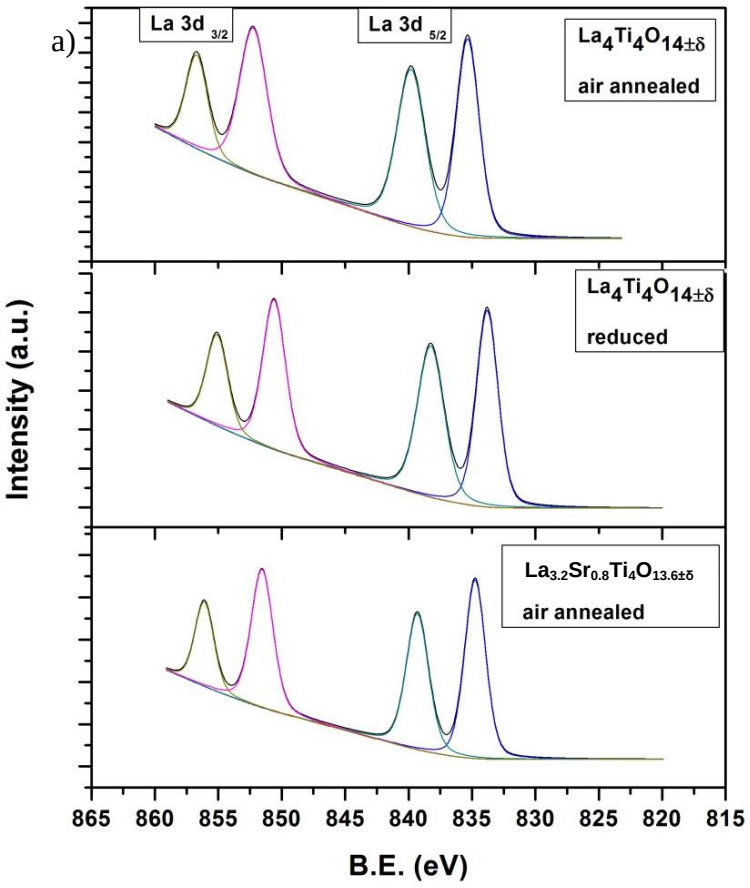
a)
La 3d 3/2
La 3d 5/2
La4Ti4O14±δ
air annealed
La4Ti4O14±δ
reduced
La3.2Sr0.8Ti4O13.6±δ
air annealed
Intensity (a.u.)
865 860 855 850 845 840 835 830 825 820 815
B.E. (eV)

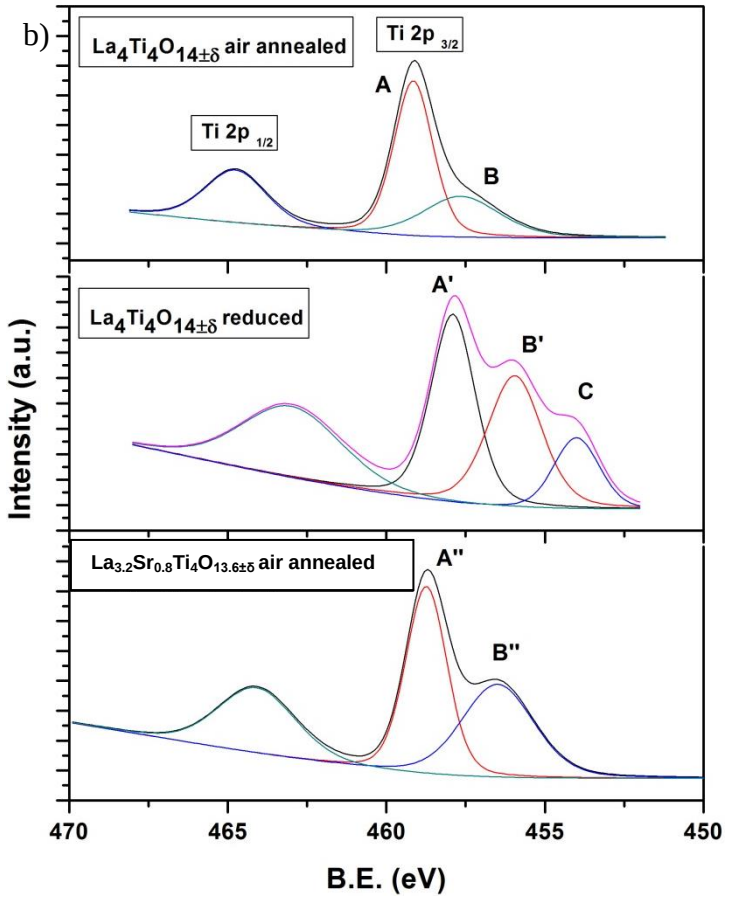
b)
La4Ti4O14±δ air annealed
Ti 2p 3/2
Ti 2p 1/2
A
B
La4Ti4O14±δ reduced
A'
B'
C
La3.2Sr0.8Ti4O13.6±δ air annealed
A''
B''
Intensity (a.u.)
470 465 460 455 450
B.E. (eV)

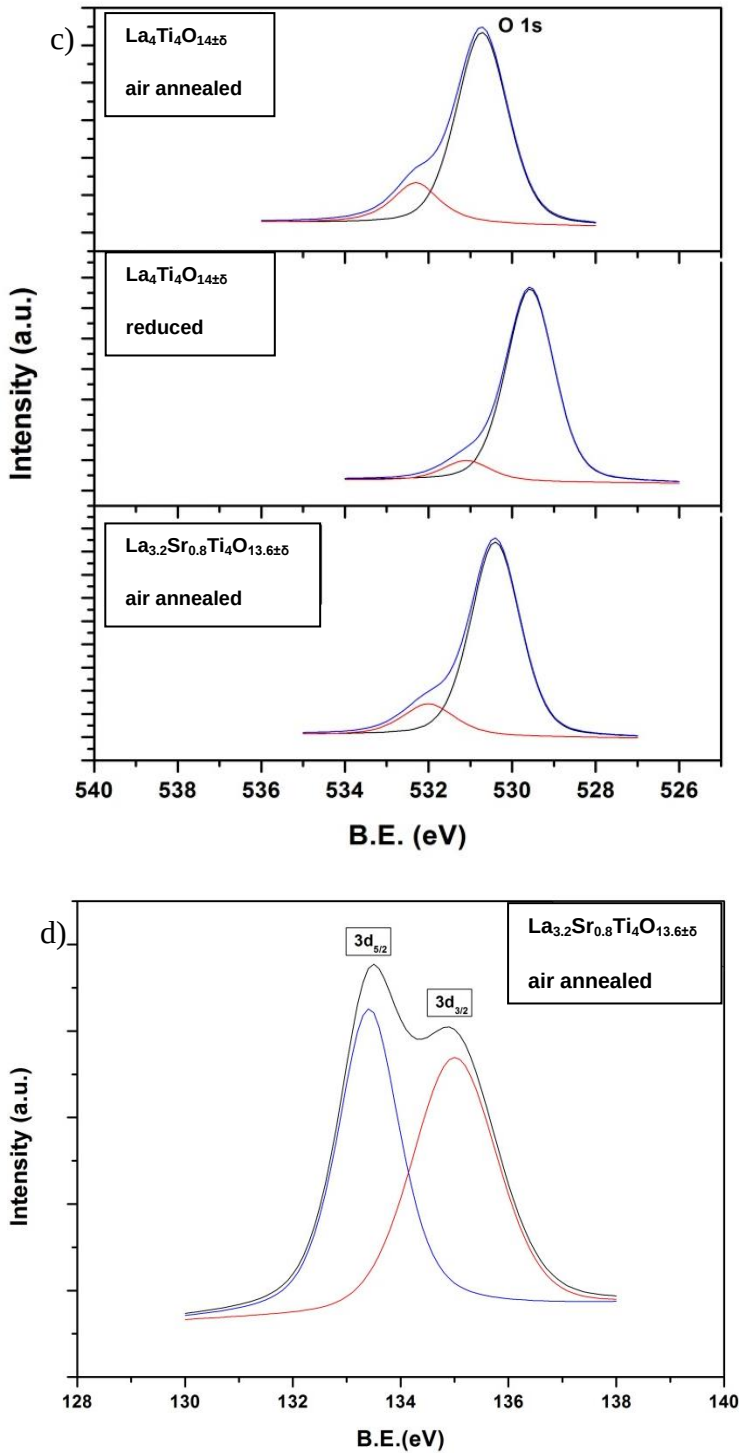

Figure 4.8: *XPS spectrum of $La_{4-x}Sr_xTi_4O_{13.6\pm\delta}$: (a) La 3d; (b) Ti 2p; (c) O 1s; (d) Sr 3d*

In order to improve the quantitative analysis of the data, the binding energy difference (ΔBE) method was used which helps to reduce scatter in the data [14]. The ΔBE values for the pure and Sr substituted $La_4Ti_4O_{14\pm\delta}$ are given in Table 4.3. The ΔBE (O-Ti) for air annealed and hydrogen reduced $La_4Ti_4O_{14\pm\delta}$ samples was calculated to be 71.5 eV and 71.6 eV respectively. These values are in good agreement with the published literature [11]. The ΔBE (O-Ti) does not change after the addition of Sr. The ΔBE (La-O) for air annealed $La_4Ti_4O_{14}$ was found to be 304.7 eV which decreased to 304.2 eV after reduction. This decrease in binding energy was due to the decrease in bonding as a result of oxygen removal after reduction. After the Sr substitution, the ΔBE (La-O) was 304.4 eV which is lower than the pure air annealed $La_4Ti_4O_{14}$ but higher than the pure reduced $La_4Ti_4O_{14\pm\delta}$. These results are in accordance with the TEM results which suggest the presence of localised planar defects/intergrowths in the reduced and Sr substituted $La_4Ti_4O_{14}$ which causes the weakening of the La-O bonds. ΔBE (Sr-O) was calculated to be 397 eV and it agrees with the reported value [13].

Table 4.3: XPS data of $La_{4-x}Sr_xTi_4O_{13.6\pm\delta}$ ceramics

Material	Peak Position (eV)				Binding Energy Difference (ΔeV)		
	La3d		Ti2P	O1s	La-O	Ti-O	Sr-O
	$La3d_{3/2}$	$La3d_{5/2}$					
$La_4Ti_4O_{14\pm\delta}$ air annealed	852.2	835.4	459.2	530.7	304.7	71.5	-
$La_4Ti_4O_{14\pm\delta}$ reduced	850.6	833.8	458	529.6	304.2	71.6	-
$La_{3.2}Sr_{0.8}Ti_4O_{13.6\pm\delta}$ air annealed	851.6	834.8	458.8	530.4	304.4	71.6	397.0

4.4 $La_4Ti_{4-x}Ta_xO_{14+\frac{x}{2}\pm\delta}$

Table 4.4 presents the theoretical and relative densities of pure and $La_4Ti_{4-x}Ta_xO_{14+\frac{x}{2}\pm\delta}$ ceramics after SPS. The theoretical density of all the ceramics increased after substitution due to higher atomic weight of Ta (~ 180.9 amu). All the ceramics were more than 98% dense.

Table 4.4: Theoretical and relative densities of $La_4Ti_{4-x}Ta_xO_{14+\frac{x}{2}\pm\delta}$ ceramics

	Theoretical Density ($g\ cm^{-3}$)	Relative Density (%)
$La_4Ti_4O_{14\pm\delta}$	5.78	99.3
$La_4Ti_{3.9}Ta_{0.1}O_{14.05\pm\delta}$	5.87	99.4
$La_4Ti_{3.8}Ta_{0.2}O_{14.1\pm\delta}$	5.95	99.2
$La_4Ti_{3.6}Ta_{0.4}O_{14.2\pm\delta}$	6.12	97.2
$La_4Ti_{3.4}Ta_{0.6}O_{14.3\pm\delta}$	6.29	96.5

Figure 4.9 shows the X ray diffraction patterns for $La_4Ti_{4-x}Ta_xO_{14+\frac{x}{2}\pm\delta}$ (x=0, 0.1, 0.2, 0.4 and 0.6) in powder, sintered, air annealed and reduced conditions. No secondary phase was observed in the powders till x = 0.4 and the peaks matched with $La_4Ti_4O_{14}$, n=4 (PDF card # 28-0517). After x=0.4, a secondary phase was produced as a result of Ta doping. This new generated phase was indexed as $La_3Ti_2TaO_{11}$ (PDF card # 00-054-0632) which is a n =3 PLS structure. All the peaks in the XRD pattern were sharp giving an indication of a large particle size (> 0.5μm).

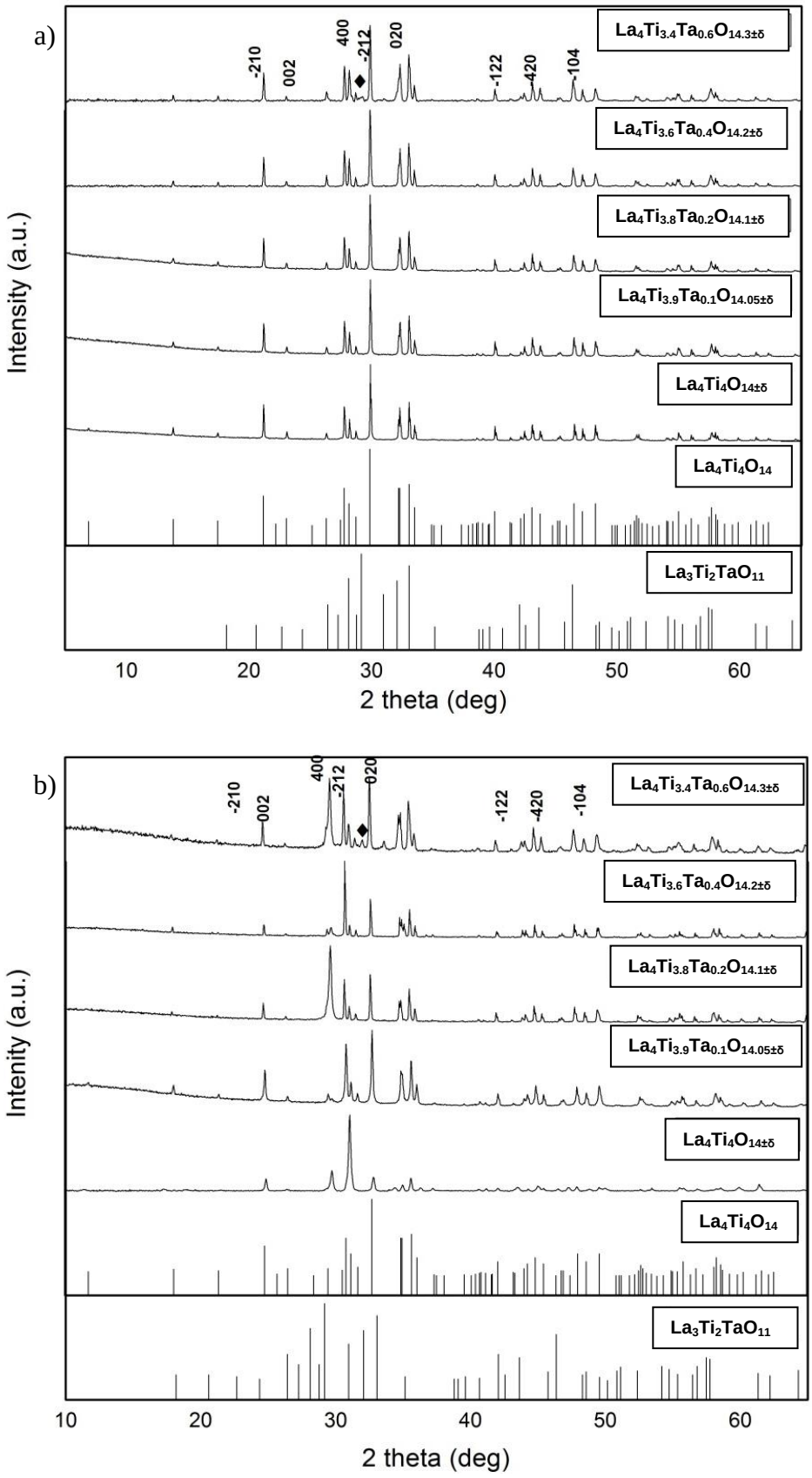
a)
-210
002
400
-212
020
-122
-420
-104
La4Ti3.4Ta0.6O14.3±δ
La4Ti3.6Ta0.4O14.2±δ
La4Ti3.8Ta0.2O14.1±δ
La4Ti3.9Ta0.1O14.05±δ
La4Ti4O14±δ
La4Ti4O14
La3Ti2TaO11
Intensity (a.u.)
10
20
30
40
50
60
2 theta (deg)
b)
-210
002
400
-212
020
-122
-420
-104
La4Ti3.4Ta0.6O14.3±δ
La4Ti3.6Ta0.4O14.2±δ
La4Ti3.8Ta0.2O14.1±δ
La4Ti3.9Ta0.1O14.05±δ
La4Ti4O14±δ
La4Ti4O14
La3Ti2TaO11
Intenity (a.u.)
10
20
30
40
50
60
2 theta (deg)

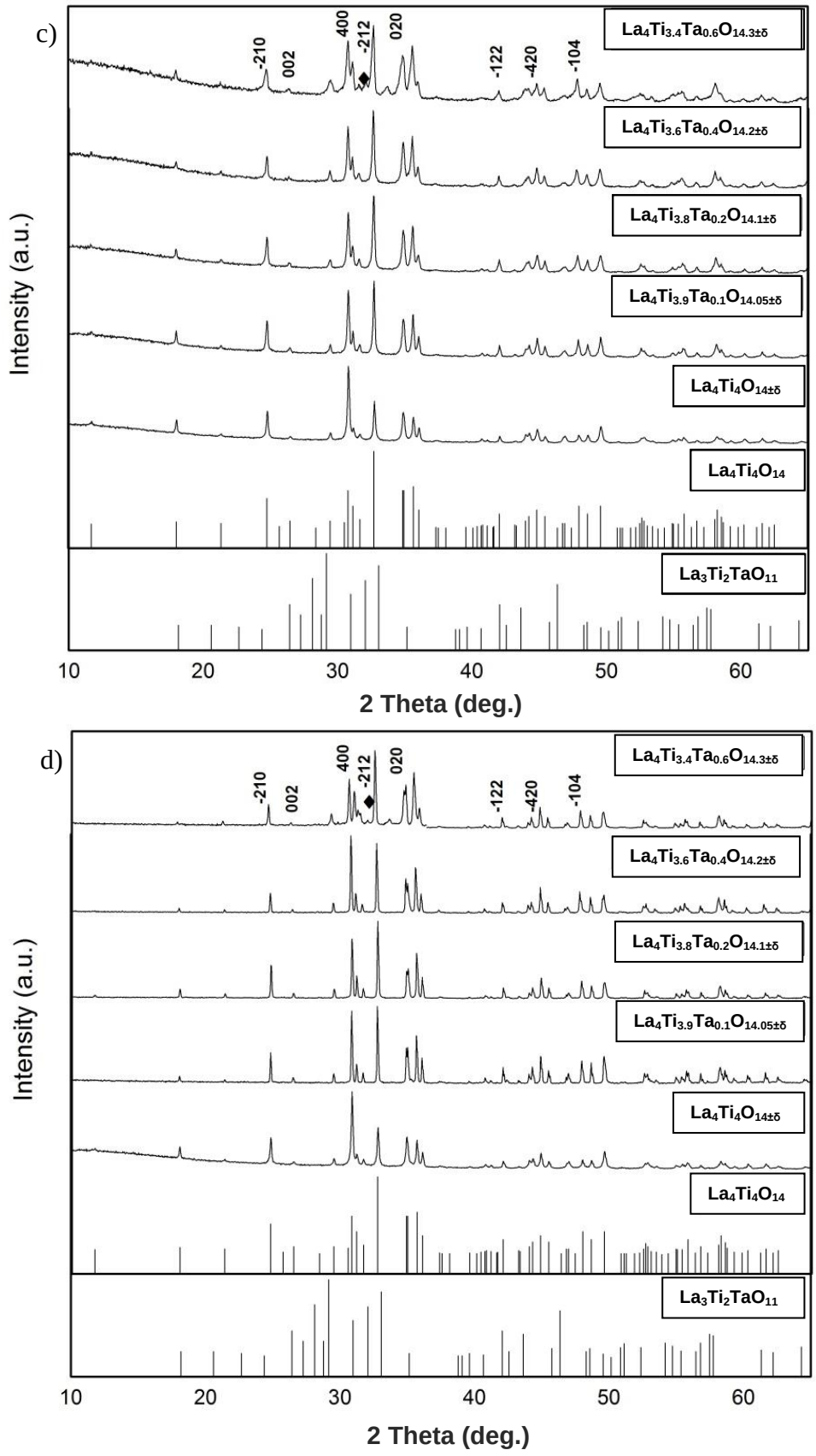

Figure 4.9: *XRD patterns of the $La_4Ti_{4-x}Ta_xO_{14+\frac{x}{2}\pm x}$: (a) powders; (b) sintered; (c) air annealed; (d) reduced samples*

For $La_4Ti_{3.4}Ta_{0.6}O_{14.3\pm\delta}$ powder, the amount of $La_3Ti_2TaO_{11}$ was estimated to be ~ 3.6 mass % which increased to ~ 4.6 mass % for sintered and air annealed ceramics. The amount of generated secondary phase was reduced to ~ 1.7 mass % after reduction. The reduced ceramics have less oxygen content and as a result the amount of second phase decreased. The decreased intensity of peak (♦) in reduced $La_4Ti_{3.4}Ta_{0.6}O_{14.3\pm\delta}$ ceramic clearly indicated the reduction in the amount of secondary phase. The peak intensity for the secondary phase was weak in the other compositions (x=0.1, 0.2 and 0.4) which did not allow the amount of secondary phase to be calculated.

Figure 4.10(a-b) shows a bright field TEM image of $La_4Ti_{3.6}Ta_{0.4}O_{14.2\pm\delta}$ air annealed ceramic with some planar defects. These defects were distributed homogeneously throughout the ceramic as shown in Figure 4.10(c). From XRD data, the formation of 3 layered PLS compound was confirmed. So, the regions of planar defects are the regions of 3 layered phase embedded inside 4 layered $La_4Ti_4O_{14}$. The structure of a 3 layer PLS compounds exist in two types, Type I and Type II. In Type I structure, the unit cell contains regular stacking of 3 layers of BO_6 octahedra, while in Type II, the unit cell contains alternate stacking of 4 and 2 layers of BO_6 octahedra. $La_3Tia_2TaO_{11}$ exists in the Type II structure as reported by Titov et al. [15]. The intergrowths in $La_4Ti_{4-x}Ta_xO_{14+\frac{x}{2}\pm\delta}$ are different from the ones in $La_{4-x}Sr_xTi_4O_{14-\frac{x}{2}\pm\delta}$. as shown in Figure 4.10(d). The intergrowths are shorter and they are within the 4 layer PLS compound. Figure 4.10(e) shows a magnified image of the region with intergrowths and the corresponding diffraction pattern is shown in Figure 4.11(f).

After reduction, the density of $La_4Ti_{3.6}Ta_{0.4}O_{14.2\pm\delta}$ decreased slightly (from 6.07 g $cm^{-3}$to 5.98 g cm^{-3}) and the density of intergrowths also decreased as observed

in the X-ray diffraction data (mass % decreased from 4.6 to 1.7). It is inconclusive to quantitatively analyse the defect density difference between air annealed and reduced $La_4Ti_{3.6}Ta_{0.4}O_{14.2\pm\delta}$ from TEM.

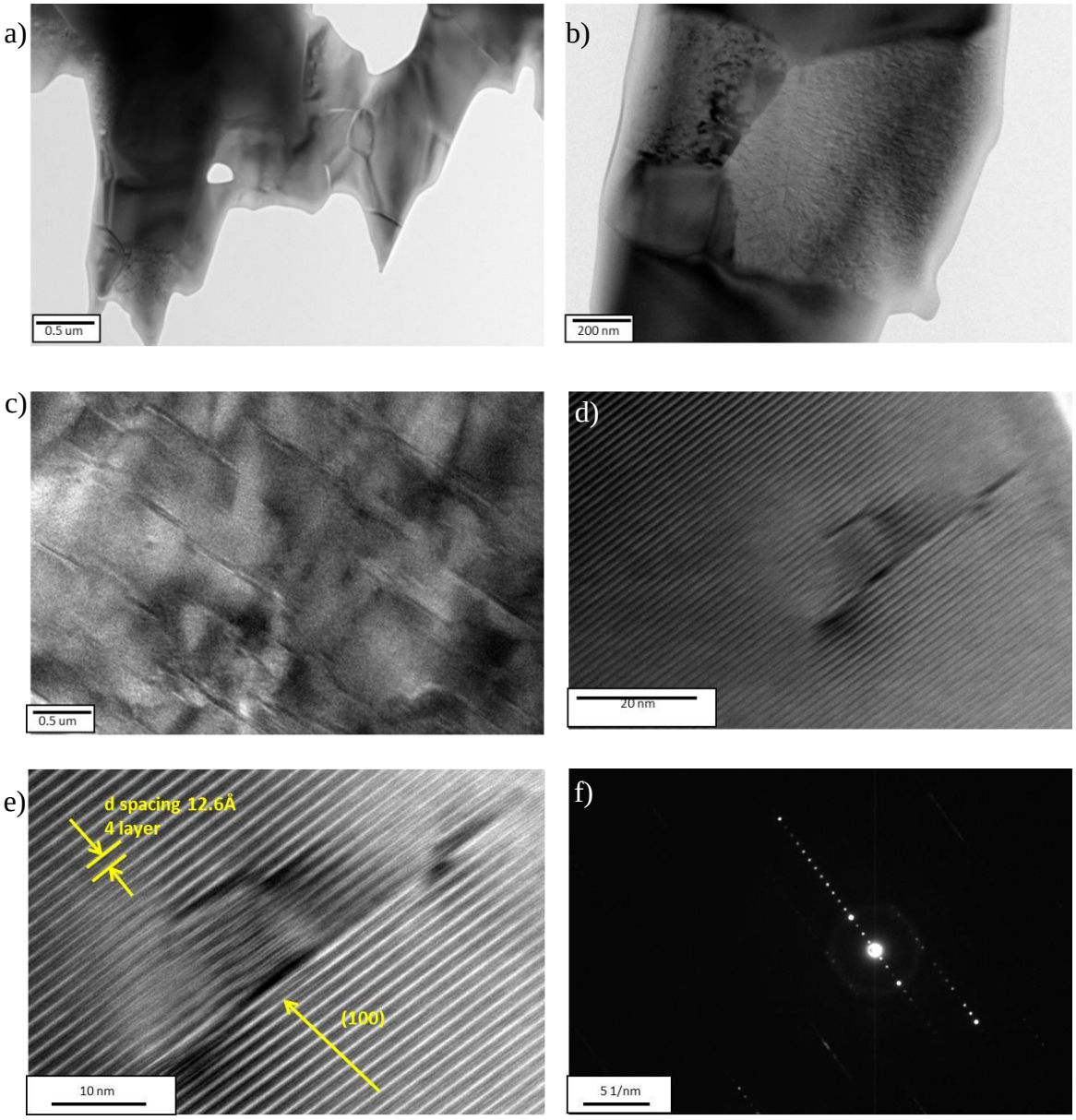

Figure 4.10: *TEM images of: (a) air annealed $La_4Ti_{3.6}Ta_{0.4}O_{14.2\pm\delta}$; (b) high magnification image of air annealed $La_4Ti_{3.6}Ta_{0.4}O_{14.2\pm\delta}$; (c) reduced $La_4Ti_{3.6}Ta_{0.4}O_{14.2\pm\delta}$; (d) high magnification image of reduced d $La_4Ti_{3.6}Ta_{0.4}O_{14.2\pm\delta}$ (e) high magnification image of reduced d $La_4Ti_{3.6}Ta_{0.4}O_{14.2\pm\delta}$ with d spacing; (f) diffraction pattern of high magnification image of reduced d $La_4Ti_{3.6}Ta_{0.4}O_{14.2\pm\delta}$*

The nanoscale intergrowths observed in the high magnification TEM images of air annealed $La_4Ti_{3.6}Ta_{0.4}O_{14.2\pm\delta}$ match exactly with the XRD results of air annealed $La_4Ti_{3.6}Ta_{0.4}O_{14.2\pm\delta}$ ceramic, where the peak width of all the peaks has increased. This peak broadening is attributed to the localized intergrowths of 3 layer PLS phase within the 4 layer structure. The broadening of the peaks followed a systematic trend increasing with increasing amount of Ta in $La_4Ti_4O_{14}$ as given in Table 4.5. After reduction, the peak width decreases and also the amount of generated secondary phase.

Table 4.5: FWHM of the $La_4Ti_{4-x}Ta_xO_{14+\frac{x}{2}\pm\delta}$ ceramics

x	**Powder**	**Sinter**	**Annealed**	**Reduced**	**Powder**	**Sinter**	**Annealed**	**Reduced**
	Peak (-212) /2θ^0				(400) /2θ^0			
0	0.14	0.15	0.16	0.14	0.14	0.16	0.17	0.18
0.1	0.12	0.14	0.16	0.11	0.14	0.14	0.18	0.11
0.2	0.14	0.13	0.20	0.13	014	0.14	0.19	0.13
0.4	0.13	0.12	0.23	0.13	0.14	0.13	0.20	0.13
0.6	0.14	0.15	0.31	0.14	0.14	0.14	0.26	0.15

Figure 4.11 compares the XPS spectra of pure and Ta substituted $La_4Ti_4O_{14}$. The explanation of $La_4Ti_4O_{14}$ air annealed and reduced data has been discussed previously (section 4.3). After Ta addition, the binding energy for La 3d doublet and the Ti 2p increased compared to those for $La_4Ti_4O_{14}$ and are given in Table 4.6. The B peak which was observed for Ti 2p in pure $La_4Ti_4O_{14\pm\delta}$ disappeared after Ta substitution. This indicates that Ti is present in Ti^{4+} form in Ta substituted $La_4Ti_4O_{14}$. The binding energy for O 1s is similar to the one in pure $La_4Ti_4O_{14\pm\delta}$.

a)

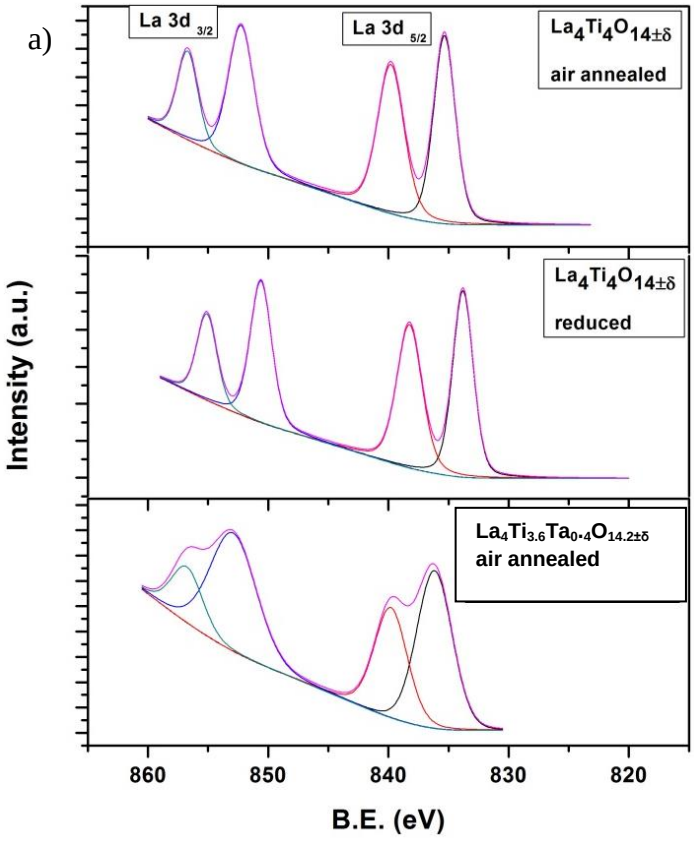
La 3d 3/2
La 3d 5/2
La4Ti4O14±δ
air annealed
La4Ti4O14±δ
reduced
La4Ti3.6Ta0.4O14.2±δ
air annealed
Intensity (a.u.)
860
850
840
830
820
B.E. (eV)

b)

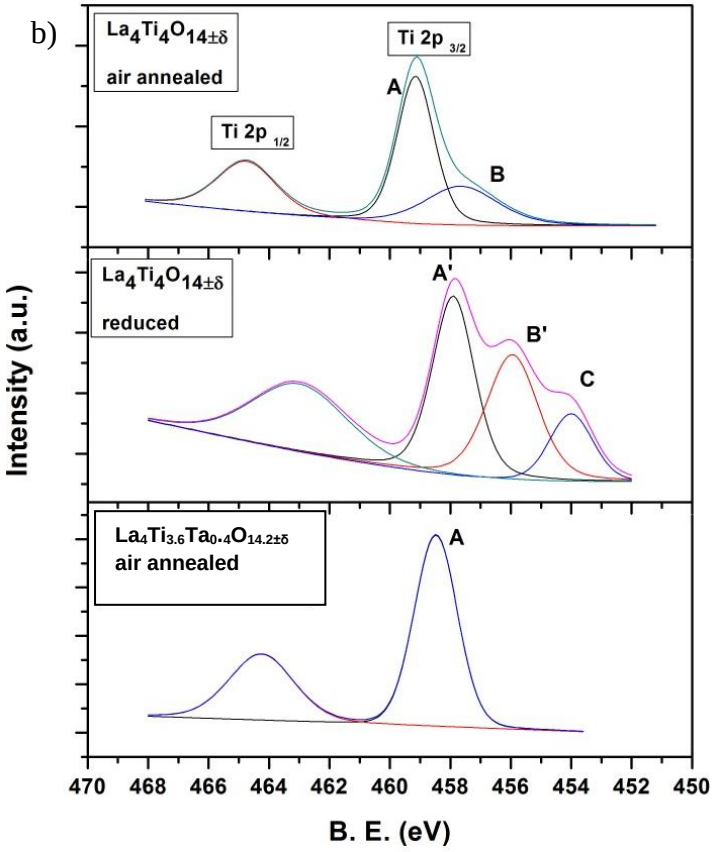
La4Ti4O14±δ
air annealed
Ti 2p 3/2
Ti 2p 1/2
A
B
La4Ti4O14±δ
reduced
A'
B'
C
La4Ti3.6Ta0.4O14.2±δ
air annealed
A
Intensity (a.u.)
470
468
466
464
462
460
458
456
454
452
450
B. E. (eV)

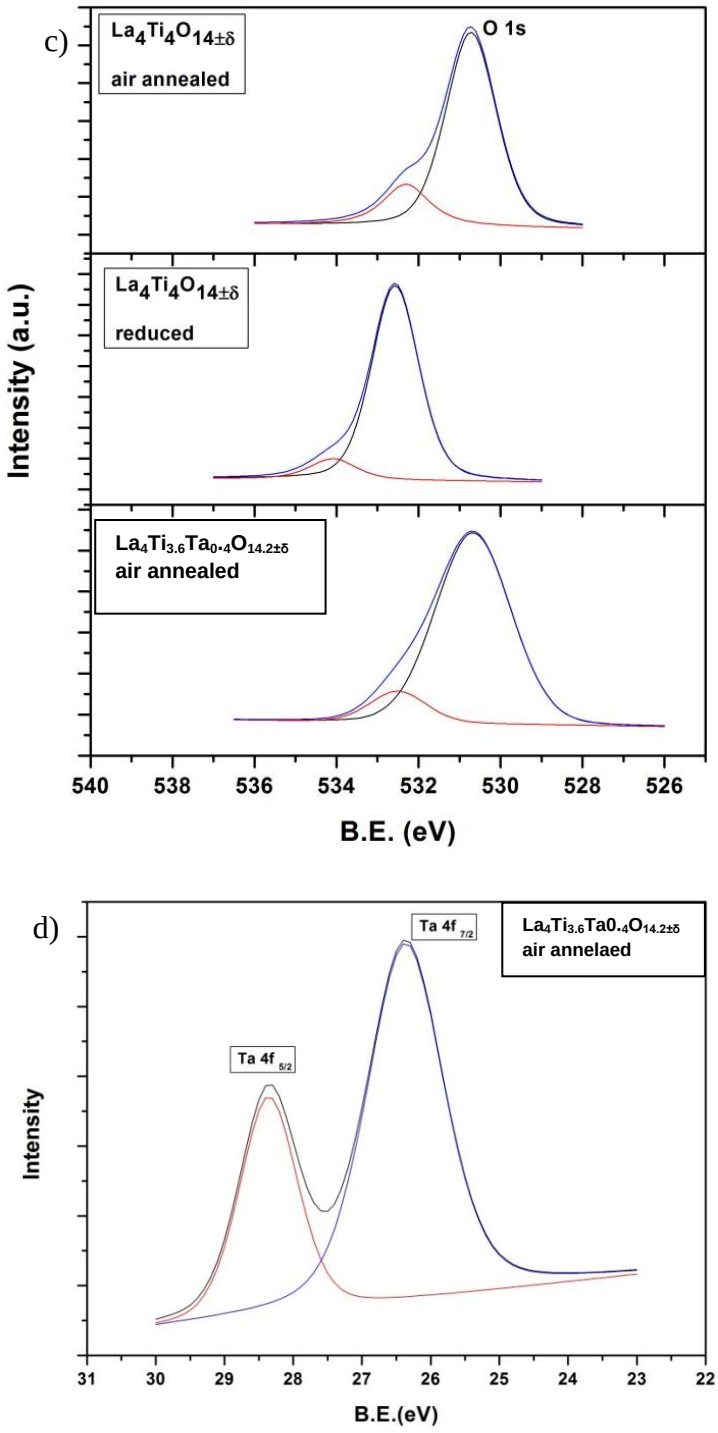

Figure 4.11: *XPS spectrum of $La_4Ti_{4-x}Ta_xO_{14+\frac{x}{2}\pm\delta}$: (a) La 3d; (b) Ti 2p; (c) O1s; (d) Ta 4f*

Table 4.6 compares the peak position and ΔBE values of all the elements of $La_4Ti_{3.6}Ta_{0.4}O_{14.2\pm\delta}$ ceramic. The ΔBE (La-O) and ΔBE (O-Ti) increases after Ta substitution in $La_4Ti_4O_{14}$. Since both La and Ti exist in two bonding states, i.e. in $La_4Ti_4O_{14}$ and $La_4Ti_{3.6}Ta_{0.4}O_{14.2\pm\delta}$, the increase in ΔBE indicates an increase in the bonding between La/Ti and oxygen.

Table 4.6: XPS data of $La_4Ti_{3.6}Ta_{0.4}O_{14.2\pm\delta}$ ceramics

Material	Peak Position (eV)				Binding Energy Difference (ΔeV)		
	La3d		Ti2P	O1s	La-O	Ti-O	Ta-O
	$La3d_{3/2}$	$La3d_{5/2}$					
$La_4Ti_4O_{14\pm\delta}$ air annealed	852.2	835.4	459.2	530.7	304.7	71.5	-
$La_4Ti_4O_{14\pm\delta}$ reduced	850.6	833.8	458	529.6	304.2	71.6	-
$La_4Ti_{3.6}Ta_{0.4}O_{14.2\pm\delta}$ air annealed	853.0	836.2	458.4	530.6	305.6	72.2	504.4

4.5 $La_4Ti_{4-x}Nb_xO_{14+\frac{x}{2}\pm\delta}$

Table 4.7 represents the theoretical and relative densities of pure and Nb substituted $La_4Ti_4O_{14}$ ceramics after SPS. The theoretical density of all the ceramics increased after substitution due to higher atomic weight of Nb (~ 92.9 amu). All the ceramics were more than 98% dense.

Table 4.7: Theoretical and relative densities of $La_4Ti_{4-x}Nb_xO_{14+\frac{x}{2}\pm\delta}$ ceramics

	Theoretical Density ($g\ cm^{-3}$)	Relative Density (%)
$La_4Ti_4O_{14\pm\delta}$	5.78	99.3
$La_4Ti_{3.8}Nb_{0.2}O_{14.1\pm\delta}$	5.85	99.5
$La_4Ti_{3.6}Nb_{0.4}O_{14.2\pm\delta}$	5.91	99.3
$La_4Ti_{3.4}Nb_{0.6}O_{14.3\pm\delta}$	5.97	98.4

X ray diffraction patterns for $La_4Ti_{4-x}Nb_xO_{14}$ (x=0, 0.2, 0.4 and 0.6) in powder, sintered, air annealed and reduced conditions are shown in Figure 4.12. All the peaks matched with $La_4Ti_4O_{14}$, n=4 (PDF card # 28-0517) until x= 0.2. After x=0.2, a second phase was generated which was indexed as $LaNbO_4$ (PDF card # 01-081-1973) which is a n = 2 PLS phase. The second phase was produced as a result of the reaction between La and Nb during calcination. For x= 0.4, a shoulder at 28.8^o (2 theta) gives an indication of the second phase. This shoulder increases with increasing Nb content. The amount of $LaNbO_4$ (by mass) was calculated by the RIR method and was found to be ~ 3 mass% and ~ 0.9 mass % for $La_4Ti_{3.4}Nb_{0.6}O_{14.3\pm\delta}$ powder and sintered $La_4Ti_{3.6}Nb_{0.4}O_{14.3\pm\delta}$ respectively.

a)

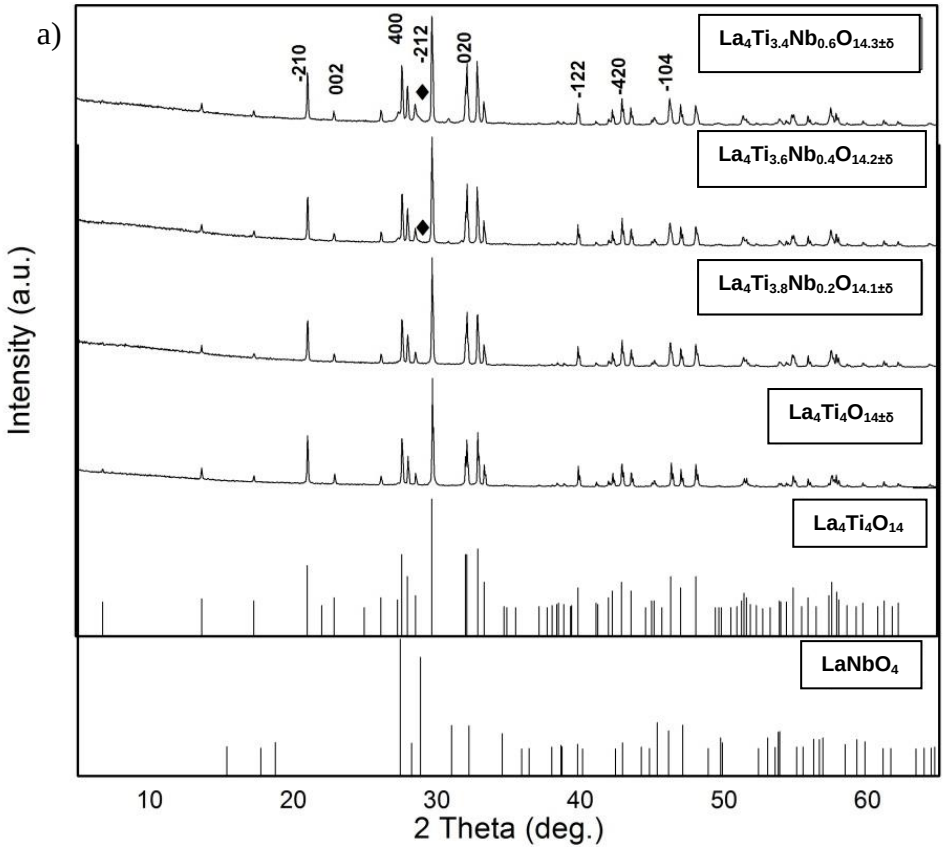
-210
002
400
-212
020
-122
-420
-104
La4Ti3.4Nb0.6O14.3±δ
La4Ti3.6Nb0.4O14.2±δ
La4Ti3.8Nb0.2O14.1±δ
La4Ti4O14±δ
La4Ti4O14
LaNbO4
Intensity (a.u.)
10
20
30
40
50
60
2 Theta (deg.)

b)

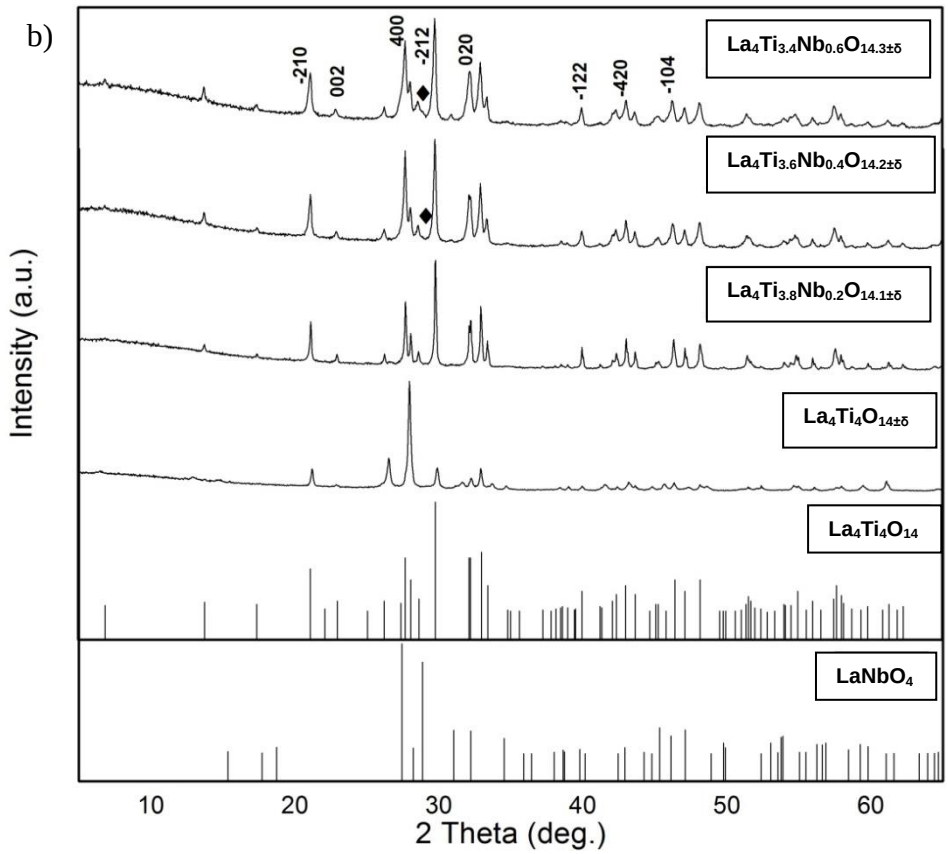
-210
002
400
-212
020
-122
-420
-104
La4Ti3.4Nb0.6O14.3±δ
La4Ti3.6Nb0.4O14.2±δ
La4Ti3.8Nb0.2O14.1±δ
La4Ti4O14±δ
La4Ti4O14
LaNbO4
Intensity (a.u.)
10
20
30
40
50
60
2 Theta (deg.)

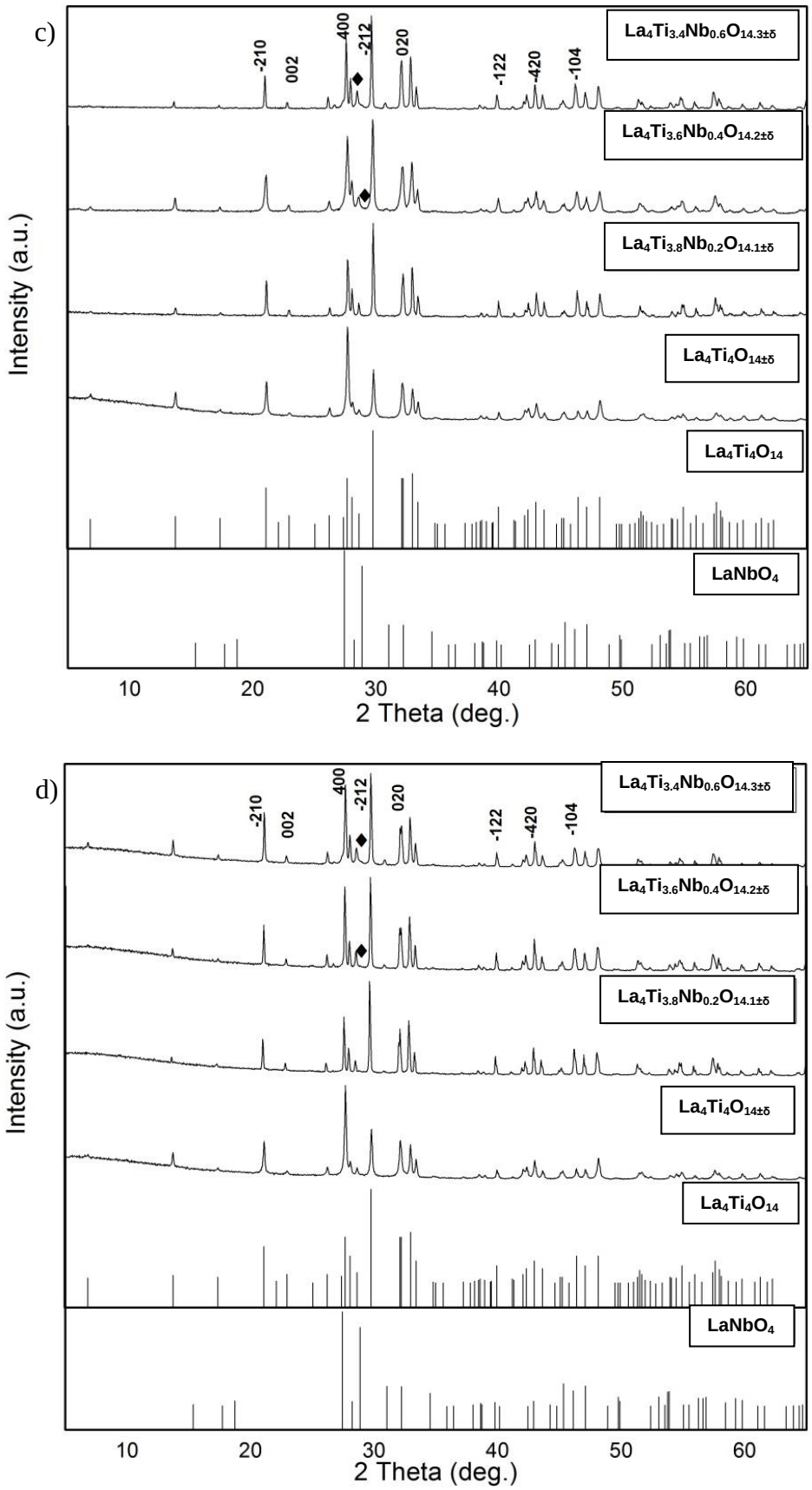

Figure 4.12: *XRD patterns of the $La_4Ti_{4-x}Nb_xO_{14.3\pm\delta}$: (a) powders; (b) sintered; (c) air annealed; (d) reduced samples*

Bright field TEM images of $La_4Ti_{3.4}Nb_{0.6}O_{14.3\pm\delta}$ air annealed ceramic are given in Figure 4.13 (a-b). As observed in section 4.4, Ta substitution in $La_4Ti_4O_{14}$ generates a 3 layered PLS compound, but Nb substitution did not form a n=3 PLS compound but formed a 2 layer PLS compound instead which was $LaNbO_4$ in this case. From the XRD data, formation of the n=2 layer PLS compound $LaNbO_4$ was confirmed and it can be clearly seen as a single phase grain in the Figure 4.13(b). The microstructure of the $LaNbO_4$ matches with that reported by Lee et al. [16]. The d spacing (~ 2.8 Å) matches with the d spacing of the $LaNbO_4$ phase as shown in Figure 4.13(c). The corresponding diffraction pattern is shown in the Figure 4.13(d). In some areas, $LaNbO_4$ was uniformly distributed while in others, it was found in clusters. The same is true for $La_4Ti_4O_{14}$ grains as shown in Figure 4.13(b and d). Figure 4.13(f) shows a high magnification image of a typical $LaNbO_4$ grain. Some planar defects were also seen in the grains of $LaNbO_4$. The origin of these defects cannot be determined due to the involvement of many variables which include SPS processing or the substitution of Ti inside $LaNbO_4$. After reduction, the density of $La_4Ti_{3.4}Nb_{0.6}O_{14\pm\delta}$ decreased slightly (from 5.8 g $cm^{-3}$to 5.76 g cm^{-3}) and the amount of $LaNbO_4$ stayed nearly the same as observed in X-ray diffraction.

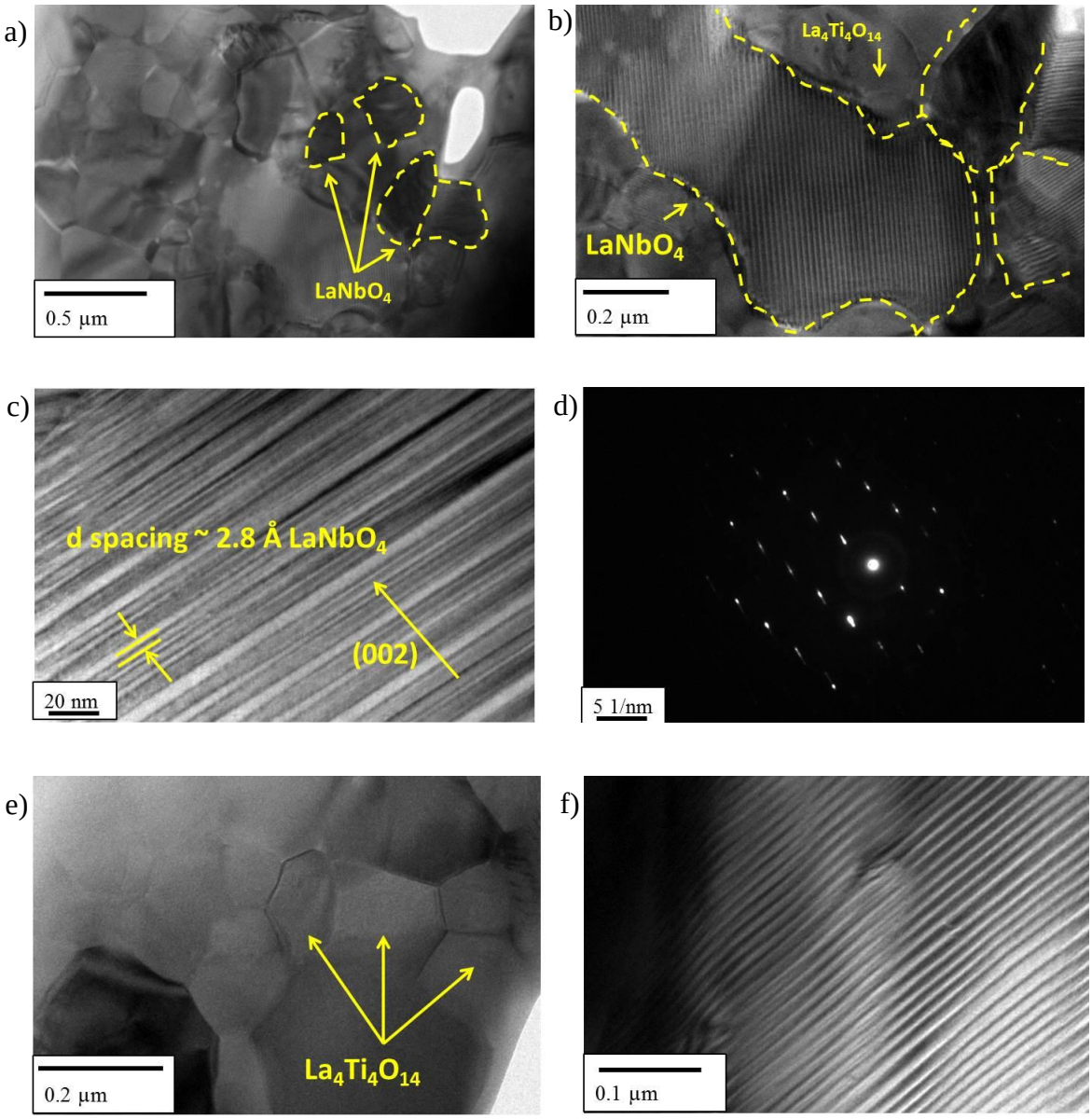

Figure 4.13: *TEM images of: (a) air annealed $La_4Ti_{3.4}Nb_{0.6}O_{14.3\pm\delta}$; (b) air annealed $La_4Ti_{3.4}Nb_{0.6}O_{14.3\pm\delta}$ showing region of $LaNbO_4$; (c) typical grain of reduced $La_4Ti_{3.4}Nb_{0.6}O_{14.3\pm\delta}$ ceramic showing $LaNbO_4$ grain; (d) corresponding diffraction pattern of $LaNbO_4$ grain; (e) a typical region showing cluster of $La_4Ti_4O_{14}$ grains in reduced ceramic; (f) a typical $LaNbO_4$ grain showing planar defects in reduced ceramic*

4.6 CONCLUSION

Sr, Ta and Nb substituted $La_4Ti_4O_{14}$ ceramics were synthesized by solid state reaction and densified by spark plasma sintering. The effect of substitution and oxidation-reduction on phase contrast and microstructure was studied. Substitution of elements in the structure produced disorder in the structure and additional heat treatment did not produce well-ordered structures. Acceptor (Sr) substitution produced nanoscale intergrowths of 5 layer PLS compound while donor (Ta) substitution produced 3 layer PLS compound. These intergrowths were different in size and appearance in acceptor and donor substituted $La_4Ti_4O_{14}$. These nanoscale intergrowths were caused by the localized disturbance in the octahedral layers. Evidence of 5 or 3 layer PLS compounds was confirmed by XRD and transmission electron microscopy. Nanoscale intergrowths number increased in the case of acceptor substitution after reduction while decreased in the case of donor substitution. Nb substitution in $La_4Ti_4O_{14}$ did not produce 3 layer PLS compound but produced 2 layer PLS compound $LaNbO_4$ which was observed as a separate phase inside the microstructure.

REFERENCES

[1] T.D. Sparks, P.A. Fuierer, D.R. Clarke, Journal of the American Ceramic Society, 93 (2010) 1136-1141.

[2] A. Sakai, T. Kanno, K. Takahashi, Y. Yamada, H. Adachi, Journal of Applied Physics, 108 (2010) 103706.

[3] Z.P. Gao, H.X. Yan, H.P. Ning, R. Wilson, X.Y. Wei, B. Shi, H. Ye, M.J. Reece, Journal of the European Ceramic Society, 33 (2013) 1001-1008.

[4] D.R. Clarke, Surface and Coating Technology, 163 (2003) 67-74.

[5] A. Rauf, Q. Yu, L. Jin, C. Zhou, Scripta Materialia, 66 (2012) 109-112

[6] P. Scherrer, Nachrichten von der Gesellschaft der Wissenschaften zu Göttingen, Mathematisch-Physikalische Klasse, 2 (1918) 98.

[7] T. Williams, H. Schmalle, A. Reller, F. Lichtenberg, D. Widmer, G. Bednorz, Journal of Solid State Chemistry, 93 (1991) 534-548.

[8] F.H. Chung, J Appl Crystallogr, 8 (1975) 17-19.

[9] V.V. Atuchin, T.A. Gavrilova, J.C. Grivel, V.G. Kesler, Journal of Physics D: Applied Physics, 42 (2009) 035305.

[10] S. Hashimoto, A. Tanaka, Surface and Interface Analysis, 34 (2002) 262-265.

[11] L. Bugyi, A. Berkó, L. Óvári, A.M. Kiss, J. Kiss, Surface Science, 602 (2008) 1650-1658

[12] W.S. Oh, C. Xu, D.Y. Kim, D.W. Goodman, Journal of Vacuum Science & Technology A, 15 (1997) 1710-1716

[13] Z. Gao, H. Ning, C. Chen, R. Wilson, B. Shi, H. Ye, H. Yan, M.J. Reece, J.L. Jones, Journal of the American Ceramic Society, 96 (2013) 1163-1170.

[14] V.V. Atuchin, T.A. Gavrilova, J.C. Grivel, V.G. Kesler, Surface Science, 602 (2008) 3095-3099.

[15] Y.A. Titov, A.M. Sych, V.Y. Markiv, N.M. Belyavina, A.A. Kapshuk, V.P. Yaschuk, Journal of Alloys and Compounds, 316 (2001) 309-315.

[16] H.-W. Lee, J.-H. Park, S. Nahm, D.-W. Kim, J.-G. Park, Materials Research Bulletin, 45 (2010) 21-24.

Chapter V. Characterization of $Sr_4Nb_4O_{14\pm\delta}$

5.1 INTRODUCTION

$Sr_4Nb_4O_{14}$ is a PLS ceramic known for its ferroelectric and piezoelectric properties [1]. Pure $Sr_4Nb_4O_{14}$ is a wide band gap semiconductor, and when doped it becomes a narrow band gap semiconductor [2]. $Sr_4Nb_4O_{14}$ shows temperature independent thermal conductivity with a value as low as ~ 1 W/m.K for textured polycrystalline ceramic in the b direction [3]. La doping in $Sr_4Nb_4O_{14}$ decreases thermal conductivity due to the higher molecular weight of La. The maximum solubility of La in single crystal $Sr_4Nb_4O_{14}$ is reported to be x= 0.8 [4]. There has been no reported investigation of the effect of non-stoichiometry and oxidation-reduction on its phase stability and microstructure. In the current research, $Sr_{4-x}La_xNb_4O_{14+\frac{x}{2}\pm\delta}$ compositions were synthesised by solid state reaction and spark plasma sintering and their microstructure and phase contrast were studied.

5.2 EXPERIMENTAL DETAILS

$Sr_{4-x}La_xNb_4O_{14+\frac{x}{2}\pm\delta}$ (where x=0, 0.2, 0.4, 0.6 and 0.8) were prepared by solid state reaction. The starting materials were La_2O_3 (99.99% purity, Sigma Aldrich), $SrCO_3$ (99.9% purity, Sigma Aldrich) and Nb_2O_5 (99.9% purity, Alfa aesar). These powders were mixed in stoichiometric ratios and ball milled using ethanol as the milling medium in a planetary ball mill for 2 hours. Mixed powders were calcined at 1250^{o}C for 4 hours. After calcination, the powders were remilled for 4 hours to break the agglomerates and reduce the particle size.

The powders were sintered using SPS at 1350^{o}C under 50 MPa of pressure for 5 minutes. A heating rate of 100^{o}C/min was employed in all cases. The sintered discs were subsequently air annealed and reduced as discussed in the previous chapter. The bulk density as measured by the Archimedes principle of all sintered samples was more than 97%.

5.3 RESULTS AND DISCUSSIONS

Table 5.1 presents the theoretical and relative densities of pure and $Sr_{4-x}La_xNb_4O_{14\pm\delta}$ after SPS. The density of all the ceramics increased after substitution due to the higher atomic weight of La (~ 138.9 amu). All the ceramics were more than 97% dense.

Table 5.1: Theoretical and relative densities of $Sr_{4-x}La_xNb_4O_{14+\frac{x}{2}\pm\delta}$ ceramics

	Theoretical Density ($g\ cm^{-3}$)	Relative Density (%)
$Sr_4Nb_4O_{14\pm\delta}$	5.21	97.7
$Sr_{3.8}La_{0.2}Nb_4O_{14.1\pm\delta}$	5.27	97.1
$Sr_{3.6}La_{0.4}Nb_4O_{14.2\pm\delta}$	5.34	97.7
$Sr_{3.4}La_{0.6}Nb_4O_{14.3\pm\delta}$	5.40	97.2
$Sr_{3.2}La_{0.8}Nb_4O_{14.4\pm\delta}$	5.47	96.9

Figure 5.1 shows the X ray diffraction patterns for all $Sr_{4-x}La_xNb_4O_{14+\frac{x}{2}\pm\delta}$ compositions in powder, as sintered, air annealed and reduced conditions. The peaks matched with $Sr_4Nb_4O_{14}$, n=4 (PDF card # 28-1246). After x=0.2, a secondary phase was produced and indexed as $LaNbO_4$ (PDF card # 01-081-1973) which is a n = 2 PLS phase. The second phase was produced because of the reaction between La and Nb during calcination as reported by Istomin et al. for the similar compound ($Sr_{1-x}La_xNb_2O_6$) [5]. This gives an indication that the solubility limit of La in $Sr_{4-x}La_xNb_4O_{14+\frac{x}{2}\pm\delta}$ is less than x=0.4 in the case of polycrystalline ceramics synthesised by conventional solid state reaction.

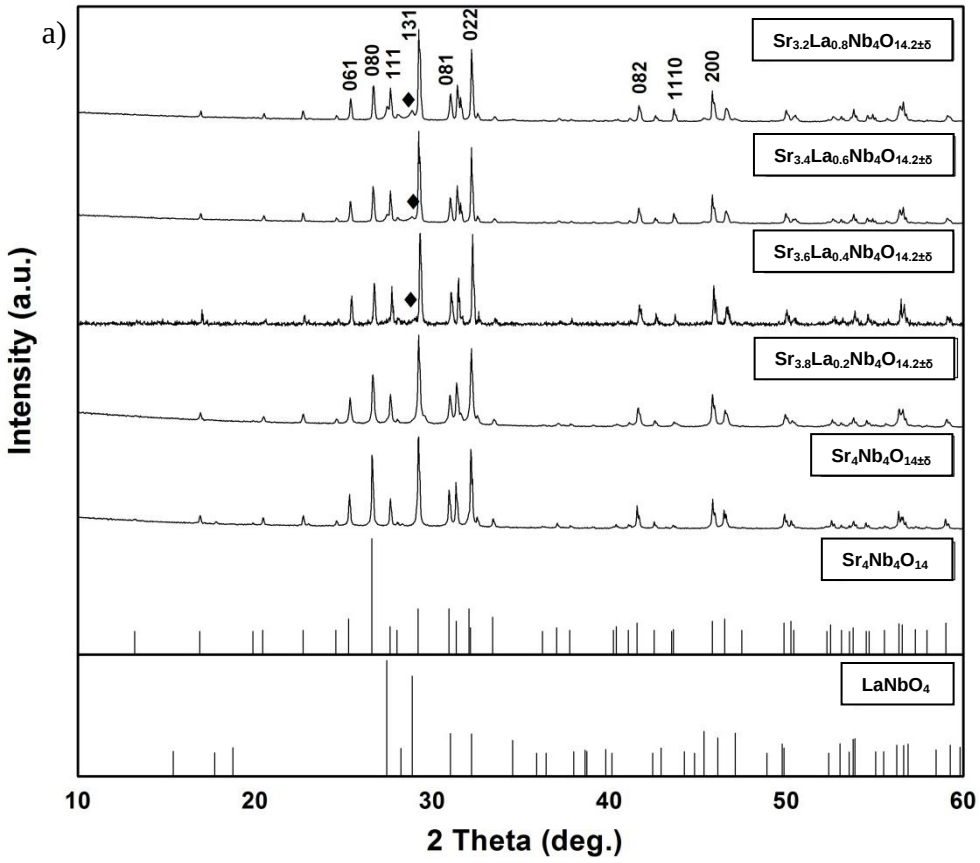
a)
061
080
111
131
081
022
082
1110
200
Sr3.2La0.8Nb4O14.2±δ
Sr3.4La0.6Nb4O14.2±δ
Sr3.6La0.4Nb4O14.2±δ
Sr3.8La0.2Nb4O14.2±δ
Sr4Nb4O14±δ
Sr4Nb4O14
LaNbO4
Intensity (a.u.)
10
20
30
40
50
60
2 Theta (deg.)

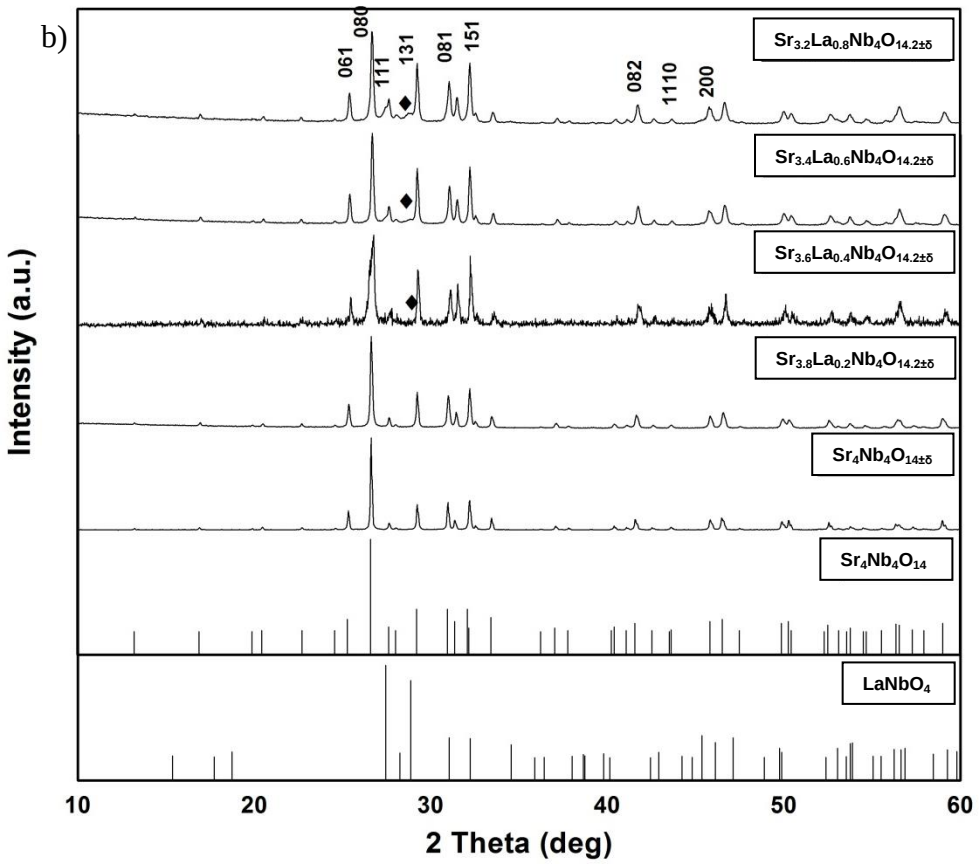
b)
061
080
111
131
081
151
082
1110
200
Sr3.2La0.8Nb4O14.2±δ
Sr3.4La0.6Nb4O14.2±δ
Sr3.6La0.4Nb4O14.2±δ
Sr3.8La0.2Nb4O14.2±δ
Sr4Nb4O14±δ
Sr4Nb4O14
LaNbO4
Intensity (a.u.)
10
20
30
40
50
60
2 Theta (deg)

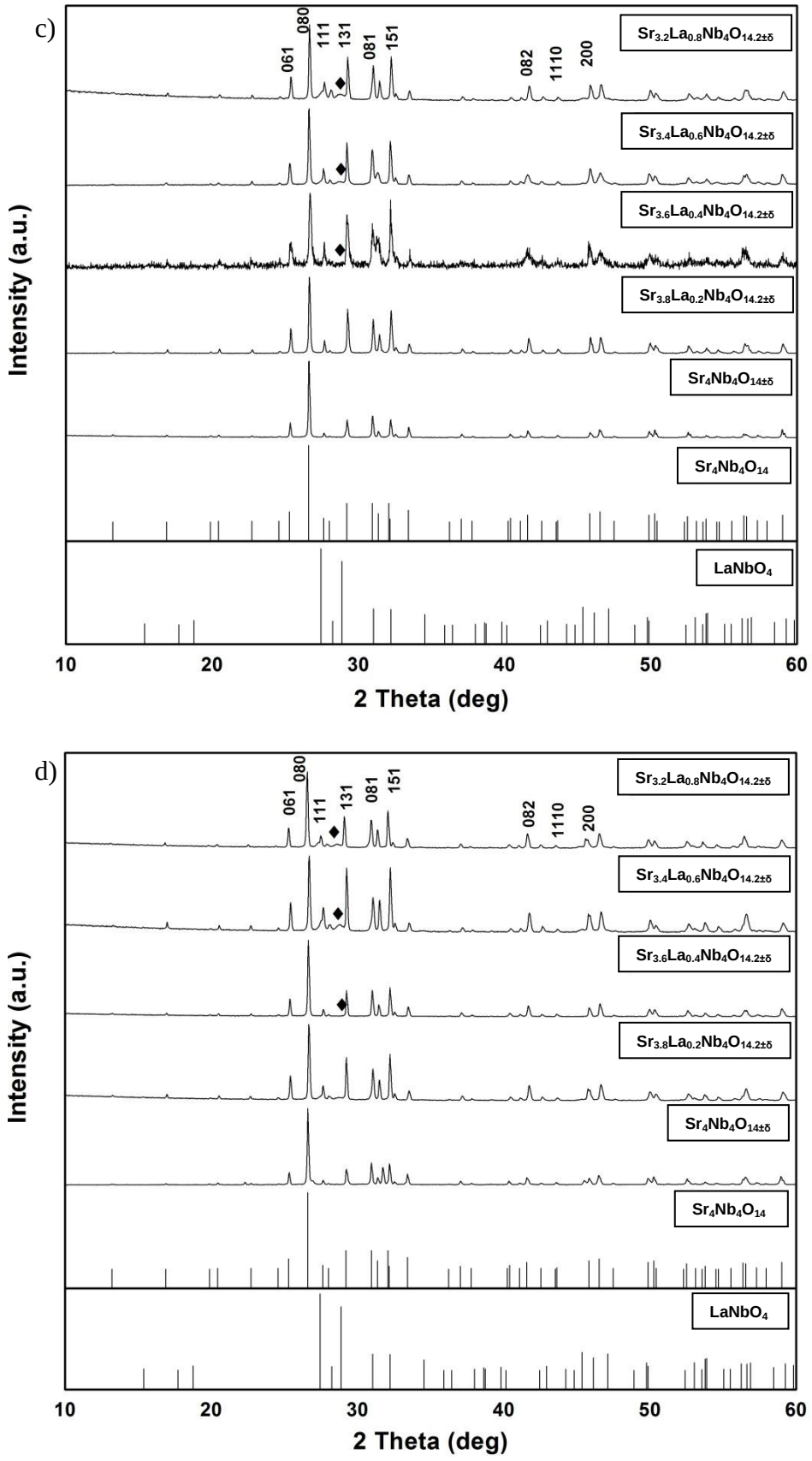

Figure 5.1: *XRD patterns of* $Sr_{4-x}La_xNb_4O_{14+\frac{x}{2}\pm\delta}$*: (a) powder; (b) sintered; (c) air annealed; (d) reduced samples*

The amount of $LaNbO_4$ was calculated by the RIR method and is given in Table 5.2

Table 5.2: Amount of 2 layer PLS compound in $Sr_{4-x}La_xNb_4O_{14+\frac{x}{2}\pm\delta}$ ceramics

	Powder (mass %)	Sintered (mass %)	Air Annealed (mass %)	Reduced (mass %)
$Sr_{3.8}La_{0.2}Nb_4O_{14.1\pm\delta}$	-	-	-	-
$Sr_{3.6}La_{0.4}Nb_4O_{14.2\pm\delta}$	-	-	-	-
$Sr_{3.4}La_{0.6}Nb_4O_{14.3\pm\delta}$	3.5	1.5	1.5	0.9
$Sr_{3.2}La_{0.8}Nb_4O_{14.4\pm\delta}$	6.4	2.2	2.4	1.5

Figure 5.2 shows SEM images of polished and then thermally etched $Sr_{4-x}La_xNb_4O_{14+\frac{x}{2}\pm\delta}$ ceramic surfaces after sintering by SPS at 1350^{o}C under 50 MPa pressure. Pure $Sr_4Nb_4O_{14}$ has elongated and plate-like grains as reported in the literature [1]. Upon substitution of La for Sr, the grains become less plate-like as shown in Figure 5.2(c).

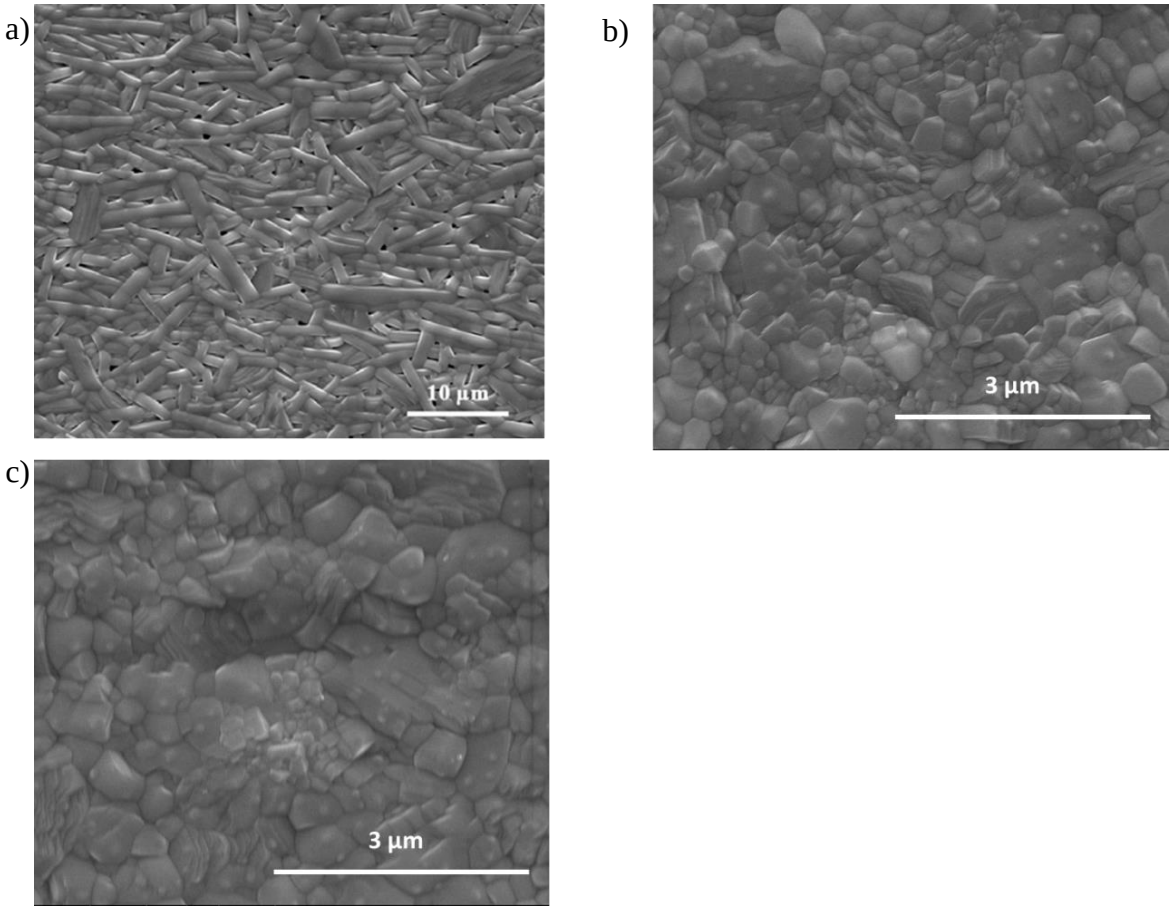

Figure 5.2: *SEM images of $Sr_{4-x}La_xNb_4O_{14+\frac{x}{2}\pm\delta}$ ceramics after polishing and etching: (a) $Sr_4Nb_4O_{14\pm\delta}$; (b) $Sr_{3.8}La_{0.2}Nb_4O_{14.1\pm\delta}$ and; (c) $Sr_{3.2}La_{0.8}Nb_4O_{14.4\pm\delta}$*

Figure 5.3(a) shows a typical bright field TEM image of $Sr_4Nb_4O_{14}$ based ceramic after air annealing. The typical grain size of the ceramic was ~ 0.3 µm and most of the grains appear defect free. Figure 5.3(b) shows a high resolution image of (020) lattice planes. The inter-planar spacing corresponds to the 4 layer $Sr_4Nb_4O_{14}$ (~ 12.6 Å). Figure 5.3(c) shows the corresponding diffraction patter. Figure 5.3 (d) shows a bright field image of $Sr_{3.2}La_{0.8}Nb_4O_{14.2\pm\delta}$ ceramic which gives an overall view of the ceramics microstructure. From the XRD data, generation of the 2 layered PLS compound $LaNbO_4$ was confirmed and is marked in Figure 5.3(e) as separate single phase grains. Figure 5.3(f) shows a magnified image of a separate single grain

of $LaNbO_4$. In some areas, $LaNbO_4$ was uniformly distributed while in other, it was found in clusters in the microstructure as shown in Figure 5.3 (d and e).

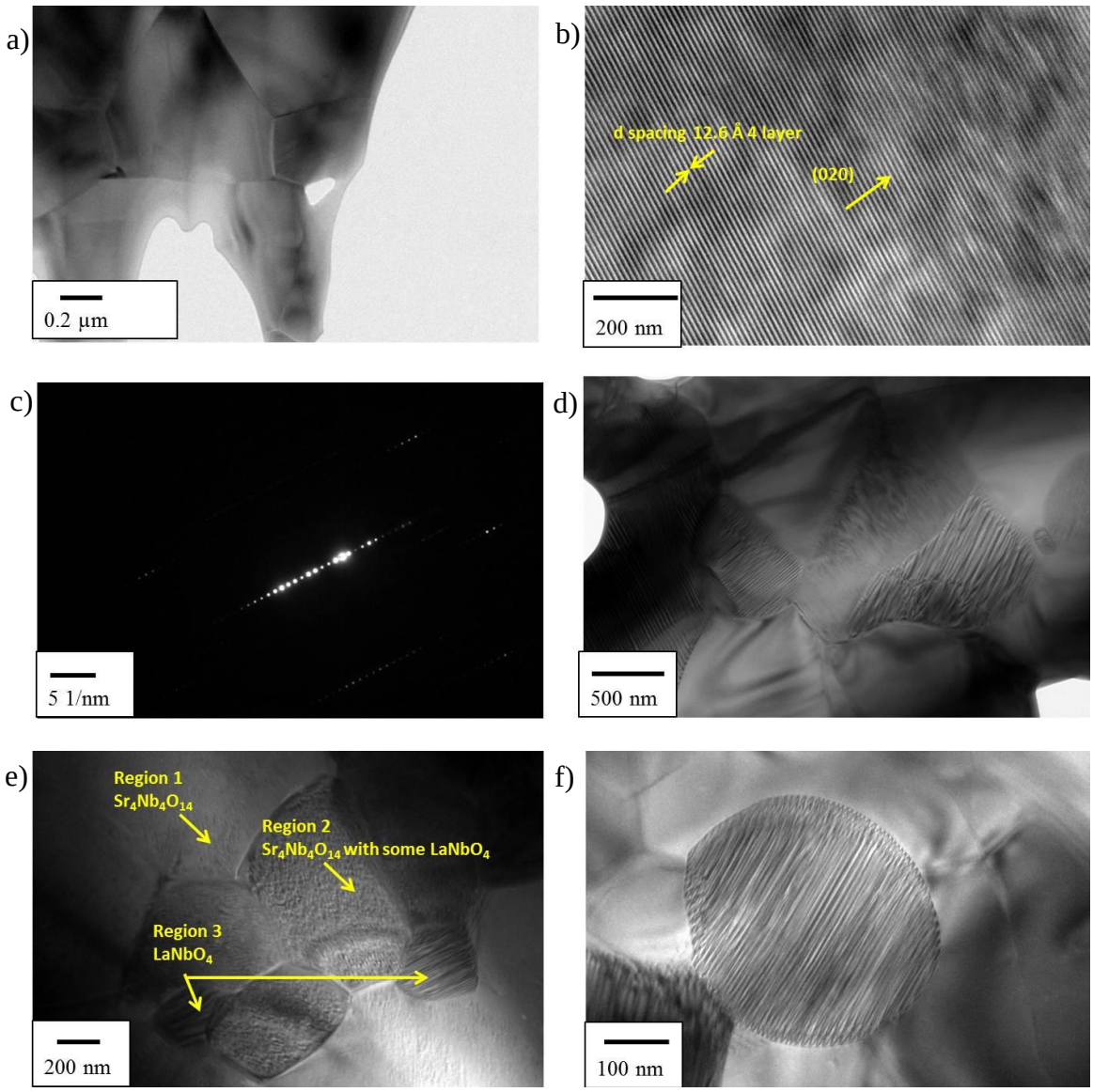

Figure 5.3: *TEM images of: (a) air annealed $Sr_4Nb_4O_{14\pm\delta}$; (b) high magnification image of air annealed $Sr_4Nb_4O_{14\pm\delta}$; (c) corresponding diffraction pattern for $Sr_4Nb_4O_{14\pm\delta}$; (d) air annealed $Sr_{3.2}La_{0.8}Nb_4O_{14.2\pm\delta}$; (e) air annealed $Sr_{3.2}La_{0.8}Nb_4O_{14.2\pm\delta}$ showing regions of $Sr_4Nb_4O_{14}$ and $LaNbO_4$; (f) high magnification image of a single $LaNbO_4$ grain*

EDS analysis was done on three regions marked as 1, 2 and 3 in Figure 5.3(e). EDS results also confirmed the Sr/Nb (region 1) and La/Nb (region 3) rich

phases and the estimated atomic percentage is given in the Table 5.3. These rough estimates gives an indication of the two separate phases presents inside the structure namely $Sr_4Nb_4O_{14}$ and $LaNbO_4$.

Table 5.3: Percentage mass amount of different elements (excluding oxygen) in $Sr_{4-x}La_xNb_4O_{14+\frac{x}{2}\pm\delta}$ ceramics

	Sr (%)	Nb (%)	La (%)	Total
Region 1	31.19	34.67	5.09	100.00
Region 2	30.89	37.09	10.96	100.00
Region 3	6.01	27.08	42.77	100.00

Figure 5.4(a-b) shows bright filed TEM image of reduced ceramics. After reduction, the density of $Sr_4Nb_4O_{14}$ decreased slightly (from 5.09 g $cm^{-3}$to 5.03 g cm^{-3}) and a few planar defects were generated. These results are consistent with XRD patterns which indicate a slight increase in FWHM of the reduced ceramics. Figure 5.4(b) shows a high resolution image of a typical planar defect in reduced $Sr_4Nb_4O_{14}$. Figure 5.4(c) shows an image of $Sr_{3.6}La_{0.4}Nb_4O_{14.2\pm\delta}$ after reduction. The density of $Sr_{3.6}La_{0.4}Nb_4O_{14+\frac{x}{2}\pm\delta}$ decreased slightly (from 5.3 g cm^{-3} to 5.18 g cm^{-3}) after reduction and the amount of secondary phase stayed nearly the same. The clusters of $Sr_4Nb_4O_{14}$ and $LaNbO_4$ were also observed in the reduced ceramic as shown in Figure 5.4(d and e). Figure 5.4(e) shows a magnified Sr/Nb rich region with planar defects inside the microstructure. It is anticipated that the $LaNbO_4$ has started to form and was distributed throughout the grain. Most of the $LaNbO_4$ grains were plain without any planar defects, but some had planar defects as La was substituted

in $Sr_4Nb_4O_{14}$ and shown in Figure 5.4(d). The shape and size of the grain is similar to those observed in section 4.5. It was not possible to determine the phase which was formed at the region of the planar defect due to the complex nature of the defects as discussed in the case of Nb and Ta doped $La_4Ti_4O_{14}$ (section 4.5).

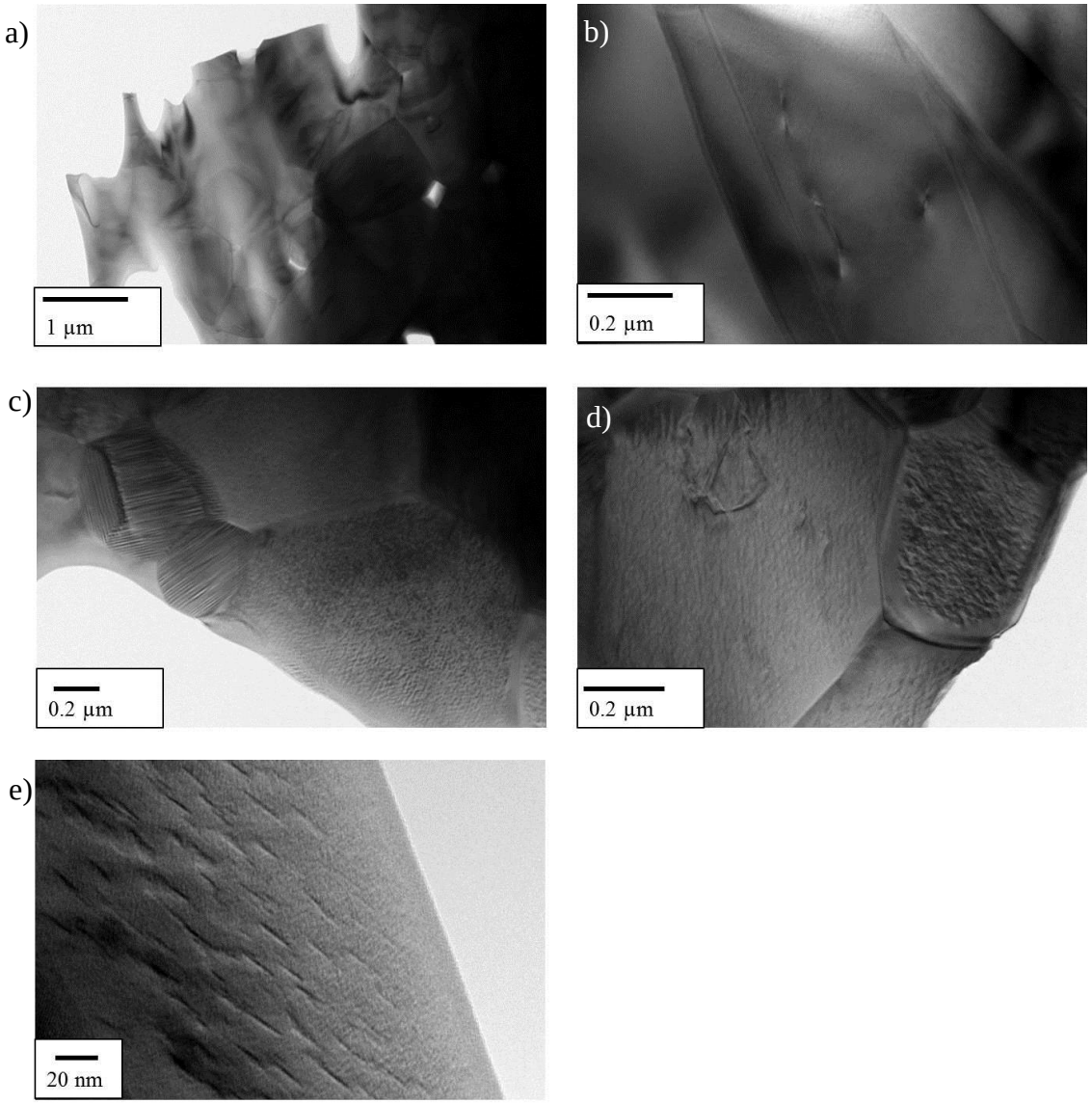

Figure 5.4: *TEM images of: (a) reduced $Sr_4Nb_4O_{14\pm\delta}$; (b) high magnification image of reduced $Sr_4Nb_4O_{14\pm\delta}$; (c-d) typical regions of reduced $Sr_{3.2}La_{0.8}Nb_4O_{14.4\pm\delta}$; (e) high magnification image of a typical Sr/Nb rich region*

Figure 5.5(a–c) shows the XPS spectra of Sr 3d, Nb 3d, O 1s and La 3d surface electrons in $Sr_4Nb_4O_{14}$ based ceramics without ion beam etching. Figure 5.4(a) shows the XPS spectra of typical Sr 3d doublet. For air annealed $Sr_4Nb_4O_{14}$ and $Sr_{3.6}La_{0.4}Nb_4O_{14.2\pm\delta}$, the intensity and peak position was the same and given in Table 5.4. This gives an indication of the stability of Sr in pure and doped ceramics, the binding energy values for Sr $3d_{5/2}$ and Sr $3d_{3/2}$ were 132.8 eV and 134.4 eV respectively. This matches well with the values reported in literature [6]. Figure 5.4(b) shows the XPS spectra of Nb 3d electrons of pure and La substituted $Sr_4Nb_4O_{14}$. The binding energy values for Nb 3d showed a clear doublet Nb $3d_{5/2}$ and Nb $3d_{3/2}$ which is a characteristic of Nb containing oxide compounds. The binding energy values for Nb $3d_{5/2}$ and Nb $3d_{3/2}$ in pure $Sr_4Nb_4O_{14}$ were ~ 206.6 eV and ~ 209.5 eV respectively which were similar to those in La substituted $Sr_4Nb_4O_{14}$ (Table 5.4). The difference between the two peaks was 2.8 eV. This value is in good agreement with the one published in literature [6]. The O 1s core level spectra are shown in Figure 5.5(c). Both spectra had two convoluted peaks. The component at 530.0 eV gives the main O 1s state of the oxygen in $Sr_4Nb_4O_{14}$ [7]. The higher binding energy component at 531.4 eV might indicate chemisorbed oxygen or absorbed hydroxyl ions. After La substitution, the peak position was at 529.8 eV.

a)

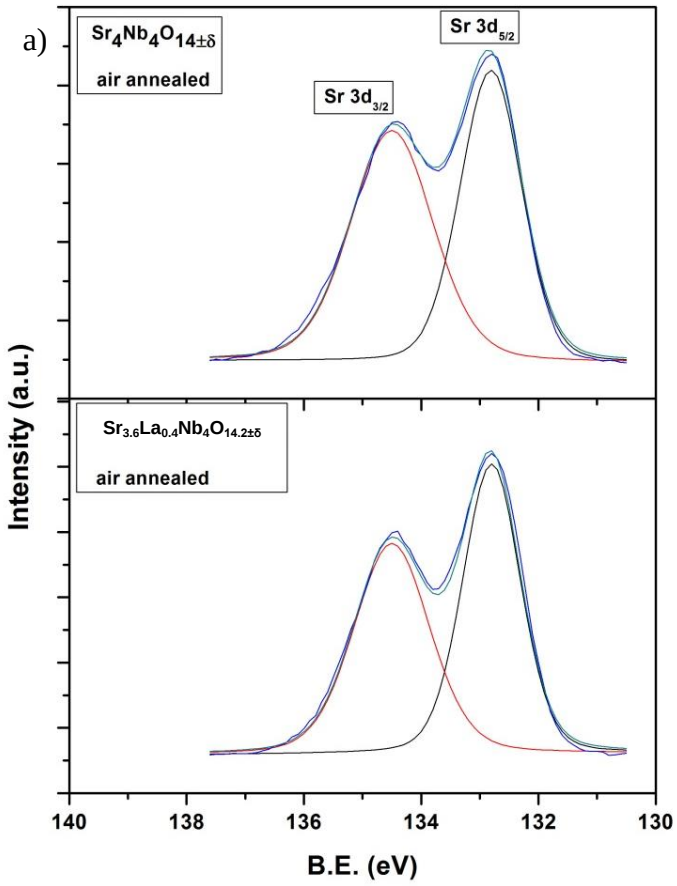
Sr4Nb4O14±δ
air annealed
Sr 3d5/2
Sr 3d3/2
Sr3.6La0.4Nb4O14.2±δ
air annealed
Intensity (a.u.)
140
138
136
134
132
130
B.E. (eV)

b)

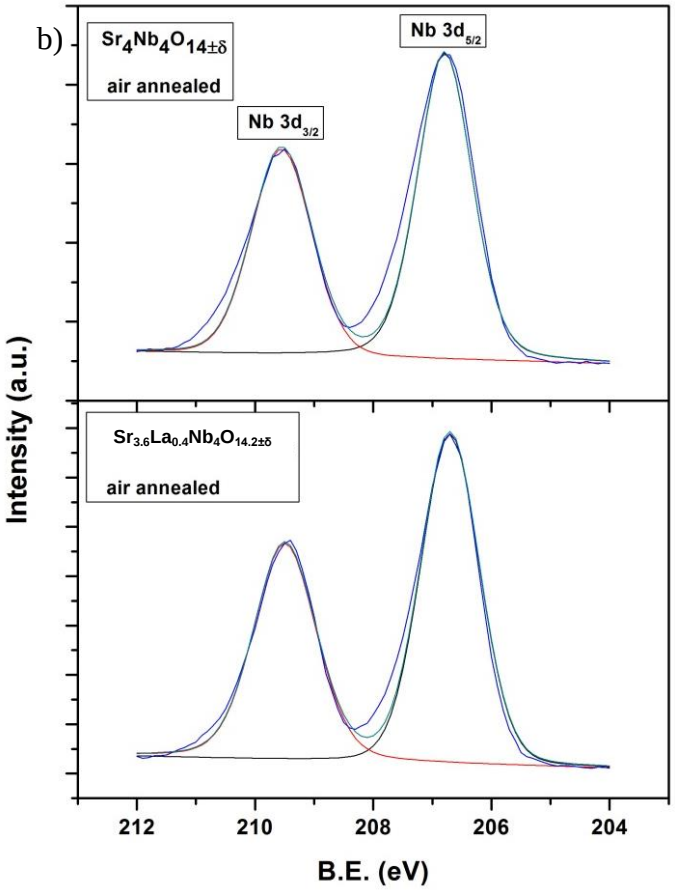
Sr4Nb4O14±δ
air annealed
Nb 3d5/2
Nb 3d3/2
Sr3.6La0.4Nb4O14.2±δ
air annealed
Intensity (a.u.)
212
210
208
206
204
B.E. (eV)

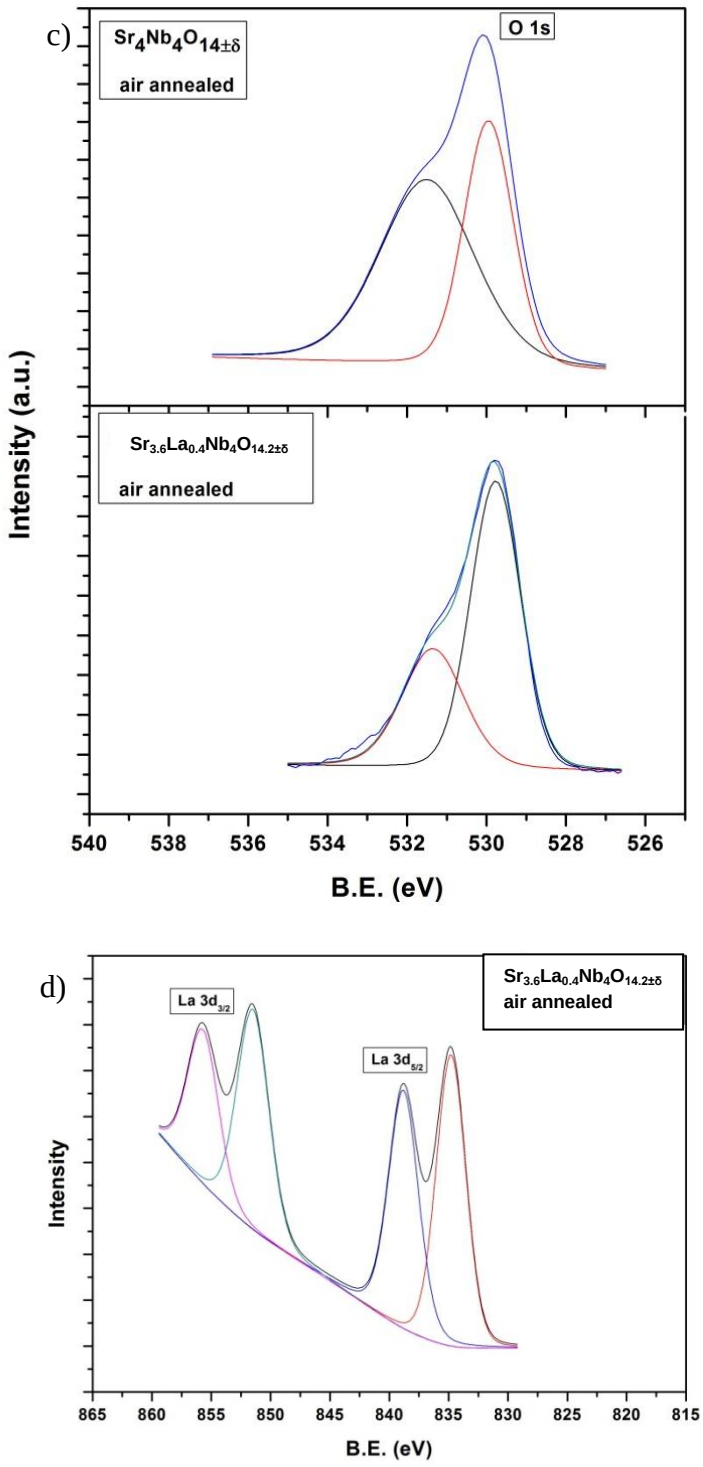

Figure 5.5: *XPS spectra of $Sr_{3.6}La_{0.4}Nb_4O_{14.2\pm\delta}$: (a) Sr 3d; (b) Nb 3d; (c) O1s and; (d) La3d*

The ΔBE values were also calculated and are presented in the Table 5.4. The ΔBE values for (Sr-O) in the case of pure and La substituted $Sr_4Nb_4O_{14}$ was 397.2 eV and 397 eV respectively. The decrease in binding energy was caused by the

weakening of the bonds as a result of the second phase. These values matched that for Sr substituted $La_4Ti_4O_{14}$ (397 eV). For ΔBE (Nb-O) the values were 323.2 eV and 323.1 eV for pure and La substituted $Sr_4Nb_4O_{14}$ respectively. These values are in good agreement with the literature [6]. For ΔBE (La-O) the value was 305.2 eV. This value was higher than that measured for $La_4Ti_4O_{14}$ (304.7 eV). Since La has gone to make $LaNbO_4$ and the ratio of La:O in $LaNbO_4$ is 1:4 which is higher than the one for $La_4Ti_4O_{14}$ which is 1:3.5, this explains the increase in the ΔBE (La-O) in La substituted $Sr_4Nb_4O_{14}$.

Table 5.4: XPS data of $Sr_{3.2}La_{0.4}Nb_4O_{14.2\pm\delta}$ ceramics

Material	Peak Position (eV)					Binding Energy Difference (ΔeV)		
	Sr3d		Nb3d		O1s	Sr-O	Nb-O	La-O
	$Sr3d_{3/2}$	$Sr3d_{5/2}$	$Nb3d_{3/2}$	$Nb3d_{5/2}$				
$Sr_4Nb_4O_{14}$ air annealed	134.4	132.8	209.5	206.8	530.0	397.2	323.2	-
$Sr_{3.2}La_{0.4}Nb_4O_{14.2\pm\delta}$ air annealed	134.4	132.8	209.4	206.7	529.8	397.0	323.1	305.2

5.4 CONCLUSION

Pure and La substituted $Sr_4Nb_4O_{14}$ were prepared by solid state reaction and spark plasma sintering. The limit of La substitution in polycrystalline $Sr_4Nb_4O_{14}$ is found to be $x< 0.4$. La substitution produced a secondary phase $LaNbO_4$ when the level of substitution increased to $x=0.4$. The amount of secondary phase decreased after sintering and reduction. La substitution also changed the size and shape of the grains and they became less plate-like. The main mechanism of La accommodation inside the structure is by the formation of the 2 layer PLS compound, $LaNbO_4$.

REFERENCES

[1] H. Ning, H. Yan, M.J. Reece, Journal of the American Ceramic Society, 93 [5] (2010) 1409.

[2] A. Sakai, T. Kanno, K. Takahashi, Y. Yamada, H. Adachi, Journal of Applied Physics, 108 (2010) 103706.

[3] T.D. Sparks, P.A. Fuierer, D.R. Clarke, Journal of the American Ceramic Society, 93 (2010) 1136-1141.

[4] A. Sakai, T. Kanno, K. Takahashi, A. Omote, H. Adachi, Y. Yamada, X.D. Zhou, Journal of the American Ceramic Society, 95 (2012) 1750-1755.

[5] S.Y. Istomin, O.G. Dyachenko, E.V. Antipov, G. Svensson, M. Nygren, Materials Research Bulletin, 29 (1994) 743-749.

[6] V.V. Atuchin, J.C. Grivel, A.S. Korotkov, Z. Zhang, Journal of Solid State Chemistry, 181 (2008) 1285-1291.

[7] Z. Gao, H. Ning, C. Chen, R. Wilson, B. Shi, H. Ye, H. Yan, M.J. Reece, J.L. Jones, Journal of the American Ceramic Society, 96 (2013) 1163-1170.

Chapter VI. Thermal Conductivity of PLS Compounds

6.1 INTRODUCTION

The aim of this chapter is to investigate the effect of acceptor-donor substitution and compositional non stoichiometry on the thermal conductivity of PLS compounds. Currently there is a limited amount of literature relating to the effect of substituting elements and compositional non stoichiometry on the thermal conductivity of PLS ceramics [1-3]. The materials investigated for thermal conductivity were $La_4Ti_4O_{14}$ and $Sr_4Nb_4O_{14}$. There are no reported data for the thermal conductivity of $La_4Ti_4O_{14}$. Liu et al. calculated minimum thermal conductivity of pyrochlore $La_2Ti_2O_7$ to be 1.27 W/m.K using Clarke's relation which will be discussed later [4]. For polycrystalline $Sr_4Nb_4O_{14}$, thermal conductivity is temperature independent (above room temperature) and has a value of ~ 1-2 W/m.K [2]. In this work, the effect of substitution and reduction on thermal conductivity is discussed in relation to the microstructures for $La_4Ti_4O_{14}$ and $Sr_4Nb_4O_{14}$ which were discussed in chapters 4 and 5.

6.2 EXPERIMENTAL DETAILS

The samples for thermal characterization were prepared by a mixed oxide route and SPS as described in sections 4.2 and 5.2. A Netszch LFA 457 microflash was employed to measure the thermal diffusivity which was then used to calculate thermal conductivity using equation 3.3. All the measurements were carried out under Ar environment. The sintered discs were ground flat but left unpolished to minimise laser reflectance. A Kontact-chemi Graphite 33 spray was used to coat both surfaces of the sample to maximise the absorption of the laser light. Measurements were taken at room temperature and then at intervals of 100 ^{o}C up to a temperature of 800 ^{o}C. Three measurements were taken at each temperature to minimize the scatter in the data. In order to ensure the thermal stability across the sample at each temperature, a period of 2 minutes between the laser shots was used. Temperature fluctuation was kept to a minimum of ± 1 ^{o}C for all measurements. The thermal diffusivity measurement was repeated to check reproducibility of the measurements and materials.

The specific heat capacity (Cp) was measured by Netzsch STA (449 F3 Jupiter®) under N_2 environment. A square sample with dimensions 4mm x 4mm x 1mm was cut from the sintered disc and ground flat. The instrument was checked for calibration by running a standard sapphire test sample and comparing the values with the standard values. The Cp data below 300 ^{o}C (573 K) were not reliable (due to non-availability of calibration for the equipment below 300 ^{o}C) and they were not used in the calculations. All the results obtained were reproducible and there was no obvious colour change of the oxidized or reduced samples after the measurements.

RESULTS

6.3 $La_4Ti_4O_{14}$

Chapter 4 reports a detailed microstructural examination of A (acceptor) and B (donor) site substituted $La_4Ti_4O_{14}$. After substitution, the crystal structure of $La_4Ti_4O_{14}$ accommodates the deviation from the stoichiometric composition by incorporating planar defects in the structure. Since these planar defects are of the order of few angstroms (typically 3 Å) it is expected to see a reduction in thermal conductivity after hydrogen reduction and/or substitution in $La_4Ti_4O_{14}$ ceramic.

6.3.1 $La_{4-x}Sr_xTi_4O_{14-\frac{x}{2}\pm\delta}$

Figure 6.1 shows the thermal diffusivity of air annealed and reduced $La_{4-x}Sr_xTi_4O_{14-\frac{x}{2}\pm\delta}$ ceramics. The thermal diffusivity of all the ceramics showed near temperature independency. The thermal diffusivity increased with increasing Sr substitution after air annealing and reduction. Compared to air annealed ceramics, the corresponding thermal diffusivity of all the ceramics decreased after reduction. This decrease was due to the increased density of the nanoscale intergrowth of 5 layer PLS structure inside the 4 layer PLS structure (Figure 4.4).

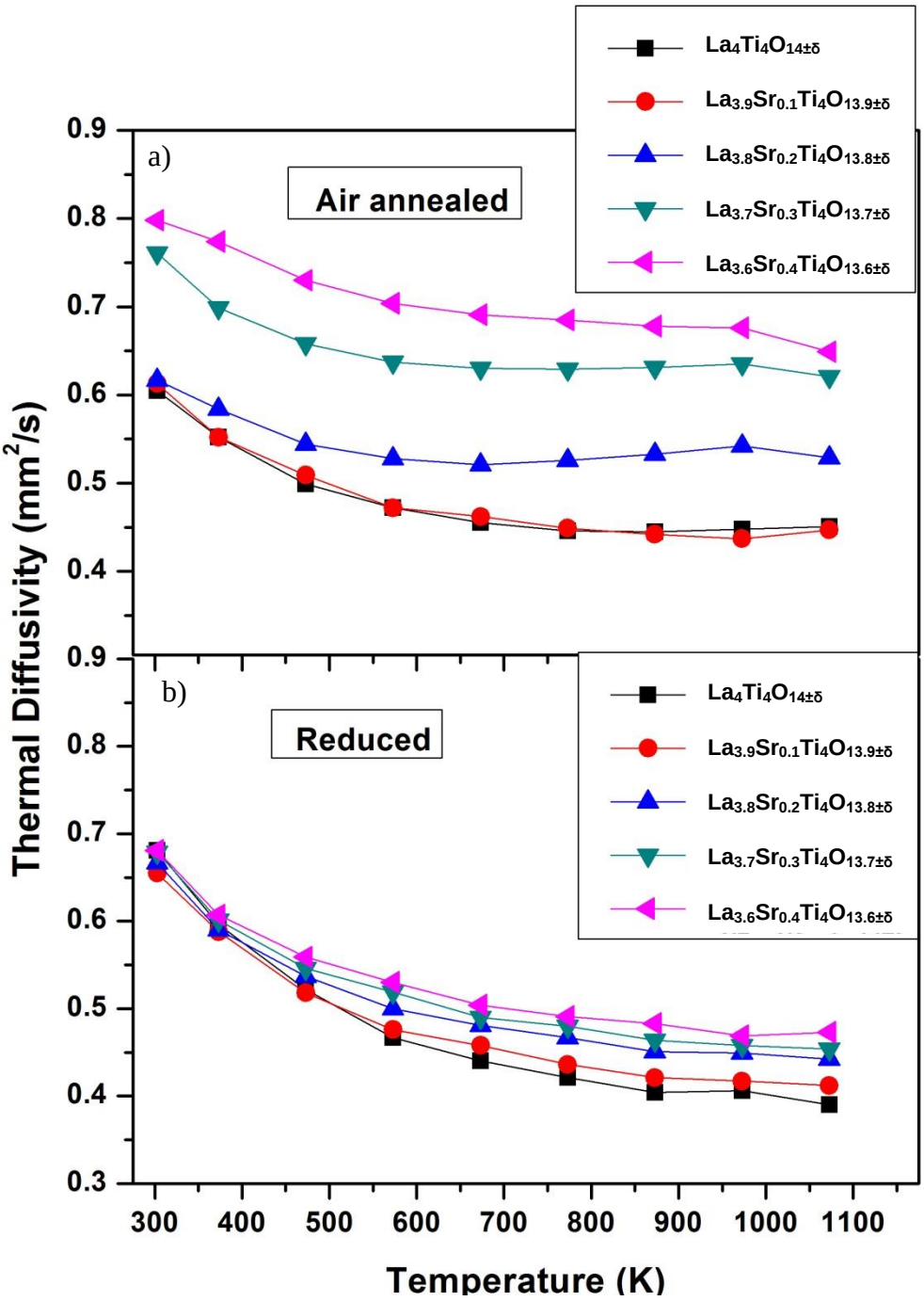

Figure 6.1: *Variation in thermal diffusivity of* $La_{4-x}Sr_xTi_4O_{14-\frac{x}{2}\pm\delta}$ *ceramics: (a) air annealed; (b) reduced*

Figure 6.2 compares the Cp measured and reported value of sapphire standard. The measured values are less than the reported values and the error in the measurement was calculated to be ~ 7%.

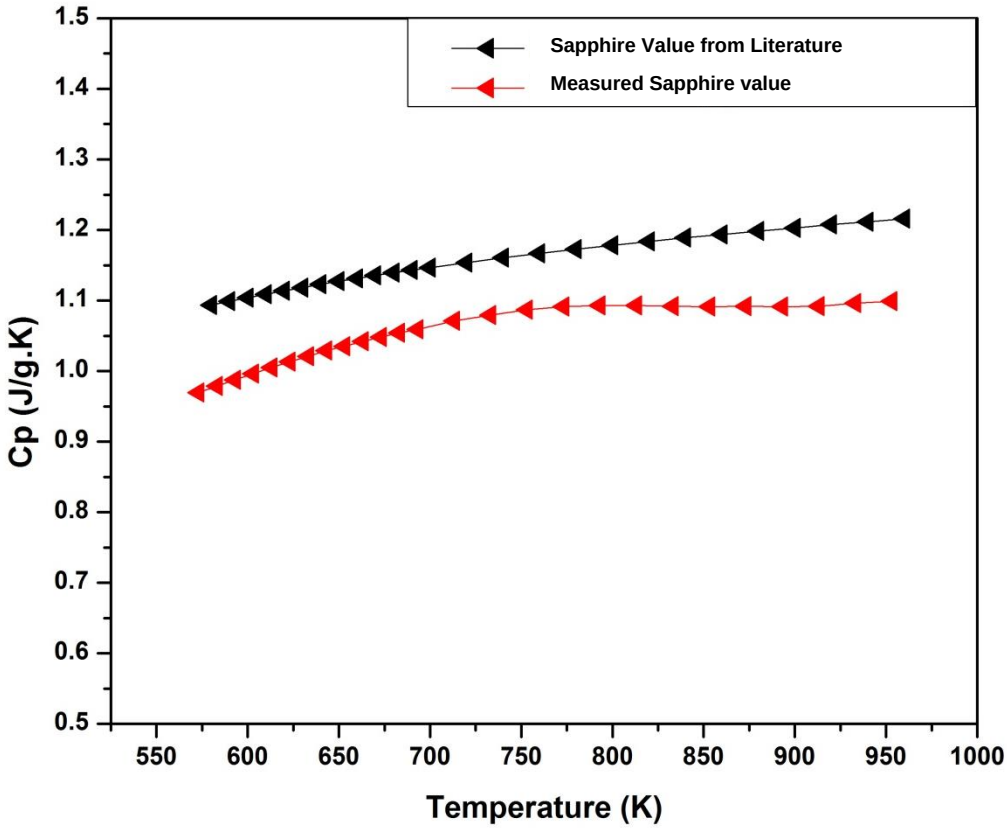

Figure 6.2: *Variation in specific heat capacity of sapphire with temperature*

Figure 6.3 shows the specific heat capacity of the $La_{4-x}Sr_xTi_4O_{14-\frac{x}{2}\pm\delta}$ ceramics. The heat capacity increases with increasing temperature and reaches a maximum value. Heat capacity of air annealed $La_4Ti_4O_{14\pm\delta}$ is higher than the reduced $La_4Ti_4O_{14\pm\delta}$. This decrease in specific heat capacity in reduced samples can be explained by the fact that due to the removal of oxygen by reduction, the binding energy decreased as observed in the section 4.3. After Sr doping, the binding energy is still lower than for the pure air annealed $La_4Ti_4O_{14\pm\delta}$ which also contributes for the decrease in the specific heat of Sr substituted $La_4Ti_4O_{14}$ [5].

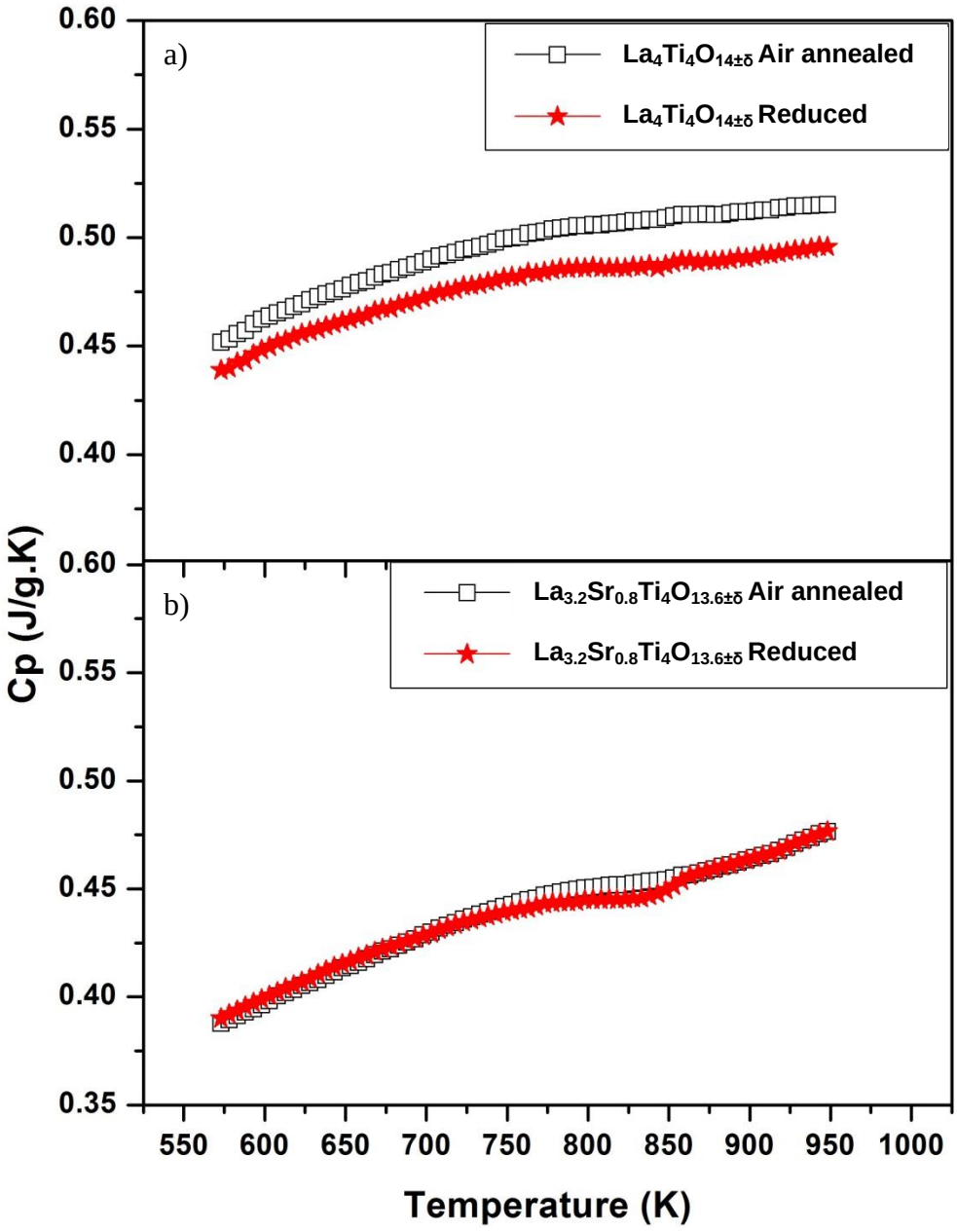

Figure 6.3: *Variation in specific heat capacity of: (a) $La_4Ti_4O_{14\pm\delta}$; (b) $La_{3.2}Sr_{0.8}Ti_4O_{13.6\pm\delta}$ ceramics with temperature*

Figure 6.4 compares the specific heat capacity of reduced $La_4Ti_4O_{14\pm\delta}$ ceramics. The ceramic was rerun to check the reproducibility of the results and the results were within the experimental error.

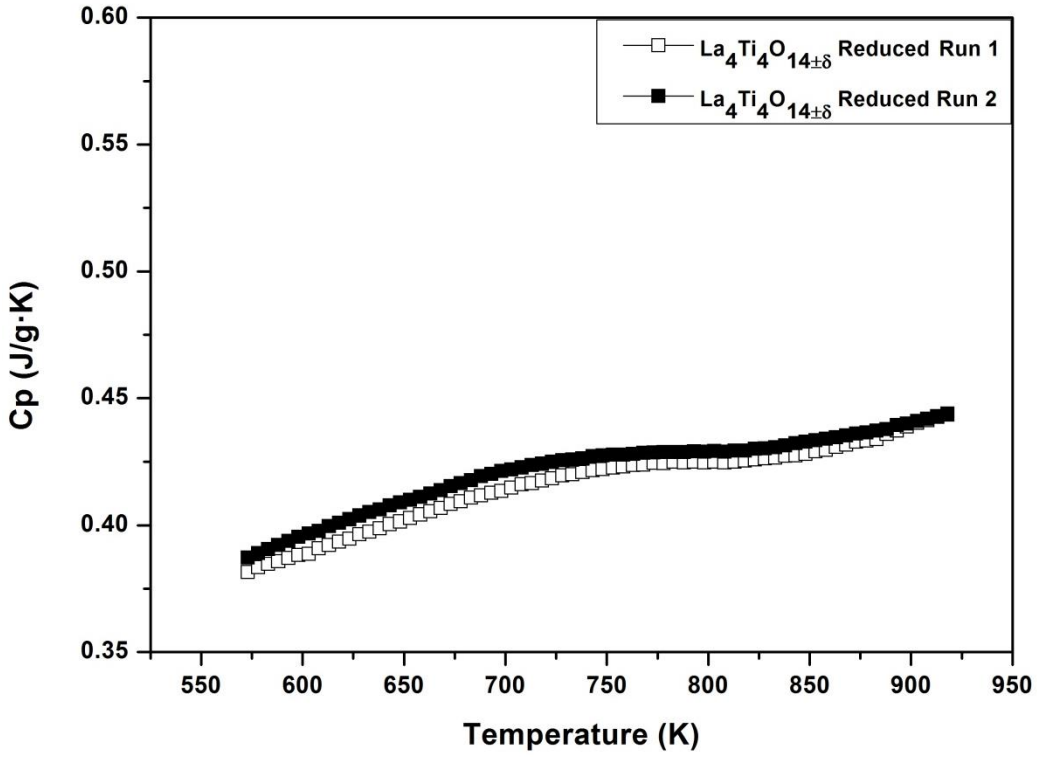

Figure 6.4: *Variation in specific heat capacity of reduced $La_4Ti_4O_{14\pm\delta}$ with temperature*

Table 6.1 gives the densities of $La_{4-x}Sr_xTi_4O_{14-\frac{x}{2}\pm\delta}$ ceramics after air annealing and after hydrogen reduction. All the ceramics were more than 98% dense and due to the lower atomic weight of Sr (87.6 amu) compared to La (138.9 amu), the theoretical density of all the Sr substituted ceramics decreased. The density of the ceramics after reduction is lower than the air annealed ceramics due to the removal of oxygen.

Table 6.1: Change in measured densities after Sr substitution and hydrogen reduction

Sample	**Density after air annealing (g/ cm^{-3})**	**Density after reduction (g/ cm^{-3})**
$La_4Ti_4O_{14\pm\delta}$	5.74±0.04	5.62±0.01
$La_{3.8}Sr_{0.2}Ti_4O_{13.9\pm\delta}$	5.68±0.08	5.59±0.03
$La_{3.6}Sr_{0.4}Ti_4O_{13.8\pm\delta}$	5.62±0.05	5.57±0.04
$La_{3.4}Sr_{0.6}Ti_4O_{13.7\pm\delta}$	5.59±0.05	5.52±0.03
$La_{3.2}Sr_{0.8}Ti_4O_{13.6\pm\delta}$	5.53±0.03	5.47±0.01

Figure 6.5 (a) shows the thermal conductivity of air annealed ceramics estimated using equation 3.3. The thermal conductivity of $La_4Ti_4O_{14\pm\delta}$ is nearly temperature independent as reported in the literature for similar PLS compounds e.g.$Sr_4Nb_4O_{14}$ [2]. The value of thermal conductivity for $La_4Ti_4O_{14\pm\delta}$ is ~ 1.2 W/m.K in this work, which is close to that of other layered structured compounds, e.g. $Bi_4Ti_3O_{12}$ [6]. After Sr substitution, the value of thermal conductivity increases with increasing temperature. Figure 6.5(b) shows the thermal conductivity of reduced $La_{4-x}Sr_xTi_4O_{14-\frac{x}{2}\pm\delta}$ ceramics. After reduction, the values of thermal conductivity decrease as compared to the air annealed samples and the value is less temperature dependent. Figure 6.5(c) and (d) compares the thermal conductivity values of air annealed and reduced ceramics.

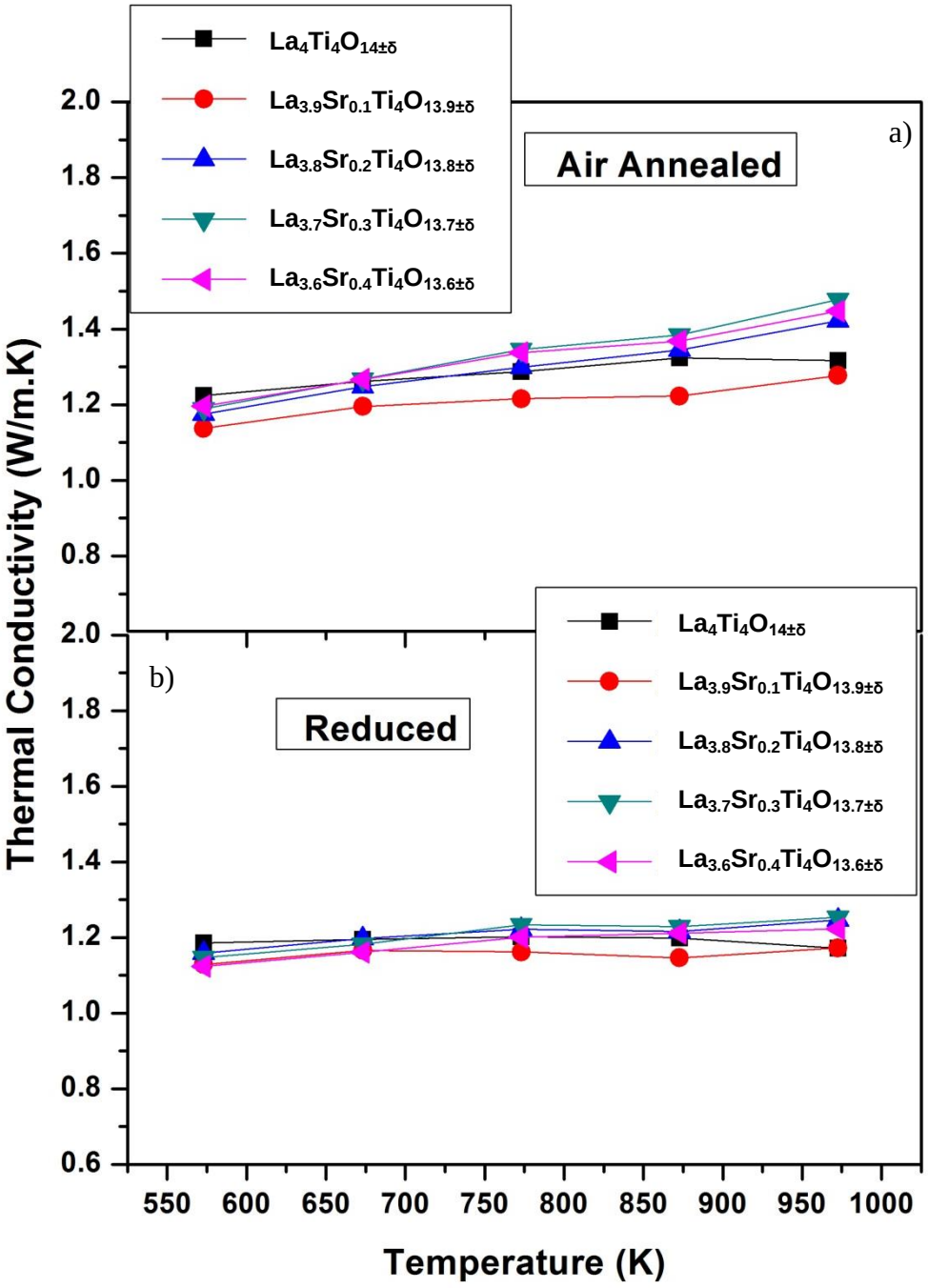
La4Ti4O14±δ
La3.9Sr0.1Ti4O13.9±δ
La3.8Sr0.2Ti4O13.8±δ
La3.7Sr0.3Ti4O13.7±δ
La3.6Sr0.4Ti4O13.6±δ
a)
Air Annealed
b)
Reduced
Thermal Conductivity (W/m.K)
Temperature (K)
2.0
1.8
1.6
1.4
1.2
1.0
0.8
0.6
550
600
650
700
750
800
850
900
950
1000

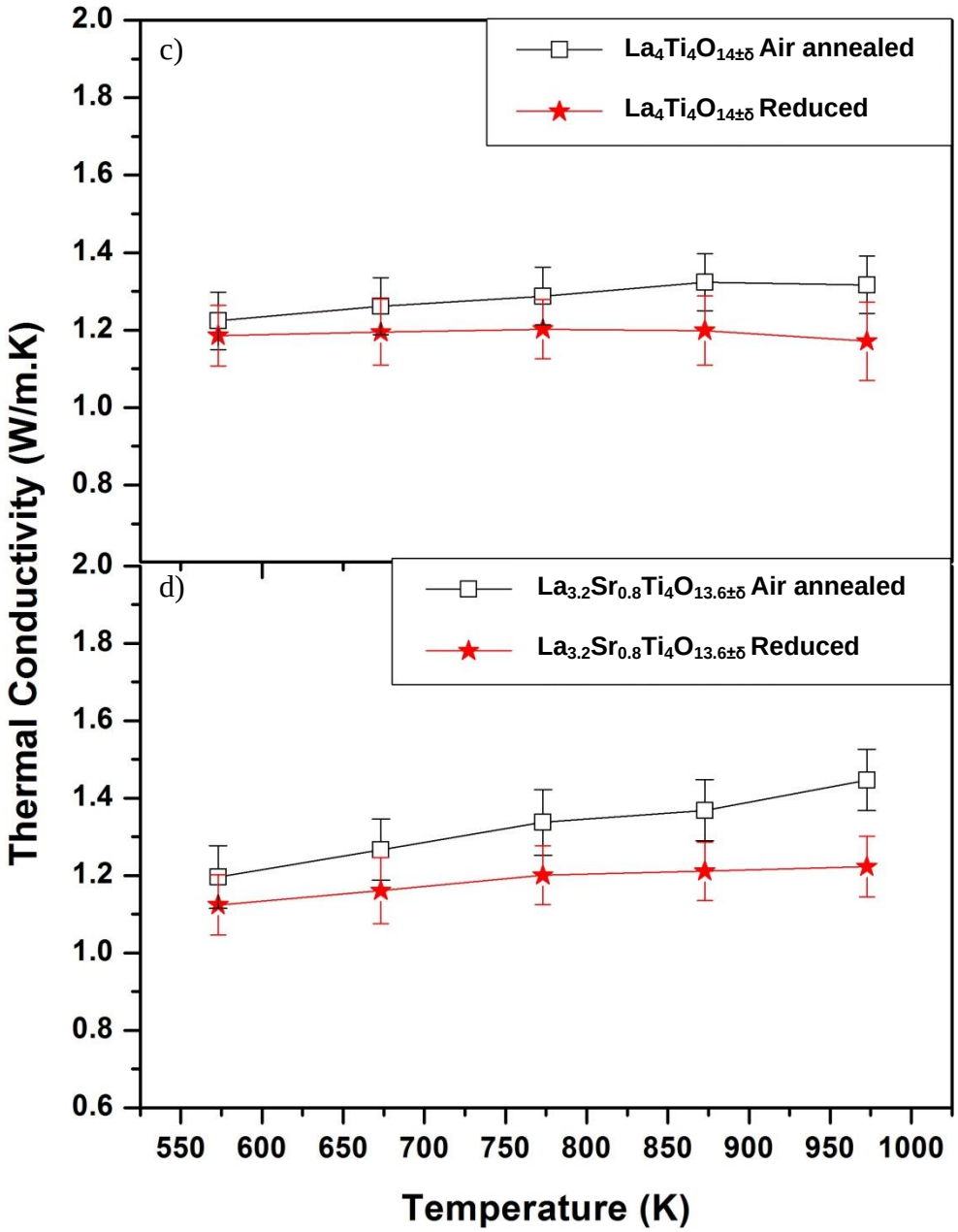

Figure 6.5: *Variation in thermal conductivity of: (a) air annealed* $La_{4-x}Sr_xTi_4O_{14-\frac{x}{2}\pm\delta}$*; (b) reduced* $La_{4-x}Sr_xTi_4O_{14-\frac{x}{2}\pm\delta}$*; (c)* $La_4Ti_4O_{14\pm\delta}$*; (d)* $La_{3.2}Sr_{0.8}Ti_4O_{13.6\pm\delta}$ *with temperature*

Figure 6.6 shows the variation of thermal conductivity with the amount of Sr at 573 K (300 ^{o}C). The thermal conductivity decreases with increasing Sr content due to the generation of nanoscale intergrowths.

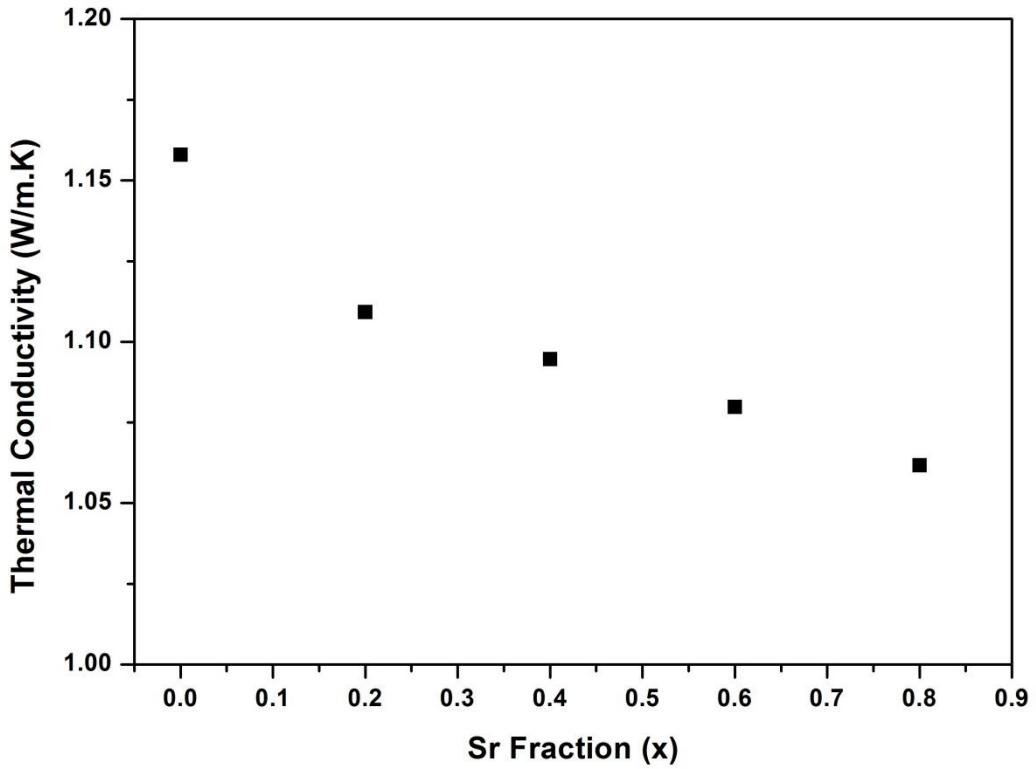

Figure 6.6: *Variation of thermal conductivityof reduced* $La_{4-x}Sr_xTi_4O_{14-\frac{x}{2}\pm\delta}$ *with Sr content at 573 K*

6.3.2 $La_4Ti_{4-x}Ta_xO_{14+\frac{x}{2}\pm\delta}$

The thermal diffusivity of air annealed and reduced $La_4Ti_{4-x}Ta_xO_{14+\frac{x}{2}\pm\delta}$ ceramics are given in Figure 6.7. The thermal diffusivity of all the ceramics is nearly temperature independent and decreased with increasing Ta addition. After reduction, the thermal diffusivity of the ceramics decreased with increasing temperature.

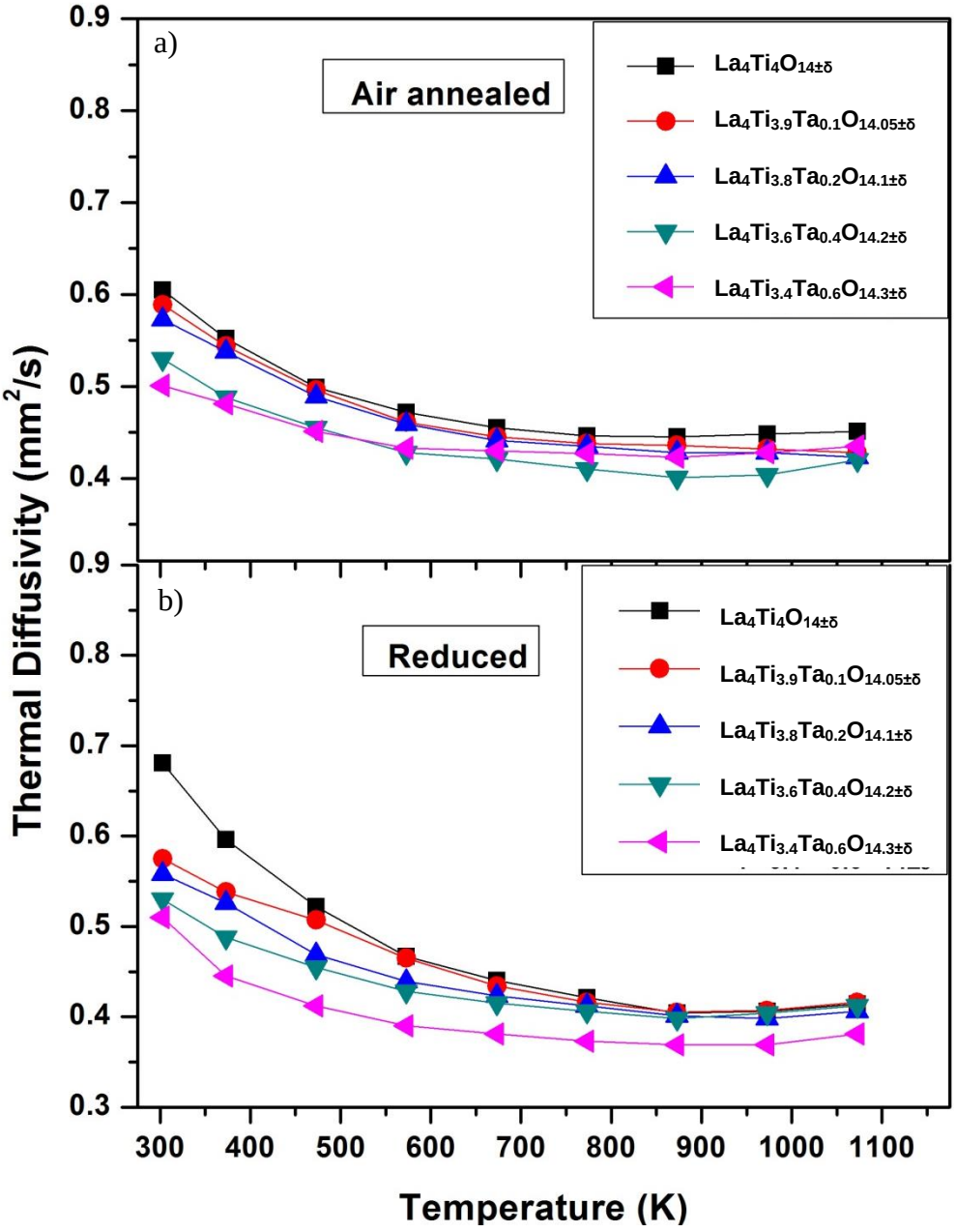

Figure 6.7: *Variation in thermal diffusivity of $La_4Ti_{4-x}Ta_xO_{14+\frac{x}{2}\pm\delta}$ ceramics: (a) air annealed; (b) reduced*

The specific heat capacity of $La_4Ti_{4-x}Ta_xO_{14+\frac{x}{2}\pm\delta}$ ceramics (x=0 and 0.6) are given in Figure 6.8. The heat capacity increases with increasing temperature and reaches a maximum value. The heat capacity for $La_4Ti_{4-x}Ta_xO_{14+\frac{x}{2}\pm\delta}$ ceramics is lower than the pure $La_4Ti_4O_{14}$. According to the Dulong Petit approximation, the product of specific heat capacity and molecular weight is roughly equal to 3R, where R is a general gas constant [7]. This means that increasing the atomic weight would decrease the specific heat capacity of a solid. The atomic weight of $La_4Ti_{4-x}Ta_xO_{14+\frac{x}{2}\pm\delta}$ ceramics increased as a result of Ta substitution in $La_4Ti_4O_{14}$. This increase in the atomic weight explains decrease in the specific heat capacity of substituted ceramics.

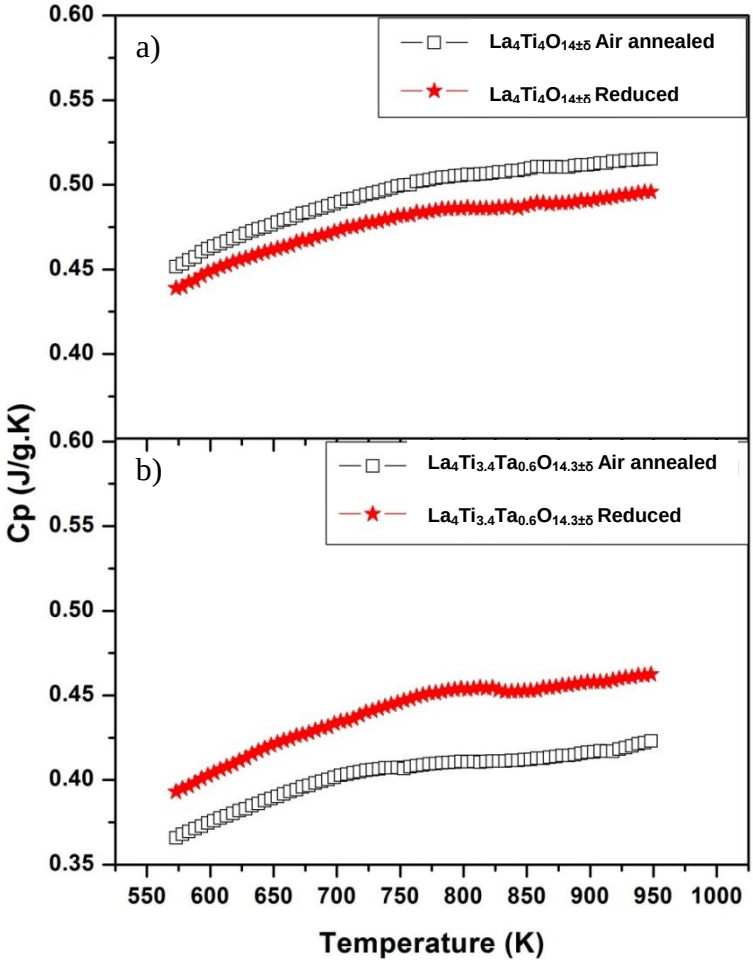

Figure 6.8: *Variation in specific heat capacity of: (a) $La_4Ti_4O_{14\pm\delta}$; (b) $La_4Ti_{3.4}Ta_{0.6}O_{14.3\pm\delta}$ ceramics with temperature*

Table 6.2 gives the densities of $La_4Ti_{4-x}Ta_xO_{14+\frac{x}{2}\pm\delta}$ ceramics. All the ceramics were more than 97% dense and due to the higher molecular weight of Ta than Ti, the theoretical density of all the Ta substituted ceramics increased. The density of the reduced ceramics is lower than the air annealed ceramics due to the removal of oxygen.

Table 6.2: Change in measured densities after Ta substitution and hydrogen reduction

Sample	**Density after air annealing (g cm^{-3})**	**Density after reduction (g cm^{-3})**
$La_4Ti_4O_{14\pm\delta}$	5.74±0.04	5.62±0.01
$La_4Ti_{3.9}Ta_{0.1}O_{14.05\pm\delta}$	5.84±0.01	5.77±0.04
$La_4Ti_{3.8}Ta_{0.2}O_{14.1\pm\delta}$	5.91±0.02	5.84±0.02
$La_4Ti_{3.6}Ta_{0.4}O_{14.2\pm\delta}$	5.95±0.04	5.90±0.03
$La_4Ti_{3.4}Ta_{0.6}O_{14.3\pm\delta}$	6.07±0.02	5.98±0.03

The thermal conductivity of air annealed ceramics is given in Figure 6.9(a). The thermal conductivity of $La_4Ti_{4-x}Ta_xO_{14+\frac{x}{2}\pm\delta}$ ceramics is nearly temperature independent. The thermal conductivity decreased with increasing Ta content. Figure 6.9(b) shows the thermal conductivity of reduced $La_4Ti_{4-x}Ta_xO_{14+\frac{x}{2}\pm\delta}$ ceramics. After reduction, the value of thermal conductivity decreased as compared to the air annealed samples. The decrease in thermal conductivity after reduction was less compared to $La_{4-x}Sr_xTi_4O_{14-\frac{x}{2}\pm\delta}$ ceramics. Figure 6.9(c) and (d) compares the thermal conductivity values of air annealed and reduced ceramics.

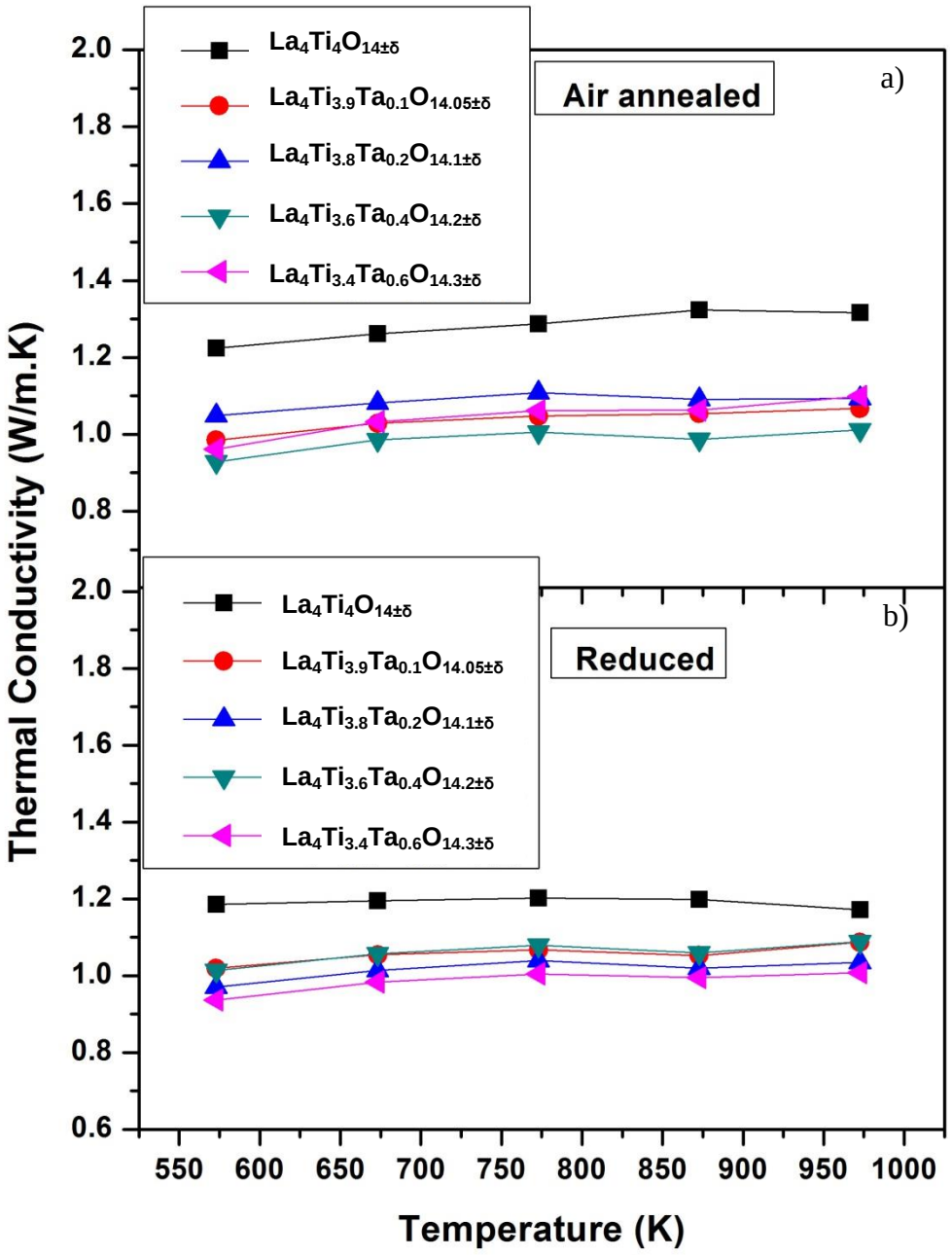
La4Ti4O14±δ
La4Ti3.9Ta0.1O14.05±δ
La4Ti3.8Ta0.2O14.1±δ
La4Ti3.6Ta0.4O14.2±δ
La4Ti3.4Ta0.6O14.3±δ
Air annealed
a)
Reduced
b)
Thermal Conductivity (W/m.K)
Temperature (K)
2.0
1.8
1.6
1.4
1.2
1.0
0.8
0.6
550
600
650
700
750
800
850
900
950
1000

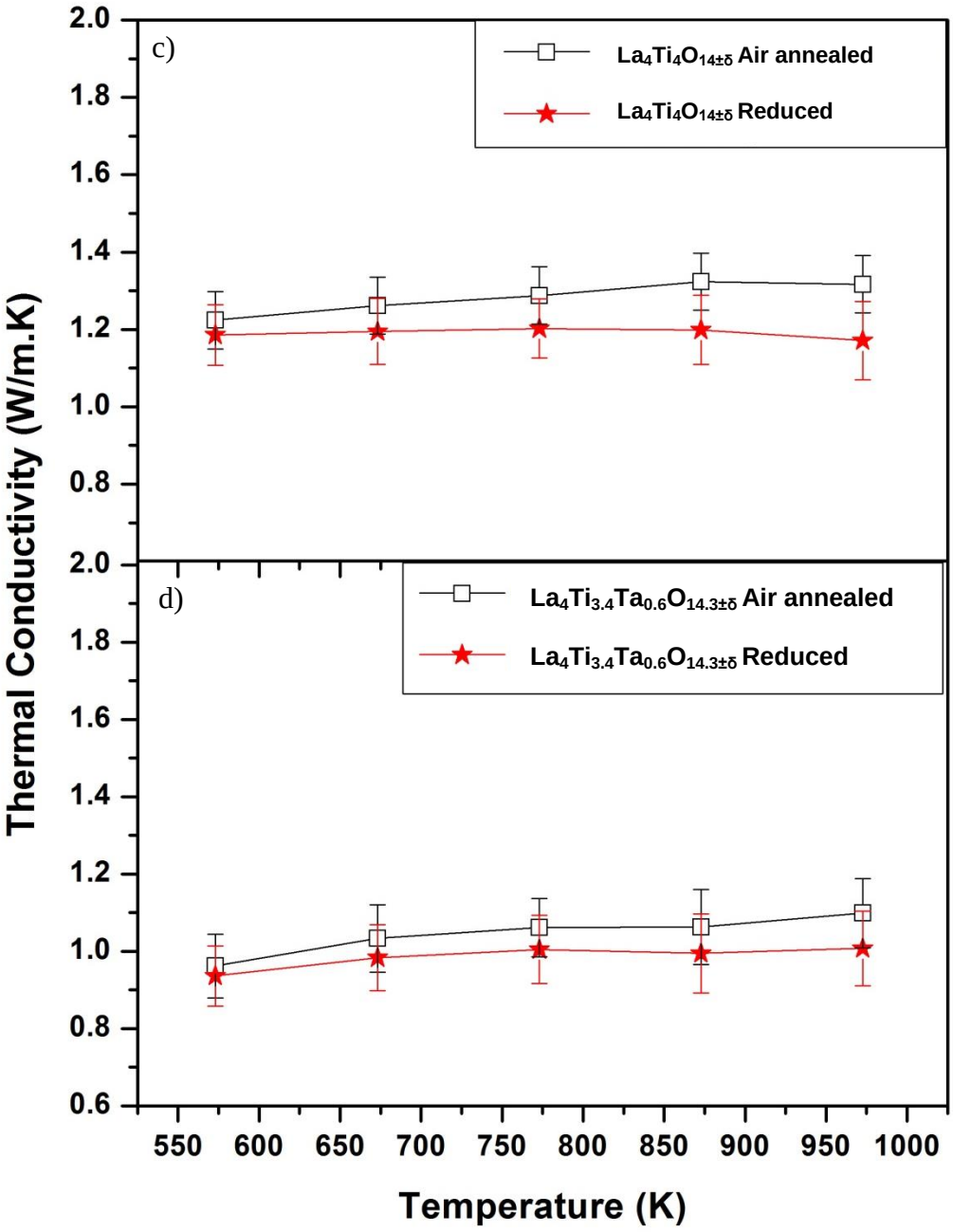

Figure 6.9: *Variation in thermal conductivity of: (a) air annealed* $La_4Ti_{4-x}Ta_xO_{14+\frac{x}{2}\pm\delta}$*; (b) reduced* $La_4Ti_{4-x}Ta_xO_{14+\frac{x}{2}\pm\delta}$*; (c)* $La_4Ti_4O_{14\pm\delta}$*; (d)* $La_4Ti_{3.4}Ta_{0.6}O_{14.3\pm\delta}$ *with temperature*

Figure 6.10 shows the data for variation of thermal conductivity with the amount of Ta at 573 K. There is a decreasing trend in thermal conductivity with increasing Ta content due to the higher molecular weight of Ta than Ti and nanoscale intergrowths.

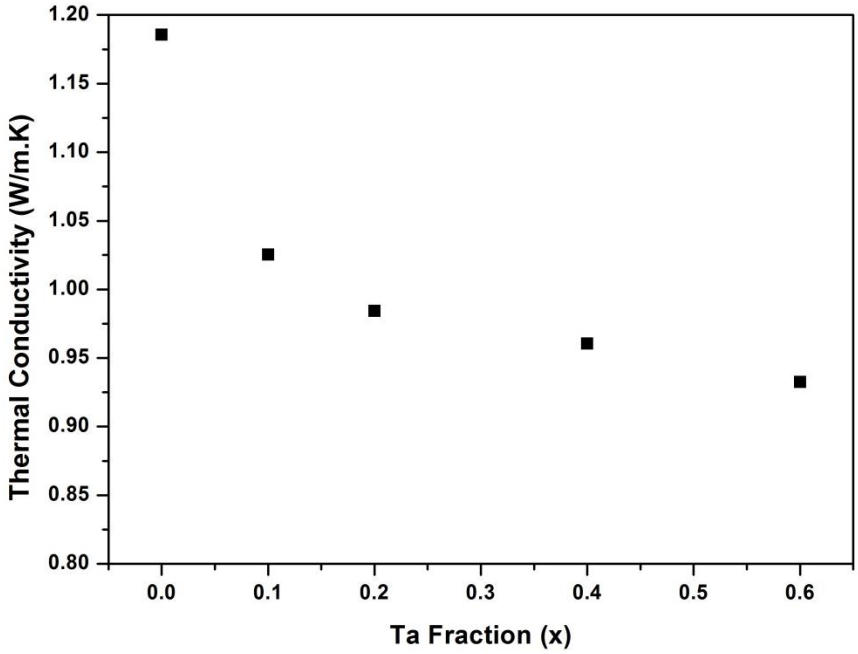

Figure 6.10: *Variation of thermal conductivity with Ta content for reduced* $La_4Ti_{4-x}Ta_xO_{14+\frac{x}{2}\pm\delta}$ *at 573 K*

6.3.3 $La_4Ti_{4-x}Nb_xO_{14+\frac{x}{2}\pm\delta}$

The thermal diffusivity data of air annealed and reduced $La_4Ti_{4-x}Nb_xO_{14\pm\delta}$ ceramics are shown in Figure 6.11. The thermal diffusivity of all the ceramics showed the same near temperature independency as $La_{4-x}Sr_xTi_4O_{14-\frac{x}{2}\pm\delta}$ and $La_4Ti_{4-x}Ta_xO_{14+\frac{x}{2}\pm\delta}$ ceramics. The thermal diffusivity decreased with increasing Nb addition both in the case of air annealed and reduced ceramics. The thermal diffusivity value of reduced $La_4Ti_{4-x}Nb_xO_{14+\frac{x}{2}\pm\delta}$ ceramics is lower than the air annealed ceramics.

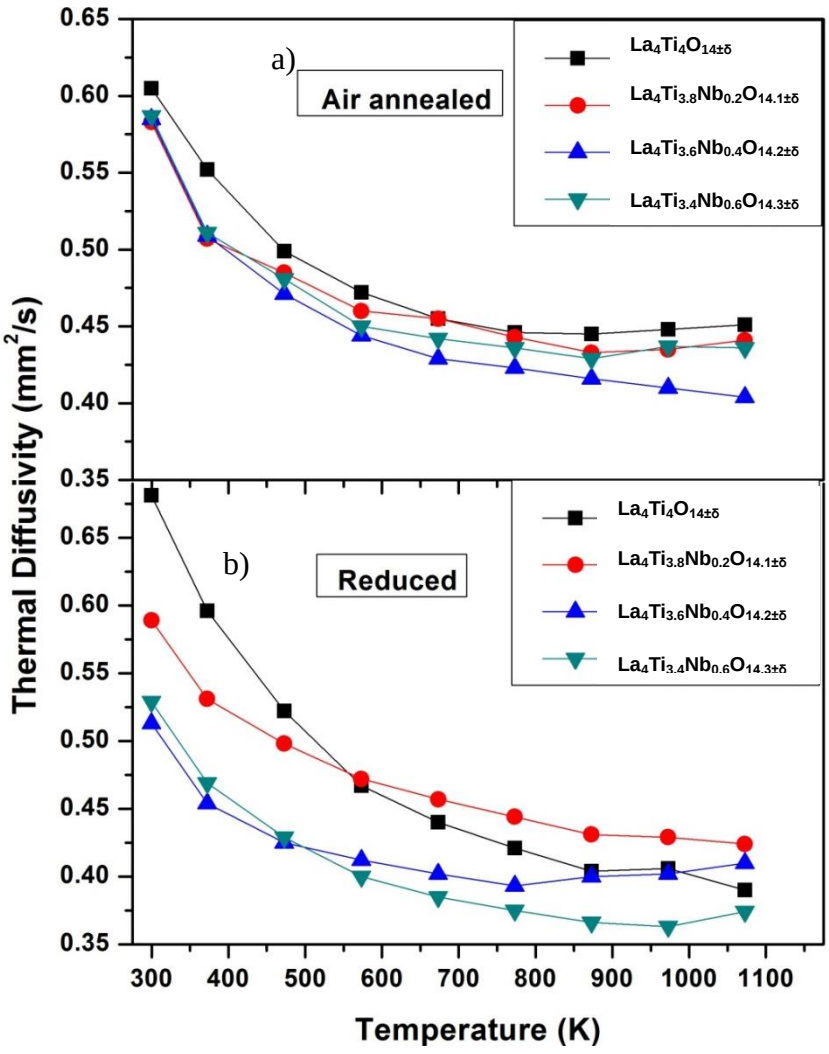

Figure 6.11: *Variation in thermal diffusivity of $La_4Ti_{4-x}Nb_xO_{14\frac{x}{2}\pm\delta}$ ceramics: (a) air annealed; (b) reduced*

Figure 6.12 shows the specific heat capacity of $La_4Ti_{4-x}Nb_xO_{14+\frac{x}{2}\pm\delta}$ ceramics. The specific heat capacity increases with increasing temperature and reaches a maximum value. The specific heat capacity decreases with increasing substitution which is according to the Dulong Petite approximation as discussed previously (section 6.3.2).

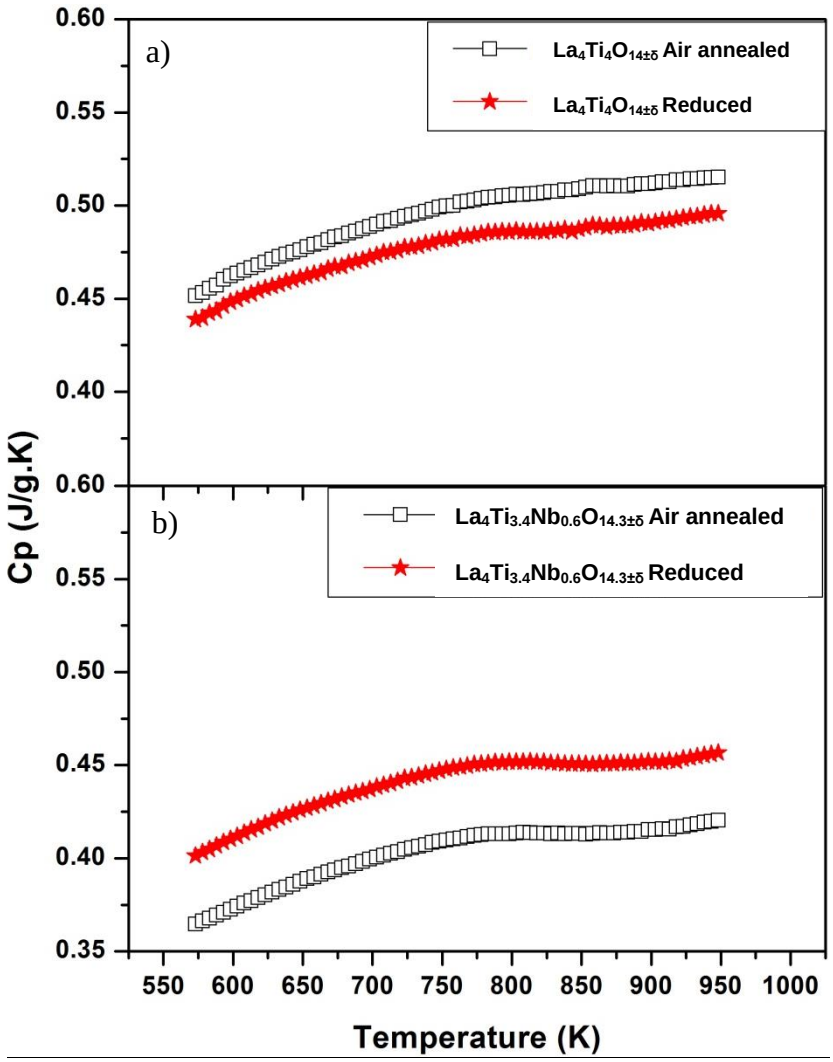

Figure 6.12: *Variation in specific heat capacity of: (a) $La_4Ti_4O_{14\pm\delta}$; (b) $La_4Ti_{3.4}Nb_{0.6}O_{14.3\pm\delta}$ ceramics with temperature*

Table 6.3 gives the densities of air annealed and reduced $La_4Ti_{4-x}Nb_xO_{14+\frac{x}{2}\pm\delta}$ ceramics. All the ceramics were more than 98% dense and due to the higher

molecular weight of Nb (92.9 amu) compared to Ti (47.87 amu), the density of the Nb substituted ceramics increased. The density of the ceramics after hydrogen reduction is lower than the air annealed ceramics due to the loss of oxygen.

Table 6.3: Change in measured densities after Nb substitution and hydrogen reduction

Sample	**Density after air annealing (g cm^{-3})**	**Density after reduction (g cm^{-3})**
$La_4Ti_4O_{14\pm\delta}$	5.74±0.04	5.62±0.01
$La_4Ti_{3.8}Nb_{0.2}O_{14.1\pm\delta}$	5.82±0.04	5.68±0.04
$La_4Ti_{3.6}Nb_{0.4}O_{14.2\pm\delta}$	5.87±0.01	5.75±0.04
$La_4Ti_{3.4}Nb_{0.6}O_{14.3\pm\delta}$	5.88±0.04	5.76±0.06

Figure 6.13(a) shows thermal conductivity of air annealed ceramics. The thermal conductivity value of $La_4Ti_{4-x}Nb_xO_{14+\frac{x}{2}\pm\delta}$ ceramics is nearly temperature independent. The value of thermal conductivity decreased with increasing Nb content. Figure 6.13(b) shows thermal conductivity of reduced $La_4Ti_{4-x}Nb_xO_{14+\frac{x}{2}\pm\delta}$ ceramics. After reduction, the value of thermal conductivity decreases as compared to the air annealed samples. Figure 6.13(c) and (d) compares thermal conductivity values of air annealed and reduced ceramics.

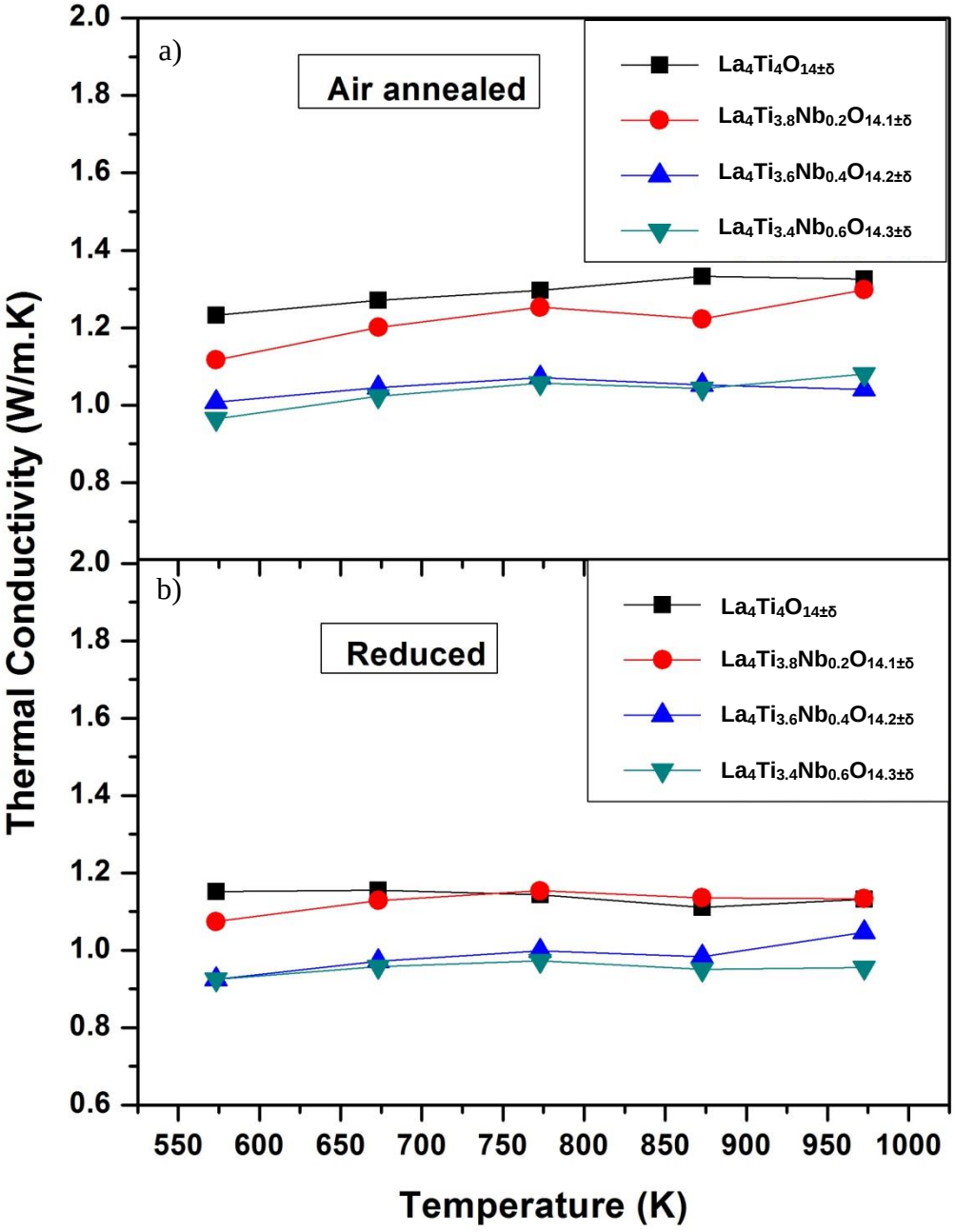
a)
Air annealed
La4Ti4O14±δ
La4Ti3.8Nb0.2O14.1±δ
La4Ti3.6Nb0.4O14.2±δ
La4Ti3.4Nb0.6O14.3±δ
b)
Reduced
La4Ti4O14±δ
La4Ti3.8Nb0.2O14.1±δ
La4Ti3.6Nb0.4O14.2±δ
La4Ti3.4Nb0.6O14.3±δ
Thermal Conductivity (W/m.K)
Temperature (K)
2.0
1.8
1.6
1.4
1.2
1.0
0.8
0.6
550
600
650
700
750
800
850
900
950
1000

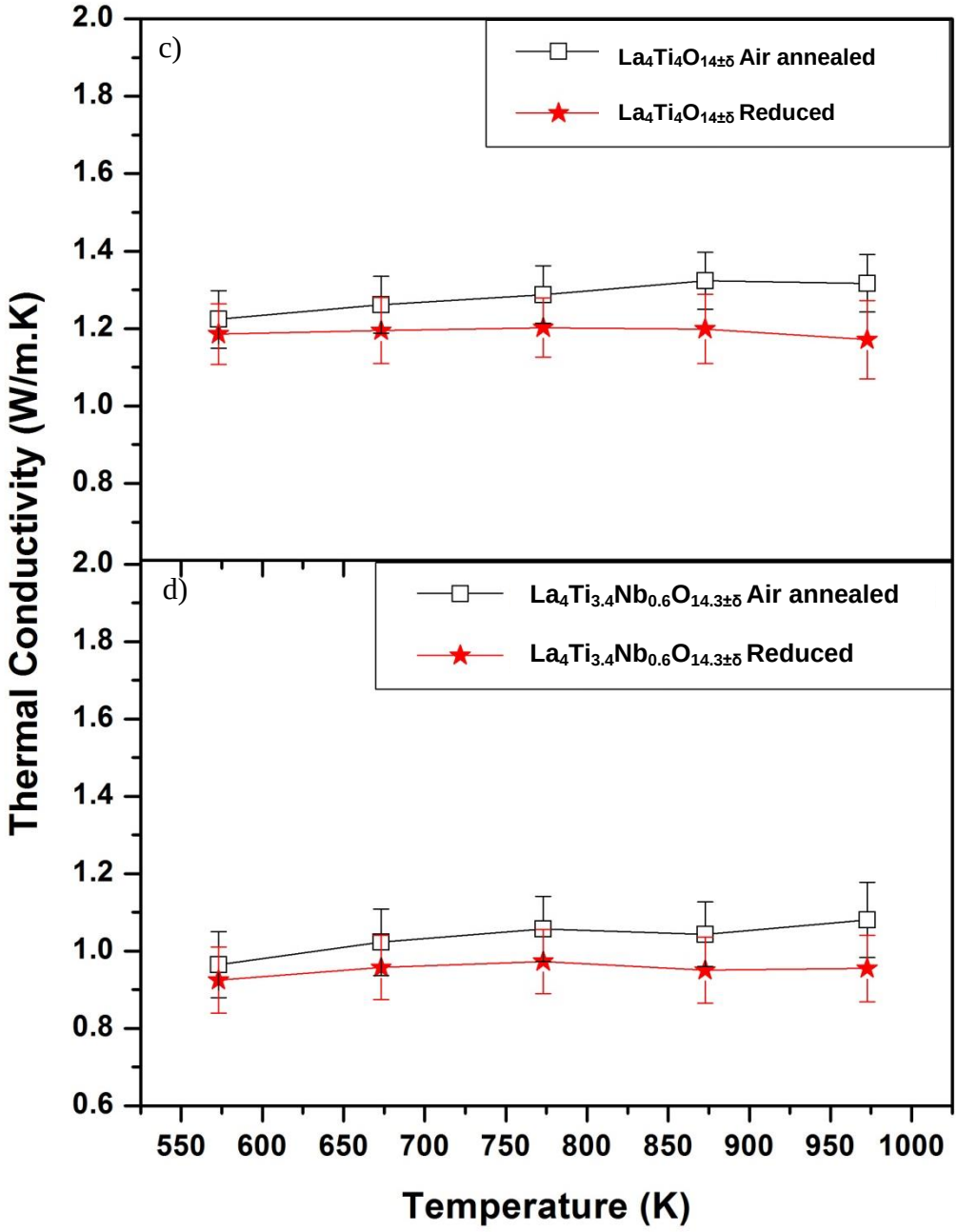

Figure 6.13: *Variation in thermal conductivity of: (a) air annealed $La_4Ti_{4-x}Nb_xO_{14+\frac{x}{2}\pm\delta}$; (b) reduced $La_4Ti_{4-x}Nb_xO_{14+\frac{x}{2}\pm\delta}$; (c) $La_4Ti_4O_{14\pm\delta}$; (d) $La_4Ti_{3.4}Nb_{0.6}O_{14.3\pm\delta}$ with temperature*

The variation of thermal conductivity with the increasing amount of Nb at 573 K is given in Figure 6.14. The thermal conductivity decreases with increasing Nb content due to the higher atomic weight of Nb (~ 92.9 amu) than Ti (~ 47.8 amu). Also, the amount of secondary phase ($LaNbO_4$) increases with increasing Nb

content, it helps in scattering phonons and thus decreasing thermal conductivity value.

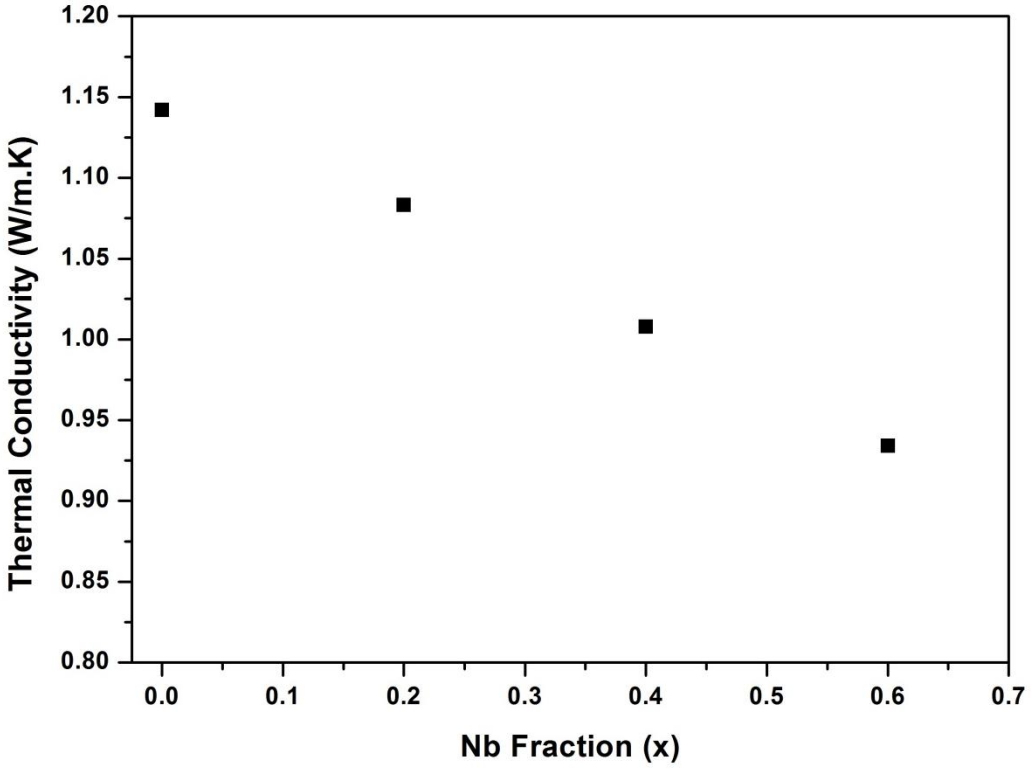

Figure 6.14: *Variation of thermal conductivity with Nb content for reduced* $La_4Ti_{4-x}Nb_xO_{14+\frac{x}{2}\pm\delta}$ *at 573 K*

6.4 $Sr_{4-x}La_xNb_4O_{14+\frac{x}{2}\pm\delta}$

Thermal properties of A site substituted $Sr_4Nb_4O_{14}$ will be discussed in this section. After substitution of Sr with La, the crystal structure of $Sr_4Nb_4O_{14}$ accommodates the non-stoichiometry by forming a second phase which is 2 layer PLS compound $LaNbO_4$ (section 5.3).

Figure 6.15 shows the thermal diffusivity of air annealed and reduced $Sr_{4-x}La_xNb_4O_{14+\frac{x}{2}\pm\delta}$ ceramics. The thermal diffusivity of all the ceramics showed the same near temperature independency as previously reported [2]. The thermal diffusivity decreased with increasing La addition. This thermal diffusivity value is lower than the one reported by Sparks et al. for polycrystalline $Sr_4Nb_4O_{14}$ [2].

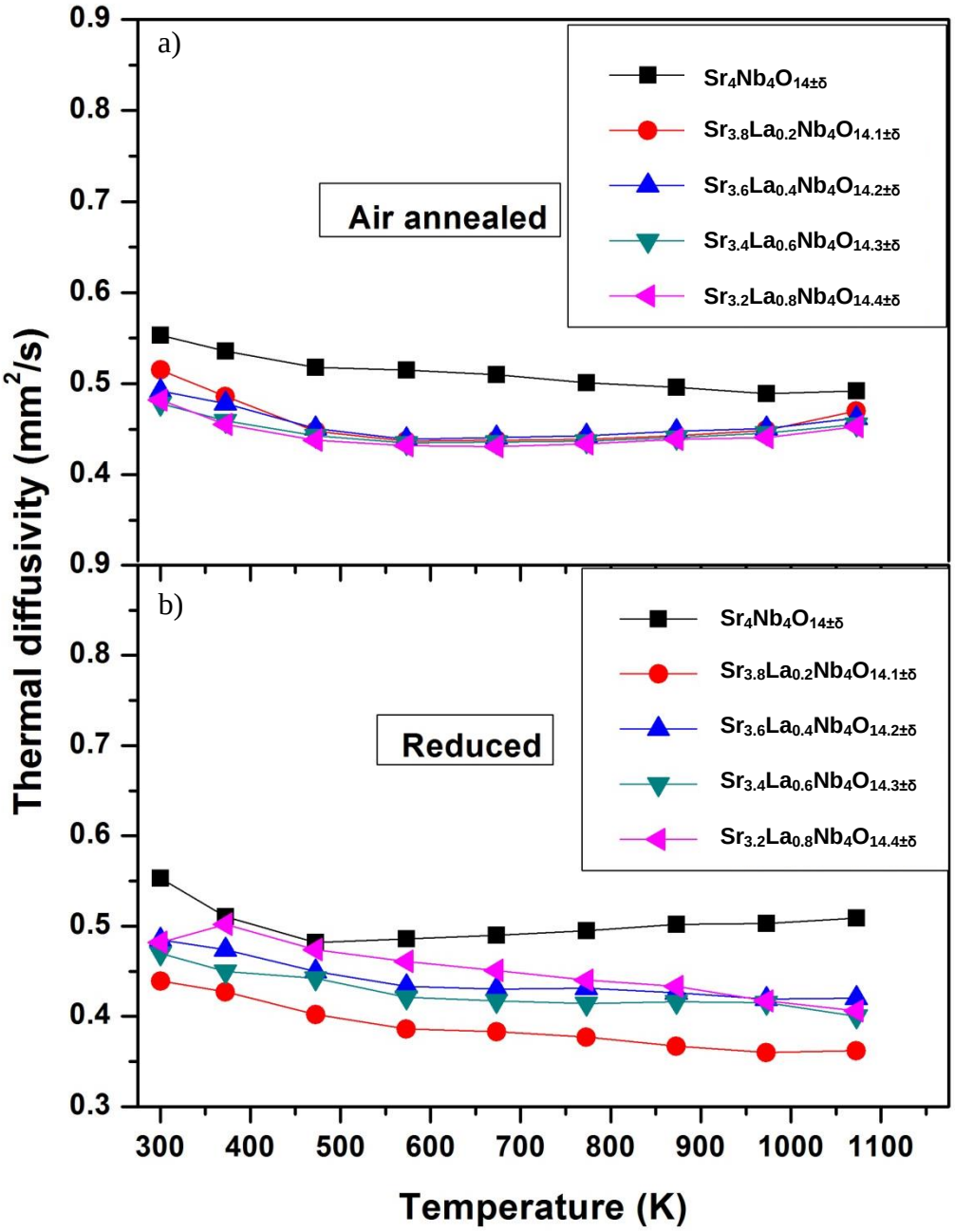

Figure 6.15: *Variation in thermal diffusivity of* $Sr_{4-x}La_xNb_4O_{14+\frac{x}{2}\pm\delta}$ *ceramics: (a) air annealed; (b) reduced*

The heat capacity of $Sr_{4-x}La_xNb_4O_{14+\frac{x}{2}\pm\delta}$ ceramics increases with increasing temperature as given in Figure 6.16 and reaches a maximum value. The heat capacity decreases with increasing La content, but after reduction, the heat capacity of all the ceramics were similar. Referring back to the Dulong Petit law, the specific heat

varies inversely to formula weight. Since La substitution for Sr increased the total formula weight of the ceramics, this in turn lowered the specific heat capacity value.

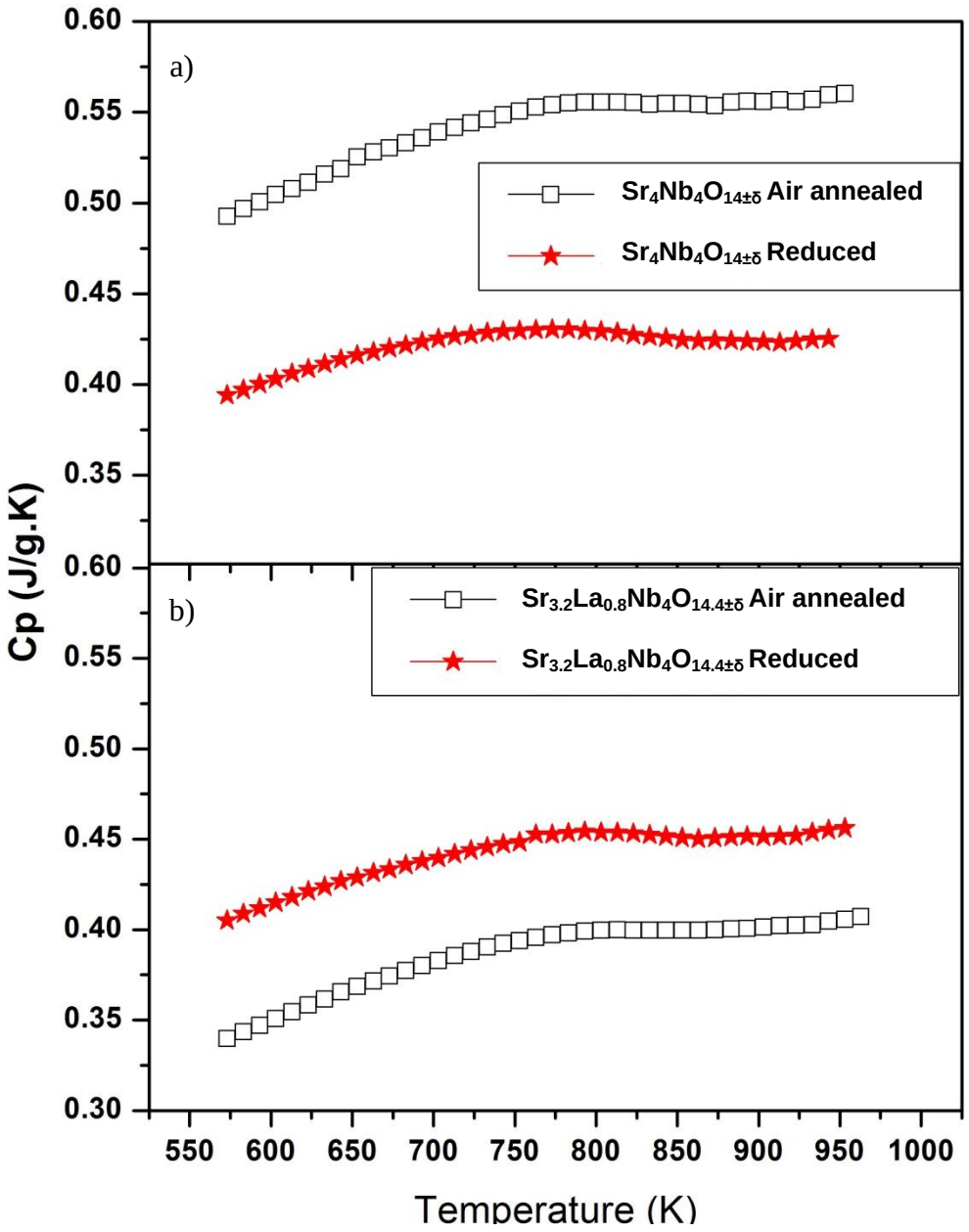

Figure 6.16: *Variation in specific heat capacity of: (a) $Sr_4Nb_4O_{14\pm\delta}$; (b) $Sr_{3.2}La_{0.8}Nb_4O_{14.4\pm\delta}$ ceramics with temperature*

Table 6.4 gives the densities of $Sr_{4-x}La_xNb_4O_{14+\frac{x}{2}\pm\delta}$ ceramics after air annealing and after reduction. All the ceramics were more than 98% dense and due to the higher molecular weight of La (138.9 amu) than Sr (87.6amu), the density of

La substituted ceramics increased. The density of the ceramics decreased after reduction.

Table 6.4: Change in measured densities after La substitution and hydrogen reduction

Sample	**Density after air annealing (g cm^{-3})**	**Density after reduction (g cm^{-3})**
$Sr_4Nb_4O_{14\pm\delta}$	5.09± 0.01	5.03±0.02
$Sr_{3.8}La_{0.2}Nb_4O_{14.1\pm\delta}$	5.12±0.03	5.07±0.02
$Sr_{3.6}La_{0.4}Nb_4O_{14.2\pm\delta}$	5.22±0.02	5.19±0.01
$Sr_{3.4}La_{0.6}Nb_4O_{14.3\pm\delta}$	5.25±0.01	5.16±0.04
$Sr_{3.2}La_{0.8}Nb_4O_{14.4\pm\delta}$	5.30±0.01	5.18±0.03

Figure 6.17(a) shows the thermal conductivity of air annealed ceramics. The thermal conductivity of $Sr_{4-x}La_xNb_4O_{14+\frac{x}{2}\pm\delta}$ ceramics decreased with increasing La substitution. Figure 6.17(b) shows thermal conductivity of reduced $Sr_{4-x}La_xNb_4O_{14+\frac{x}{2}\pm\delta}$ ceramics. After reduction, the value of thermal conductivity decreased until x= 0.2 and then increased. Figure 6.17(c) and (d) compares thermal conductivity values of air annealed and reduced $Sr_{4-x}La_xNb_4O_{14+\frac{x}{2}\pm\delta}$ (x=0 and 0.8) ceramics. For $Sr_4Nb_4O_{14}$, the thermal conductivity decreases after reduction. This decrease is consistent with the pure $La_4Ti_4O_{14}$ in which thermal conductivity decreases after reduction due to the generation of planar defects. For $Sr_{4-x}La_xNb_4O_{14+\frac{x}{2}\pm\delta}$, the thermal conductivity increases after reduction. This increase is related to the decreasing amount of secondary phase $LaNbO_4$ (Table 5.2) which resulted in less phonon scattering and thus increasing thermal conductivity.

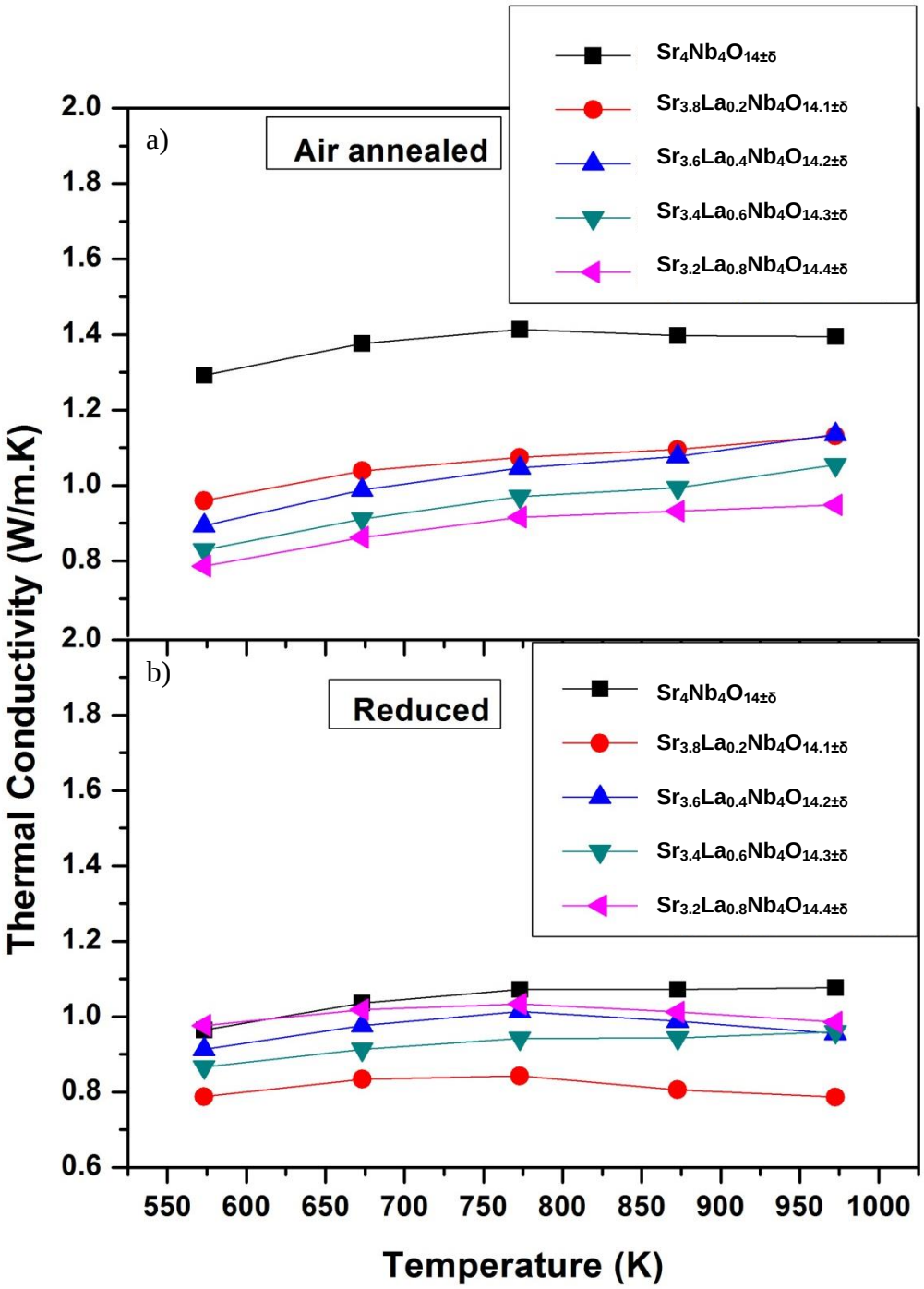
a)
Air annealed
b)
Reduced
Sr4Nb4O14±δ
Sr3.8La0.2Nb4O14.1±δ
Sr3.6La0.4Nb4O14.2±δ
Sr3.4La0.6Nb4O14.3±δ
Sr3.2La0.8Nb4O14.4±δ
Thermal Conductivity (W/m.K)
Temperature (K)
2.0
1.8
1.6
1.4
1.2
1.0
0.8
0.6
550
600
650
700
750
800
850
900
950
1000

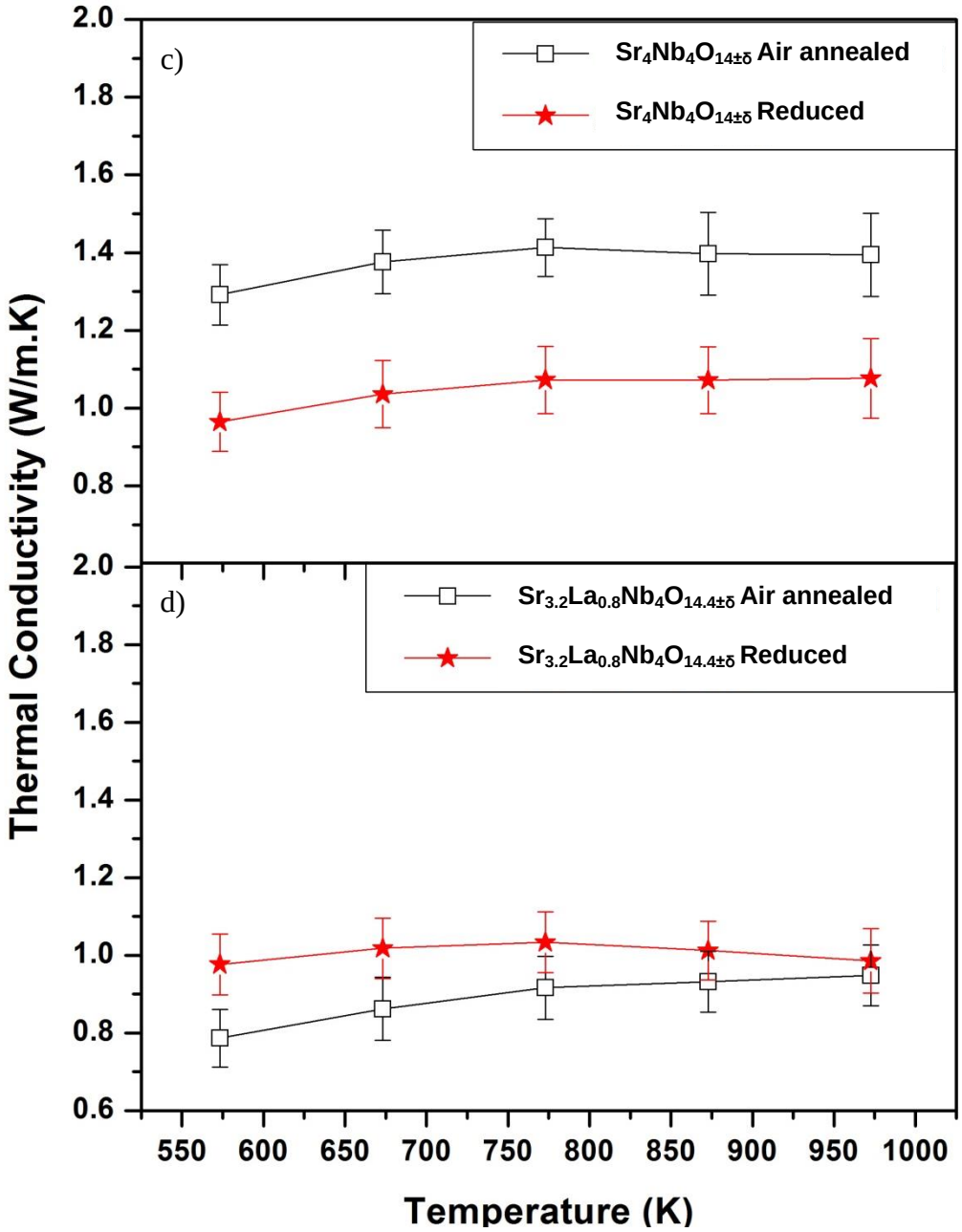

Figure 6.17: *Variation in thermal conductivity of: (a) air annealed $Sr_{4-x}La_xNb_4O_{14+\frac{x}{2}\pm\delta}$; (b) reduced $Sr_{4-x}La_xNb_4O_{14+\frac{x}{2}\pm\delta}$; (c) $Sr_4Nb_4O_{14\pm\delta}$; (d) $Sr_{3.2}La_{0.8}Nb_4O_{14.4\pm\delta}$ with temperature*

Figure 6.18 shows the variation of thermal conductivity with the amount of La at 573 K. Thermal conductivity tends to decrease with increasing La content after air annealing. This decrease is the result of the mass difference caused by the substitution of La for Sr and the secondary phase ($LaNbO_4$).

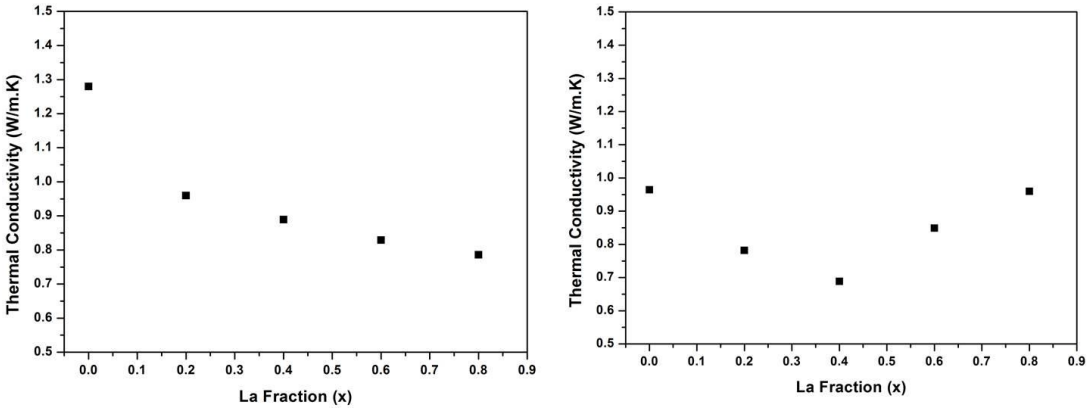

Figure 6.18: *Variation of thermal conductivity with La content at 573 K: (a) air annealed and; (b) reduced*

6.5 DISCUSSIONS

The thermal conductivities of $La_4Ti_4O_{14}$ and $Sr_4Nb_4O_{14}$ ceramics follow near room temperature independency after air annealing and reduction. The thermal conductivity was in the range of ~ 1.2 W/m.K. After substitution, the thermal conductivity decreases slightly.

The thermal conductivity of a material depends upon its lattice and electronic contributions. The electronic contribution of thermal conductivity can be calculated by the Wiedemann–Franz law and is given by

$$\kappa_{elec} = LT\sigma \qquad (2.4)$$

Where κ_{elec} is the electronic contribution of thermal conductivity, L is the Lorenz number, T is the absolute temperature and σ is the electrical conductivity. The value of L was taken from literature and it was 2.44×10^{-8} $W\Omega K^{-2}$ at 573 K. Electrical conductivity was measured using the four probe method under vacuum

with laboratory built equipment [8] and was estimated to be ~ 0.5 S/m for $La_{3.2}Sr_{0.8}Ti_4O_{13.6\pm\delta}$. This was the highest electrical conductivity measured for the substituted PLS ceramics in this work. Based on these values, the κ_{elec} for $La_4Ti_4O_{14}$ and $Sr_4Nb_4O_{14}$ based compositions was estimated to be ~ $7x10^{-9}$ W/m.K.

In the case of $La_4Ti_4O_{14}$, the thermal conductivity of air annealed and reduced ceramics increased after Sr substitution but decreased after Ta/Nb substitution. This change in thermal conductivity can be explained by looking at the dependency of thermal conductivity on average atomic mass. [9]

$$\kappa_{min} = 0.87 k_B \Omega^{-2/3} \left(\frac{E}{\rho}\right)^{1/2} \quad (6.1)$$

Where E is the elastic modulus, ρ is the density and Ω is the average atomic volume and k_B is the Boltzmann's constant. The minimum thermal conductivity values are presented in Table 6.5.

The average atomic volume for $La_4Ti_4O_{14}$ and $Sr_4Nb_4O_{14}$ based compositions was calculated by following relation and tabulated in Table 6.5 [10]

$$\Omega = \frac{M}{m\rho N_A} \quad (6.2)$$

Where M is the average molar mass of the unit cell, m is the number of atoms per formula unit, ρ is the density and N_A is the Avogadro's number.

From the above two expressions, it is evident that the large mean atomic mass and low elastic modulus favour low thermal conductivity [9]. The atomic

masses of $La_4Ti_4O_{14}$ and $Sr_4Nb_4O_{14}$ based compositions are given in table 6.5. (The atomic weights were calculated based on the formula $La_2Ti_2O_7$ and $Sr_2Nb_2O_7$).

Table 6.5: Relative formula weight, mean atomic volume and minimum thermal conductivity of air annealed $La_4Ti_4O_{14}$ and $Sr_4Nb_4O_{14}$ based compositions at 973 K

Composition	Formula weight (amu)	Mean Atomic Volume (nm^3)	Minimum Thermal Conductivity (W/m.K)	Experimental Thermal Conductivity (W/m.K)
$La_4Ti_4O_{14\pm\delta}$	485.54	0.01280	1.33	1.31±0.07
$La_{3.8}Sr_{0.2}Ti_4O_{13.9\pm\delta}$	479.61	0.01280	1.35	1.17±0.09
$La_{3.6}Sr_{0.4}Ti_4O_{13.8\pm\delta}$	473.68	0.01280	1.36	1.24±0.07
$La_{3.4}Sr_{0.6}Ti_4O_{13.7\pm\delta}$	467.76	0.01270	1.38	1.25±0.07
$La_{3.2}Sr_{0.8}Ti_4O_{13.6\pm\delta}$	461.83	0.01270	1.38	1.25±0.08
$La_4Ti_{3.9}Ta_{0.1}O_{14.05\pm\delta}$	492.59	0.01270	1.30	1.08±0.08
$La_4Ti_{3.8}Ta_{0.2}O_{14.1\pm\delta}$	499.65	0.01270	1.29	1.03±0.09
$La_4Ti_{3.6}Ta_{0.4}O_{14.2\pm\delta}$	514.55	0.01300	1.24	1.09±0.10
$La_4Ti_{3.4}Ta_{0.6}O_{14.3\pm\delta}$	527.86	0.01310	1.20	1.00±0.09
$La_4Ti_{3.8}Nb_{0.2}O_{14.1\pm\delta}$	490.84	0.01270	1.30	1.13±0.08
$La_4Ti_{3.6}Nb_{0.4}O_{14.2\pm\delta}$	496.15	0.01270	1.28	1.04±0.09
$La_4Ti_{3.4}Nb_{0.6}O_{14.3\pm\delta}$	501.45	0.01280	1.25	0.95±0.09
$Sr_4Nb_4O_{14\pm\delta}$	473.04	0.01400	1.19	1.07±0.10
$Sr_{3.8}La_{0.2}Nb_4O_{14.1\pm\delta}$	478.99	0.01380	1.19	0.78±0.12

$Sr_{3.6}La_{0.4}Nb_4O_{14.2\pm\delta}$	484.91	0.01390	1.18	0.95±0.09
$Sr_{3.4}La_{0.6}Nb_4O_{14.3\pm\delta}$	490.84	0.01390	1.17	0.96±0.11
$Sr_{3.2}La_{0.8}Nb_4O_{14.4\pm\delta}$	496.77	0.01400	1.16	0.98±0.07

It is evident from Table 6.5 that after substitution, the atomic mass decreased in the case of $La_{4-x}Sr_xTi_4O_{14-\frac{x}{2}\pm\delta}$ and increased in the case of $La_4Ti_{4-x}Ta_xO_{14+\frac{x}{2}\pm\delta}$, $La_4Ti_{4-x}Nb_xO_{14+\frac{x}{2}\pm\delta}$ and $Sr_{4-x}La_xNb_4O_{14+\frac{x}{2}\pm\delta}$ compared to the pure $La_4Ti_4O_{14}$ and $Sr_4Nb_4O_{14}$. Assuming E to be nearly constant for all the compositions [11, 12], the thermal conductivity will increase in the case of $La_{4-x}Sr_xTi_4O_{14-\frac{x}{2}\pm\delta}$ and decrease in the case of $La_4Ti_{4-x}Ta_xO_{14+\frac{x}{2}\pm\delta}$, $La_4Ti_{4-x}Nb_xO_{14+\frac{x}{2}\pm\delta}$ and $Sr_{4-x}La_xNb_4O_{14+\frac{x}{2}\pm\delta}$ due to increasing molecular weight. After the substitution of Sr in $La_4Ti_4O_{14}$, the thermal conductivity became less temperature dependent and increased slightly with increasing temperature. In the case of Ta, Nb and La substituted ceramics, the thermal conductivity decreased with the increasing substitution following the same temperature independency. After reduction, the thermal conductivity decreased further.

In the case of substituted $La_4Ti_4O_{14}$ and $Sr_4Nb_4O_{14}$, a high density of nanoscale intergrowths and secondary phase were found inside the microstructure. So the behaviour of thermal conductivity depends upon the atomic mass difference and the nanoscale intergrowths/secondary phase. Also, the experimental thermal conductivity values are lower than the minimum thermal conductivity value. This decrease in thermal conductivity by substituting different elements can be explained by the fact that substituted elements incorporates nanoscale intergrowths in the structure to accommodate non stoichiometry. The phonons are scattered by these nanoscale intergrowths to reduce thermal conductivity compared to the pure

compound (and theoretical minimum thermal conductivity values). The combined effect of phonon scattering from the nanoscale intergrowths and the substituted atoms resulted in a change in thermal conductivity.

In order to estimate the effect of nanoscale intergrowths/secondary phase on thermal conductivity, the difference between the calculated thermal conductivity (given in Table 6.5) and the measured thermal conductivity was calculated. This difference was found to be negligible in the case of pure compounds. As the amount of substituted elements increased, the difference increased to ~ 20% which was the result of nanoscale intergrowths/secondary phase in lowering thermal conductivity.

The Debye temperature (θ_D) for $La_4Ti_4O_{14}$ and $Sr_4Nb_4O_{14}$ based compositions was calculated by the following relationship [13] and the data is shown in the Table 6.6.

$$\theta_D = \frac{h}{k_B}\left[\frac{3}{4\pi\Omega}\right]^{1/3} V \qquad (6.3)$$

Where *h* is the Plank's constant and *V* is the velocity of sound in solids. The phonon mean free path (η) is defined as the average distance a phonon travels before being scattered. η can be calculated by using the high temperature limit of Debye equation and the Dulong Petit equation [2]. A temperature of 973 K was chosen for the calculation.

$$\eta = \frac{\kappa\Omega}{k_B V} \qquad (6.4)$$

where κ is the real time thermal conductivity value. η for all the air annealed ceramics is presented in the Table 6.6.

Table 6.6: Phonon mean free path and Debye temperature for air annealed $La_4Ti_4O_{14}$ and $Sr_4Nb_4O_{14}$ based compositions

Composition	Phonon mean free path η (Å)	Debye Temperature (K)
$La_4Ti_4O_{14\pm\delta}$	2.7	568
$La_{3.8}Sr_{0.2}Ti_4O_{13.9\pm\delta}$	2.7	572
$La_{3.6}Sr_{0.4}Ti_4O_{13.8\pm\delta}$	2.8	573
$La_{3.4}Sr_{0.6}Ti_4O_{13.7\pm\delta}$	2.9	578
$La_{3.2}Sr_{0.8}Ti_4O_{13.6\pm\delta}$	2.9	581
$La_4Ti_{3.9}Ta_{0.1}O_{14.05\pm\delta}$	2.3	565
$La_4Ti_{3.8}Ta_{0.2}O_{14.1\pm\delta}$	2.2	561
$La_4Ti_{3.6}Ta_{0.4}O_{14.2\pm\delta}$	2.2	550
$La_4Ti_{3.4}Ta_{0.6}O_{14.3\pm\delta}$	2.4	542
$La_4Ti_{3.8}Nb_{0.2}O_{14.1\pm\delta}$	2.7	567
$La_4Ti_{3.6}Nb_{0.4}O_{14.2\pm\delta}$	2.2	564
$La_4Ti_{3.4}Nb_{0.6}O_{14.3\pm\delta}$	2.3	560
$Sr_4Nb_4O_{14\pm\delta}$	2.9	604
$Sr_{3.8}La_{0.2}Nb_4O_{14.1\pm\delta}$	2.3	606
$Sr_{3.6}La_{0.4}Nb_4O_{14.2\pm\delta}$	2.3	605
$Sr_{3.4}La_{0.6}Nb_4O_{14.3\pm\delta}$	2.2	605
$Sr_{3.2}La_{0.8}Nb_4O_{14.4\pm\delta}$	2.0	603

The η for air annealed $La_4Ti_4O_{14}$ based compositions increased slightly from ~ 2.7 Å to ~ 3.0 Å after Sr substitution while it decreased to ~ 2.3 Å after Ta/Nb

substitution. For air annealed $Sr_4Nb_4O_{14}$, η was estimated to be ~ 3.0 Å which decreased to ~ 2.0 Å after La substitution.

In perovskites (e.g. $SrTiO_3$) the lattice parameter is 3.95 Å (XRD PDF # 00-035-0734) while in PLS structure, the layers are presented along (110) cut of the unit cell. From this information, the thickness of individual layer for $La_4Ti_4O_{14}$ was calculated to be ~ 2.7 Å while the separation between the perovskite blocks in the unit cell was found to be ~ 2.04 Å as shown in Figure 6.19. The η values (Table 6.6) are similar to the thickness of individual perovskite layer (2.7 Å) and the separation between the perovskite blocks (2.04 Å). From this information, it can be concluded that the phonon mean free path approaches the atomic dimensions which explains the temperature independency of thermal conductivity for PLS materials.

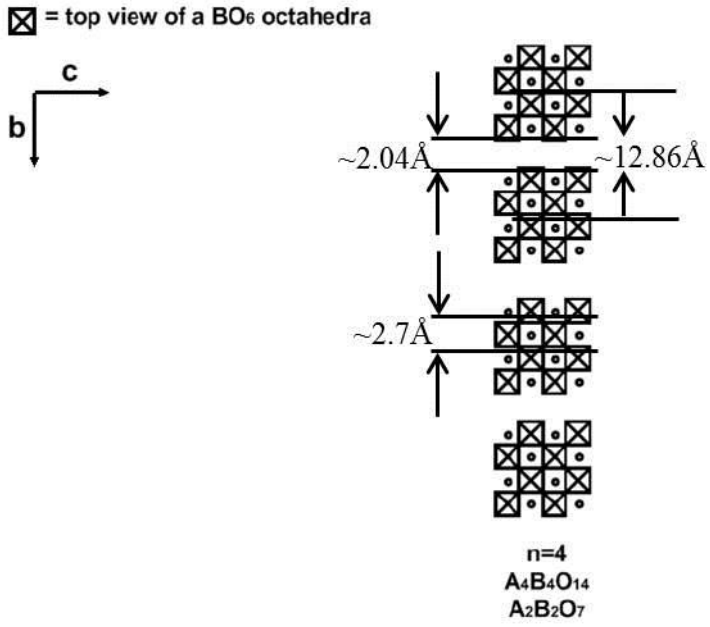

Figure 6.19: *Schematic representation of a typical non distorted $La_4Ti_4O_{14}$ projected along a axis*

6.6 CONCLUSION

Acceptor and donor substituted $La_4Ti_4O_{14}$ and donor substituted $Sr_4Nb_4O_{14}$ were synthesised by spark plasma sintering. The effect of oxidation/reduction and compositional non stoichiometry were studied on thermal properties. Sr/Ta substitution and reduction produced nanoscale intergrowths to accommodate the compositional non-stoichiometry. An extremely low thermal conductivity value of ~ 0.93 W/m.K (at 573 K) was observed in the case of reduced $La_4Ti_{3.4}Ta_{0.6}O_{14.3\pm\delta}$ ceramic as a result of the nanoscale intergrowths. This value is amongst the lowest value ever reported for the untextured oxide materials. Nb substitution in $La_4Ti_4O_{14}$ and La substitution in $Sr_4Nb_4O_{14}$ did not produce nanoscale intergrowths but produced $LaNbO_4$ as a separate phase.

REFERENCES

[1] A. Sakai, T. Kanno, K. Takahashi, Y. Yamada, H. Adachi, Journal of Applied Physics, 108 (2010) 103706.

[2] T.D. Sparks, P.A. Fuierer, D.R. Clarke, Journal of the American Ceramic Society, 93 (2010) 1136-1141.

[3] A. Sakai, T. Kanno, K. Takahashi, A. Omote, H. Adachi, Y. Yamada, X.D. Zhou, Journal of the American Ceramic Society, 95 (2012) 1750-1755.

[4] B. Liu, J.Y. Wang, F.Z. Li, Y.C. Zhou, Acta Materialia, 58 (2010) 4369-4377.

[5] Z.G. Liu, J. H. Ouyang, Y. Zhou, Bulletin of Materials Science, 32 (2009) 603-606.

[6] Y. Shen, D.R. Clarke, P.A. Fuierer, Applied Physics Letters, 93 (2008) 102907.

[7] B.S. Mitchell, Transport Properties of Materials, in: An Introduction to Materials Engineering and Science, John Wiley & Sons, inc. , Canada, 2004, pp. 320.

[8] G. Li, J.Y. Yang, Y. Xiao, L.W. Fu, J.Y. Peng, Y. Deng, P.W. Zhu, H.X. Yan, J. Electron.Mater. 42 (2013) 675–678.

[9] M.R. Winter, D.R. Clarke, Journal of the American Ceramic Society, 90 (2007) 533-540.

[10] C.G. Levi, Curr Opin Solid St M, 8 (2004) 77-91.

[11] D.R. Clarke, Surf Coat Tech, 163 (2003) 67-74.

[12] R. Korobko, S.K. Kim, S. Kim, S.R. Cohen, E. Wachtel, I. Lubomirsky, Advanced Functional Materials, 23 (2013) 6076-6081.

[13] R. Freer, Journal of Materials Science, 16 (1981) 3225-3227.

Chapter VII. Thermoelectric Properties of co-doped $CoSb_3$

7.1 INTRODUCTION

Skutterudites such as cobalt antimonide ($CoSb_3$) [3] have been the focus of the research for intermediate temperature thermoelectric applications (25 ^oC to 550 ^oC) [1, 2]. $CoSb_3$ has a melting point of 873 ^oC [4] with high carrier concentration and Seebeck coefficient (~ 60μV/K) [5]. However, due to strong covalent bonding, the intrinsic thermal conductivity is ~ 10 W/m.K which is a high value for thermoelectric applications [6]. $CoSb_3$ has cubic structure (Space group Im3) with two naturally formed vacant atomic cages per unit cell. These cages favour the PGEC approach and can be partially filled with a variety of atoms like rare earths or alkali metals [7]. These atoms are loosely bonded and rattle inside the cage which causes phonons to scatter and effectively decreases the thermal conductivity without degrading the electrical properties [8, 9]. Substitution of Te for Sb is an effective way of improving the electrical properties of $CoSb_3$. A significant reduction in electrical resistivity for $Co_4Sb_{12-x}Te_x$ was observed as compared to pure $CoSb_3$ because Te serves as an electron donor in the $CoSb_3$ structure [10].

Ytterbium (Yb) is an effective dopant in the $CoSb_3$ structure due to its high atomic mass and (173.04 amu) and small ionic size (0.0858nm). By partially filling the cages in $CoSb_3$ structure with Yb, the thermal conductivity is significantly decreased (~ 4 W/m.K) [11] while slightly affecting the Seebeck coefficient and electrical resistivity [6].

In the present work, we used the concept of PGEC for $CoSb_3$ to reduce thermal conductivity while maintaining the electrical properties. Previous work on mixed stuffing and substitution reported lattice thermal conductivity of 1.5 W/m.K [12] and 1.3 W/m.K [13]. These reports utilized indium (In) stuffing in germanium (Ge) substituted and nickel (Ni) substituted $CoSb_3$ materials respectively. For the first time ytterbium stuffed and tellurium substituted $CoSb_3$ was synthesized in order to decrease thermal conductivity without affecting electrical conductivity and Seebeck coefficient.

7.2 EXPERIMENTAL DETAILS

Pure and Yb and Te doped $CoSb_3$ based compositions were synthesised by mechanical alloying. Commercially available powders of Co (99.8% pure), Sb (99.5% pure), Te (99.999% pure) and Yb (99.8% pure) were mixed in the stoichiometric ratios to obtain $CoSb_3$ (CS), $CoSb_{2.85}Te_{0.15}$ (CST) and $Yb_{0.075}CoSb_{2.85}Te_{0.15}$ (YCST). Mixing of powders was carried out inside an Ar filled glove box in steel jars to avoid oxidation of the powders. The steel jars were loaded into the planetary ball mill and rotated at a speed of 350 rpm for 40 hours [14]. The mechanically alloyed powders were sintered into 20 millimetre discs by SPS at 600 ^oC for 5 minutes in an argon environment. A heating rate of 100^oC/min was used. All the samples were more than 98% dense as measured by the Archimedes principle. The samples were cut into 3 x 3 x 15 mm bars for electrical resistivity and Seebeck coefficient measurement via temperature differential and four point probe methods in lab-made apparatus under vacuum.

7.3 RESULTS AND DISCUSSIONS

Figure 7.1 shows XRD of sintered $CoSb_3$ based materials. The diffraction peaks indicate that the major phase is $CoSb_3$ (XRD PDF card: 76-0470) with slight amounts of impurity phases which are $CoSb_2$ (XRD PDF card: 65-4102) and $CoTe_2$ (XRD PDF card: 89-2091). These results are consistent with the previous studies, [10] which indicate that the formation of a secondary phase is a common problem. All of the peaks of the major phase in the Te substituted material are shifted towards low angle, which indicates that the lattice parameter has increased. This indicates that the Te and Yb atoms were accommodated into the structure of $CoSb_3$.

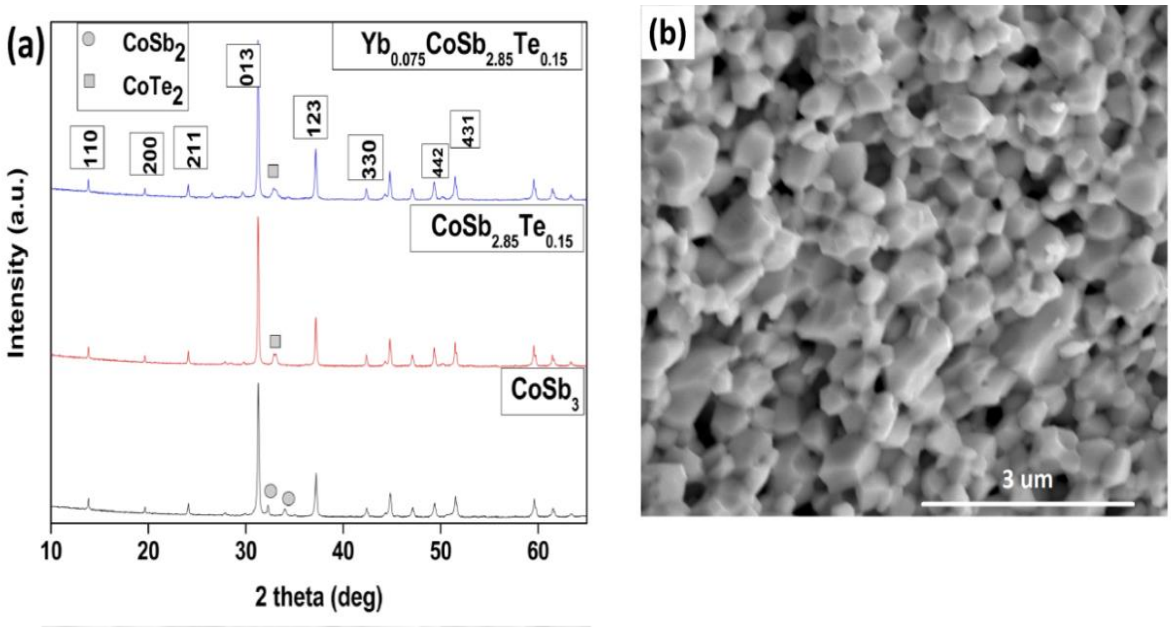

Figure 7.1: *(a) X ray diffraction patterns for $CoSb_3$ based materials; (b) SEM micrograph of $CoSb_3$*

SEM images showed that the $CoSb_3$ had high density (~ 98%) and consisted of angular grains ~ 0.8 µm. For the materials doped and substituted with Yb and Te,

the grains size decreased to 0.27 μm and 0.19 μm for CST and YCST respectively without affecting the grain shape.

Figure 7.2(a) shows electrical resistivity data for the $CoSb_3$ based materials. The electrical resistivity of $CoSb_3$ decreased with increasing temperature consistent with its semiconducting properties [15]. A considerable decrease in electrical resistivity was observed upon Te addition compared to that of pure CS. The electrical resistivity increased with increasing temperature indicating metallic like behaviour [16]. As mentioned earlier, Te atoms serve as electron donors in the CS lattice, thus providing more electrons to the structure leading to decreased electrical resistivity. This increased carrier concentration raises the Fermi level giving rise to a degenerate semiconductor [17]. Yb addition to CST further reduced electrical resistivity slightly as shown in Figure 7.2(a). This indicates that Yb donates its outermost electrons, which further decreases electrical resistivity [18].

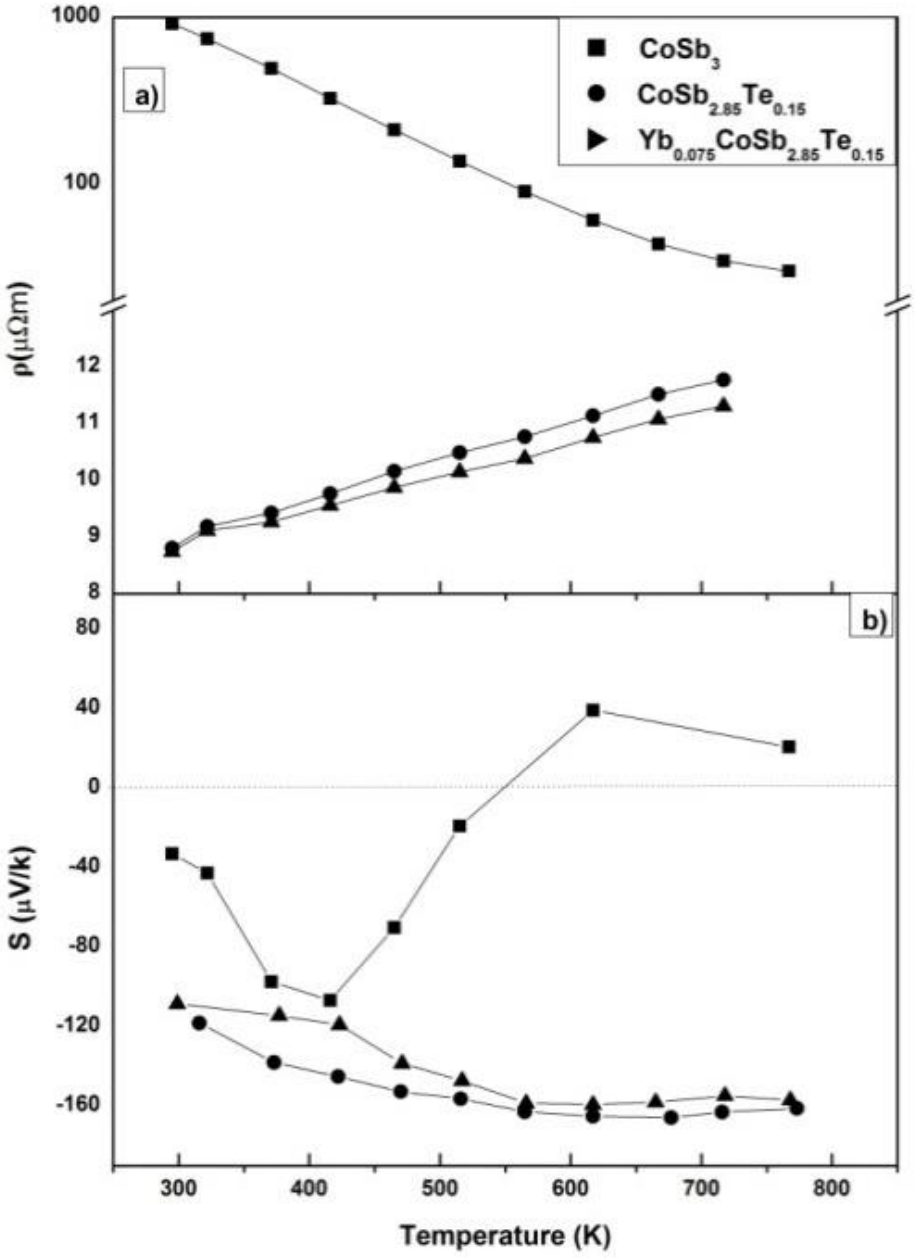

Figure 7.2: *Variation of: (a) electrical resistivity; (b) Seebeck coefficient with temperature for $CoSb_3$ compositions*

Figure 7.2(b) shows Seebeck coefficient data for the $CoSb_3$ based materials. At room temperature CS behaves as an n type semiconductor but at temperatures higher than 600 K, it behaves as a p type semiconductor, which is consistent with other reports [19]. This is because the mobility of the holes produced by the strong intrinsic conduction is much higher in the temperature range of more than 600 K

than the electron mobility produced by the weak extrinsic conduction [20]. Addition of Yb and Te at the same time to $CoSb_3$ resulted in a higher negative Seebeck value that increased with increasing temperature. A maximum value of ~ 160 μV/K was achieved at 600 K. This increase is gradual and the value of Seebeck coefficient remains nearly constant in the temperature range of ~ 600-800 K. Considering the Fermi Dirac statistics, the Seebeck coefficient values can be expressed as [21]

$$S = \frac{k_B}{e}\left(2\frac{F_1(\xi)}{F_0(\xi)} - \xi\right) \tag{2.6}$$

Where k_B is the Boltzmann constant, e is the unit charge, Fn(ξ) is the nth order Fermi integral and ξ is the reduced Fermi energy. Since the Fermi energy decreases with temperature, the (negative) Seebeck coefficient increases with increasing temperature. In the temperature range of 600-800 K, the value of the Seebeck coefficient remains nearly constant which is attributed to the mixed conduction [22]. The combined effect of both the charge carriers in CST and YCST results in the Seebeck coefficient being nearly constant.

The most dramatic impact of Yb stuffing and Te substitution in $CoSb_3$ is on its thermal conductivity. In Figure 7.3(a) the total thermal conductivity (κ_T) of YCST is plotted against temperature. For comparison, κ_T of CS and CST are also plotted. In the case of pure $CoSb_3$ the κ_T decreases with increase in temperature and reaches a minimum at ~ 550 K. After reaching the minimum the value of κ_T increases with increase in temperature. This increase of thermal conductivity at higher temperature is related to the bipolar effect which will be explained later.

From the data it is obvious that the simultaneous addition of Yb and Te is more effective than substituting Te alone into $CoSb_3$. A minimum value of 2.19 W/mK was observed at ~ 550 K for YCST. This value is lower than the one reported for single crystal $CoSb_3$ (4 W/m.K) [23], and $Yb_{0.26}Co_4Sb_{12}$/GaSb nanocomposite (2.6W/m.K) [22]. Our value is comparable to Yb doped nanostructured $CoSb_3$ (2.15 W/m.K) [24], which indicates that instead of employing costly nanostructuring processing, a very low value of thermal conductivity can be achieved by simultaneous stuffing and substitution.

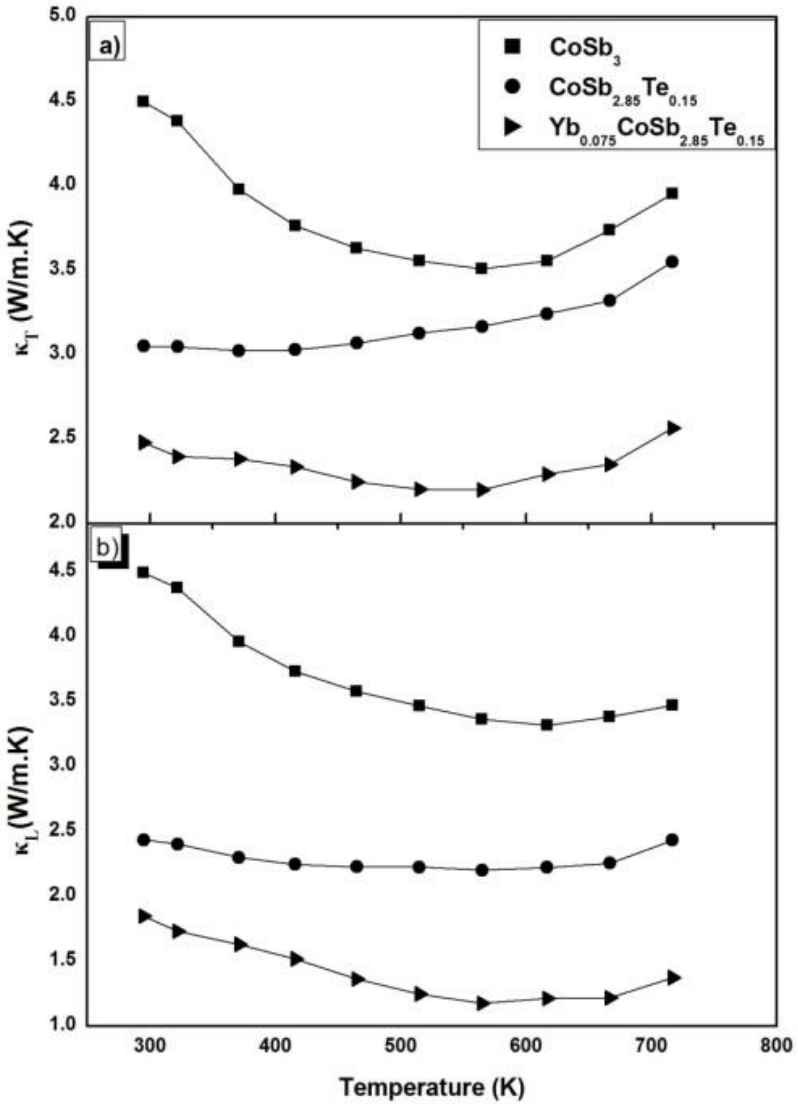

Figure 7.3: *Variation of: (a) total thermal conductivity; (b) lattice thermal conductivity with temperature for $CoSb_3$ based compositions*

In order to study the effect of Yb stuffing and Te substitution on lattice thermal conductivity (κ_L), the lattice thermal conductivity was calculated by subtracting the electronic contributions to the thermal conductivity (κ_e) from total thermal conductivity. κ_e was calculated by using Weidman- Franz Law which is written as

$$\kappa_{elec} = LT\sigma \tag{2.4}$$

Where L is the Lorenz number, T is the absolute temperature and σ is the electrical conductivity. Assuming $CoSb_3$ is a homogeneous material with a parabolic band dominated by acoustic phonon scattering at low temperatures ($\kappa_{Lattice}$ α T^{-1}), the Lorenz number is given as [21]

$$L = \left(\frac{k_B}{e}\right)^2 \left(\frac{3F_0(\xi)F_2(\xi) - 4F_1^{\,2}(\xi)}{F_0^{\,2}(\xi)}\right) \tag{2.5}$$

ξ increases by the addition of Yb in $CoSb_{2.85}Te_{1.5}$ which indicates that the $CoSb_3$ is still a degenerate semiconductor which is in consistent with the electrical resistivity. The calculated L values for CS, CST and YCST were $2.3x10^{-08}$ $V^{2/}K^2$, $1.8x10^{-08}$ $V^{2/}K^2$ and $1.9x10^{-08}$ $V^{2/}K^2$ respectively which are in good agreement with literature [17].

Figure 7.3(b) shows the variation of the lattice thermal conductivity with temperature. An almost 70% reduction in lattice thermal conductivity of CS was produced by the addition of Yb and Te to $CoSb_3$, reaching a minimum value of 1.17 W/m.K. This is lower than the one reported by Malik et. al (1.5 W/m.K) for In

stuffed and Ge doped $CoSb_3$ [11] and (~ 1.3W/m.K) for In stuffed and Ni doped $CoSb_3$ [12]. This value is even lower than double stuffed $CoSb_3$ with Yb and Ba (2.2 W/m.K) [8]. However, the lattice thermal conductivity is still higher than the calculated minimum thermal conductivity of 0.66 W/m.K for YCST calculated using [25]

$$\kappa_{min} = 0.87 k_B \Omega^{-2/3} \left(\frac{E}{\rho}\right)^{1/2} \quad (6.1)$$

Where E is the elastic modulus taken as 148 GPa [26].

In order to investigate the effect of Yb and Te on $CoSb_3$, the phonon mean free path (η) of all the 3 materials were calculated by using [27]

$$\eta = \frac{\kappa \Omega}{k_B V} \quad (6.4)$$

Where κ is the lattice thermal conductivity and V is the velocity of sound in the solids calculated through elastic modulus and density data. Substituting the respective values of κ, Ω, k_B and V into the equation, η for CS, CST and YCST were estimated to be ~ 1.57 nm, 0.98 nm and 0.76 nm respectively. From these values it is evident that the phonon mean free path was almost halved by the addition of Yb and Te (compared to CS) which corresponds to the separation between the rare earth elements rattling inside a crystal (~ 8 Å) [28].

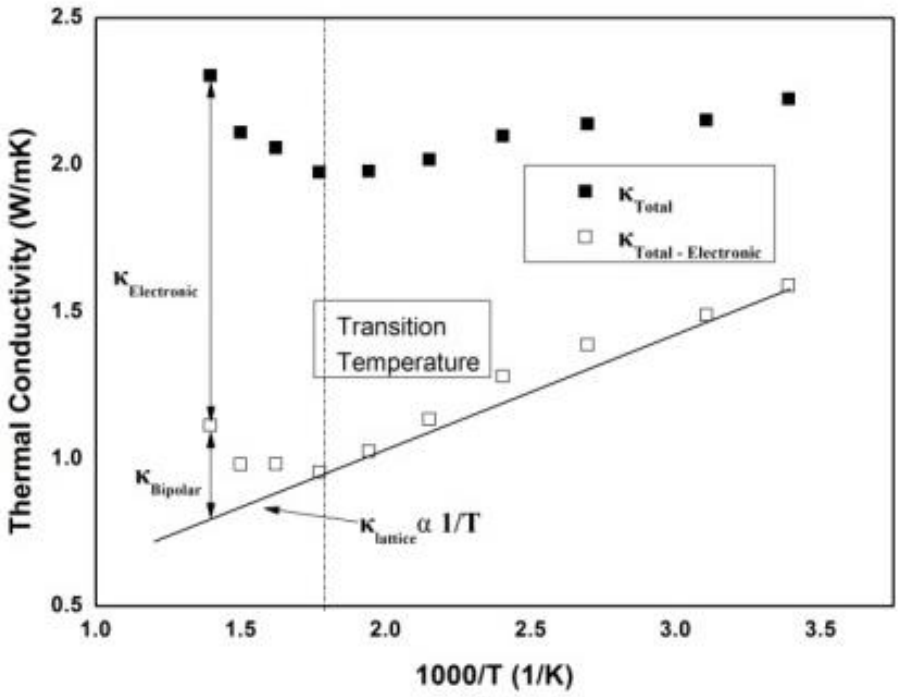

Figure 7.4: *Components of total thermal conductivity with T^{-1} for YCST*

The minor charge carriers which start operating in the higher temperature region (550 K to 750 K) not only affect the Seebeck coefficient, but also increase thermal conductivity. Electrons - holes pairs are generated by the absorption of energy at the hot end. These pairs recombine by releasing energy when they move to the cold end and thus increase thermal conductivity. This phenomenon is called as bipolar diffusion. So, the total thermal conductivity can now be presented by

$$\kappa_{Total} = \kappa_{electronic} + \kappa_{Lattice} + \kappa_{Bipolar} \quad (7.1)$$

In order to determine the contribution of bipolar diffusion to thermal conductivity in the intrinsic conduction range, a method proposed by Kitgawa et al. is employed [29]. Figure 7.4 shows variation of $\kappa_{Lattice}$ ($\kappa_{Lattice} = \kappa_{Electronic} - \kappa_{Total}$) and κ_{Total} for YCST as a function of T^{-1}. κ_{Total} can be separated into $\kappa_{electronic}$, $\kappa_{Lattice}$ and

$\kappa_{Bipolar}$. Since at low temperatures, the lattice thermal conductivity is proportional to T^{-1} according to the assumption made, the $\kappa_{Lattice}$ was estimated by extrapolating the linearity to high temperatures. As can be seen, the $\kappa_{Lattice}$ is the dominant contribution to total thermal conductivity at low temperatures but at higher temperatures, a prominent increase in $\kappa_{Bipolar}$ was observed. From the above discussion it can be concluded that above the bipolar transition temperature, intrinsic conduction dominates.

Figure 7.5 shows variation of zT with temperature calculated from measured Seebeck coefficient, electrical resistivity and total thermal conductivity. zT value increases with increase in temperature for doped compositions and reaches a value of ~ 0.70 at 600 K for YCST. This increase in zT value is due to the low value of lattice thermal conductivity produced by the partial filling by Yb atoms of the cage like structure of $CoSb_3$.

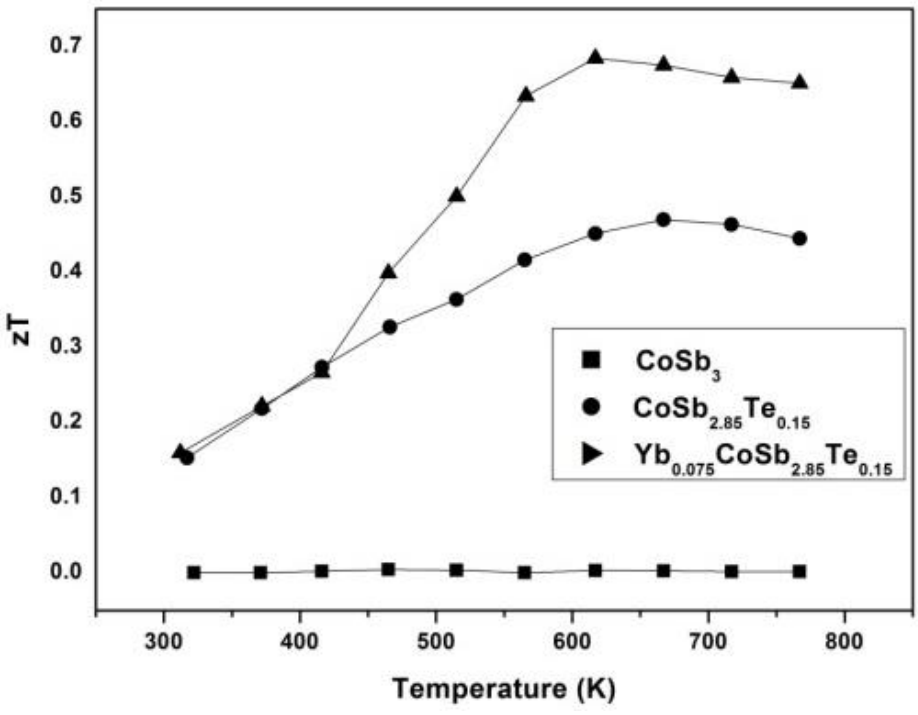

Figure 7.5: *Temperature dependence of zT for $CoSb_3$ based compositions*

7.4 CONCLUSION

Combined Yb stuffed and Te substituted $CoSb_3$ was synthesized by mechanical alloying and spark plasma sintering. Lattice thermal conductivity was significantly reduced to a very low value of 1.17 W/m.K by the addition of Yb atoms into $CoSb_{3-x}Te_x$ without significantly affecting Seebeck coefficient and electrical resistivity. This value is comparable to those of produced by the costly processing of nanostructured materials. A zT value of ~ 0.70 was obtained at 600 K.

REFERENCES

[1] G. Li, J.Y. Yang, Y. Xiao, L.W. Fu, J.Y. Peng, Y. Deng, P.W. Zhu, H.X. Yan, Journal of Electronic Materials, 42 (2013) 675-678.

[2] J.J. Zhang, B. Xu, L.M. Wang, D.L. Yu, Z.Y. Liu, J.L. He, Y.J. Tianb, Applied Physics Letters, 98 (2011) 072109.

[3] A. Harnwunggmoung, K. Kurosaki, H. Muta, S. Yamanaka, Applied Physics Letters, 96 (2010) 202107.

[4] H.Y. Geng, S. Ochi, J.Q. Guo, Applied Physics Letters, 91 (2007) 022106.

[5] W.-S. Liu, B.-P. Zhang, J.-F. Li, L.-D. Zhao, Journal of Physics D: Applied Physics, 40 (2007) 566-572.

[6] G.S. Nolas, M. Kaeser, R.T. Littleton, T.M. Tritt, Applied Physics Letters, 77 (2000) 1855.

[7] B.C. Sales, D. Mandrus, R.K. Williams, Science, 272 (1996) 1325-1328.

[8] X. Shi, H. Kong, C.P. Li, C. Uher, J. Yang, J.R. Salvador, H. Wang, L. Chen, W. Zhang, Applied Physics Letters, 92 (2008) 182101.

[9] H. Li, X.F. Tang, Q.J. Zhang, C. Uher, Applied Physics Letters, 93 (2008) 252109.

[10] W.S. Liu, B.P. Zhang, L.D. Zhao, J.F. Li, Chemistry of Materials, 20 (2008) 7526-7531.

[11] G. S. Nolas M. Kaeser, R. T. Littleton, T. M. Tritt, Applied Physics Letters, 77 (2000) 1855.

[12] R. Chandra Mallik, E. Mueller, I.-H. Kim, Journal of Applied Physics, 111 (2012) 023708.

[13] J. Jae-Yong, P. Kwan-Ho, K.I.M. Il-Ho, S.-M. Choi, W.-S. Seo, Journal of the Korean Physical Society, 57 (2010) 773.

[14] J. Yang, Y. Chen, J. Peng, X. Song, W. Zhu, J. Su, R. Chen, Journal of Alloys and Compounds, 375 (2004) 229-232.

[15] J.X. Zhang, Q.M. Lu, K.G. Liu, L. Zhang, M.L. Zhou, Materials Letters, 58 (2004) 1981-1984.

[16] Y. Zhu, H. Shen, L. Zuo, H. Guan, Solid State Communications, 151 (2011) 1388-1393.

[17] W.-S. Liu, B.-P. Zhang, J.-F. Li, H.-L. Zhang, L.-D. Zhao, Journal of Applied Physics, 102 (2007) 103717.

[18] A. Zhou, L. Liu, P. Zhai, W. Zhao, Q. Zhang, Journal of Applied Physics, 109 (2011) 113723.

[19] W.-S. Liu, B.-P. Zhang, J.-F. Li, L.-D. Zhao, Journal of Physics D: Applied Physics, 40 (2007) 6784-6790.

[20] M.J. Kim, I.H. Kim, Met Mater Int, 16 (2010) 459-463.

[21] H. Anno, K. Matsubara, Y. Notohara, T. Sakakibara, H. Tashiro, Journal of Applied Physics, 86 (1999) 3780-3786.

[22] Z. Xiong, X.H. Chen, X.Y. Huang, S.Q. Bai, L.D. Chen, Acta Materialia, 58 (2010) 3995-4002.

[23] T. Caillat, A. Borshchevsky, J.P. Fleurial, Journal of Applied Physics, 80 (1996) 4442-4449.

[24] H. Li, X. Tang, X. Su, Q. Zhang, C. Uher, Journal of Physics D: Applied Physics, 42 (2009) 145409.

[25] C.G. Levi, Curr Opin Solid St M, 8 (2004) 77-91.

[26] X.Q. Yang, P.C. Zhai, L.S. Liu, Q.J. Zhang, Journal of Applied Physics, 109 (2011) 123517.

[27] T.D. Sparks, P.A. Fuierer, D.R. Clarke, Journal of the American Ceramic Society, 93 (2010) 1136-1141.

[28] B.C. Sales, D. Mandrus, B.C. Chakoumakos, V. Keppens, J.R. Thompson, Physical Review B, 56 (1997) 15081-15089.

[29] H. Kitagawa, M. Wakatsuki, H. Nagaoka, H. Noguchi, Y. Isoda, K. Hasezaki, Y. Noda, Journal of Physics and Chemistry of Solids, 66 (2005) 1635-1639.

Chapter VIII. Conclusions and Future Work

8.1 CONCLUSION

In this research, the effect of substitution and oxidation-reduction on the microstructure and thermoelectric properties was studied. Research was conducted on oxide and non-oxide materials. For oxide ceramics, $La_4Ti_4O_{14}$ and $Sr_4Nb_4O_{14}$ were studied. $La_{4-x}Sr_xTi_4O_{14-\frac{x}{2}\pm\delta}$ (x=0, 0.2, 0.4, 0.6 and 0.8), $La_4Ti_{4-x}Ta_xO_{14+\frac{x}{2}\pm\delta}$ (x=0, 0.1, 0.2, 0.4 and 0.6), $La_4Ti_{4-x}Nb_xO_{14+\frac{x}{2}\pm\delta}$ (x=0, 0.2, 0.4 and 0.6) and $Sr_{4-x}La_xNb_4O_{14+\frac{x}{2}\pm\delta}$ (x=0, 0.2, 0.4, 0.6 and 0.8) were prepared by solid state reaction. The grain shape and size decreased as compared to the pure compositions.

Acceptor substituted $La_4Ti_4O_{14}$ produced nanoscale intergrowths of 5 layer PLS ceramic and the amount increased after reduction while donor substitution produced intergrowths of 3 layer PLS ceramic which increased after oxidation and decreased after reduction. This was observed by XRD when additional peaks appeared. $La_4Ti_{4-x}Nb_xO_{14+\frac{x}{2}\pm\delta}$ and $Sr_{4-x}La_xNb_4O_{14+\frac{x}{2}\pm\delta}$ did not produce intergrowths but a second phase $LaNbO_4$.

Microstructural and thermal properties were characterised for these materials. Reduction produced some planar defects arising in the pure compositions. TEM confirmed the existence of intergrowths of 5 layer region in $La_{4-x}Sr_xTi_4O_{14-\frac{x}{2}\pm\delta}$ but the existence of 3 layer regions could not be determined in $La_4Ti_{4-x}Ta_xO_{14+\frac{x}{2}\pm\delta}$. This was due to the complex nature of 3 layer PLS ceramics. Formation of $LaNbO_4$ as a separate phase was also confirmed in $La_4Ti_{4-x}Nb_xO_{14+\frac{x}{2}\pm\delta}$ and $Sr_{4-x}La_xNb_4O_{14+\frac{x}{2}\pm\delta}$. The

solubility limit of La in polycrystalline $Sr_{4-x}La_xNb_4O_{14+\frac{x}{2}\pm\delta}$ and Nb in polycrystalline $La_4Ti_{4-x}Nb_xO_{4+\frac{x}{2}\pm\delta}$ is x=0.2.

The thermal properties of the PLS compounds were characterized. All PLS materials showed anomalously low thermal conductivity values. Heavy element substitution (La, Nb and Ta) reduced thermal conductivity while light element (Sr) increased thermal conductivity with increasing amount of substitution due to the mass contrast. Apart from the mass contrast, the thermal conductivity decreased with increasing amount of nanoscale intergrowths which were generated to accommodate compositional non-stoichiometry. A ~ 20% decrease in the theoretical minimum thermal conductivity was achieved due to the nanoscale intergrowths. A very low thermal conductivity value of ~ 0.93 W/m.K was observed in Ta substituted $La_4Ti_4O_{14}$.

For non-oxide ceramics, $CoSb_3$ was chosen due to its cage-like structure. $CoSb_3$ stuffed with Yb and substituted with Te ($Yb_yCoSb_{3-x}Te_x$) was synthesized by mechanical alloying and spark plasma sintering. Electrical and thermal properties were characterized for pure and doped material. A Seebeck coefficient value of ~ 160 μV/K was obtained at ~ 600-800 K for $Yb_{0.075}CoSb_{2.85}Te_{0.15}$. Electric resistivity dropped from ~ 1000 μΩm for pure $CoSb_3$ to ~ 9 μΩm for $Yb_{0.075}CoSb_{2.85}Te_{0.15}$. Lattice thermal conductivity was significantly reduced to a very low value of 1.17 W/m.K by the addition of Yb atoms into $CoSb_{2.85}Te_{0.15}$ without significantly affecting Seebeck coefficient and electrical resistivity. This value is comparable to those of produced by the costly processing of nanostructured materials. A zT value of ~ 0.70 was obtained at 600K.

This research has shown that by engineering the defect chemistry and compositional non-stoichiometry of thermoelectric materials, it is possible to significantly reduce their thermal conductivity without compromising their electrical properties.

8.2 FUTURE WORK

8.2.1 Grain Size Effect

Reducing grain size can significantly reduce thermal conductivity. This effect on thermal conductivity is not studied in PLS compounds. Hence, it would be very useful to compare the effect of grain size on thermal properties of these $A_4B_4O_{14}$ ceramics. This effect can also be related to investigate the electric properties. Spark Plasma Sintering helps to minimise the grain size of the nano-sized ceramics during sintering.

8.2.2 Textured PLS thermoelectrics

As the PLS compounds have plate-like grains and with the help of SPS, these compounds can be textured. A two-step texturing method has been reported in literature to synthesise dense ceramics. Exploring the PLS materials for texturing with different substitution and studying the effect of different variables to control the texturing and grain growth. This can lead to a systematic study to improve thermoelectric properties in PLS materials.

8.2.3 Different PLS compounds

In this research 4 layer PLS compounds have studied and it has been shown that the disorder helps in reduction of thermal conductivity. Other members

of the PLS family i.e. 2 and 3 layer PLS compound ($LaNbO_4$, $La_3Ti_2TaO_{11}$, $LaTaO_4$ etc.) have similar layered crystal structure. There are no known reports of thermal conductivity for these compounds. It may be possible to obtain low thermal conductivity values in these materials and explore the effect of heavy element substitution on A and/or B site.

8.2.4 Melt Spinning of Skutterudite

Melt spinning of skutterudite has been reported to yield good thermoelectric properties. The composition $Yb_{0.075}CoSb_{2.85}Te_{0.15}$ has not been explored by melt spinning. Since this composition has yielded a zT value of ~ 0.7, synthesising this composition with melt spinning can lead to improve zT value of this material. Since $Yb_{0.075}CoSb_{2.85}Te_{0.15}$ is an n type compound, its p type counterpart can also be studied by melt spinning and SPS.

List of my publications

1. H. Porwal, P. Tatarko, S. Grasso, **J. Khaliq**, I. Dlouhý and M. J. Reece, ‘‘Graphene reinforced alumina nano-composites’’, *Carbon*, 2013, **64**, 359-369
2. S. Grasso, N. Tsujii, Q. H. Jiang, **J. Khaliq**, S. Maruyama, M. Miranda, K. Simpson, T. Mori and M. J. Reece, ‘‘Ultra low thermal conductivity of disordered layered p-type bismuth telluride’’, *Journal of Materials Chemistry C*, 2013, **1**,2362-2367
3. G.Viola, H. Ning, X. Wei, M. Deluca, A. Adomkevicius, **J. Khaliq**, M. J. Reece and H. Yan, ‘‘Dielectric relaxation, lattice dynamics and polarization mechanisms in $Bi_{0.5}Na_{0.5}TiO_3$-based lead-free ceramics’’, *Journal of Applied Physics*, 2013, **114**, 014107
4. **J. Khaliq**, Q Jiang, J. Yang, K. Simpson, H. Yan and M. J. Reece, ‘‘Utilizing the phonon glass electron crystal concept to improve the thermoelectric properties of combined Yb-stuffed and Te-substituted $CoSb_3$’’, *Scripta Materialia*, 2014, **72-73**, 63-66
5. Q. Jiang, H. Yan, **J. Khaliq**, H. Ning, S. Grasso, and M. J. Reece, ‘‘Large ZT enhancement in hot forged nanostructured p-type $Bi_{0.5}Sb_{1.5}Te_3$ bulk alloys, *Journal of Materials Chemistry A*, 2014, **2**, 5785
6. **J. Khaliq**, C. Li, K. Chen, B. Shi, H. Ye, K. Simpson, H. Yan, A.M. Grande and M. J. Reece, Reduced thermal conductivity induced by nanoscale intergrowths in perovskite like layered structure $La_2Ti_2O_7$, (Under Preparation)